Civil and Environmental Engineering Report Series
Report No. 3
May 2026

CAN23-121: Parameter and Performance Investigation of a Multi-directional Ring Particle Damper

Lydia Foster[1]
Nicholas E. Wierschem[1*]
J. Brent Knight[2]

[1]University of Tennessee
[2] NASA Marshall Space Flight Center
[*]nwiersch@utk.edu



THE UNIVERSITY OF
TENNESSEE
KNOXVILLE

DEPARTMENT OF CIVIL &
ENVIRONMENTAL ENGINEERING

The University of Tennessee is a Public Land Grant University that was founded in 1794 as Blount College. Instruction in civil engineering began at the University of Tennessee in 1834, then East Tennessee College, after Joseph Estabrook became president. In 1993 the department's name changed to Civil and Environmental Engineering to reflect the significance of Environmental Engineering in the department's activities. In 2013, the department moved into the newly constructed John D. Tickle Engineering Building. The bridge connecting the John D. Tickle Engineering Building with Estabrook Road is featured on the cover page of this report series and serves as a symbol for the department.

Contact:
Department of Civil and Environmental Engineering
325 John D. Tickle Building
851 Neyland Drive, Knoxville TN 37996-2313
Phone: 865-974-2503
Fax: 865-974-2669
E-mail: cee@utk.edu

The material in this document is based upon work supported by NASA under award No 80NSSC24M0077. Any opinions, findings, and conclusions or recommendations expressed in this material are those of the author(s) and do not necessarily reflect the views of the National Aeronautics and Space Administration.

The PI for this project was Nicholas Wierschem. Lydia Foster was the graduate student researcher. J. Brent Knight was the NASA technical collaborator for this project.

Abstract

Particle dampers can be mounted or incorporated into vibrating host structures and consist of a chamber filled with particles, often ball-bearings. When subjected to structural vibration, the particle motion induces collisions and friction that dissipate energy, reducing the overall system response. NASA hardware is exposed to complex vibration due to its launch environment, making effective vibration mitigation essential for maintaining functionality. Additionally, NASA hardware is often subjected to multi-directional bending, torsional, and breathing modes, characterized as radial deformation of the host structure. While particle dampers offer a low-complexity and cost-efficient passive vibration control solution, previous studies have primarily focused on vibration and mitigation in one direction only. This work proposes and experimentally evaluates a multi-directional passive vibration mitigation device called a ring particle damper. A ring particle damper is composed of a hollow ring configuration, consisting of cavities filled with particles. Due to the unique geometry, the multi-directional performance of the device is unclear. An experimental investigation was conducted to evaluate how the device's parameters influence its performance and assess how effective the device is at mitigating multi-directional vibration. The ring particle damper was attached to a thin-walled hollow cylindrical host structure, exhibiting bending, breathing, and torsional modes similar to NASA hardware (Figure 1). The system response was evaluated using RMS acceleration, auto-power spectral densities, transfer functions, H_2 norm, and $H\infty$ norm. Across most response metrics of the performance experiments conducted, the results indicate that the ring particle damper provides effective damping of mitigating multi-directional vibration at peak displacement and acceleration locations along the host structure. Reductions of approximately 40 to 60% in modal amplitudes were observed for first bending, second bending, and breathing modes relative to corresponding control cases (Figure *2*). The ring particle damper demonstrated potential for energy dissipation under torsional excitation. However, due to the complex coupled modal behavior of the cylindrical structure, pure torsional response mitigation remained unclear. These findings demonstrate the potential of the ring particle damper as an effective multi-directional vibration mitigation solution, and support further development of this concept.

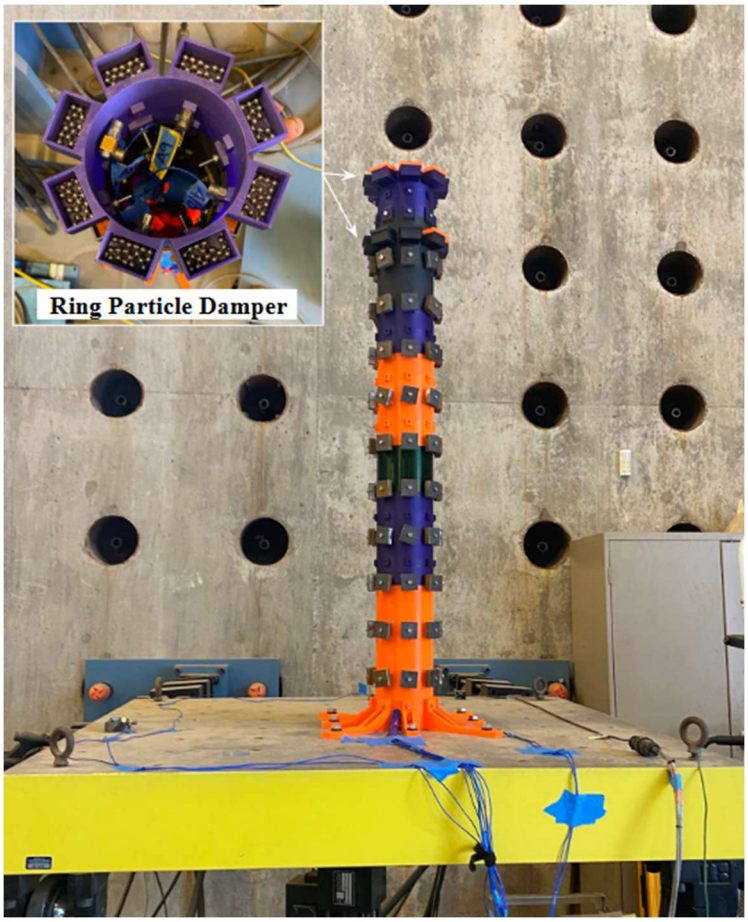


Figure 1. Experimental configuration of a 4-ft structure mounted on a shake table, showing two ring particle dampers installed at the 48-in and 42-in elevations.

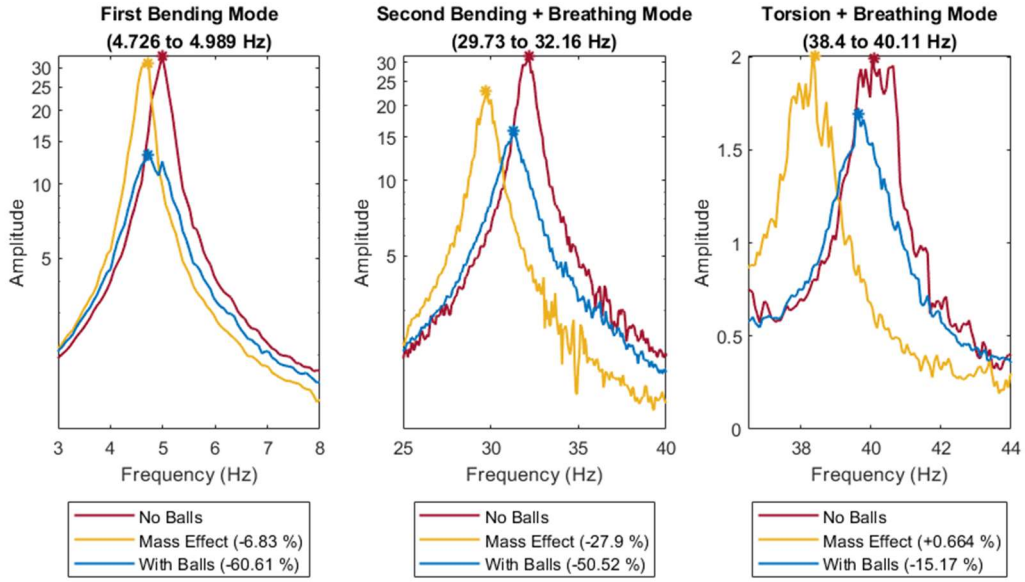


Figure 2.Transfer function overview of the performance of the ring particle dampers. The percentages indicate the percent change normalized with respect to the "no particles" control case.

Table of Contents

List of Tables ..... **v**

List of Figures ..... **vi**

1. Introduction **1**

2. Experimental Specimen Design and Fabrication **2**

2.1. Numerical Experiments *2*

2.2. Specimen Fabrication *10*

3. Experimental Methods **19**

3.1 Test Setups *19*

3.2 Input Excitation *21*

3.3 Instrumentation and Sensor Layout *25*

3.3.1 Initial Parametric Study Sensor Layout *26*

3.3.2 Effectiveness Demonstration Sensor Layout *27*

3.4 Response metrics *27*

3.4.1 Control Cases *28*

3.4.2 Low Pass Filtering and High Frequency Results *28*

3.4.3 RMS Acceleration *29*

3.4.3 Auto-Power Spectral Density *29*

3.4.4 Transfer Functions *30*

3.4.5 Additional Frequency Response metrics *30*

4. Initial Parametric Studies **31**

4.1. Results and Discussions *31*

4.1.1 Optimal Particle Packing Ratio *31*

4.1.2 Initial White Noise Excitation Amplitude *36*

4.1.3 Initial Container Usage *38*

4.1.4 Optimal Device Location *40*

4.1.5 Cavity Layer Usage *43*

4.1.6 Device Cavity Lining Material *45*

4.1.7 Sinusoidal Excitation *48*

4.1.8 Sine Sweep Excitation *51*

5. Effectiveness Demonstration 55

5.1. Results and Discussions 55

5.1.1 Multi-Directional White Noise Excitation Amplitude 55

5.1.2 Particle Material Type 60

5.1.3 Multi-Directional Container Usage 64

5.1.4 Torsional Excitation 66

6. Lessons Learned 69

6.1 Numerical Modal Analysis Using Autodesk Inventor 69

6.2 3D Printing Fabrication and Construction 69

6.3 Instrumentation and Sensor Layout 70

7. Recommendations for Future Work 70

8. Conclusions 70

Appendix A: Results from Initial Parametric Studies 1

Appendix B: Results from Effectiveness Demonstration 1

List of Tables

Table 1. Aluminum material properties 3
Table 2. PLA material properties 5
Table 3. Autodesk Inventor modal analysis results of the host structure design 6
Table 4. Measured table-mounted acceleration representing the excitation applied to the structure on the small shake table. 22
Table 5. Measured table-mounted acceleration representing the excitation applied in the X-direction to the structure on the big shake table. 24
Table 6. Measured table-mounted acceleration representing the excitation applied in the Y-direction to the structure on the big shake table. 24
Table 7. Measured table-mounted acceleration representing the excitation applied in the theta-Z direction to the structure on the big shake table. 24
Table 8. Summary of optimal particle ratio mass tests 32
Table 9. Device cavity lining study particle packing ratios 46
Table 10. Measured table-mounted acceleration representing the sinusoidal excitation applied in the X-direction to the structure on the small shake table. 49
Table 11. Measured table-mounted acceleration representing the sine sweep excitation applied in the X-direction to the structure on the small shake table. 53

List of Figures

Figure 1. Experimental configuration of a 4-ft structure mounted on a shake table, showing two ring particle dampers installed at the 48-in and 42-in elevations. ii
Figure 2.Transfer function overview of the performance of the ring particle dampers. The percentages indicate the percent change normalized with respect to the “no particles” control case. ii
Figure 3. Initial host structure Inventor model 3
Figure 4. Host structure Inventor model with added masses at device locations 4
Figure 5. Host structure Autodesk Inventor model with a distributed mass system and device mass modeled 5
Figure 6. Autodesk Inventor modal analysis result showing the first bending mode with a predicted frequency of 4.42 Hz. 7
Figure 7. Autodesk Inventor modal analysis result showing a breathing mode, classified as a two-point configuration (top view) with top-concentrated expansion (profile view), and a predicted frequency range of 13.89 Hz and 16.00 Hz. 7
Figure 8. Autodesk Inventor modal analysis result showing a breathing mode, classified as a two-point configuration (top view) with mid-concentrated expansion (profile view), and a predicted frequency range of 20.89 Hz and 21.66 Hz. 8
Figure 9. Autodesk Inventor modal analysis result showing the second bending mode with a predicted frequency range of 25.93 Hz and 26.10 Hz. 8
Figure 10. Autodesk Inventor modal analysis result showing a torsion mode with a predicted frequency of 27.18 Hz. 9
Figure 11. Autodesk Inventor modal analysis result showing an axial mode with a predicted frequency range of 55.05 Hz. 9
Figure 12. Initial Autodesk Inventor rendering of test structure 10
Figure 13. Standard cylinder segment design 11
Figure 14. Segment connection 11
Figure 15. Cylinder segment connection details 12
Figure 16. Example of a system weight mounted on the host structure 12
Figure 17. Cylinder segment with accelerometer mounting surface design 13
Figure 18. Tangential accelerometer attachment connection 14
Figure 19. Cylinder base segment design 14
Figure 20. Leg design 15
Figure 21. Base connection design adaptability between shake tables 16
Figure 22. Ring particle damper cylinder segment design 17
Figure 23. Ring particle damper container geometry. All dimensions are in inches. 17
Figure 24. Layer cap design 18
Figure 25. Mass cap design 18
Figure 26. Default test setup for parametric studies. Elevations are measured from the bottom of the structure. 20

Figure 27. Default test setup for effectiveness demonstrations studies. Elevations are measured from the bottom of the structure. 21
Figure 28. Autopower spectral densities (APSDs) of the table-mounted acceleration measured by sensor T2 on the small shake table under various excitation amplitudes. The APSDs are separated into three graphs to improve clarity and for individual curves to be easily distinguished. 23
Figure 29. Frequency response function of the big shake table under white noise excitation at various input scaling factors. The APSDs are separated into three graphs to correspond to the excitation scale factor applied in each axis of motion. 25
Figure 30. Default sensor layout for parametric studies on the small shake table. Elevations are measured from the bottom of the structure. Table-mounted and structure-mounted accelerometers are denoted as (T) and (A). 26
Figure 31. Default sensor layout for parametric studies on the big shake table. Elevations are measured from the bottom of the structure. Table-mounted and structure-mounted accelerometers are denoted as (T) and (A). 27
Figure 32. Frequency response function example of the full frequency range (0 to 825 Hz) 29
Figure 33. Frequency response function example of the relevant frequency range (0 to 50 Hz). 29
Figure 34. Particle bearing packing ratios 33
Figure 35. Percent change in RMS response as a function of particle packing ratio (Study 1). Measurements from the top (T) and bottom (B) particle layers are shown. Values are normalized to the corresponding no-particle case. 34
Figure 36. Percent change in frequency domain response metrics (H2 and H∞) as a function of particle packing ratio (Study 1). Measurements from the top (T) and bottom (B) particle layers are shown. Values are normalized to the corresponding no-particle case..... 34
Figure 37. Percent change in frequency domain response metrics (H2 and H∞) as a function of particle packing ratio (Study 2). Measurements from the top (T) and bottom (B) particle layers are shown. Values are normalized to the corresponding no-particle case..... 35
Figure 38. Frequency response function for sensor, A9, comparing no-particle case, added mass case, and particle-filled 15 (T) and 18 (B) packing ratios. Percent changes are normalized with the corresponding no-particle case..... 36
Figure 39. Percent change in the transfer function amplitude response at the first bending mode and second bending/top breathing modes with varying white-noise excitation amplitudes on the small shake table. Values are normalized to the corresponding no-particle case. 37
Figure 40. Percent change in the RMS response with varying white-noise excitation amplitudes on the small shake table. Values are normalized to the corresponding no-particle case..... 38
Figure 41. Initial container usage study configurations..... 38
Figure 42. Percent change in the transfer function amplitude responses at the first bending mode and second bending/ top breathing modes with respect to different particle damper container configurations on the small shake table. The values are normalized to the corresponding no-particle case..... 39

Figure 43. Percent change in the APSD amplitudes at the first bending mode and second bending/top breathing modes for different ring particle damper locations along the height of the structure (Study 1). Elevations indicate the distance from the bottom of the structure. Values are normalized to the corresponding no-particle case. 41
Figure 44. Optimal device location study 2 42
Figure 45. Percent change in the transfer function amplitudes at the first bending mode and second bending/top breathing modes for different ring particle damper locations along the height of the structure (Study 2). Elevations indicate the distance from the bottom of the structure. Values are normalized to the corresponding no-particle case. 43
Figure 46. Cavity layer usage “with particles” test configurations. 44
Figure 47. Percent change in the RMS response for different cavity layer configurations. “1 Layer” represents the one cavity packed with 35 particles, and “2 Layers” refers to two cavities used with a (15 Top / 18 Bottom) packing ratio. Values are normalized to the corresponding no-particle case. 44
Figure 48. Percent change in the transfer function amplitude response for different cavity layer configurations at the first bending mode and the second bending/ top breathing mode. “1 Layer” represents the one cavity packed with 35 particles, and “2 Layers” refers to two cavities used with a (15 Top / 18 Bottom) packing ratio. Values are normalized to the corresponding no-particle case. 45
Figure 49. Cylinder segment with steel cavity lining (top view) 46
Figure 50. Percent change in the RMS response as a function of different particle damper cavity materials. PLA and steel packing ratios are shown, and the percent changes are normalized with respect to the corresponding no-particle case. 47
Figure 51. Percent change in the APSD amplitude at the first bending mode and second bending/top breathing modes as a function of different particle damper cavity materials. PLA and steel packing ratios are shown, and the percent changes are normalized with respect to the corresponding no-particle case. 48
Figure 52. Frequency response function at the first bending mode under sinusoidal excitation, comparing the no-particle case, the with-particle case, and the added mass case at varying excitation amplitudes. The excitation frequency was 5.21 Hz for the no-particle configuration, and 5.01 Hz for the with-particles and added mass configurations. 49
Figure 53. Percent change in the APSD amplitude at the first bending mode under varying sinusoidal excitation amplitudes. The excitation frequency was 5.21 Hz for the no-particle configuration, and 5.01 Hz for the with-particles and added mass configurations. Values are normalized to the corresponding no-particle case. 50
Figure 54. Percent change in frequency domain response metrics (H2 and H∞) under sinusoidal excitation amplitudes. The excitation frequency was 5.21 Hz for the no-particle configuration, and 5.01 Hz for the with-particles and added mass configurations. Values are normalized with respect to corresponding no-particle configurations. 50

Figure 55. Frequency response function of the small shake table under 30-second sine sweep excitation from 3.5 to 6.5 Hz at various input scaling factors. The APSDs are separated into two graphs to improve clarity and for individual curves to be easily distinguished..... 51
Figure 56. Acceleration time histories of sine sweep tests at various amplitudes. Excitation is applied in the X- direction to the structure on the small shake table. 52
Figure 57. Percent change in RMS response for a 30-second sine sweep test from 3.5 to 6.5 Hz at varying in excitation amplitude. Values are normalized to the corresponding no-particle case... 53
Figure 58. Percent change in transfer function amplitude response at first bending mode for a 30-second sine sweep test from 3.5 to 6.5 Hz at varying in excitation amplitude. Values are normalized to the corresponding no-particle case. 54
Figure 59. Percent change in frequency domain response metrics (H2 and H∞) for a 30-second sine sweep test from 3.5 to 6.5 Hz at varying in excitation amplitudes. Values are normalized to the corresponding no-particle case..... 54
Figure 60. Percent change in RMS response of the +X sensor under varying excitation amplitudes applied in the +X axis of the big shake table. Values are normalized to the corresponding no-particle configuration. 56
Figure 61. Percent change in RMS response of the +Y sensor under varying excitation amplitudes applied in the +Y axis of the big shake table. Values are normalized to the corresponding no-particle configuration. 56
Figure 62. Percent change in RMS response of the +X and +Y sensors under varying excitation amplitudes applied simultaneously along the +X and +Y axes of the big shake table. Values are normalized to the corresponding no-particle configuration. 57
Figure 63. Percent change in transfer function amplitude response of the + X sensor at first bending mode and second bending/top breathing modes under varying excitation amplitudes applied in the +X axis of the big shake table. Values are normalized to the corresponding no-particle configuration. 58
Figure 64. Percent change in transfer function amplitude response of the +Y sensor at first bending mode and second bending/top breathing modes under varying excitation amplitudes applied in the +Y axis of the big shake table. Values are normalized to the corresponding no-particle configuration. 59
Figure 65. Percent change in transfer function amplitude response of the +X and +Y sensor at first bending mode and second bending/top breathing modes under varying excitation amplitudes applied simultaneously along the +X and +Y axes of the big shake table. Values are normalized to the corresponding no-particle configuration. 60
Figure 66. Percent change in RMS response of the +X and +Y sensors, comparing the particle material type under varying excitation amplitudes applied simultaneously in the +X and +Y axes of the big shake table. Particle packing ratios are defined as distinct top (T) and bottom (B) layers. Values are normalized to the corresponding no-particle configuration. 61
Figure 67. Percent change in frequency domain response metrics (H2 and H∞) of the +X sensor, comparing particle material type under varying excitation amplitudes applied simultaneously in

the +X and +Y axes of the big shake table. Particle packing ratios are defined as distinct top (T) and bottom (B) layers. Values are normalized to the corresponding no-particle configuration. .. 62
Figure 68. Percent change in frequency domain response metrics (H2 and H∞) of the +Y sensor, comparing particle material type under varying excitation amplitudes applied simultaneously in the +X and +Y axes of the big shake table. Particle packing ratios are defined as distinct top (T) and bottom (B) layers. Values are normalized to the corresponding no-particle configuration. .. 63
Figure 69. Multi-Direction Container Usage Study Configurations..... 64
Figure 70. Percent change in transfer function amplitude response of the +X sensor at the first bending mode, comparing ring particle damper container usages under varying excitation amplitudes applied simultaneously in the +X and +Y axes of the big shake table. Values are normalized to the corresponding no-particle configuration..... 65
Figure 71. Percent change in transfer function amplitude response of the +X sensor at the second bending/ top breathing mode, comparing ring particle damper container usages under varying excitation amplitudes applied simultaneously in the +X and +Y axes of the big shake table. Values are normalized to the corresponding no-particle configuration. 66
Figure 72. Frequency response function of the torsion sensor (A12-A8) considering input of base torsion as represented by sensor (T1-T2) at second bending modes and torsion/breathing modes, comparing particle material type under varying torsional excitation amplitudes applied in the theta-Z axis (scale factor = 1) of the big shake table. Values are normalized to the corresponding no-particle configuration..... 67
Figure 73. Percent change in transfer function response of the torsion sensor (A12-A8) considering input of base torsion as represented by sensor (T1-T2) at second bending modes and torsion/breathing modes, comparing particle material type under varying torsional excitation amplitudes applied in the theta-Z axis of the big shake table. Values are normalized to the corresponding no-particle configuration..... 68

1. Introduction

NASA hardware is exposed to extreme vibration environments during launch, making effective vibration mitigation essential for the systems to remain safe and functional. One promising low-complexity and cost-effective passive vibration control solution is the particle damper. Particle dampers consist of a chamber containing ball-bearing particles that can be mounted or integrated into vibrating host structures. The structural vibration induces particle motion, resulting in energy dissipation through friction and collisions between the particles and chamber walls. Despite the complexity of particle-collision interactions, the net effect increases system damping and response attenuation.

Previous studies of particle damper designs have investigated the effects of device parameters, such as particle size and particle material, as well as various loading conditions, such as harmonic and random vibration. These studies have demonstrated effective mitigation of vibrations for systems excited in a single direction. However, relatively few investigations have assessed their performance under multi-directional vibration. This limitation adds complexity to its application to NASA hardware, as the hardware is exposed to vibrations in multiple directions simultaneously with important modes of vibrations of multi-directional bending modes, torsional modes, longitudinal modes and breathing modes. The latter are characterized by radial expansion and contraction. Conventional particle dampers' designs have primarily considered vibration and mitigation in one direction only and may be insufficient to mitigate multi-directional dynamic modes. While one approach is to utilize multiple particle dampers, each turned to a specific direction, designing these devices independently can lead to inefficiencies and potential overdesign. In contrast, a single particle damper device designed to mitigate multi-directional vibrations can achieve a reduced total system mass while improving efficiency by covering multiple modes.

This project proposes a multi-directional passive vibration mitigation solution referred to as a ring particle damper (RPD). The device consists of a ring configuration with multiple disconnected cavities filled with particles, which is mounted onto the host structure. The cavity configuration allows particle interaction while preventing particles from accumulating in one region of the device. The geometric arrangement of these cavities allows for significant particle movement in response to vibrations of the host structure oriented in any radial direction, with the potential to dissipate energy associated with bending, breathing, and torsional modes. While the results of previous particle damper parametric studies can provide a helpful insight, they do not directly translate to the ring particle damper configuration, and how the device’s parameters affect its performance is unclear.

The objective of the collaborative project between the University of Tennessee and NASA MSFC is to investigate and accelerate the development of the ring particle damper as an effective solution for mitigating multi-directional, radial, and torsional vibrations. The evaluation was organized into three phases. The first phase consists of the design and fabrication of the

experimental host structure and ring particle damper. Numerical analyses were used to design a thin-walled cylindrical host structure, exhibiting bending, breathing, and torsional modes relevant to NASA hardware. The second phase consisted of an initial experimental parametric study evaluating how the device's properties influence the performance of the proposed ring particle damper, such as the device position on the host structure, the ratio of total particle mass to the host structure, and load magnitude. The third phase assessed the most promising device configuration under multi-directional vibration.

The project primarily emphasizes laboratory experimental testing to provide characteristic proof-of-concept validation of the ring particle damper. Simplified numerical models are not well-suited for particle damper analysis, as an accurate representation of particle interaction requires high-fidelity modeling of individual particle interaction and leading to increased analytical complexities. As a result, experimental testing was the focus of the project.

The findings of this work contribute to the advancement of the ring particle damper. The report is organized as follows: Section 2 describes the design and fabrication process of the host structure and ring particle dampers, Section 3 outlines the experimental methods and response metrics, Section 4 presents the results and discussion of the initial parametric studies, Section 5 details the results and findings of the effectiveness demonstration studies, Section 6 outlines the lessons learned from the project, Section 7 presents recommendations for future work, and Section 8 details the conclusions of the project.

2. Experimental Specimen Design and Fabrication

An experimental specimen was designed and fabricated to investigate the ring particle damper's performance in mitigating multi-directional, radial, and torsional vibration. The specimen design consisted of a host structure and the ring particle damper. The host structure is a long, thinned-wall cylindrical structure with a fixed base. The host structure was designed to have important modes that are relevant in NASA hardware, such as multi-directional bending modes, breathing modes, and torsional modes. Specifically, the design sought to achieve a first mode under 10 Hz, a breathing mode under 20 Hz, and a torsional mode under 30 Hz.

2.1. Numerical Experiments

A parametric study was performed to determine the diameter, height, wall thickness, and material needed to achieve the relevant modes of vibrations and range of natural frequencies. Autodesk Inventor was utilized to design and evaluate the dynamic properties of the host structure. The software uses a finite element modal analysis method to determine the first ten natural frequencies and mode shapes of the model. A convergence study was performed to determine the optimal mesh size, balancing the accuracy and computation speed. An average element size of 0.048 was consistently used for each design iteration. With this average element size, the mesh is considered to be relatively fine. The average element size is reported in Inventor as a dimensionless quantity

defined as a fraction of the model's bounding box length, which was modeled in inches. Scaled by the model's height of 48 in, this equates to an average element size of 2.3 in.

Aluminum was the first material chosen for conducting design iterations, maintaining consistent material properties in each iteration (Table 1). A simple thinned-walled cylinder with a fixed base was modeled and iterated. A 4-ft tall aluminum cylinder with a 4-inch diameter and ¼ -inch wall thickness resulted in a first mode of 48.05 Hz (Figure 3). The analysis results indicated the cylinder's self-weight alone was not sufficient to reach the frequency goals of the design.

Table 1. Aluminum material properties

Material Property	*Value*
Young's Modulus	9,993 ksi
Density	0.098 lb/in^3
Poisson's Ratio	0.33
Yield Strength	39.89 ksi
Tensile Strength	44.96 ksi

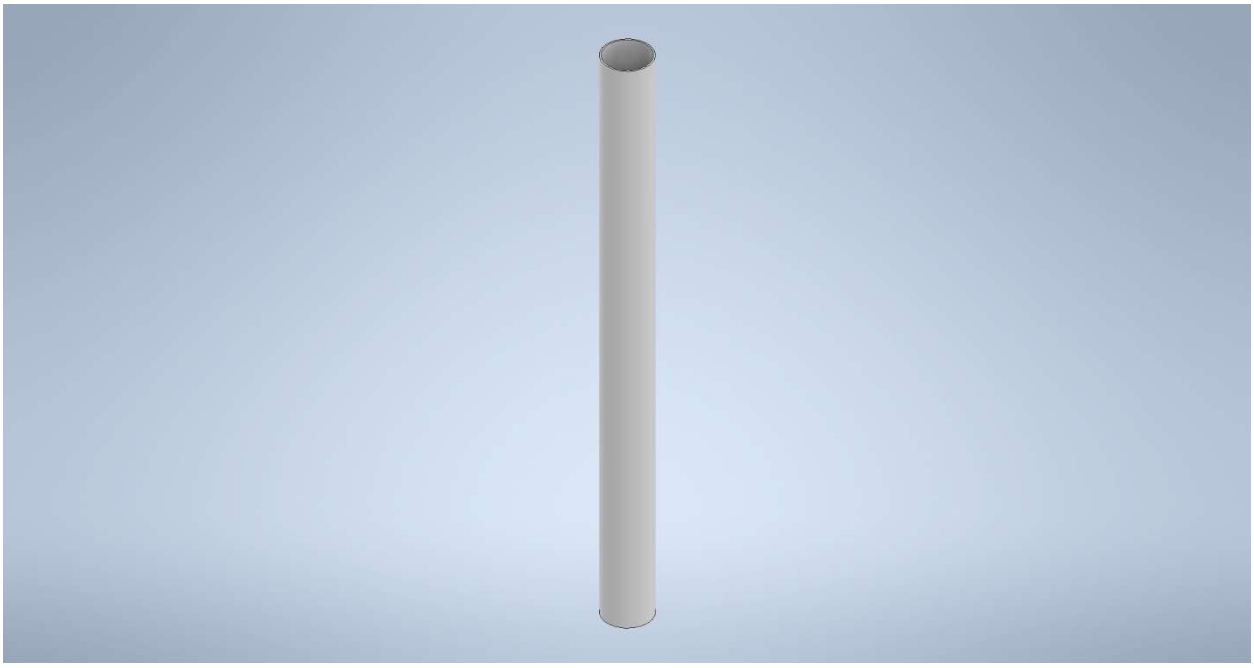


Figure 3. Initial host structure Inventor model

Additional mass was added to the host structure to help further reduce its natural frequencies. To represent the RPD mass, eight discontinuous mass cubes were modeled 45 degrees around the outer circumference of the cylinder and positioned at potential RPD locations (Figure *4*). The top and midpoint locations were selected due to high magnitudes of displacement points

seen in previous modal analysis iterations. A 4-ft tall aluminum cylinder with a 6-inch diameter, 3/16-inch wall thickness, and 128.33 lbs. of added mass was able to achieve a first mode of 10.11 Hz. However, this host structure design was deemed not feasible as the added weight was too significant, and a thin-walled hollow tube with the required parameters could not be easily sourced or fabricated. To improve design feasibility and sourcing flexibility, the host structure was changed to a plastic material. Polylactic acid (PLA) plastic material was selected with the intention of 3D printing the host structure. The use of PLA, rather than common flight hardware material, was driven primarily by the convenience to source and fabricate the test structure. While PLA exhibits different material properties than typical flight hardware, these differences are not expected to significantly influence the result of the elastic testing. Thus, the general trends in observations with a PLA-based host structure are expected to be similar to those using typical space hardware materials.

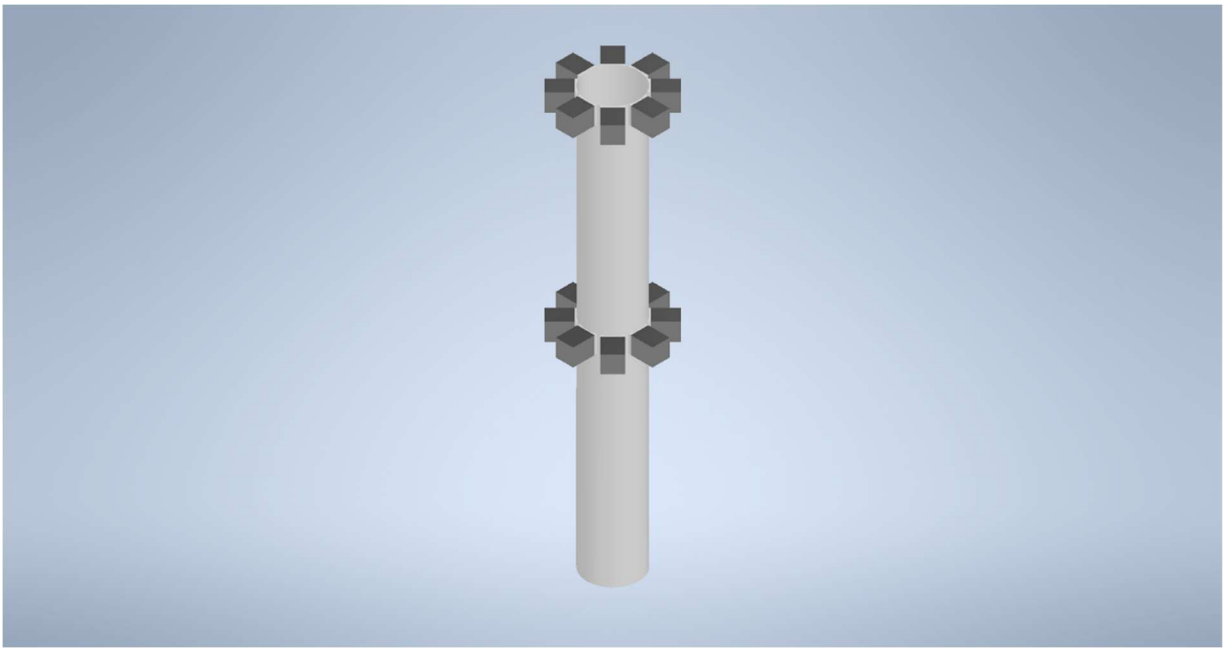


Figure 4. *Host structure Inventor model with added masses at device locations*

The modal analysis was performed with consistent PLA material properties for each iteration (Table 2). Based on the final aluminum design, significant system mass was required to achieve a first natural frequency under 10 Hz. To achieve this low natural frequency and allow the model to obtain the more complex higher modes, added distributed masses were applied to the host structure system with a total of eighty square weights attached to the outer circumference of the cylinder. In the Autodesk Inventor model, the component mate constraint tool was used to represent a fixed connection of these masses to the cylinder. At each height, eight weights were spaced at equal distances around the outer shell of the cylinder, and ten rows of the eight weight groups were distributed equally along the cylinder height (Figure 5). Additionally, to include in the model the added mass due to the RPD cavities, two RPD groups were sized and modeled in PLA material at the top and midpoint locations along the cylinder height. A 4-ft PLA cylinder with a 5-inch

diameter, 0.05-inch wall thickness, two PLA RPD groups, and a total of 23.90 lbs. of system mass was needed to achieve the host structural modes of vibration objectives (Table 3). Specifically, the first mode, a first bending mode, under 10 Hz in both the X and Z directions. A breathing mode with radial expansion concentrated at the top of the cylinder was predicted under 20 Hz in both directions (Figure 7). A torsional mode was evaluated to be 27.18 Hz, meeting the 30 Hz frequency target (Figure 10). Duplicate mode shapes were observed in the modal analysis results, exhibiting identical or closely predicted natural frequencies (e.g., M1 and M2 or M7 and M8). These repeated modes were expected due to the axisymmetric geometry of the hollow tube, corresponding to orthogonal bending directions that share similar stiffness and mass properties.

Table 2. PLA material properties

Material Property	*Value*
Young's Modulus	341 ksi
Density	0.047 lb/in^3
Poisson's Ratio	0.34
Yield Strength	6.56 ksi
Tensile Strength	8.31 ksi

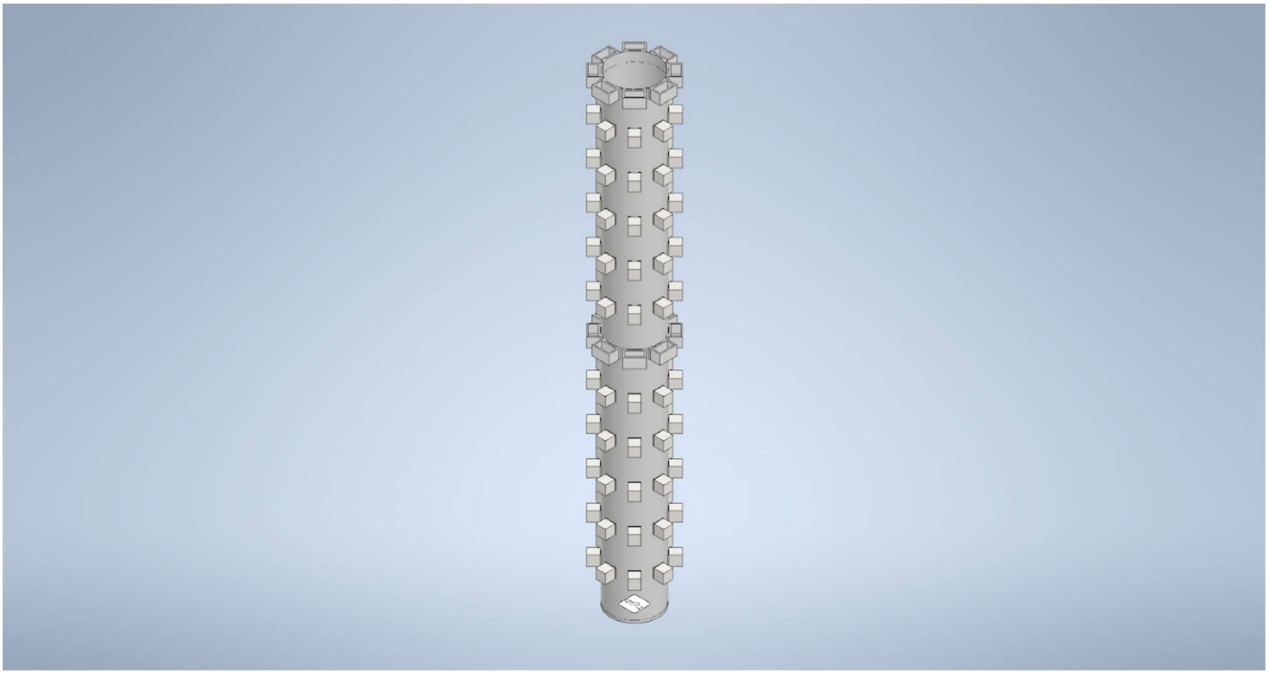


Figure 5. Host structure Autodesk Inventor model with a distributed mass system and device mass modeled

Table 3. Autodesk Inventor modal analysis results of the host structure design

Mode	Frequency (Hz)	Mode Classification	Mode Shape
M1	4.42	First Bending in the X-Direction	Figure 6
M2	4.42	First Bending in the Y-Direction	
M3	13.89	Breathing: 2 Point, Top Concentration	Figure 7
M4	16.00	Breathing: 2 Point, Top Concentration	
M5	20.89	Breathing: 2 Point, Mid Concentration	Figure 8
M6	21.66	Breathing: 2 Point, Mid Concentration	
M7	25.93	Second Bending in the X-Direction	Figure 9
M8	26.10	Second Bending in the Y-Direction	
M9	27.18	Torsion	Figure 10
M10	55.05	Axial	Figure 11

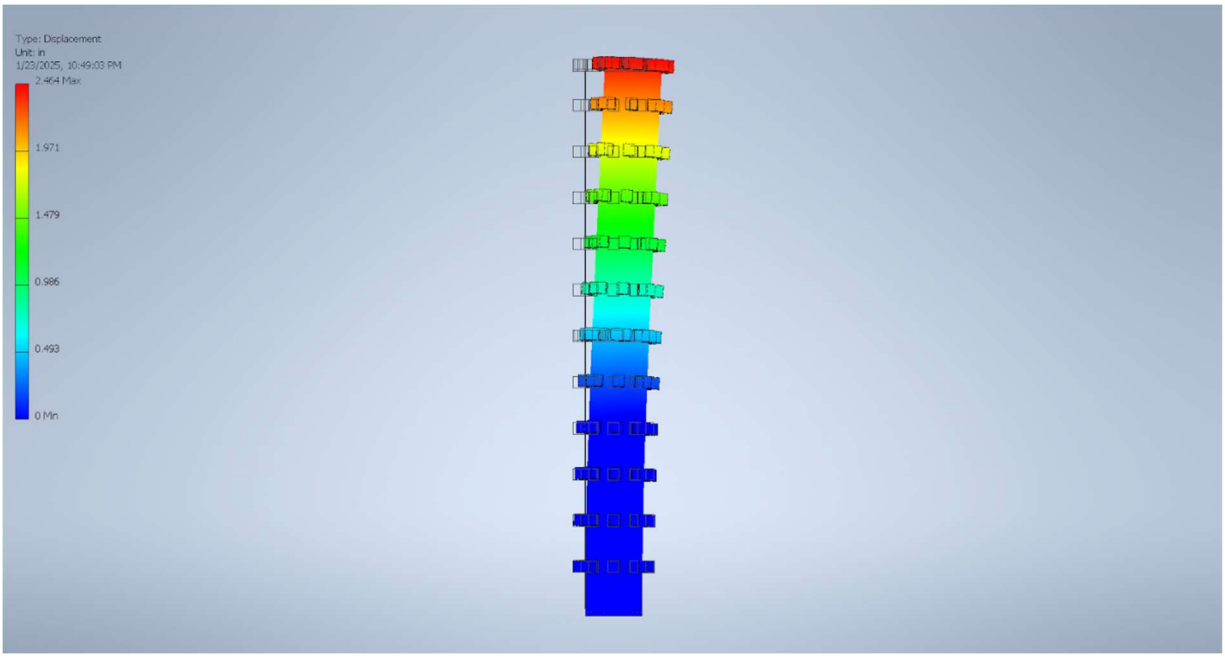
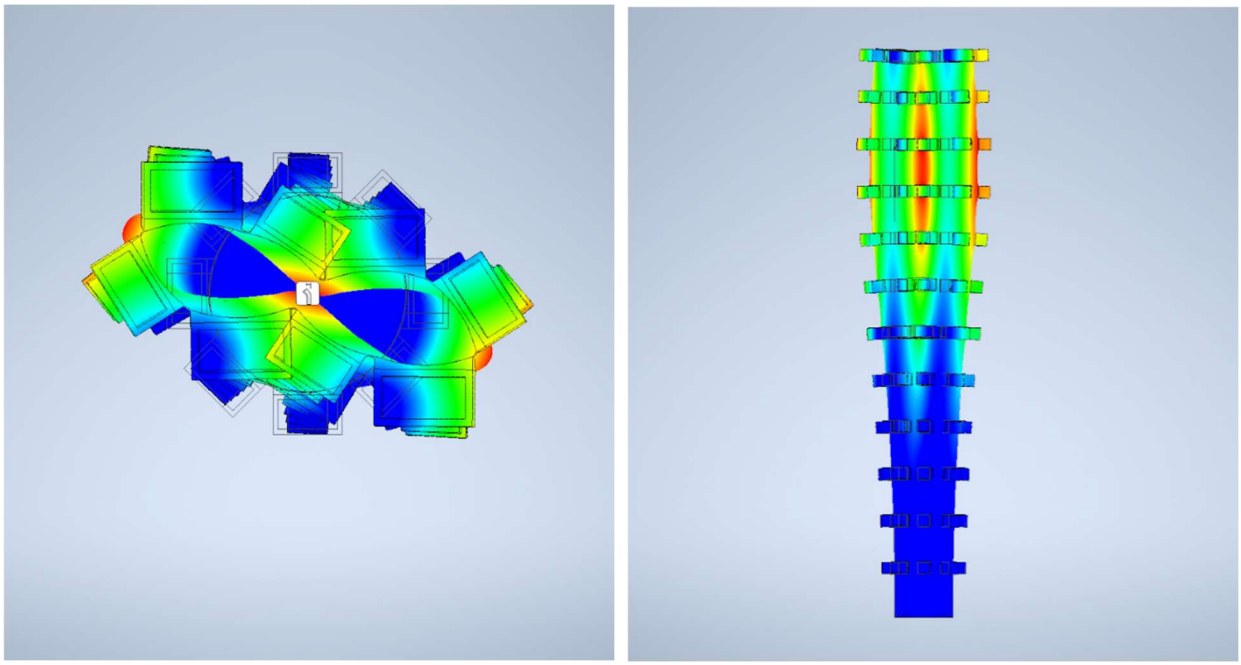
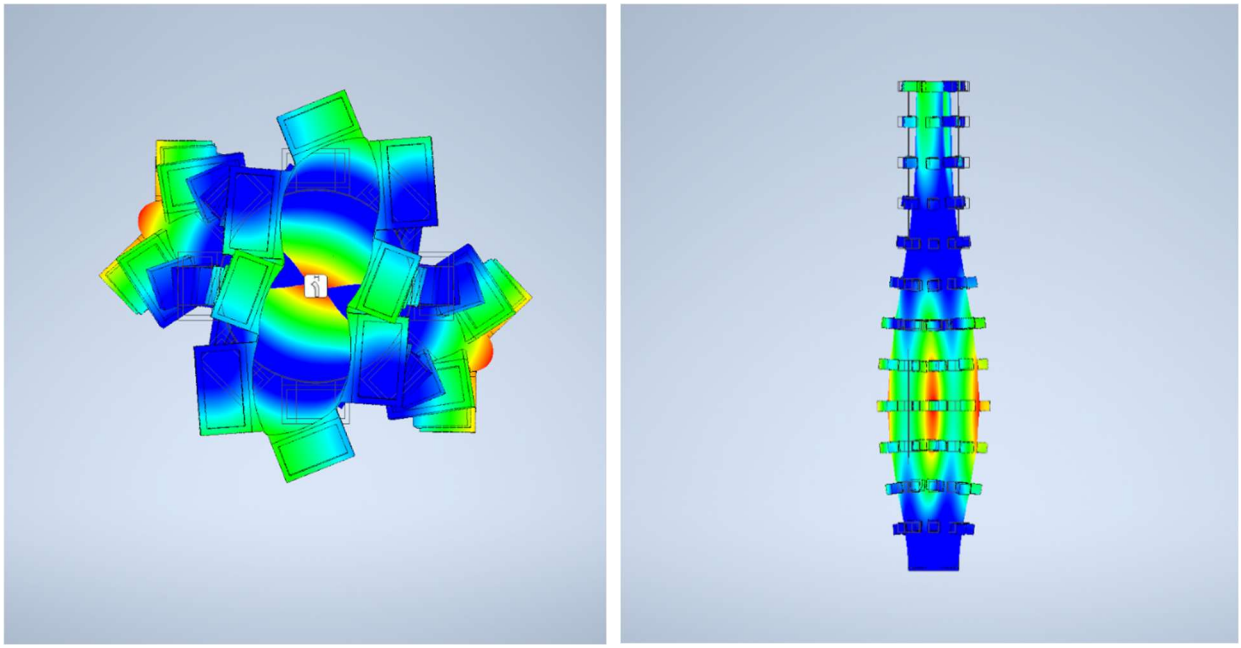


Figure 6. Autodesk Inventor modal analysis result showing the first bending mode with a predicted frequency of 4.42 Hz.



(a) Top View (b) Profile View

Figure 7. Autodesk Inventor modal analysis result showing a breathing mode, classified as a two-point configuration (top view) with top-concentrated expansion (profile view), and a predicted frequency range of 13.89 Hz and 16.00 Hz.



(a) Top View (b) Profile View

Figure 8. Autodesk Inventor modal analysis result showing a breathing mode, classified as a two-point configuration (top view) with mid-concentrated expansion (profile view), and a predicted frequency range of 20.89 Hz and 21.66 Hz.

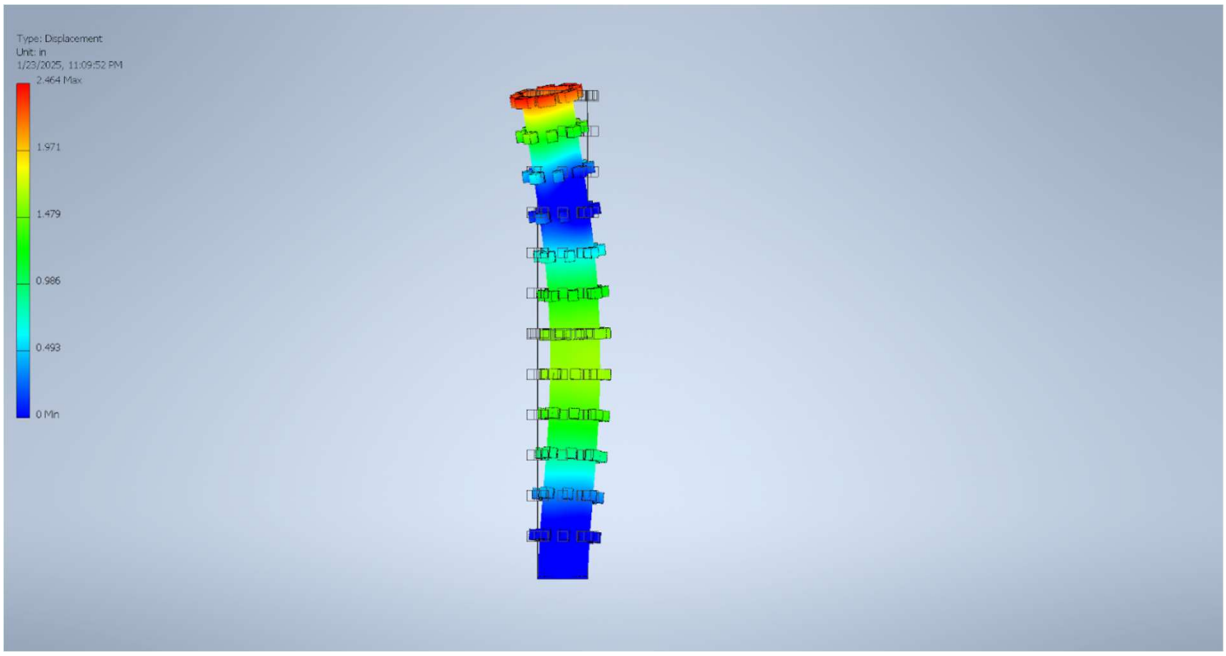
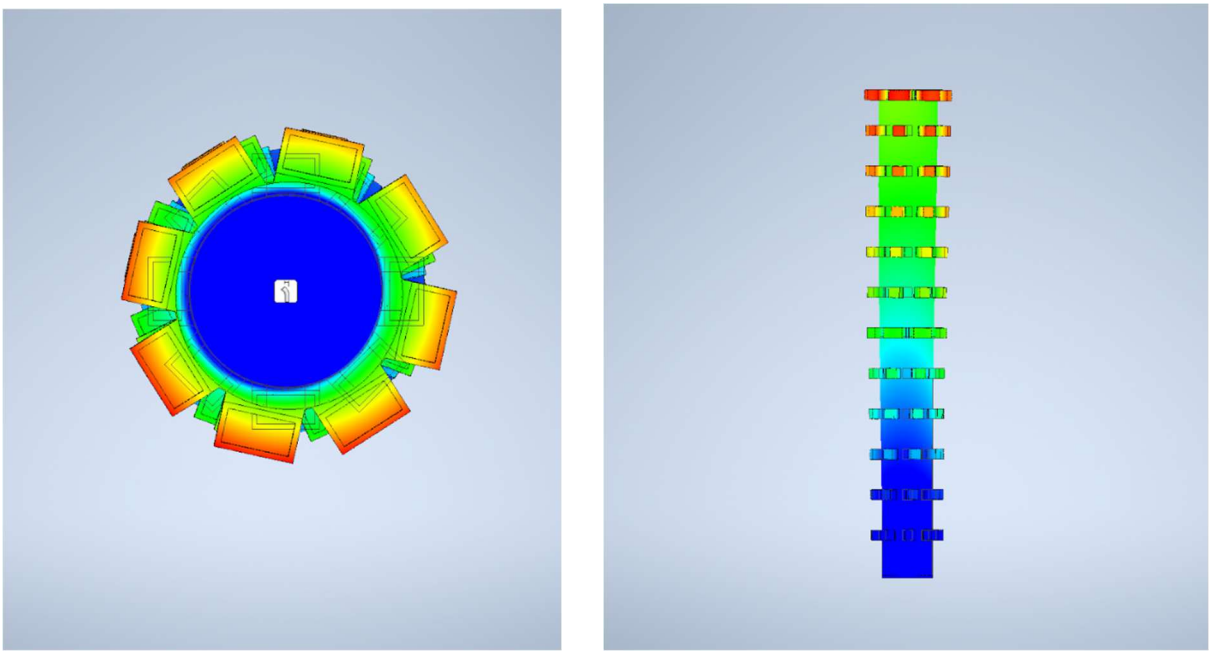


Figure 9. Autodesk Inventor modal analysis result showing the second bending mode with a predicted frequency range of 25.93 Hz and 26.10 Hz.



(a) Top View (b) Profile View

Figure 10. Autodesk Inventor modal analysis result showing a torsion mode with a predicted frequency of 27.18 Hz.

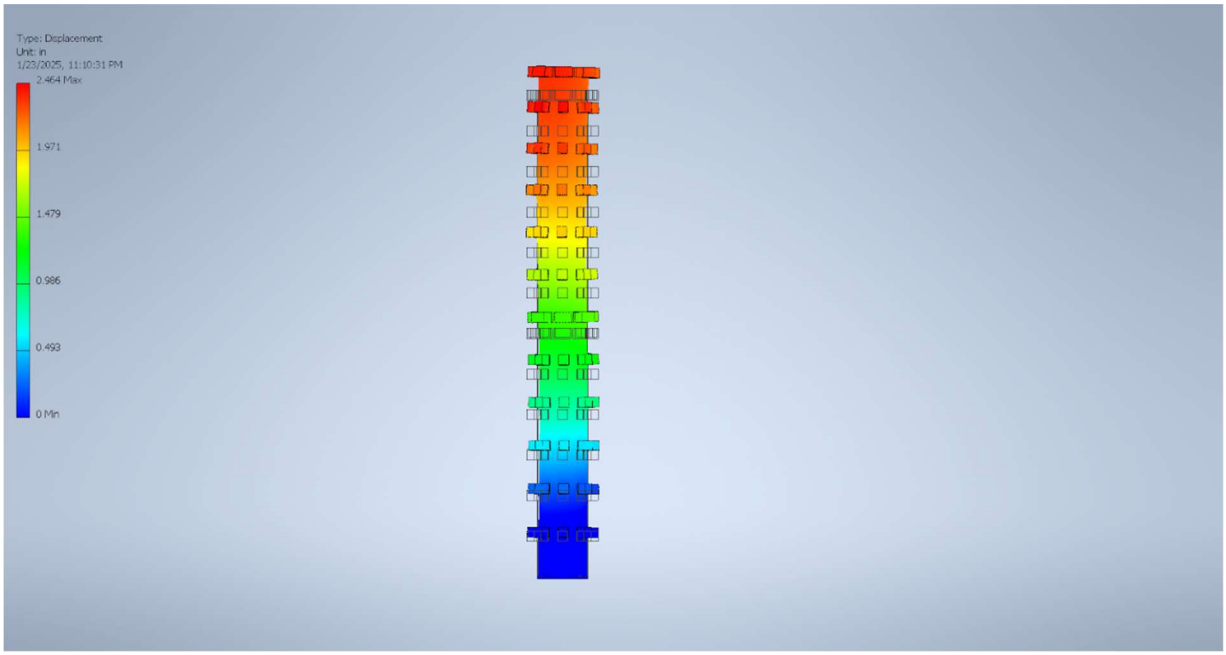


Figure 11. Autodesk Inventor modal analysis result showing an axial mode with a predicted frequency range of 55.05 Hz.

2.2. Specimen Fabrication

The host structure, system weights, and RPD containers were rendered in Inventor to produce 3D print files and fabrication details (Figure 12). The RPD containers and host structure were fabricated using Original Prusa i3 MK3S+ 3D printers with PLA filament. The system weights were fabricated with steel metal plates and cut to size with water-jetting applications.

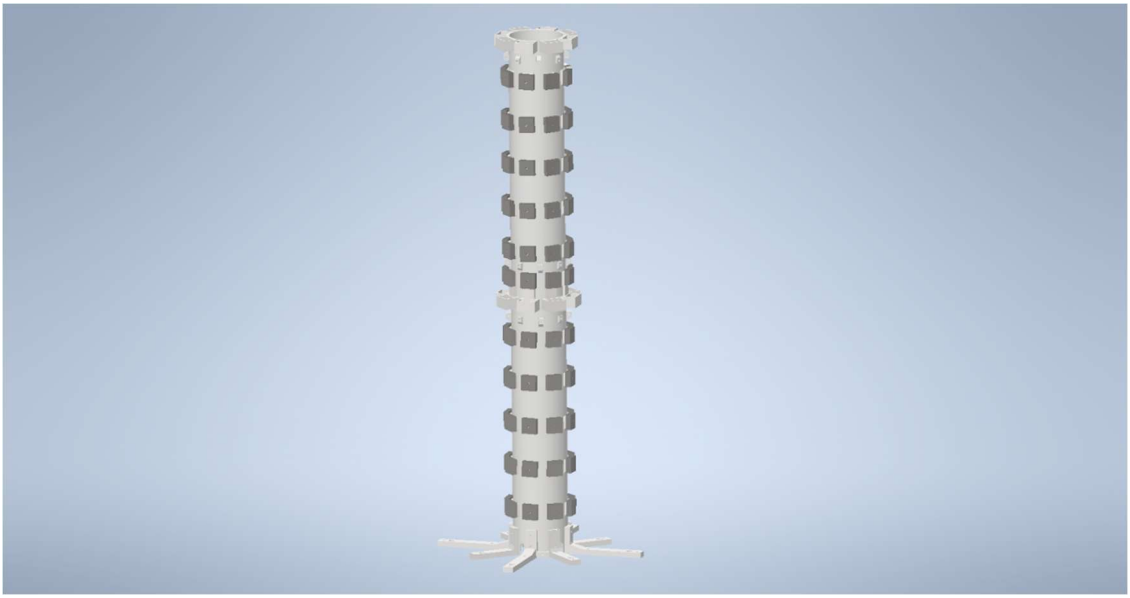


Figure 12. Initial Autodesk Inventor rendering of test structure

The 3D printers have a maximum vertical print height limitation of 8.30 inches. The 4-ft host structure was divided into twelve 4-inch segments, with eight male and female connectors located at the top and bottom of the cylinder segments (Figure 13). The connection was designed to provide a flat and flush surface on the outer and inner walls of the cylinder, serving a dual purpose by linking the cylinder segments and providing a mounting surface for the added system weights (Figure 14). The weight and segments were secured with the same No. 10 bolt with a flat washer placed on the exterior side of the connection, and a lock washer was placed between the interior side and the nut (Figure 15). The lock washer was included to prevent vibrations from loosening these connections.

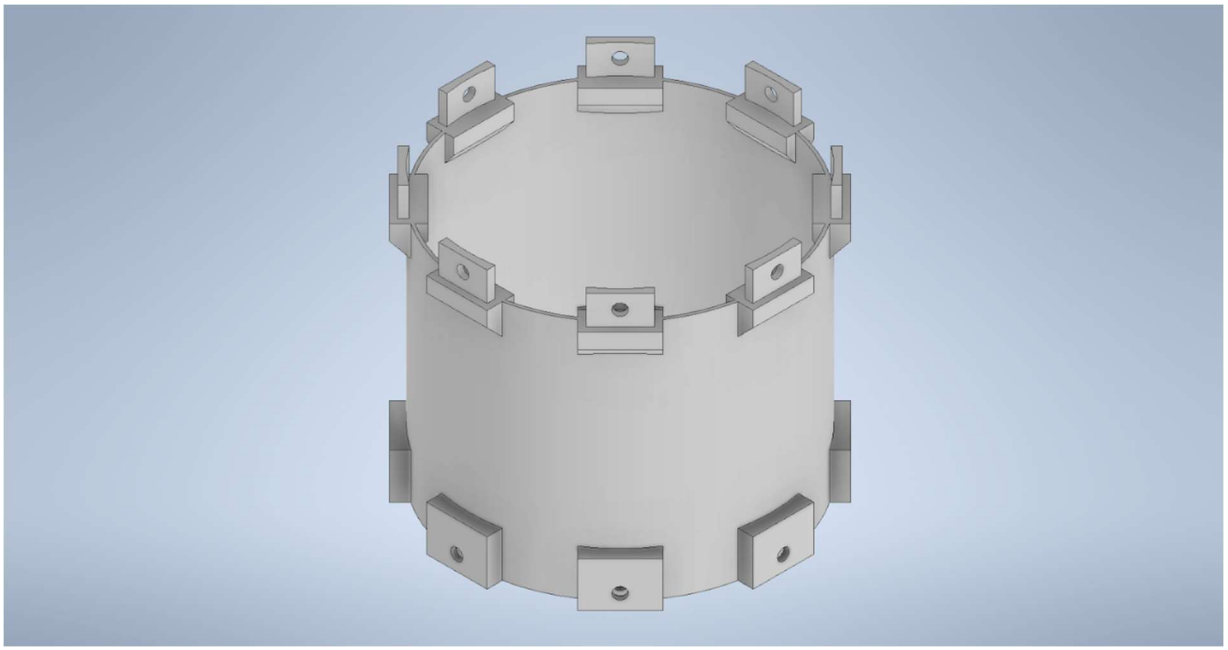


Figure 13. Standard cylinder segment design



Figure 14. Segment connection

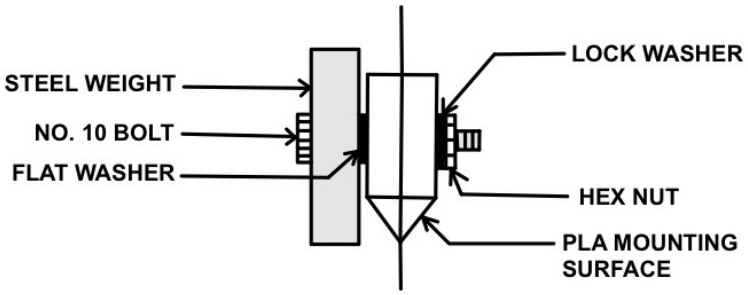


Figure 15. Cylinder segment connection details

A total of 23.90 lb of additional system weights were added and distributed along the height of the cylinder. The weights were organized into ten groups of eight, totaling 80 weights. Steel was chosen for the weight material due to its higher density (0.28 lb/in^3) and availability. Considering the weight of fasteners and PLA connections, each steel weight needed to be at least 0.25 pounds to achieve the host structural modes of vibration objectives. A square shape was selected to keep the design flat and flush with the mounting surface. A ½-inch-thick, 1.4-inch-square design was chosen to meet the weight requirements. The weights were made from a ½-inch thick metal plate and cut to size using water-jetting, with a No.10 bolt hole centered in the square (Figure 16).



Figure 16. Example of a system weight mounted on the host structure

PCB Piezotronics Model 352C33 uniaxial, IEPE accelerometers were selected to measure the host structure's acceleration response. With high sensitivity and a ±50 g measurement range, they are suitable for capturing the translational and radial movement. The accelerometer layout

included 90-degree points around the cylinder circumference at the midpoint and top height of the cylinder. A tangential attachment point was designed to capture the torsional movement. The accelerometer was designed to be attached using a screw mounting method. A No. 10 bolt was used to secure the sensor to the host structure. PCB Piezotronics recommends the mounting surface be flat and smooth for the best measurement results. Four 1/2-inch square mounting surfaces were added and spaced 90 degrees apart. around the inner circumference (Figure 17). The mounting surfaces were placed at the midpoint of the cylinder segment, 2 inches from the top and bottom, to allow clearance between the sensor and cylinder segment connections. To capture the torsional motion, an additional tangential mounting connection was designed to allow a sensor to be placed tangent to 90-degree accelerometers (Figure *18*).

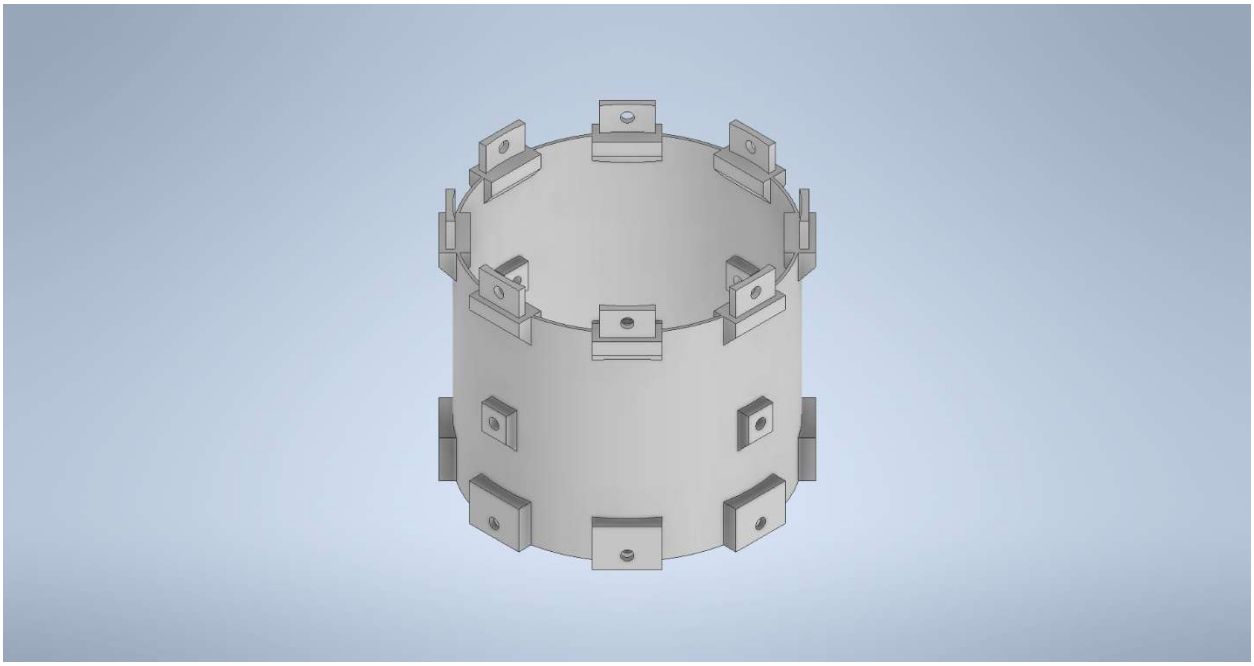
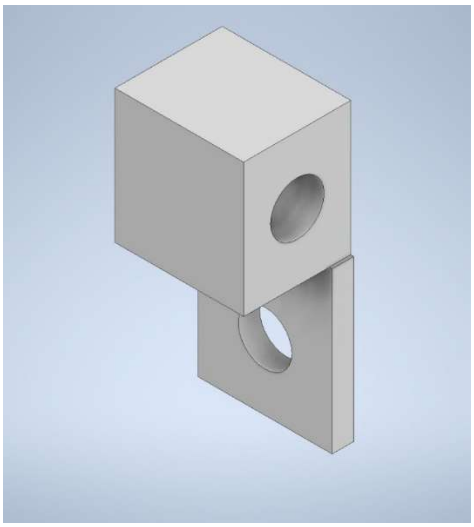
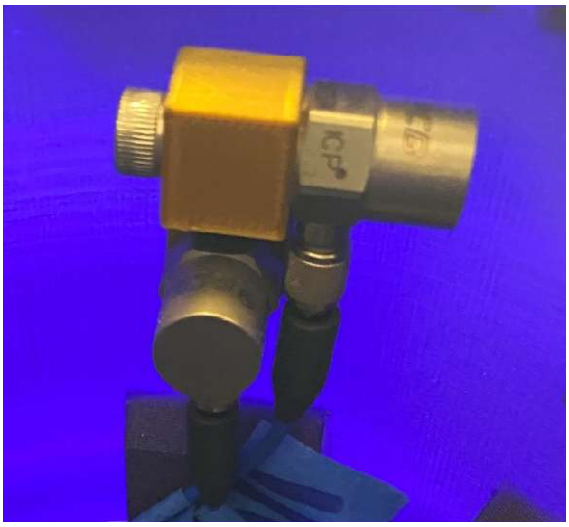


Figure 17. Cylinder segment with accelerometer mounting surface design



(a) Inventor Connection Rendering



(b) 3D Fabrication with Accelerometer Attached

Figure 18. *Tangential accelerometer attachment connection*

The cylinder segment at the base was designed as a fixed connection to the shake table. Similar to the eight attachment points to connect the cylinder segments, the base connection was designed to have eight flat and flush attachment locations around the circumference of the cylinder, ensuring a secure and fixed connection (Figure 19). A small door cut-out was added to allow accelerometer wires to be attached to the inner mounting surfaces and then ran out towards the data acquisition hardware.

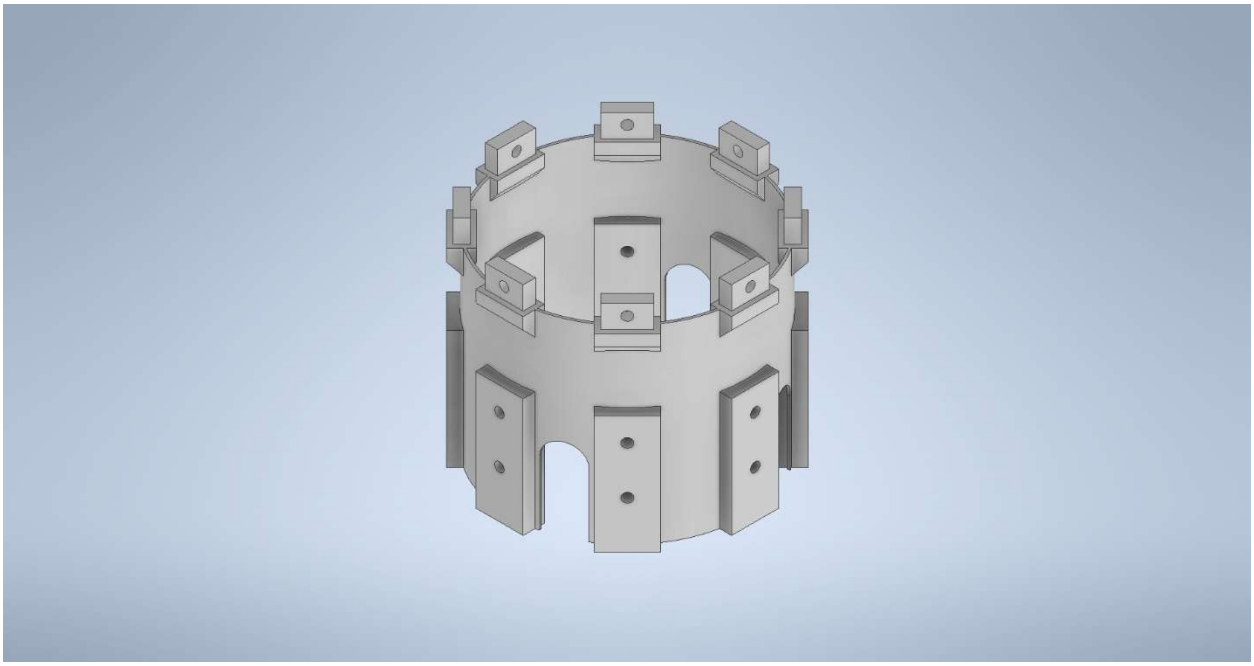
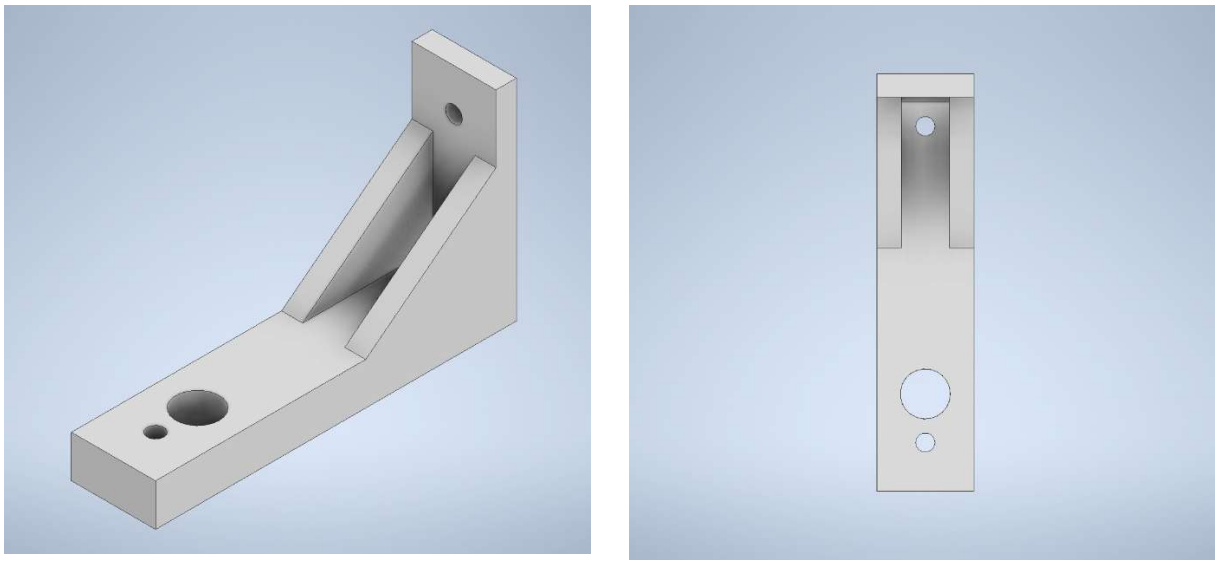


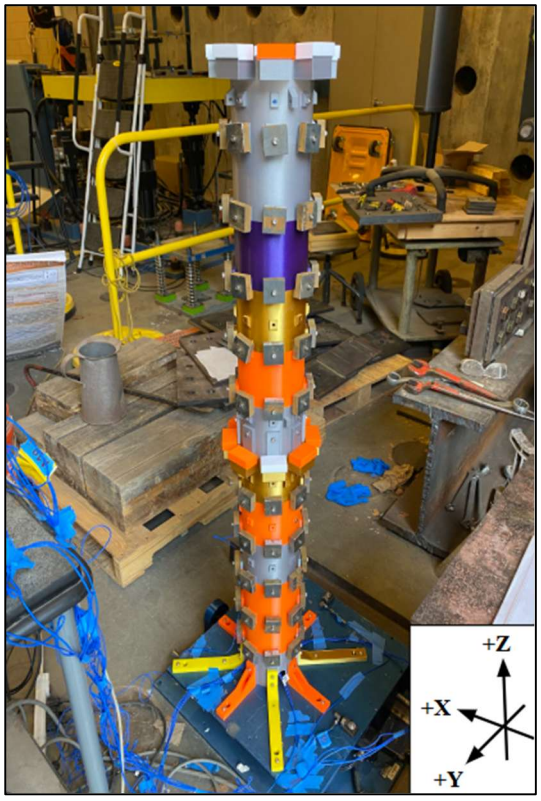
Figure 19. Cylinder base segment design

The parametric studies tests would be performed on the unidirectional, 18-inch x 18-inch, “small” shake table, and the effectiveness demonstration tests would be conducted on the multi-directional, 1.2 m x 1.2 m, “big” shake table. To reduce 3D printing fabrication time and material usage, a base connection was designed to allow the host structure to be interchangeably placed on the small or big shake table. The host structure was attached to the table with eight L-shaped leg profiles with stiffeners to add additional stability and strength (Figure 20). The leg attached to the table was designed with three bolt holes to allow for flexible table usage. Two of the holes were designed for No. 10 bolt holes to allow a fixed connection to the small shake table at 3.25 in. spacing. One of the holes was designed for a ½ inch. bolt to connect to the large shake table at 6 in. spacing (Figure 21). The leg attached to the host structure was designed with two No.10 bolt holes. Similar to the cylinder segment attachment, a flat washer and a lock washer were used to prevent vibration from loosening the connection.

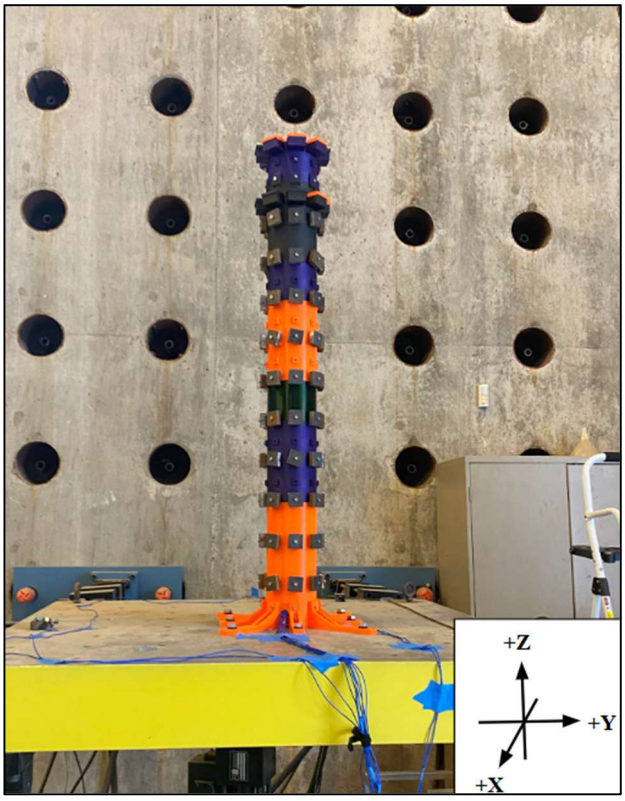


(a) Elevation View (b) Plan View

Figure 20. Leg design



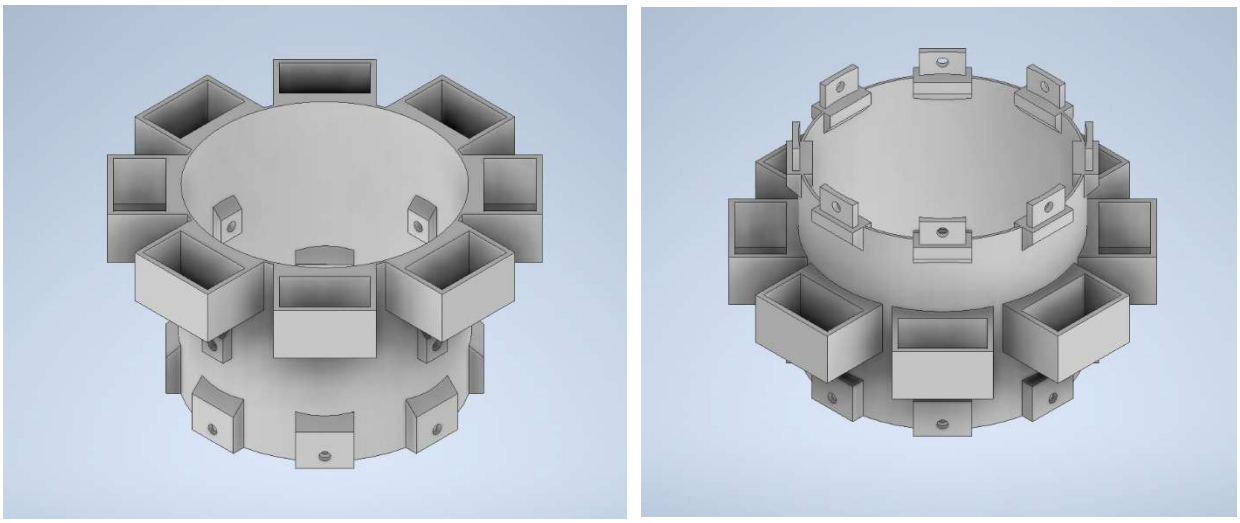
(a) Small Shake Table Attachment



(b) Big Shake Table Attachment

Figure 21. Base connection design adaptability between shake tables

The RPD containers needed to have a fixed connection to the host structure. Two additional PLA cylinder segments were designed to contain the RPD at the top and midpoint locations (Figure 22). A discontinuous RPD design was selected to decrease impedance to radial expansion and contraction. Eight particle damper containers were oriented 45 degrees around the outer cylinder circumference. Limited by the surface area along the cylinder shell, a maximum container size was designed to be 1.75 inches long, 1.4 inches wide, and 1 inch deep with a cavity size of 1.55 inches by 0.90 inches by 0.90 inches (Figure 23). The container geometry established a discontinuous ring with a 0.20-inch space between the boxes.



(a) Top RPD Cylinder Segment Design (b) Middle RPD Cylinder Segment Design

Figure 22. Ring particle damper cylinder segment design

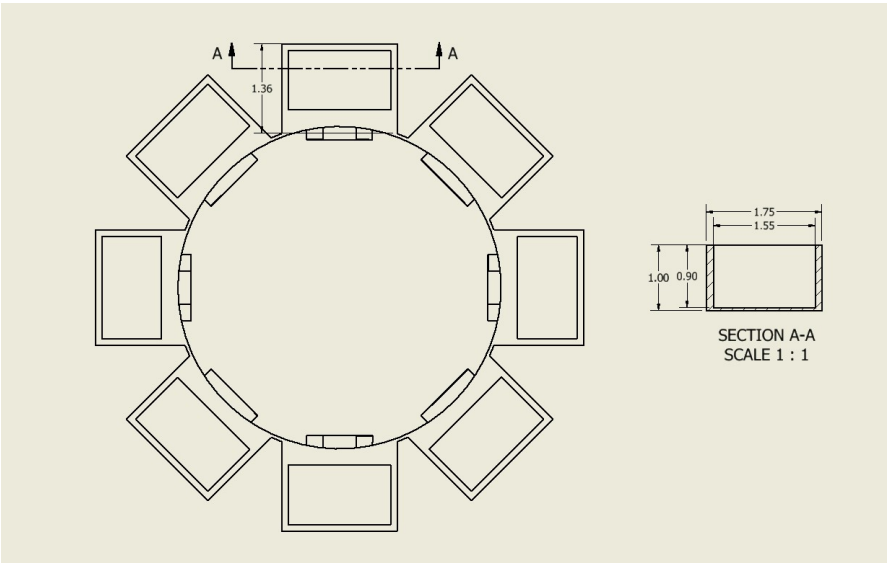
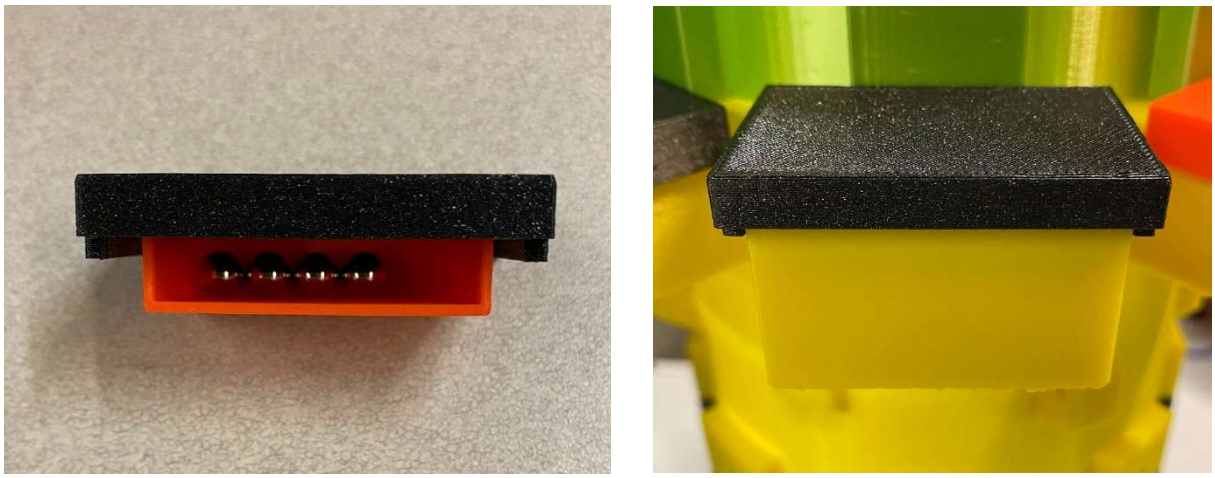


Figure 23. Ring particle damper container geometry. All dimensions are in inches.

A removable layer cap was designed for the RPD cavities to provide flexibility in testing configurations, enabling two distinct layers for particle interactions (Figure 24). Based on the layer heights of approximately 0.45 inches, 1/4-inch diameter steel ball bearings were selected as the particle material. Additionally, to assess the effect of the particles added mass to the system, a solid mass cap was fabricated as a control configuration to represent the equivalent added mass of the particles (44.4 grams per cavity). The mass cap was dimensioned to fit tightly within the RPD cavity geometry and printed with solid filament to ensure comparable inertial properties to the particles (Figure 25).

A durability test of the 3D-printed specimen was conducted by subjecting the host structure to twenty consecutive 300-second white noise ground motions at the maximum excitation amplitude tested in small shake table experiments (X=1.0), corresponding to an average RMS acceleration of 0.2953g. The consistent frequency response of the host structure provided more confidence that the PLA material maintained structural durability and was suitable for use in the subsequent parametric studies.



(a) Layer Cap Configuration (b) Layer Cap on RPD Cavity

Figure 24. Layer cap design

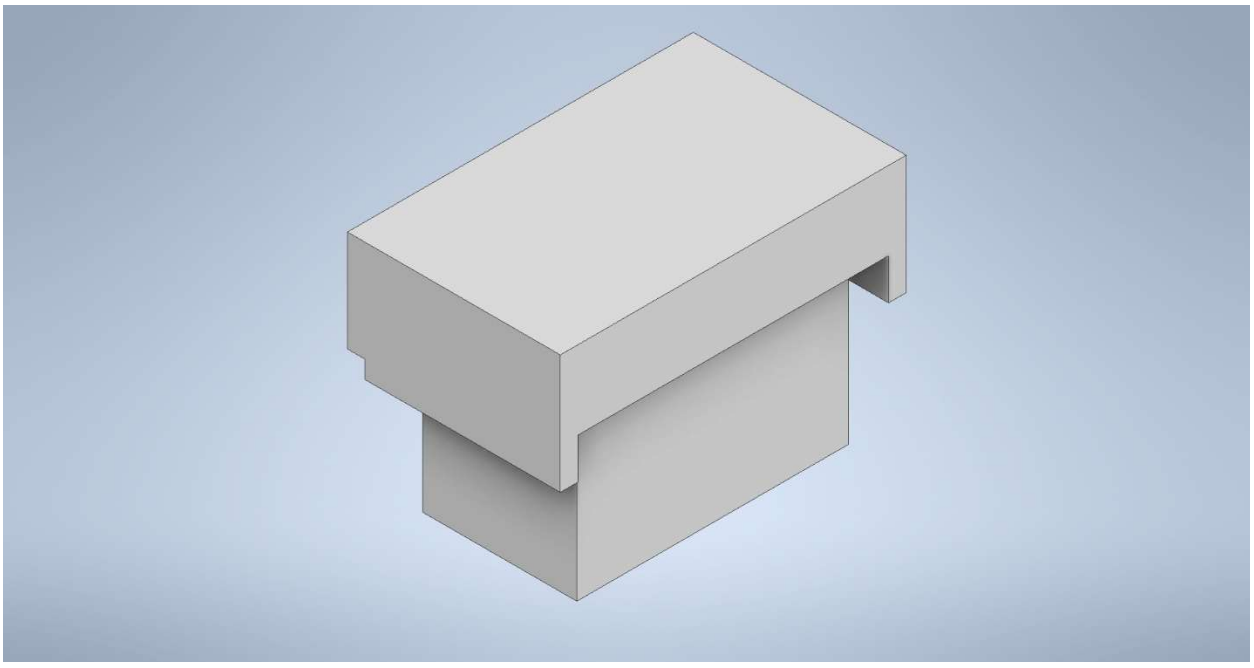


Figure 25. Mass cap design

3. Experimental Methods

The evaluation of the device was assessed in two experimental phases. Initial parametric studies were conducted to investigate how the parameters of the ring particle damper impact its behavior. Observations from the initial studies included the device configuration that demonstrated peak performance and was implemented in the second set of experiments. The second area of focus was assessing the effectiveness of the ring particle damper to mitigate multi-directional vibration. The experimental methods section presents the test setups, input loading, instrumentation, and response locations to evaluate the performance of the device.

3.1 Test Setups

The initial parametric studies were conducted on the "small shake table." An 18-inch x 18-inch, single-axis motion shake table that can provide a nameplate maximum acceleration of 2.5 g. The host structure was secured with two No. 10 bolts in each leg, with a total of 16 bolts attached to the shake table. For all the initial parametric tests, except the device location study, the host structure was constructed with an initial, "default" configuration, consisting of a ring particle damper mounted at 24 inches and 48 inches elevations (Figure 26). The effectiveness demonstrations were performed on the "big shake table," a 1.2 m x 1.2 m, six-degree-of-freedom shake table that can provide a nameplate 4.0 g peak horizontal acceleration and a 2.5 g peak vertical acceleration. The host structure was securely fastened using eight ½-inch bolts, with one bolt per leg. The host structure was assembled in its "default" configuration with the RPD positioned at the 42-inch and 48-inch elevation (Figure 27).

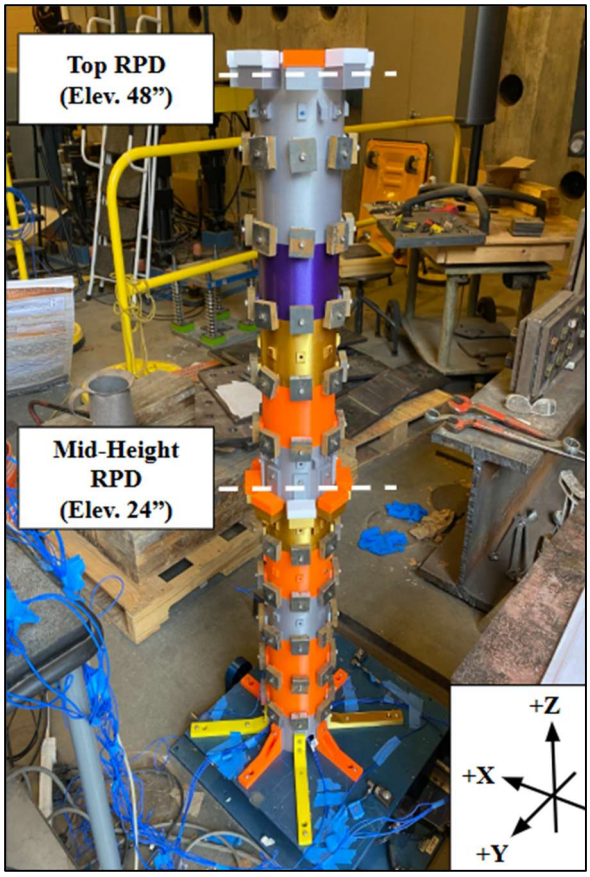


Figure 26. Default test setup for parametric studies. Elevations are measured from the bottom of the structure.

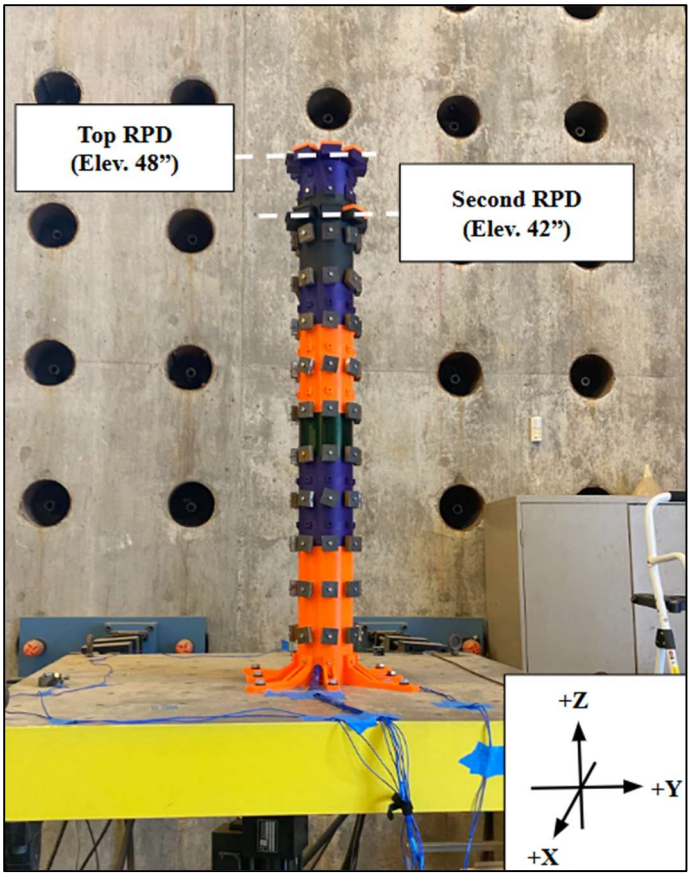


Figure 27. Default test setup for effectiveness demonstrations studies. Elevations are measured from the bottom of the structure.

3.2 Input Excitation

For the small shake table, the input ground motion consisted of a 300-second white noise signal applied in the x-direction. Load amplitude scaling factors were applied to the white noise, ranging from 1.0 to 0.25 in increments of 0.075. A set "default" scaling factor of X=0.75 was used for studies with a fixed input load amplitude. A representative RMS acceleration of the excitation applied to the structure was obtained from a table-mounted accelerometer (T2), using a consistent "no particle" configuration and low-pass filter with a 50 Hz cutoff. Although perfect white noise is not achieved for each case, the representative RMS reflects comparable excitation across configurations (Table 4). Minor variations in RMS are expected for each test due to the nature of the white-noise excitation and table-structure interaction effects. The resulting excitation was consistent in the frequency domain over the frequency range of interest (Figure 28).

Table 4. Measured table-mounted acceleration representing the excitation applied to the structure on the small shake table.

Excitation Amplitude Label	*Representative RMS (g)*
X=0.25	0.0690
X=0.325	0.0895
X=0.40	0.1070
X=0.475	0.1386
X=0.50	0.1364
X=0.55	0.1521
X=0.625	0.1636
X=0.70	0.1831
X=0.75	0.2048
X=0.775	0.2047
X=0.85	0.2248
X=0.925	0.2538
X=1.0	0.2953

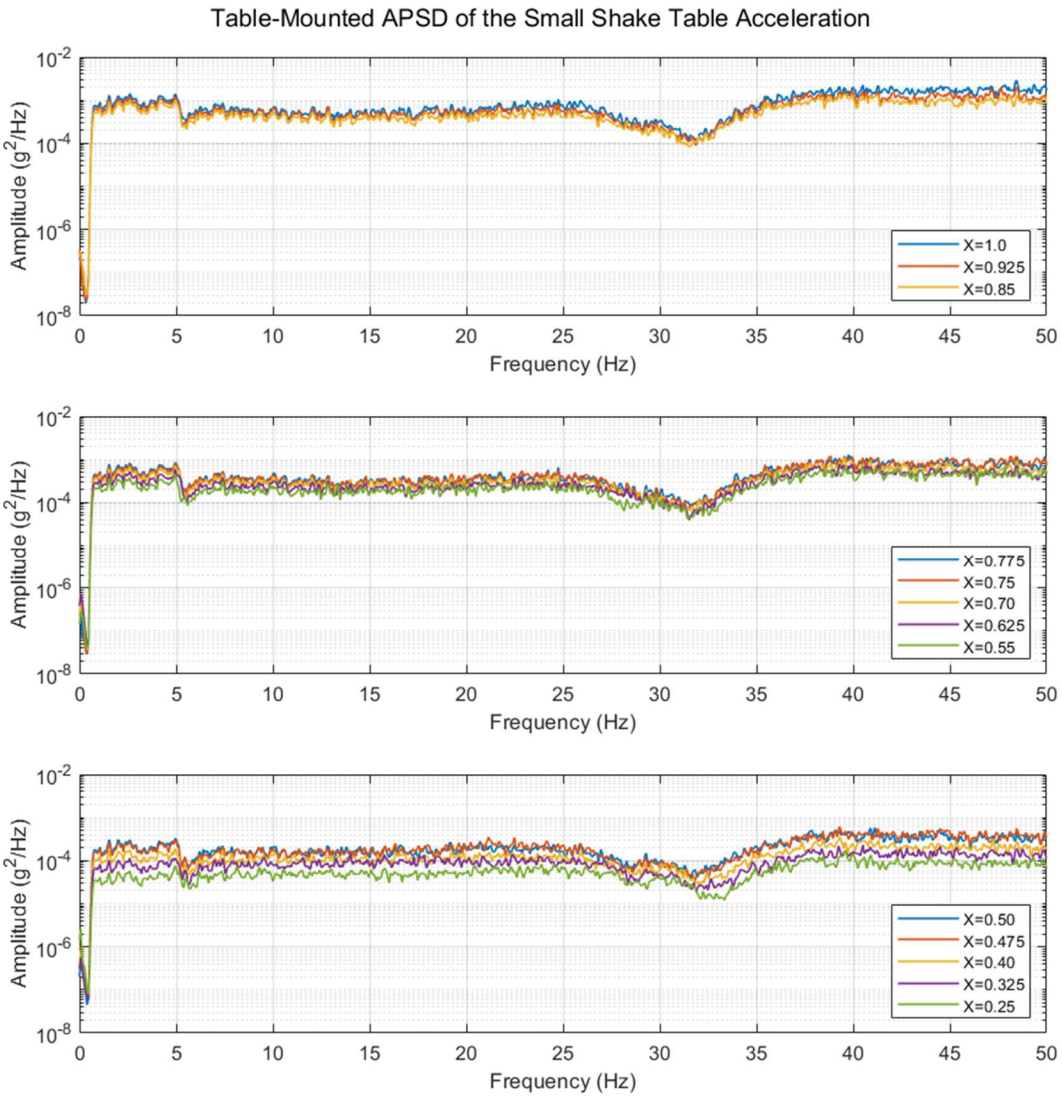


Figure 28. Autopower spectral densities (APSDs) of the table-mounted acceleration measured by sensor T2 on the small shake table under various excitation amplitudes. The APSDs are separated into three graphs to improve clarity and for individual curves to be easily distinguished.

The input excitations for the big shake table consisted of a 300-second white noise ground motion in the x-direction, y-direction, combined x-y directions, and theta-z direction. Load amplitude scaling factors were applied to the ground motion files to achieve comparable excitation levels in each direction. Similar to the small shake table, perfect white noise was not achieved for every case. However, the representative RMS reflects a comparable excitation across configurations. The representative RMS was calculated using the "no particle" configuration table-mounted sensors and applying a low-pass filter with a cut-off of 50 Hz. The x-direction RMS was

obtained from the x-direction sensor (T2) (Table 5), the y-direction RMS was from the y-direction sensor (T1) (Table 6), and the theta-Z RMS was computed from the rotational acceleration determined by subtracting the two table-mounted accelerometers in the y-direction (T1-T2) and dividing by the distance between the two sensors, measured at 30 inches, assuming small angles (Table 7). Additionally, the excitations were verified to produce comparable magnitudes across the 3-50 Hz frequency range (Figure 29Figure 29).

Table 5. Measured table-mounted acceleration representing the excitation applied in the X-direction to the structure on the big shake table.

Excitation Amplitude Label	*Representative RMS (g)*
X=0.245	0.0349
X=0.475	0.0700
X=0.70	0.0975
X=0.95	0.1309

Table 6. Measured table-mounted acceleration representing the excitation applied in the Y-direction to the structure on the big shake table.

Excitation Amplitude Label	*Representative RMS (g)*
Y=0.25	0.0331
Y=0.50	0.0670
Y=0.75	0.0905
Y=1.0	0.1143

Table 7. Measured table-mounted acceleration representing the excitation applied in the theta-Z direction to the structure on the big shake table.

Excitation Amplitude Label	*Representative RMS (rad/s^2)*
Theta-Z=1.0	0.0038
Theta-Z=2.0	0.0090
Theta-Z=3.0	0.0145
Theta-Z=4.0	0.0202

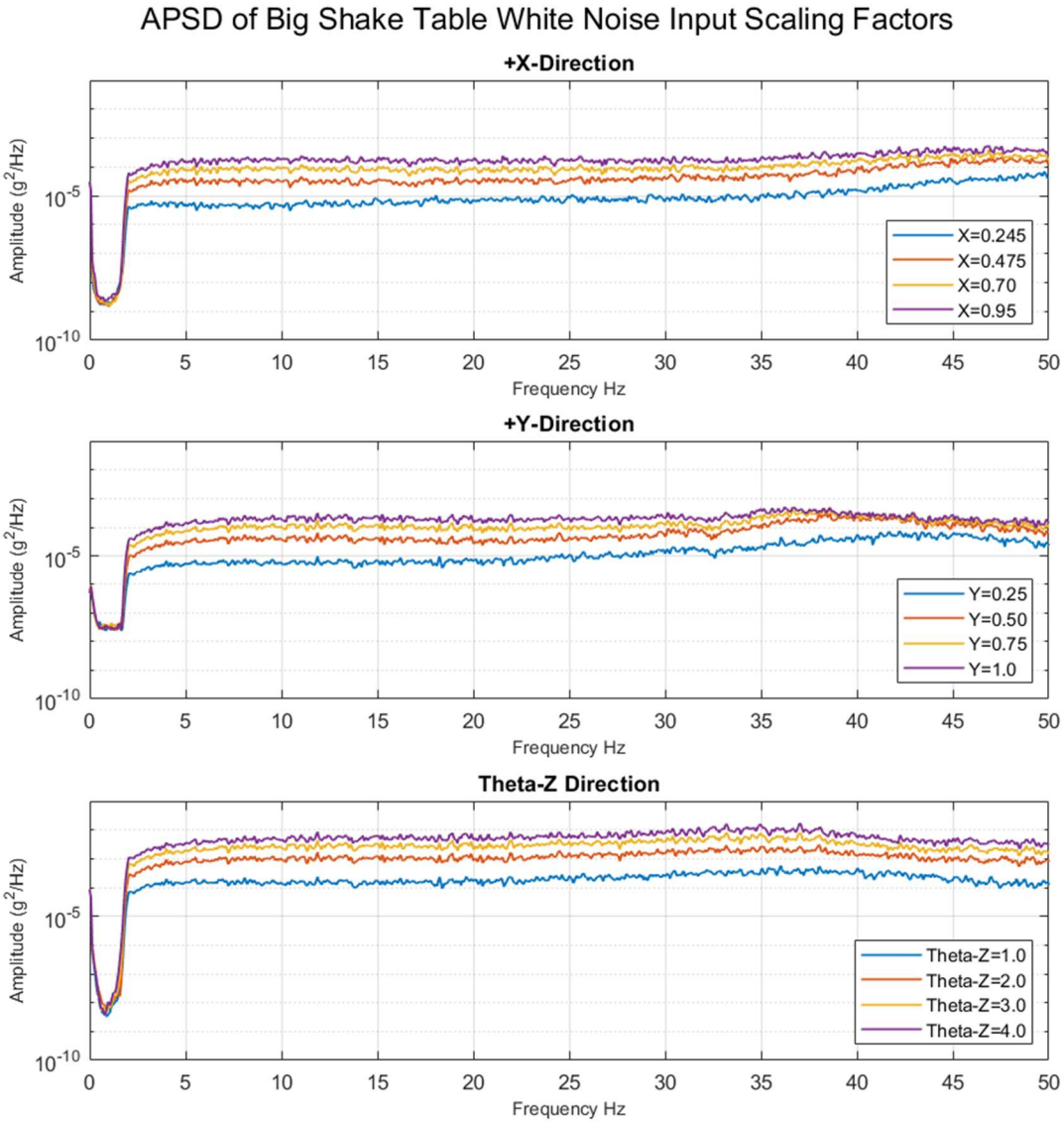


Figure 29. Frequency response function of the big shake table under white noise excitation at various input scaling factors. The APSDs are separated into three graphs to correspond to the excitation scale factor applied in each axis of motion.

3.3 Instrumentation and Sensor Layout

The data was collected using a National Instruments compact data acquisition (cDAQ) to record the acceleration responses. The system was limited to three input modules, providing twelve available channels for accelerometer measurements. A total of twelve PCB Piezotronics ICP accelerometers were strategically placed to measure the acceleration input and response. The

cDAQ was connected to a computer using NI LabVIEW software to acquire data measurements. This system includes automatic anti-alias filtering. A consistent sampling rate of 1651.61 Hz was applied to all experiments, and the accelerometer sensitivities were pre-calibrated and incorporated into the output data files.

3.3.1 Initial Parametric Study Sensor Layout

Twelve accelerometers were attached to the small shake table and host structure to capture the input and response accelerations (Figure 30). Two accelerometers were mounted on the shake table in the x and y directions to capture the ground motion input. To capture the translational response, three accelerometers were secured in the positive x-direction, and two accelerometers were attached in the positive y-direction at elevations of 18 inches, 26 inches, and 46 inches from the base. The radial expansion and contraction were measured with two additional accelerometers in the opposite x-directions at the 26-inch and 48-inch locations, and one sensor in the negative y-direction was used at the 26-inch location. Two sensors were placed tangent to the y-direction sensors at 26 inches and 46 inches in height. These sensors were used to calculate the torsional acceleration by subtracting the signals from a corresponding x-direction sensor.

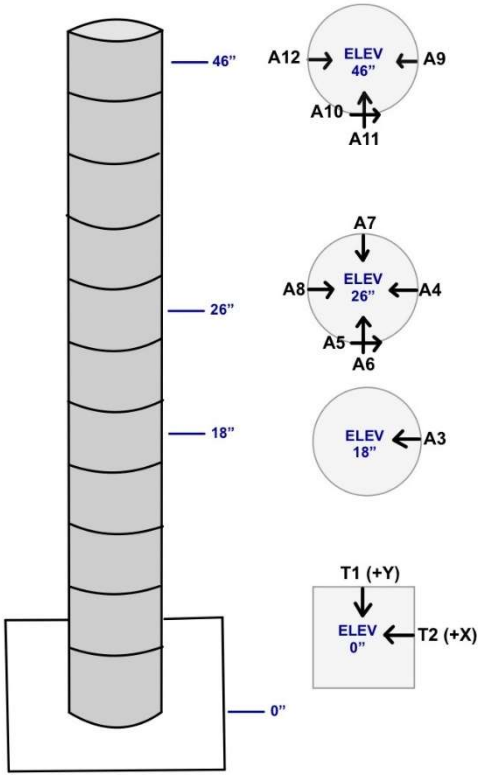
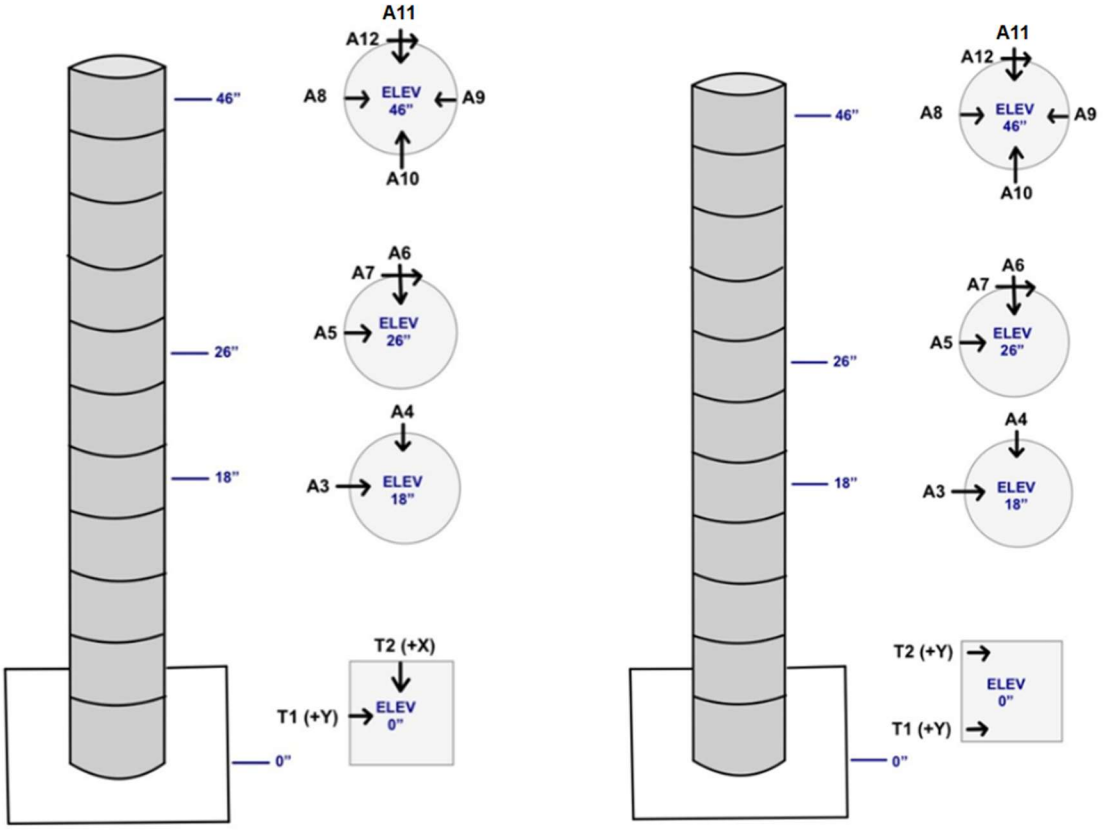


Figure 30. Default sensor layout for parametric studies on the small shake table. Elevations are measured from the bottom of the structure. Table-mounted and structure-mounted accelerometers are denoted as (T) and (A).

3.3.2 Effectiveness Demonstration Sensor Layout

For effective demonstration studies, the sensor layout varied based on the loading condition: for translational excitation, the accelerometers were mounted to the table to align with the x and y actuators. For the torsional tests, both sensors were positioned along the y-axis to capture the theta-z rotational motion (Figure 31). The host structure was instrumented to measure translation, radial, and torsional responses. Three accelerometers were mounted at the 18-inch, 26-inch, and 46-inch heights to measure translational accelerations in the positive x and y directions. The radial expansion and contraction were recorded with two accelerometers oriented in opposition to the translational sensors at the 26-inch and 46-inch locations. The torsional response was captured using two additional sensors faced tangent to the x-direction accelerometers at heights of 26 inches and 46 inches.



(a) Translational Ground Motion (b) Torsional Ground Motion

Figure 31. Default sensor layout for parametric studies on the big shake table. Elevations are measured from the bottom of the structure. Table-mounted and structure-mounted accelerometers are denoted as (T) and (A).

3.4 Response metrics

The recorded output data files were imported into MATLAB for post-processing. Among the ten accelerometers instrumented on the host structure, the top-mounted sensors (46-inch elevation)

experienced the largest accelerations. Thus, the analyses primarily focused on the positive x-direction accelerometer (A9) for parametric studies and the positive x and y-directions accelerometers (A11 and A9) for the effectiveness demonstration experiments. Both time-domain and frequency-domain response metrics were utilized to evaluate the performance of the device in comparison to the control cases. All the response metrics were computed in MATLAB using consistent processing parameters, such as low-pass filtering, a standardized number of Fourier transform points, windowing, and overlap settings were applied to ensure comparability across configurations.

3.4.1 Control Cases

To assess the relative contributions of particle collision and inertial effects, two control configurations were tested in addition to the ring particle damper configuration containing the particles, "with particles" case. A "no particle" case consisted of empty device cavities to establish a structural response baseline. An "added mass" case incorporated the 3D-printed solid mass caps in the cavities to replicate the equivalent added mass of the ball bearings without particle motion. The "added mass" and "with particles" cases were normalized with respect to the corresponding "no particles" cases, using equation 1.

$$Percent\ Change = \frac{X - X_o}{X_o} * 100\% \qquad \textit{Equation 1}$$

Where X is the measured response of the "with particles" or "added mass" case, and X_o represents the measured response of the "no particles" case. The differences among the configurations helped isolate the particle collision effects from added mass effects, providing a clearer understanding of the effective damping performance.

3.4.2 Low Pass Filtering and High Frequency Results

Without additional filtering, acceleration signals for the "with particles" cases often exhibited an increased response when compared to the "added mass" and "no particles" control cases at higher frequencies. The auto-power spectral density results, an example of which is shown in Figure 32, show that these increases tend to be because of increases in response "with particles" compared to the "no particles" condition at high frequencies of about 150 Hz and beyond. However, this increase is occurring at frequencies beyond the frequency range relevant to the device's structural response of interest. To focus the analysis on relevant frequency content, a low-pass filter with a 50 Hz cut-off was applied before calculating the root mean square acceleration, H_2 norm, and $H\infty$ norm. Additionally, the frequency domain response metrics were limited to the 0 to 50 Hz range to emphasize the dominant modes of interest, reducing the influence of high-frequency noises present in the signals (Figure 33).

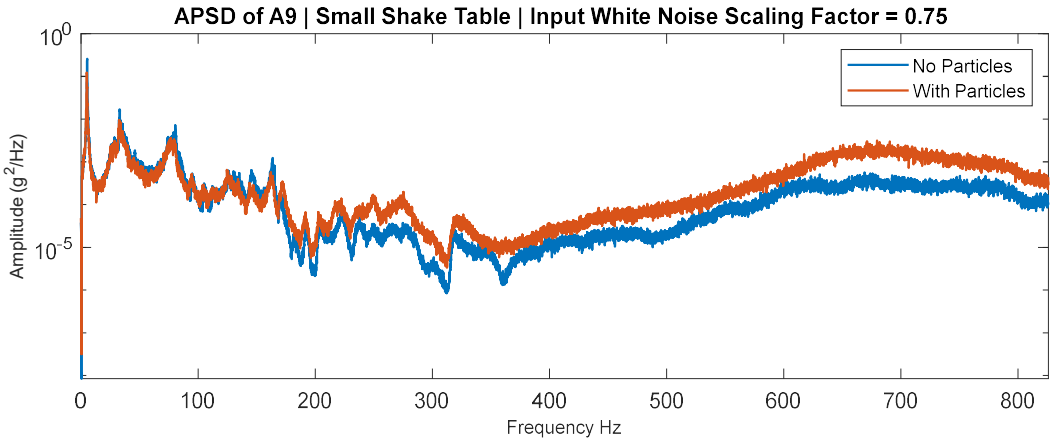


Figure 32. Frequency response function example of the full frequency range (0 to 825 Hz)

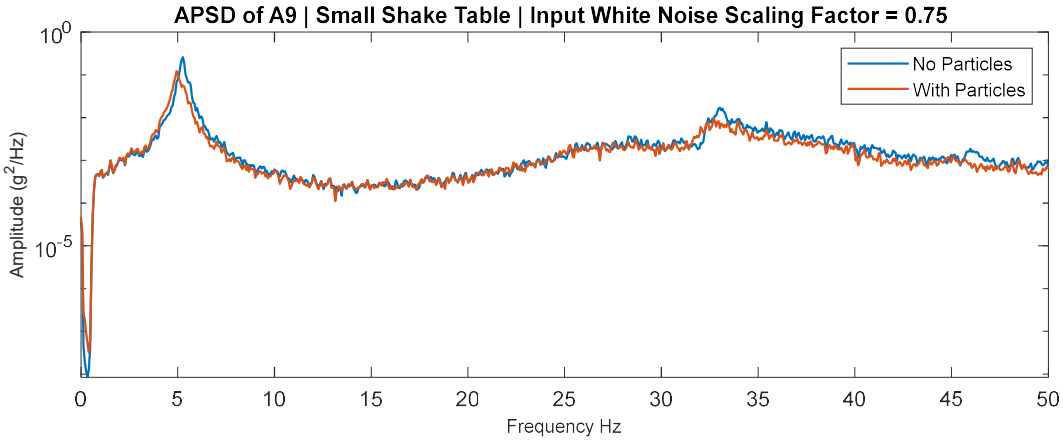


Figure 33. Frequency response function example of the relevant frequency range (0 to 50 Hz)

3.4.3 RMS Acceleration

The root mean square (RMS) acceleration was computed from the time history of each experiment. A low-pass filter with a cut-off frequency of 50 Hz was used to better capture the relevant behavior of the RPD. The RMS acceleration results of the "with particles" and "added mass" cases were each normalized by the corresponding "no particles" case to determine the RMS percent change. A negative RMS percentage indicated a decrease in RMS acceleration response, indicating an increase in the damping performance in comparison to the corresponding "no particles" control case.

3.4.3 Auto-Power Spectral Density

An auto-power spectral density (APSD) was computed for each configuration to assess a signal's energy response across frequencies. Under translational excitations (x-only, y-only, and combined

x-y), two dominant natural frequencies were observed between 4-6 Hz and 25-35 Hz. A modal analysis of the measured responses indicates that the 4-6 Hz range corresponds to the first bending modes in both the x and y directions, and the 25-35 Hz range represents a combination of the "second" bending modes and a top-concentrated breathing mode in the x and y directions. Similar to the Autodesk Inventor modal analysis results, the 4-6 Hz range includes the two first bending modes (M1 and M2), and the 25-35 Hz range includes the two second bending modes (M7 and M8), reflecting the overlapping frequencies. For torsional excitation, three dominant frequency ranges were identified: 31-33 Hz, 36-42 Hz, and 38-40 Hz. To isolate torsional motion, four accelerometers mounted on the host cylinder were used as opposing pairs. Accelerometer A12 (46" elevation) was positioned 90 degrees from A8. The difference in the signals (A12-A8) was calculated to capture a measure related to the tangential acceleration. This represents a measure of the torsional response as this value would be zero if the response is only longitudinal. A modal analysis was performed on the torsional data to confirm that the mode shapes corresponded to the first bending, top-concentrated breathing, second bending, and a torsional mode with breathing present. The APSD amplitudes at each natural frequency were extracted to normalize the "with particles" and "added mass" cases against the corresponding "no particles" baseline, allowing for an assessment of the relative damping effectiveness in terms of percent changes from the "no particles" case.

3.4.4 Transfer Functions

Transfer functions were analyzed to assess the dynamic relationship between the ground motion input and host structure response. For translational excitation, the top accelerometers in the positive x-(A11) and y-directions (A9) served as output signals, while the corresponding table accelerometers (T2 and T1) were used as the input signals. Similar to the APSD results, two dominant natural frequencies were identified between 4-6 Hz and 25-35Hz. Under torsional excitation, the differential accelerations at the 46-inch (A12-A8) elevations were used as the output signals to isolate the rotational response, with the input signal defined as the differential table motion (T1-T2). The torsional transfer functions displayed three primary natural frequencies at 31-33 Hz, 36-42 Hz, and 38-40 Hz, corresponding second bending and a torsional mode with breathing present. For both loading types, the amplitudes at the natural frequencies were extracted and normalized by the "no particles" case, enabling a quantitative comparison of the damping performance for the "with particles" and "added mass" configurations.

3.4.5 Additional Frequency Response metrics

The H_2 and $H\infty$ norms were additional measures calculated to assess damping performance in the frequency domain. Specifically, H_2 was determined to quantify the area under the transfer function curve between the table input and host structure response, and the $H\infty$ norm was computed to measure the maximum amplitude of the transfer function curve. A low-pass filter with a cut-off of 50 Hz was applied to both response metrics to focus on the relevant frequency range. Both H_2 and

H∞ norm values for the “with particles” and “added mass” cases were normalized with respect to the “no particles” baseline, using equation 1.

4. Initial Parametric Studies

The first area of focus was to develop an understanding of how the parameters of the ring particle damper impact its performance. The initial parametric studies investigated properties such as ground motion load amplitude, optimal ratio of total particle mass to the host structure mass, the device position on the host structure, and the device cavity material, were evaluated to identify the most effective parameter combination for further dynamic testing and effectiveness demonstration.

4.1. Results and Discussions

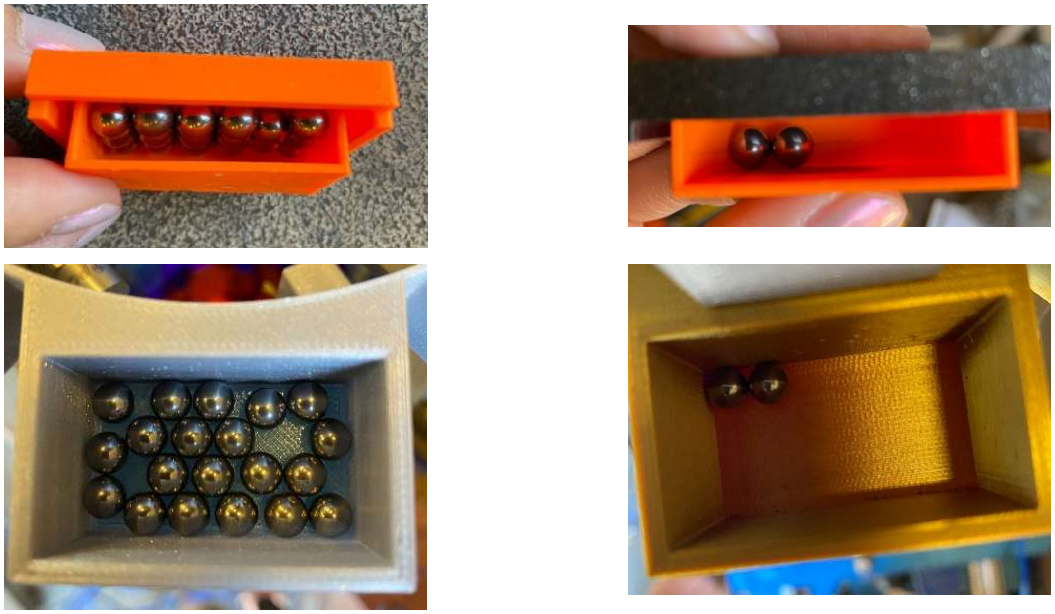
The section presents and discusses the results observed from the initial parametric studies, evaluating the ring particle damper device behavior. The discussion integrates both the time-domain and frequency-domain response metrics to identify performance trends and conclusions to determine the most effective configuration for further dynamic testing in the second experimental phase. The results are organized by parametric investigation type, addressing the corresponding experimental findings and implications for the device performance. Appendix A contains all response metrics discussed in the initial parametric studies.

4.1.1 Optimal Particle Packing Ratio

The purpose of the optimal particle ratio mass study was to examine how variations in the particle packing ratio, defined as the proportion of the cavity volume occupied by the ¼-inch diameter ball bearings, affect the device’s damping performance. Using the cap-layer cavity configuration, each cavity was subdivided into two stacked compartments, together forming a single cavity, to increase particle-particle and particle-wall interaction. The packing ratios for the upper and lower layers were estimated to have comparable spacing between particles (Table 8). The particle mass percent ratio is defined as the particle mass relative to the total structural mass, 25.034 lbmass, which was determined from the Inventor model. The “with particles” configurations were evaluated relative to the “no particles” control case to best analyze the particle-induced damping effects. An initial particle packing ratio study (Study 1) was conducted, consisting of eight tests. The packing ratios ranged from highly compacted cavity configurations with minimum free volume for particle collisions (17 top / 20 bottom) to configurations with significant available space between particles (2 top / 2 bottom) (Figure 34). A second particle packing ratio study (Study 2) further examined nine additional tests to assess whether incremental changes in particles will influence the damping performance. For both studies, the experiments were performed on the small shake table, using a consistent excitation amplitude of X=0.75.

Table 8. Summary of optimal particle ratio mass tests

Top Layer No. of Particles	Bottom Layer No. of Particles	Total Particle Mass (lbmass)	Particle Mass Ratio
	Study 1		
17	20	1.3853	5.53 %
15	18	1.2355	4.94 %
13	16	1.0858	4.34 %
10	12	0.8237	3.29 %
8	10	0.6739	2.69 %
6	7	0.4867	1.94 %
4	5	0.3370	1.35 %
2	2	0.1498	0.60 %
	Study 2		
15	19	1.3853	5.08%
15	18	1.2355	4.94%
15	17	1.0858	4.79%
14	19	0.8237	4.94%
14	18	0.6739	4.79%
14	17	0.4867	4.64%
16	19	0.3370	5.23%
16	18	0.1498	5.08%
16	17	1.2730	4.94%



(a) Tightly Confined Packing Ratio (17 Top / 20 Bottom)

(b) High Free Volume Packing Ratio (2 Top / 2 Bottom)

Figure 34. Particle bearing packing ratios

Across all packing ratios, the "with particles" cases produced a negative percent difference from the "no particles" control cases for the majority of response metrics, indicating that each packing ratio had a positive contribution to damping (Figure 35). A notable trend in the frequency domain was that the most compacted packing ratio (17 top / 20 bottom) exhibited similar performance to the most spacious configurations, suggesting that overly compacted particle configurations restrict particle collision interactions and reduce the device's energy dissipation capabilities (Figure 34, Figure 35, and Figure 36). The (15 top / 18 bottom) packing ratio exhibited the largest, or near largest, percent change across the majority of response metrics. Although some response metrics suggest an alternative optimal packing ratio, the (15 top / 18 bottom) configuration was selected based on engineering judgement as the most promising performance, providing a balance between a larger particle count and available free volume.

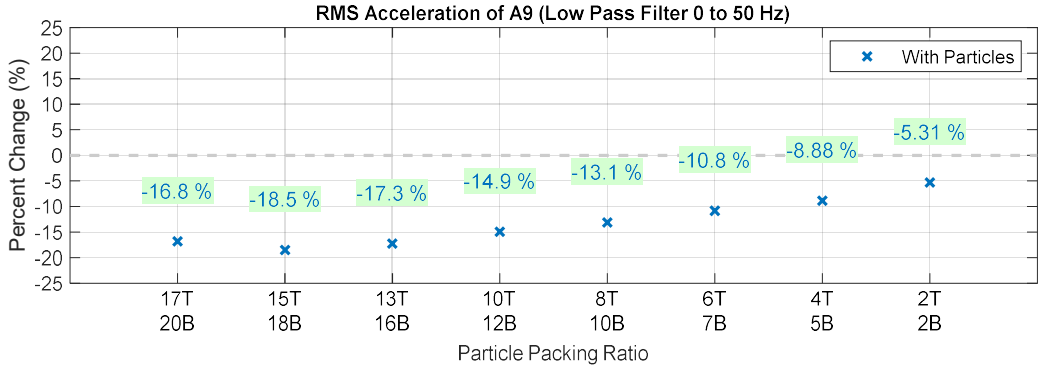


Figure 35. Percent change in RMS response as a function of particle packing ratio (Study 1). Measurements from the top (T) and bottom (B) particle layers are shown. Values are normalized to the corresponding no-particle case.

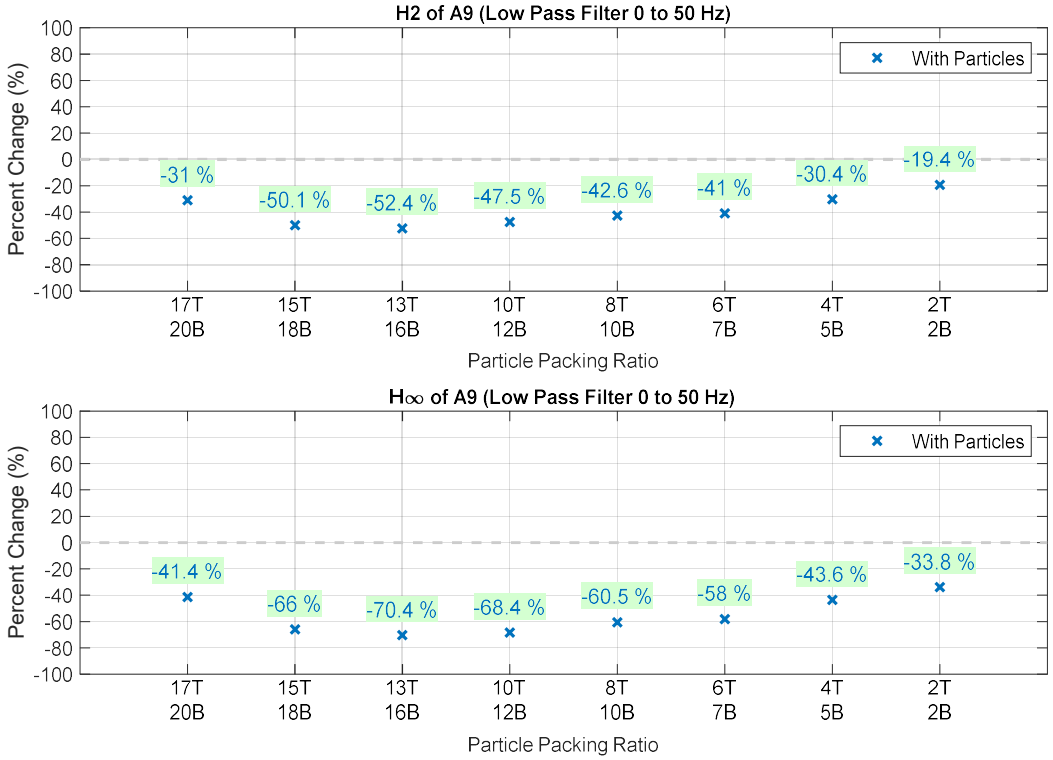


Figure 36. Percent change in frequency domain response metrics (H2 and H∞) as a function of particle packing ratio (Study 1). Measurements from the top (T) and bottom (B) particle layers are shown. Values are normalized to the corresponding no-particle case.

To further investigate how free volume influences damping performance, an additional nine packing ratio configurations were tested to determine whether slight adjustments, such as adding or removing one to two particles, to the (15 top / 18 bottom) ratio would enhance the damping response. Across all response metrics, the percent difference from the "no particles" case exhibited minor variations and no consistent trends, indicating that small incremental changes in particles did not lead to a clear enhanced configuration (Figure 37). The "optimal" packing ratio identified in the initial tests (15 top / 18 bottom) was selected as the "default" packing ratio for the remainder of the experiments. The mass-caps were fabricated to replicate (15 top / 18 bottom) added mass and used as a control case. The frequency response function (FRFs) of the (15 top / 18 bottom) packing ratio exhibited significant amplitude reductions to the first bending mode and the second bending/top breathing mode (Figure 38Figure 38).

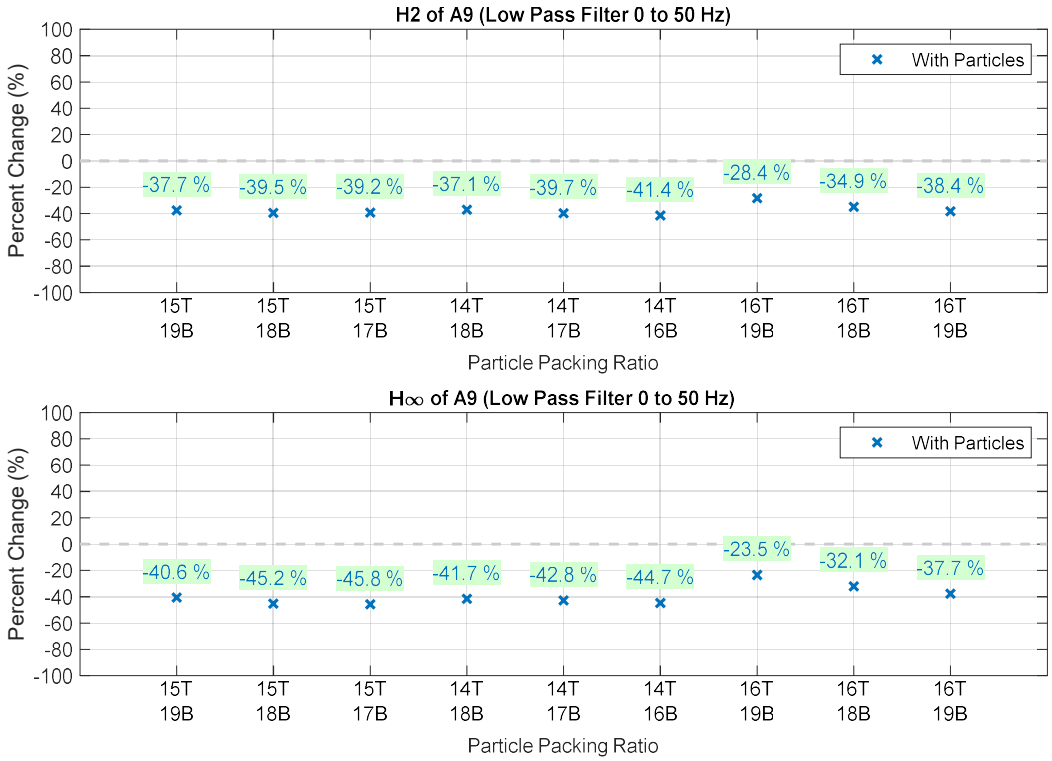


Figure 37. Percent change in frequency domain response metrics (H2 and H∞) as a function of particle packing ratio (Study 2). Measurements from the top (T) and bottom (B) particle layers are shown. Values are normalized to the corresponding no-particle case.

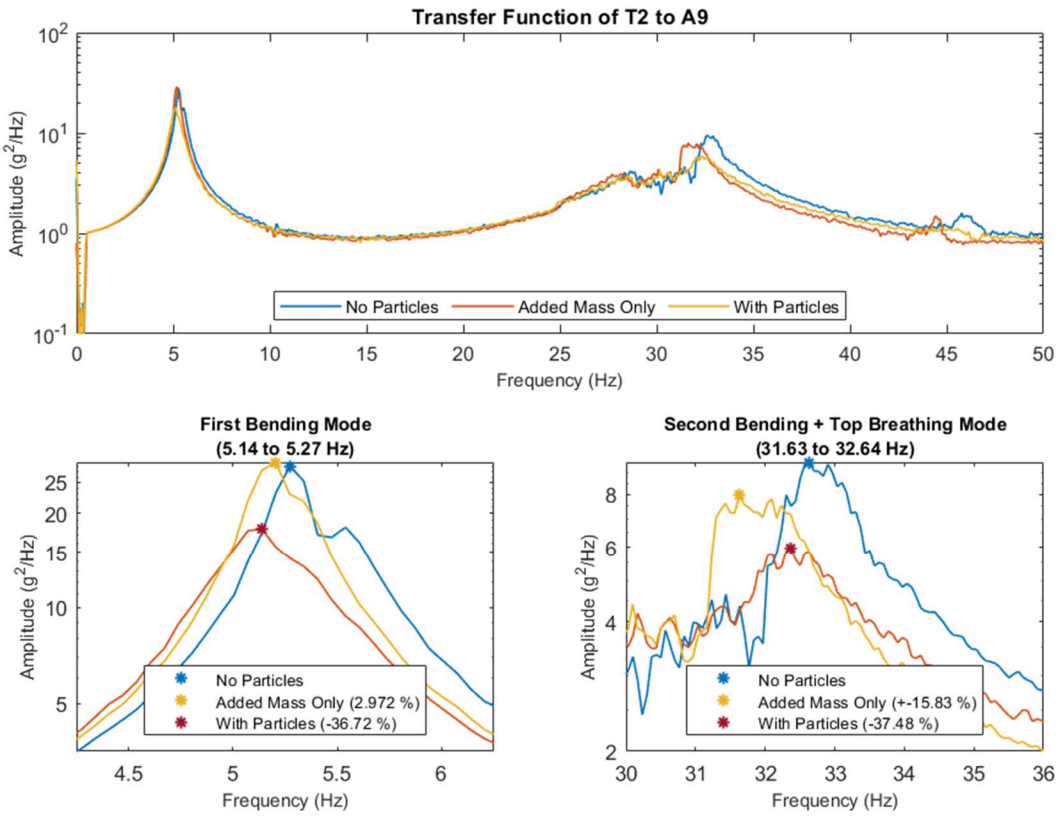


Figure 38. Frequency response function for sensor, A9, comparing no-particle case, added mass case, and particle-filled 15 (T) and 18 (B) packing ratios. Percent changes are normalized with the corresponding no-particle case.

4.1.2 Initial White Noise Excitation Amplitude

An initial load amplitude study was conducted to investigate the device's performance subjected to varying amplitude levels of white noise ground excitation. Acceleration and displacement gains on the small shake table were scaled from 1.0 down to 0.25 in increments of 0.075 (Table 4). The default (15 top / 18 bottom = 4.94 % particle mass ratio) "with particles" configuration was used for each test, and corresponding "no particles" and "added mass" control cases were performed at each amplitude level.

Across all amplitude scaling factors, the "with particles" cases demonstrated increased system damping, demonstrating that the device provided damping across a wide range of tested amplitudes. In the frequency domain, the "with particles" case percent changes from the "no particles" cases were consistently lower than the normalized "added mass" cases, confirming that the observed energy dissipation was primarily attributed to particle-particle and particle-wall interactions rather than added mass effects alone (Figure 39). In the time domain, at lower

excitation levels (X=0.25 to X=0.55), the device exhibited reduced damping effectiveness with percent changes similar to or slightly above its "added mass" cases (Figure 40). These observations indicate an effective excitation threshold is required for the ring particle damper to provide effective damping performance beyond its added mass effects. In this study, excitation amplitudes above X=0.625, corresponding to a representative RMS of 0.1636 g (Table 4), were sufficient threshold to achieve effective damping performance.

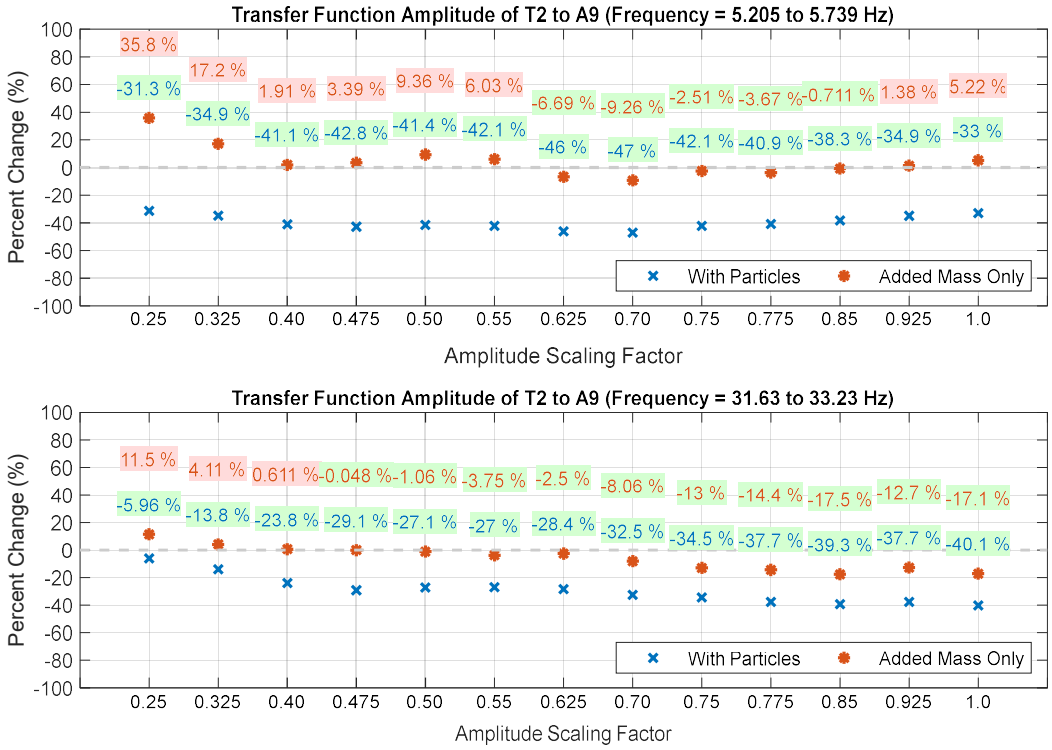


Figure 39. Percent change in the transfer function amplitude response at the first bending mode and second bending/top breathing modes with varying white-noise excitation amplitudes on the small shake table. Values are normalized to the corresponding no-particle case.

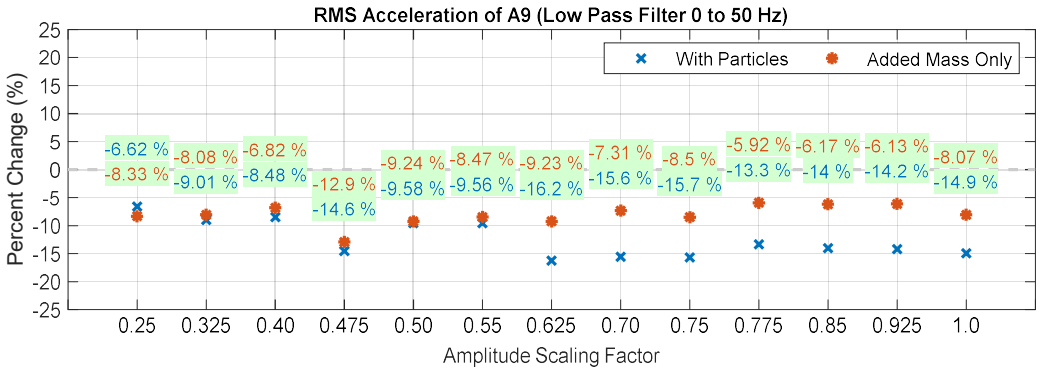


Figure 40. Percent change in the RMS response with varying white-noise excitation amplitudes on the small shake table. Values are normalized to the corresponding no-particle case.

4.1.3 Initial Container Usage

An initial container usage study was conducted to evaluate how the device performance is affected by different container configurations, such as the device with full container usage, where all eight cavities at each level are filled with particles, and half container usage, where only four cavities at each level are filled with particles. Additionally, the container usage study was used to assess whether the device performance is directionally dependent. Two half-container usage configurations were tested: four containers filled in a 0-degree orientation parallel to the direction of the ground motion, and four containers filled 45-degree offset relative to the ground motion (Figure 41). A consistent X=0.75 white noise was applied to each test. All "filled" containers used a (15 top / 18 bottom) packing ratio, and a corresponding "added mass" and "no particles" configurations were tested as control cases. The mass particle ratio of the full container usage was 4.94%, and the two half-container usage configurations had a mass particle ratio of 2.47%. The mass particle ratios are relative to the total structural mass, 25.034 lbmass.

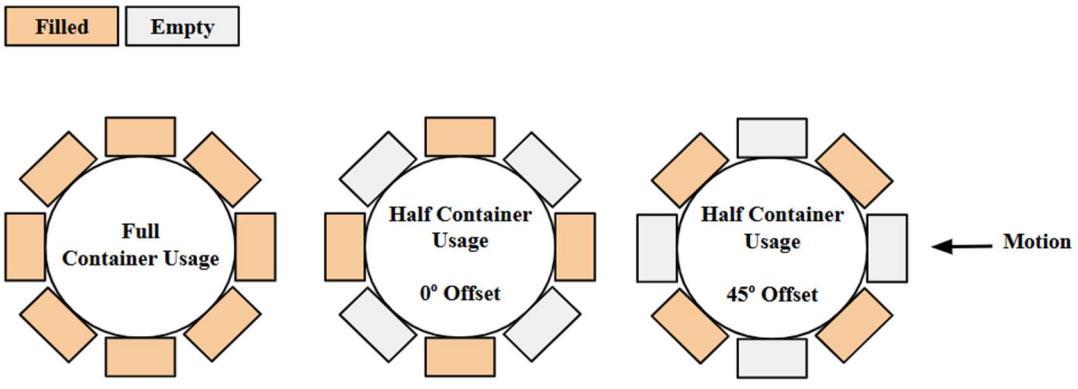


Figure 41. Initial container usage study configurations

Across all response metrics, each container configuration demonstrated improved damping performance with a percent difference less than zero, and below the corresponding (added mass / no particles) percent differences. As expected, the full container configuration produced lower ratios compared to the two half-container usage configurations due to the increased added mass and greater particle interaction occurring. Between the two half container configurations, the 0-degree and 45-degree offsets exhibited similar performances across the RMS, APSD, transfer functions, H_2 norm, and $H\infty$ norm response metrics. For the first bending mode (4-6 Hz frequency range), the performance of the half container configurations exhibits similar percent differences, suggesting the device is independent of directional placement (Figure 42). In contrast, for the second bending/top breathing mode (25-35 Hz frequency range), the 0-degree configuration exhibited performance similar to the full configuration and outperformed the 45-degree configuration. These results suggest that the directional placement influences the device's effectiveness at reducing higher-frequency modes.

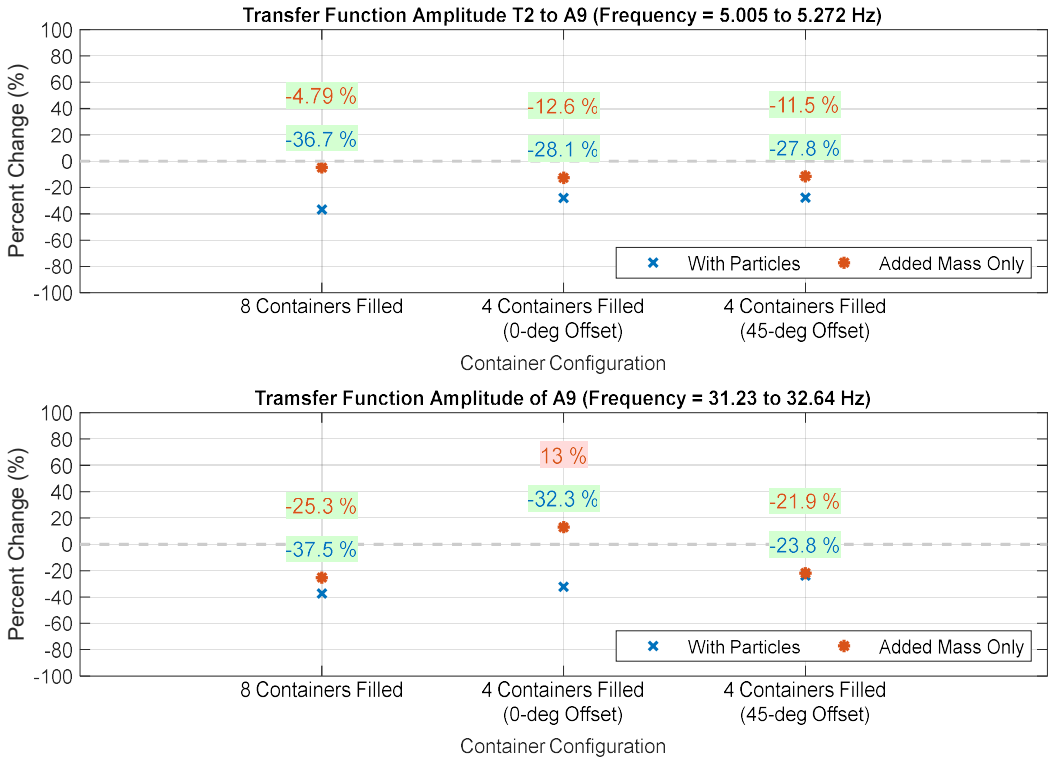


Figure 42. Percent change in the transfer function amplitude responses at the first bending mode and second bending/ top breathing modes with respect to different particle damper container configurations on the small shake table. The values are normalized to the corresponding no-particle case.

4.1.4 Optimal Device Location

The optimal device location study was performed to assess the effectiveness of a single device placement compared with using two devices (Study 1). The tests were conducted with the devices positioned at the top (46 inches) and mid (26 inches) heights, as well as top-only and mid-only configurations. All device containers used the (15 top / 18 bottom) packing ratio , and a 0.75 white noise scaling factor with corresponding “no particles” and “added mass” control cases. The particle mass ratio for the two devices is 4.94 %, while the single device had a particle mass ratio of 2.47% relative to the total structural mass of 25.034 lbmass.

Across all configurations, the percent difference from the “no particles” control case was below zero for every response metric, and in most cases, were also lower than the “added mass” percentages, indicating damping contributions were beyond added inertial mass. As expected, the configuration with devices at the top and mid-height yielded the lowest ratios overall. However, the top-only configuration performed comparably to the configuration with two devices (Figure 43). In contrast, the mid-only configuration produced percentages similar to its corresponding added mass control cases, suggesting the damping at mid-height is dominated by inertial effects rather than particle interaction. This trend was consistent across all response metrics. The results indicate the top device is primarily responsible for the observed damping in the two-device configuration, and the mid-high device is less effective. This may indicate that the particle damper, to be effective, needs to be located very close to the point of max displacement

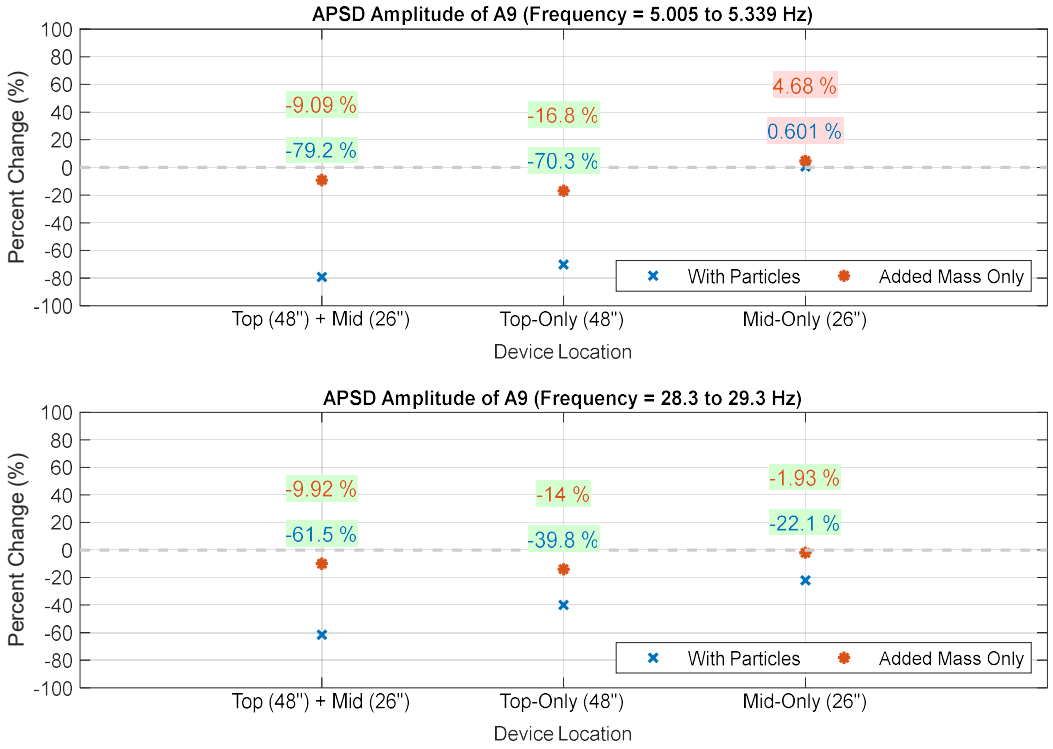


Figure 43. Percent change in the APSD amplitudes at the first bending mode and second bending/top breathing modes for different ring particle damper locations along the height of the structure (Study 1). Elevations indicate the distance from the bottom of the structure. Values are normalized to the corresponding no-particle case.

Based on the initial conclusions, the study further explored alternative device placements within the upper half of the host structure to identify locations more effective than the mid-height position, such as the top (48-inch) and 34-inch heights, or the top and 42-inch heights (Study 2) (Figure 44). All tests used a consistent (15 top / 18 bottom = 4.94% particle mass ratio) packing ratio and white noise scaling factor of X=0.75, along with corresponding “no particles” and “added mass” control cases.

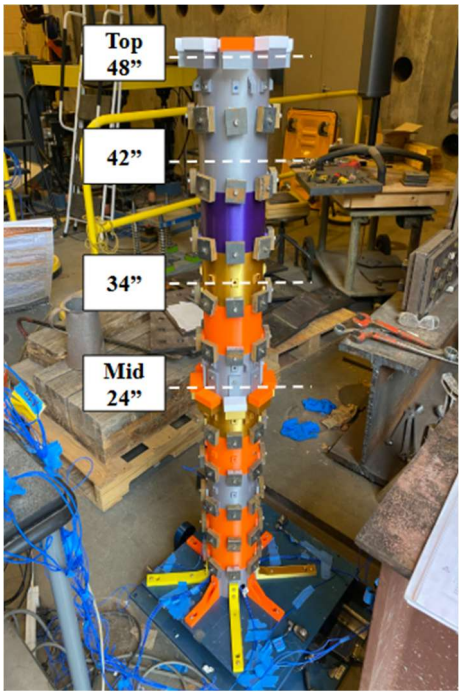


Figure 44. Optimal device location study 2

All configurations demonstrated improved damping relative to the “no particles” control case. For the RMS, H_2 norm, and H∞ norm results, the top and 34-inch configuration performed slightly worse than the original, top and mid-height configuration, while the top and 48-inch configuration produced the lowest normalized ratios, indicating the most effective damping locations. For the first mode in the APSD and transfer function amplitudes, the damping performance improved as the secondary device location increased along the host structure. For the second mode, the top and 34-inch configuration exhibited the least effective performance, and the top and 48-inch configuration performed the best, suggesting the optimal device placement aligns with maximum modal displacement of the host structure, as expected. The top and 48-inch configuration consistently produced percent differences below zero, and under the corresponding (added mass / no particles) percent change, confirming the energy dissipation is governed by particle collisions rather than added mass effects. Additionally, the top and 48-inch configuration outperformed the top and mid configuration across all response metrics, demonstrating that the placement of the device farther from the mid-height does not diminish the second mode damping effectiveness (Figure *45*).

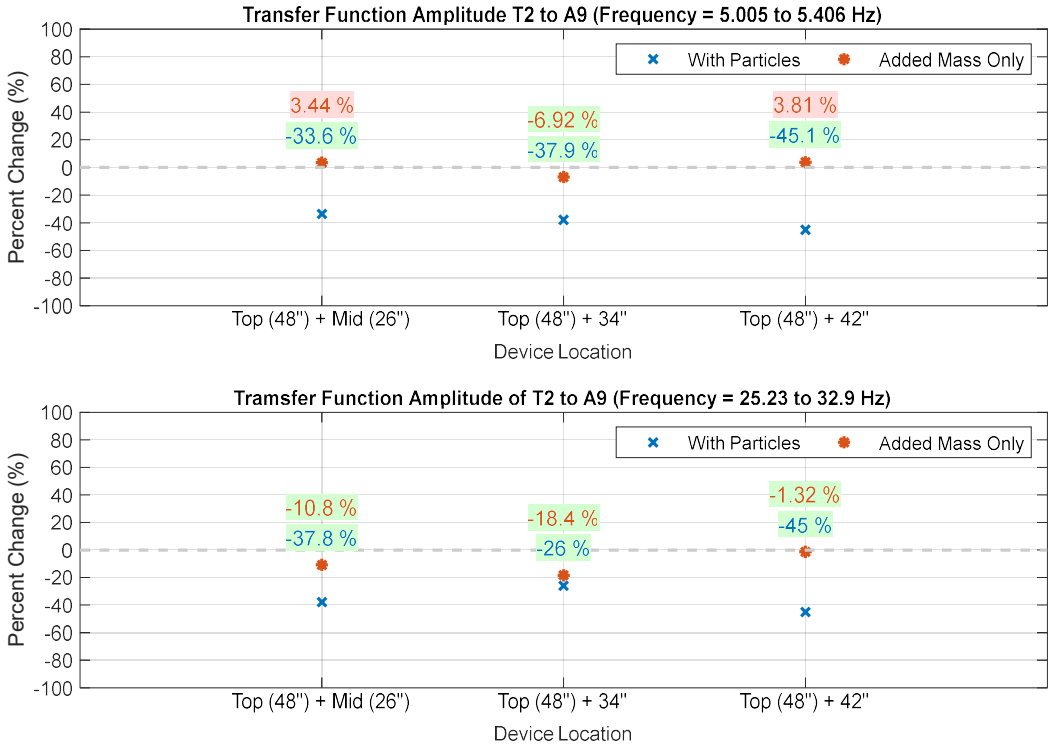
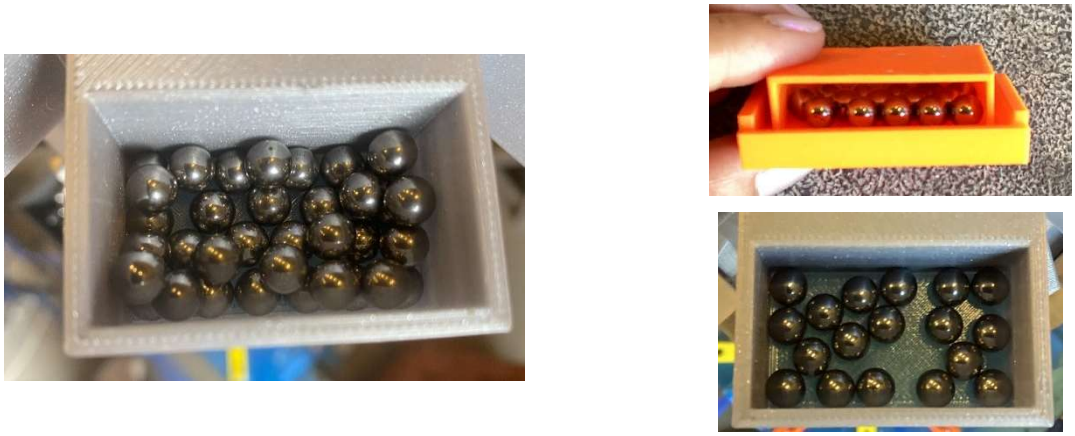


Figure 45. *Percent change in the transfer function amplitudes at the first bending mode and second bending/top breathing modes for different ring particle damper locations along the height of the structure (Study 2). Elevations indicate the distance from the bottom of the structure. Values are normalized to the corresponding no-particle case.*

4.1.5 Cavity Layer Usage

The cavity layer usage study was conducted to assess the damping performance of RPD configurations utilizing either one cavity layer or two cavity layers with the cap-layer design. The host structure was assembled with two RPD located at the 48-inch and 42-inch heights. The two cavity layers utilized a particle packing ratio of (15 top / 18 bottom = 4.94% particle mass ratio), while the single cavity layer contained 35 particles (5.23% particle mass ratio), corresponding to an equivalent total mass of the cap-layer print and particles of the two cavity layer configuration (Figure 46). The cavity configurations were tested under a white noise excitation, ranging from X=1.0 to X=0.35 in increments of 0.10. A corresponding “no particles” and “added mass” tests were performed at each excitation amplitude.



(a) One Cavity Layer (b) Two Cavity Layers

Figure 46. Cavity layer usage "with particles" test configurations.

Across both time-domain and frequency-domain response metrics, the single cavity layer configuration exhibited trends similar to those seen in the two cavity layer configuration. In the time domain, both configurations showed comparable percent reductions relative from the "no particle" cases, with the two cavity layers displaying slightly improved performance of approximately 3-10% (Figure 47). In the frequency domain, both configurations exhibited similar trends across the excitation amplitude range in the second bending / top breathing mode (Figure 48). However, the two cavity layer exhibited an improved damping performance in the first bending mode compared to the single cavity layer configuration. Because the single cavity layer did not provide significant improvement in damping performance, the two-cavity layer configuration was utilized for the remainder of the studies due to its potential 15-30% increase in damping performance in the first bending mode.

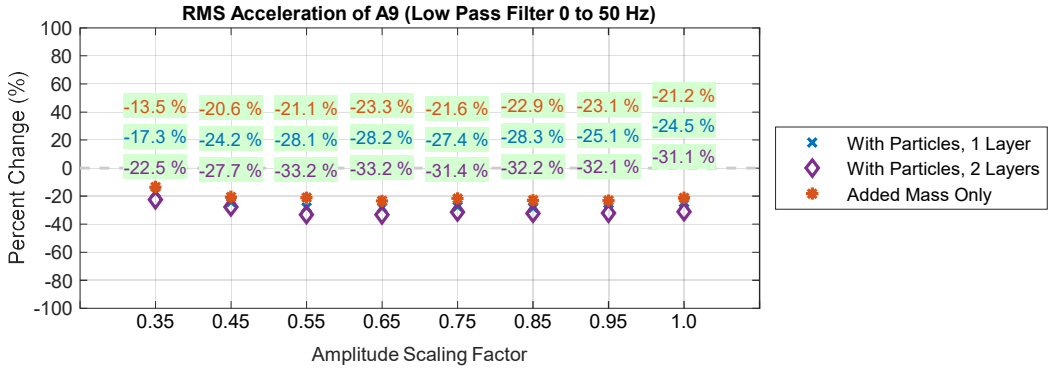


Figure 47. Percent change in the RMS response for different cavity layer configurations. "1 Layer" represents the one cavity packed with 35 particles, and "2 Layers" refers to two cavities used with a (15 Top / 18 Bottom) packing ratio. Values are normalized to the corresponding no-particle case.

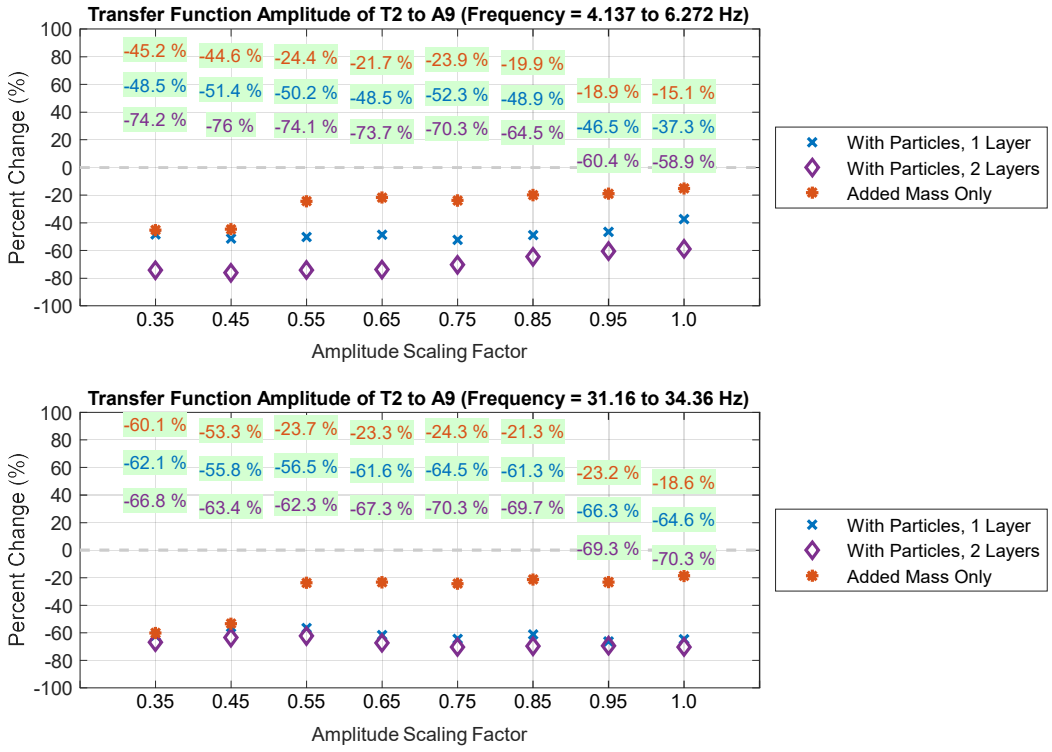


Figure 48. Percent change in the transfer function amplitude response for different cavity layer configurations at the first bending mode and the second bending/ top breathing mode. "1 Layer" represents the one cavity packed with 35 particles, and "2 Layers" refers to two cavities used with a (15 Top / 18 Bottom) packing ratio. Values are normalized to the corresponding no-particle case.

4.1.6 Device Cavity Lining Material

The device cavity lining material study evaluated the damping performance of PLA cavity walls to steel liner walls with the idea that steel offers increased durability, potentially enhancing energy dissipation through increased plastic deformation of the particles. A new cylinder segment was fabricated with enlarged cavity dimensions to accommodate a steel tube liner (Figure 49). The host structure was assembled with two devices located at the top (48 inches) and at the 42-inch height. Each device used a single-layer particle configuration with a range of packing ratios selected to maintain comparable available free volume across the two lining materials (Table *9*). The particle mass percent ratio is defined as the particle mass relative to the total structural mass, 25.034 lbmass, which was determined from the Inventor model. A corresponding "no particles" test was performed for both the PLA and steel-lined cylinder segments, and a consistent white noise of X=0.75 was applied for each test.



Figure 49. Cylinder segment with steel cavity lining (top view)

Table 9. Device cavity lining study particle packing ratios

PLA Cavity Lining			***Metal Cavity Lining***		
No. Particles		**Particle Mass Ratio**	**No. Particles**		**Particle Mass Ratio**
19		2.84 %	***15***		3.38 %
18		2.69 %	***14***		3.16 %
17		2.54 %	***13***		2.93 %

16		2.39 %	***12***		2.71 %
15		2.24 %	***11***		2.48 %

For both materials, the "with particles" percent changes from the "no particles" case were less than zero across all response metrics, indicating that both configurations provided damping. In both cases, the RMS percent change decreased as the number of particles decreased, with the PLA lining performing slightly better than the steel lining (Figure 50). For the first mode of the APSD, the steel lining produced a greater percent change from the "no particles" case. In the second mode, the PLA lining exhibited an increase in damping performance results compared to the steel lining. For the transfer functions, H_2 norm, and H∞ norm measures, the PLA and steel lining showed comparable performance (Figure 51). The steel liner increased system mass and did not display significantly improved damping response; therefore, the PLA-lined device was selected for use in the effectiveness demonstration.

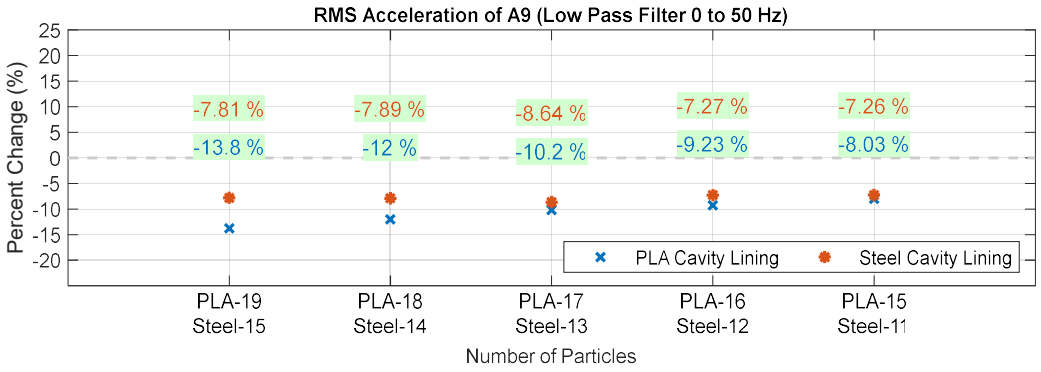


Figure 50. Percent change in the RMS response as a function of different particle damper cavity materials. PLA and steel packing ratios are shown, and the percent changes are normalized with respect to the corresponding no-particle case.



Figure 51. Percent change in the APSD amplitude at the first bending mode and second bending/top breathing modes as a function of different particle damper cavity materials. PLA and steel packing ratios are shown, and the percent changes are normalized with respect to the corresponding no-particle case.

4.1.7 Sinusoidal Excitation

The sinusoidal excitation study evaluated the effective damping performance of the ring particle damper at the host structure's resonance frequency. The tests were conducted with the devices positioned at the top (48-inch) and 42-inch elevations, using the (15 top / 18 bottom = 4.94% particle mass ratio) particle packing ratio for the "with particles" case. The "no particle" case was loaded with a frequency of 5.2057 Hz, while the "with particles" and "added mass" cases were excited with a frequency of 5.0055 Hz. Utilizing prior measurements, these frequencies correspond to the response of the host structure of each configuration. Using resonance frequencies specific to each case enables the device performance to be compared under equivalent loading conditions. Four sinusoidal amplitudes were evaluated with a representative RMS and peak acceleration, detailed in Table 10. These scaling factors differ from amplitude scaling factors due to the nonlinear transient behavior and high-frequency content superimposed on the command frequency. Additionally, the small shake table's effective ground motion can excite more than the primary frequency. The representative RMS and peak acceleration were derived from the "no particles" case, using a low-pass filter with a cutoff of 50 Hz.

Table 10. Measured table-mounted acceleration representing the sinusoidal excitation applied in the X-direction to the structure on the small shake table.

Excitation Amplitude Label	*Representative RMS (g)*	*Peak Acceleration (g)*
X=0.00070	0.0030	0.0208
X=0.00084	0.0798	0.3493
X=0.00095	0.1070	0.4941
X=0.001	0.1146	0.5139

At the lowest excitation (X=0.00070), the "with particles" and "added mass" cases exhibited higher modal amplitudes than the "no particles" case in the APSD metrics (Figure 52). However, at higher excitation levels (X≥0.00085), the device demonstrated effective damping at the first bending mode, exhibiting a greater percent reduction compared to the corresponding "added mass" cases (Figure 53). In the H2 and H∞ metrics, the ring particle damper exhibited effective performance under sinusoidal loading, consistent with its behavior under white noise excitation (Figure 54).

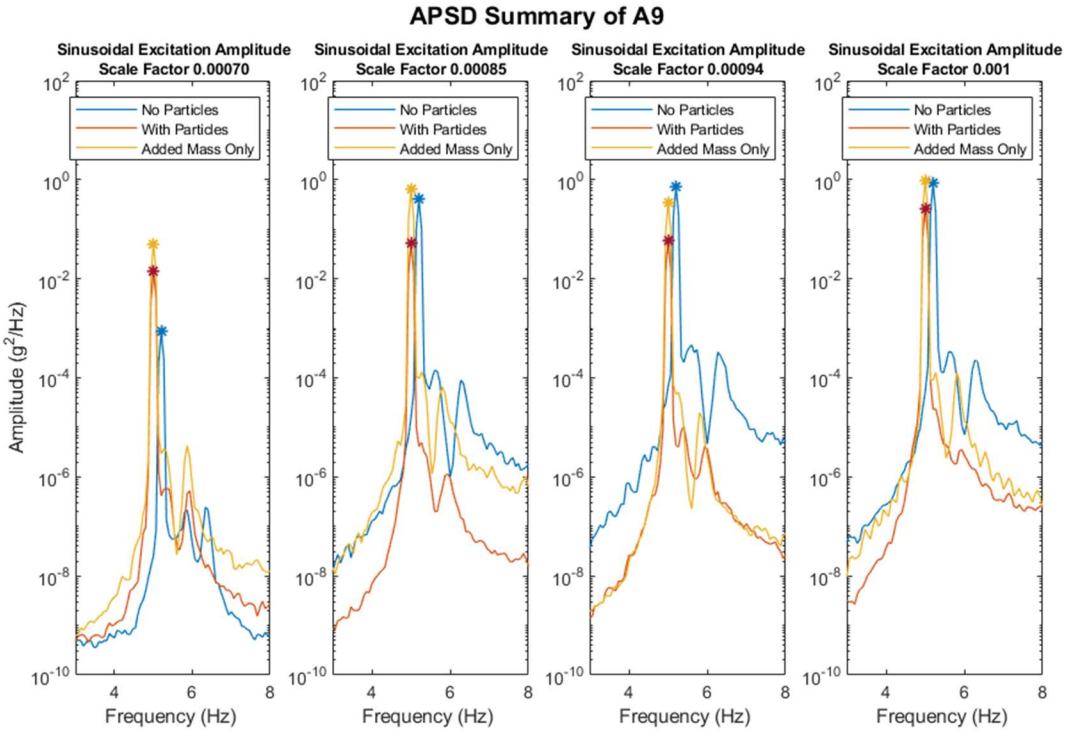


Figure 52. Frequency response function at the first bending mode under sinusoidal excitation, comparing the no-particle case, the with-particle case, and the added mass case at varying excitation amplitudes.

The excitation frequency was 5.21 Hz for the no-particle configuration, and 5.01 Hz for the with-particles and added mass configurations.

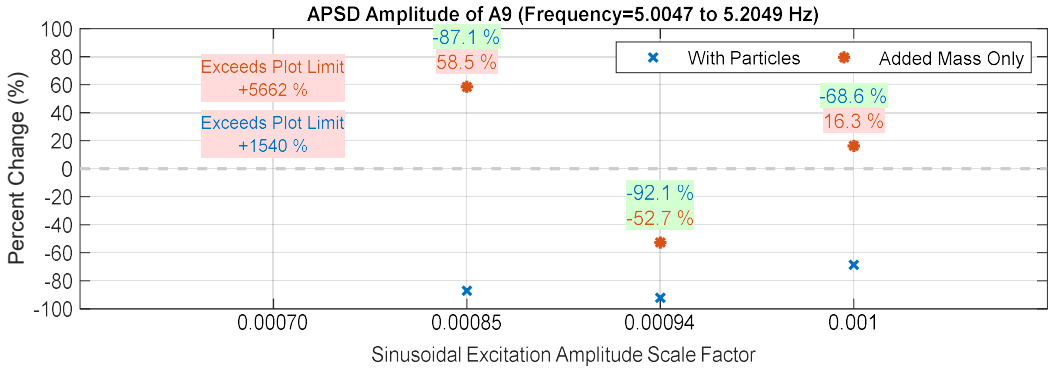


Figure 53. Percent change in the APSD amplitude at the first bending mode under varying sinusoidal excitation amplitudes. The excitation frequency was 5.21 Hz for the no-particle configuration, and 5.01 Hz for the with-particles and added mass configurations. Values are normalized to the corresponding no-particle case.

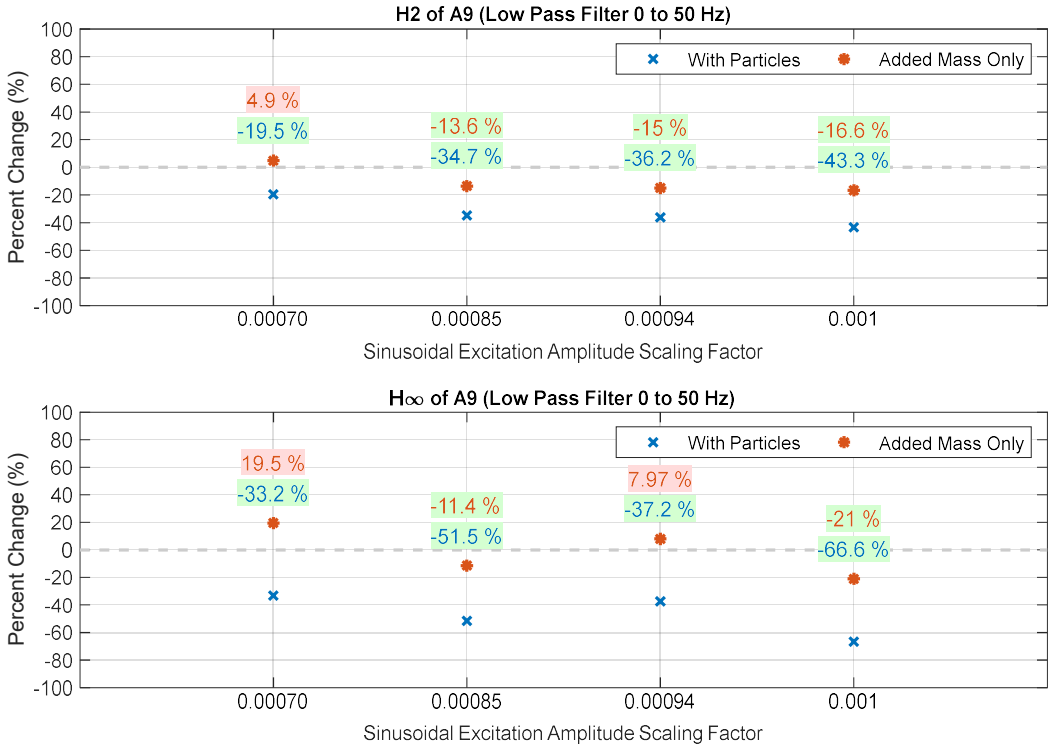


Figure 54. Percent change in frequency domain response metrics (H2 and H∞) under sinusoidal excitation amplitudes. The excitation frequency was 5.21 Hz for the no-particle configuration, and 5.01 Hz for the with-particles and added mass configurations. Values are normalized with respect to corresponding no-particle configurations.

4.1.8 Sine Sweep Excitation

To ensure the sinusoidal excitation study captured the resonance frequency between 4 to 6 Hz, a sine sweep study was conducted to evaluate the ring particle damper's performance. The sweep gradually increased from 3.5 to 6.5 Hz over 30 seconds at six different sinusoidal amplitudes (Figure 55). The structure was configured with the devices located at the 48-inch and 42-in elevations, and the "with particles" cases consistently used a (15 top / 18 bottom = 4.94% particle mass ratio) particle packing ratio. Six sine sweep amplitudes were evaluated (Figure 56), with representative RMS and peak accelerations summarized in Table 11Table 10. The representative values were determined from the "no particles" with a low-pass filter at a 50 Hz cutoff.

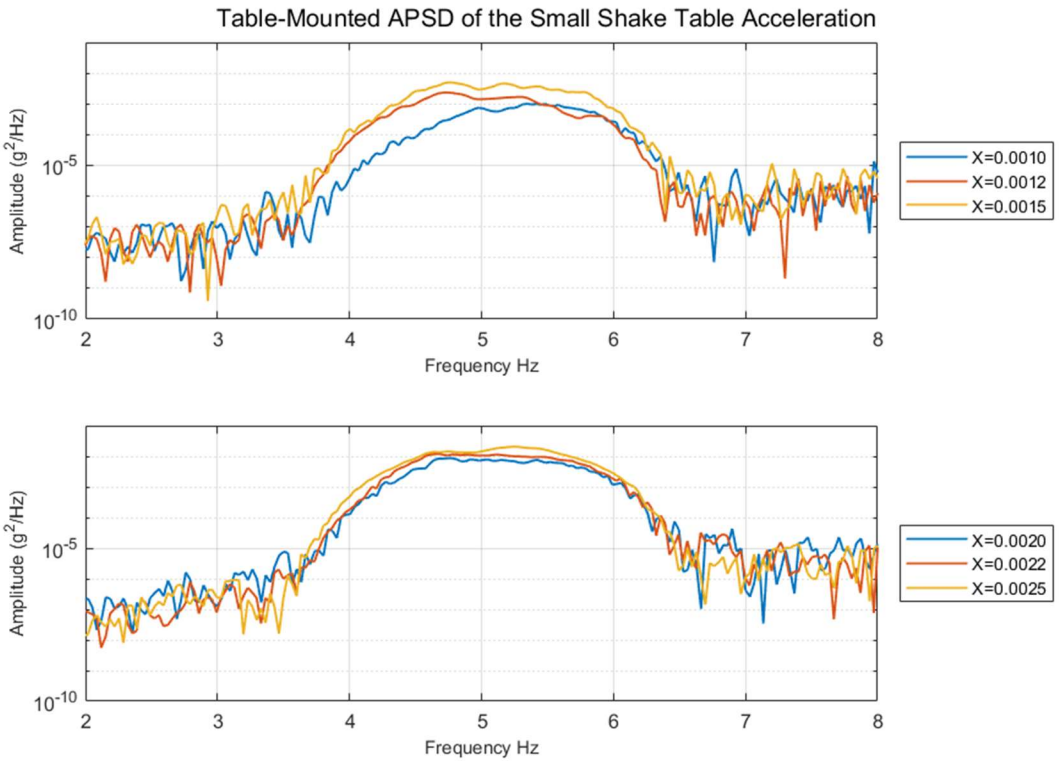


Figure 55. Frequency response function of the small shake table under 30-second sine sweep excitation from 3.5 to 6.5 Hz at various input scaling factors. The APSDs are separated into two graphs to improve clarity and for individual curves to be easily distinguished.

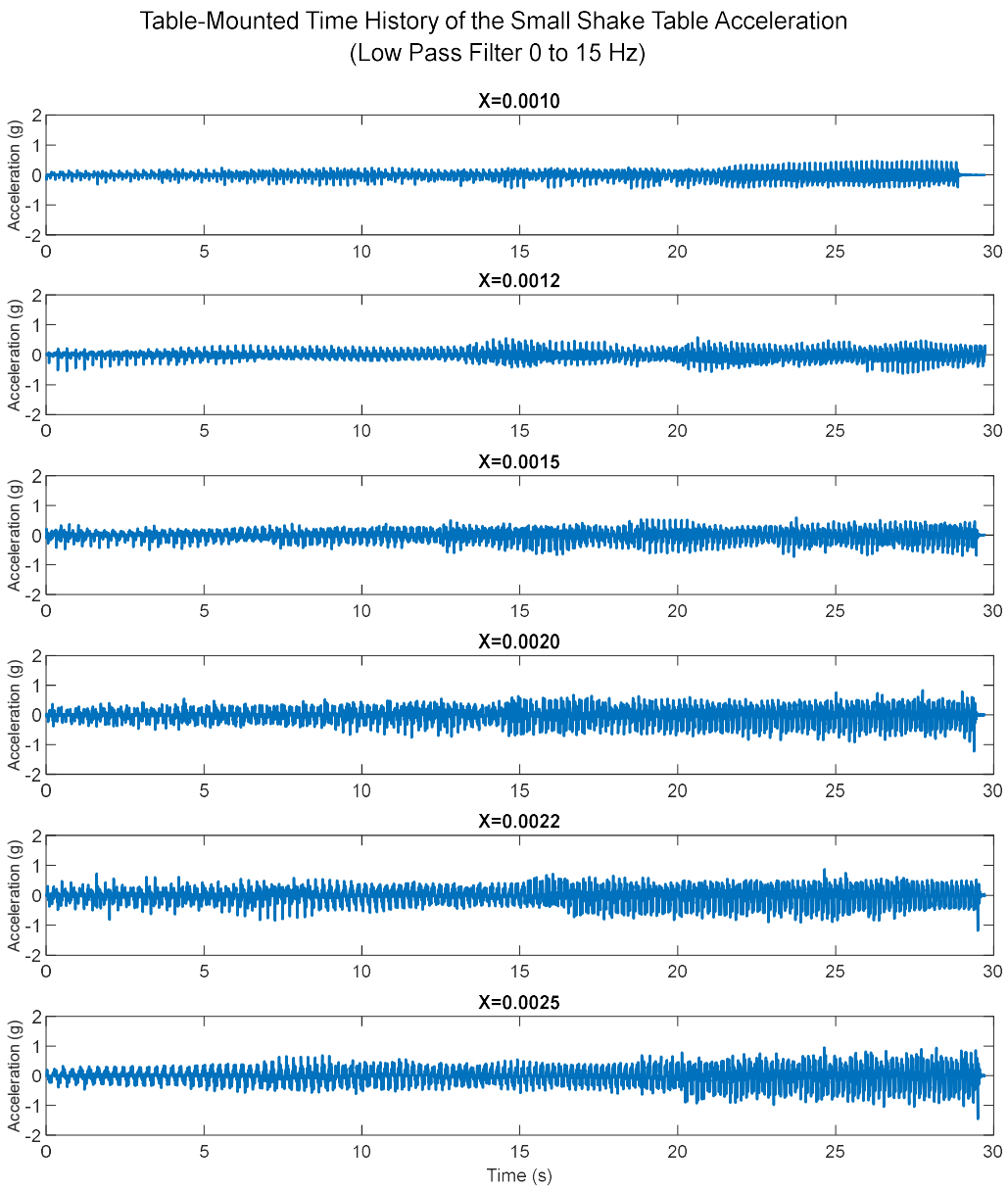


Figure 56. Acceleration time histories of sine sweep tests at various amplitudes. Excitation is applied in the X- direction to the structure on the small shake table.

Table 11. Measured table-mounted acceleration representing the sine sweep excitation applied in the X-direction to the structure on the small shake table.

Excitation Amplitude Label	*Representative RMS (g)*	*Peak Acceleration (g)*
X=0.0010	0.1081	0.6242
X=0.0012	0.1297	0.7232
X=0.0015	0.1649	0.7675
X=0.0020	0.2273	1.0470
X=0.0022	0.2383	1.0809
X=0.0025	0.2576	1.1708

The ring particle damper exhibited conflicting performance across different response metrics. For example, at low amplitude levels (X=0.001 and X=0.002), the RMS acceleration percent change for the "with particles" case was similar to the "added mass" cases, suggesting the damping is primarily due to added inertia effects (Figure 57). However, at higher sine amplitudes (X≥0.002), the RMS acceleration indicates effective damping beyond attributed added mass effects. In the frequency domain, the transfer function amplitude at the first bending mode displays performance comparable to or exceeding that of the "no particle" case at the higher excitation amplitudes (X≥0.002), indicating reduced performance of the device (Figure 58). Similarly, the H_2 and H∞ metrics show that at high amplitudes (X≥0.002), the percent difference is similar to or exceeds the corresponding "no ball" case (Figure 59). Overall, the sine sweep results indicate the ring particle damper's effectiveness

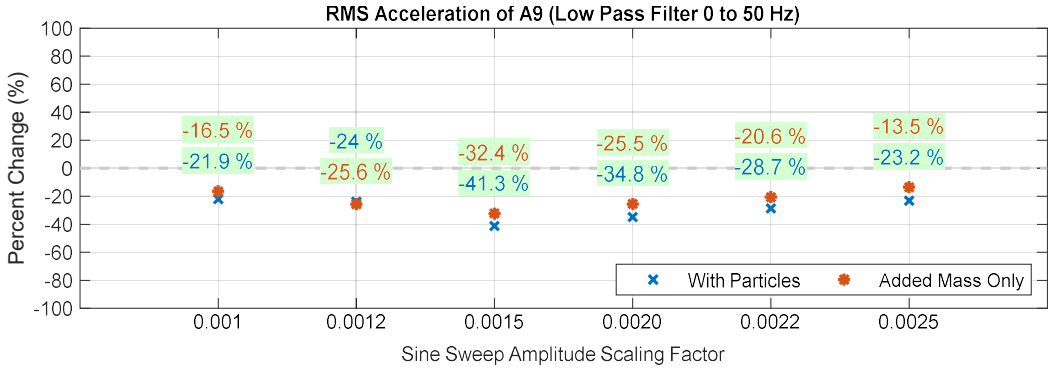


Figure 57. Percent change in RMS response for a 30-second sine sweep test from 3.5 to 6.5 Hz at varying in excitation amplitude. Values are normalized to the corresponding no-particle case.

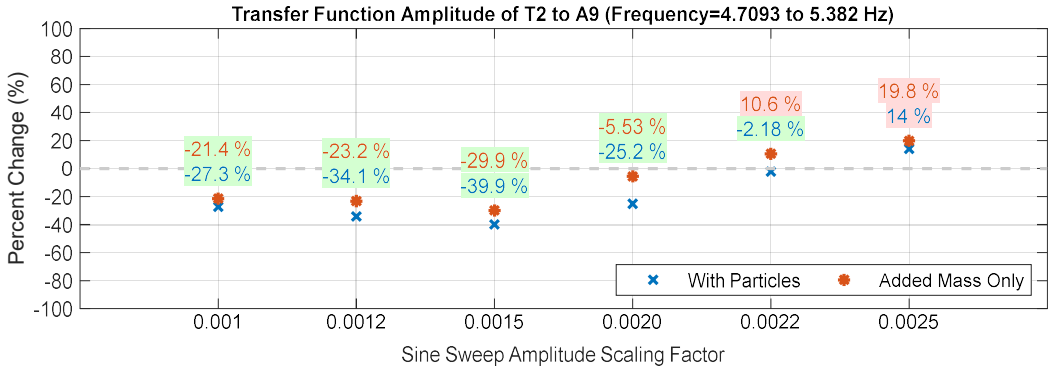


Figure 58. Percent change in transfer function amplitude response at first bending mode for a 30-second sine sweep test from 3.5 to 6.5 Hz at varying in excitation amplitude. Values are normalized to the corresponding no-particle case.

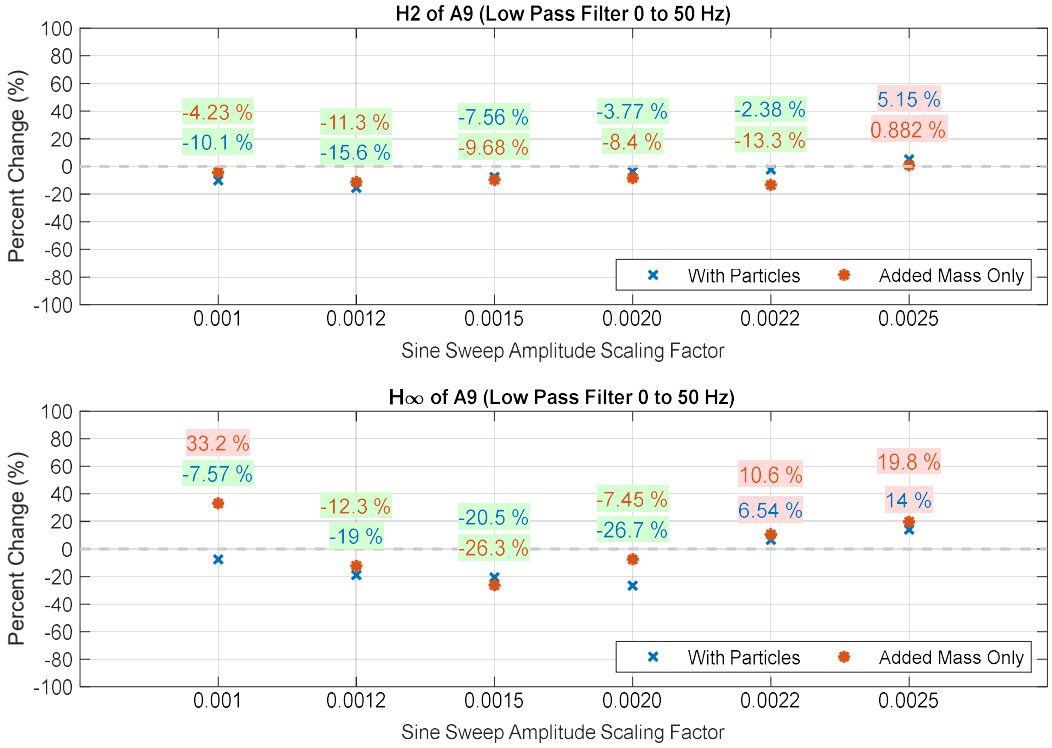


Figure 59. Percent change in frequency domain response metrics (H2 and H∞) for a 30-second sine sweep test from 3.5 to 6.5 Hz at varying in excitation amplitudes. Values are normalized to the corresponding no-particle case.

5. Effectiveness Demonstration

Based on the observation in the initial parametric study, the most effective ring particle damper configuration was selected for further dynamic testing under multi-directional excitations. The host structure was configured with a ring particle damper at 48-inch and 42-inch height elevations, with the cavities using an optimal packing ratio of 15 particles on the top layer and 18 particles on the bottom layer, corresponding to a 4.94% particle mass ratio. Additional parametric investigations, including a load amplitude study, a study of the ratio of total particle mass to host structure, and torsional ground motion, were performed to further demonstrate the damping performance of the ring particle damper device under multi-directional vibration.

5.1. Results and Discussions

The section presents and discusses the results from the effective demonstration studies conducted to assess the multi-directional performance of the device. Both time-domain and frequency-domain response metrics were analyzed to measure the device's damping effectiveness under various loading conditions. The effective demonstration experiments were developed based on the initial parametric study findings to verify the performance under further dynamic testing. Appendix B contains all response metrics discussed in the effectiveness demonstration studies.

5.1.1 Multi-Directional White Noise Excitation Amplitude

The load amplitude study focused on assessing the device's performance at mitigating multi-directional vibration at different excitation levels. The host structure was subjected to excitation in the x-only, y-only, and x-y combination directions at four amplitude levels, previously outlined in the experimental methods section.

Similar to the initial parametric study, the "with particles" percent difference from the "no particles" cases were negative across all response metrics, indicating increased performance due to the presence of the ring particle dampers. The majority of the "with particles" percent differences were greater than the "added mass" cases, demonstrating that the particle interactions are contributing to the damping performance rather than the effects of increased system weight. In the time and frequency domain response metrics, the damping performance exhibits similar percent reductions across the x-only excitation (Figure 60 and Figure 63), y-only excitation (Figure 61 and Figure 64) and combined x-y directions (Figure 62 and Figure 65). For the second bending/top breathing mode, the percent differences between the "with particles" and "added mass" cases are reduced in the second bending/top breathing mode (25 to 35 Hz frequency range) compared to the first bending mode (4 to 6 H frequency range), suggesting the inertial effects are contributing more to the second mode. The consistency in the time and frequency domains indicates that the ring particle damper allows effective mitigation of vibration in multiple directions simultaneously, and the device is not directionally dependent, as seen across all excitation amplitude levels.

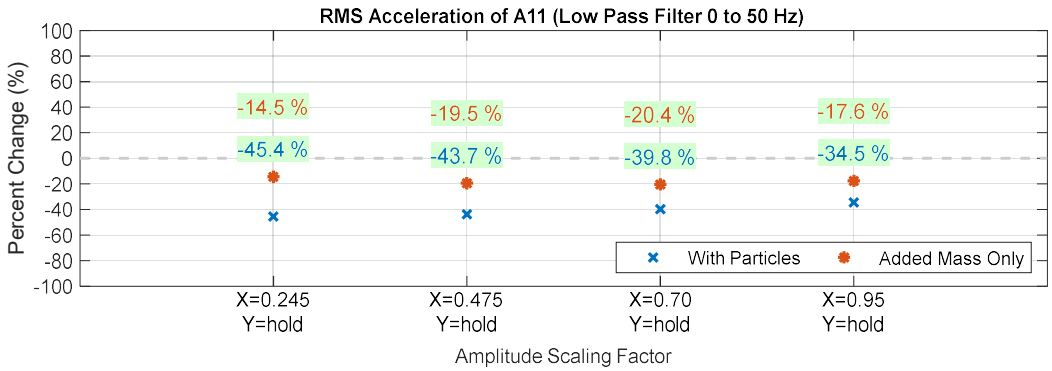


Figure 60. Percent change in RMS response of the +X sensor under varying excitation amplitudes applied in the +X axis of the big shake table. Values are normalized to the corresponding no-particle configuration.

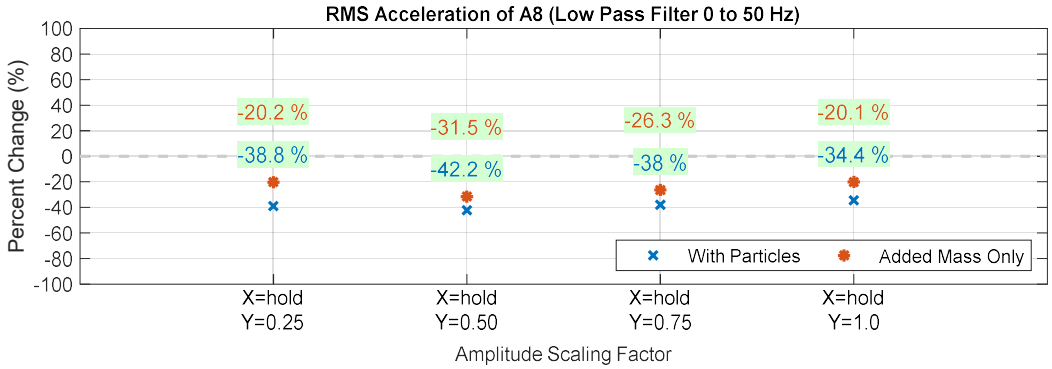


Figure 61. Percent change in RMS response of the +Y sensor under varying excitation amplitudes applied in the +Y axis of the big shake table. Values are normalized to the corresponding no-particle configuration.

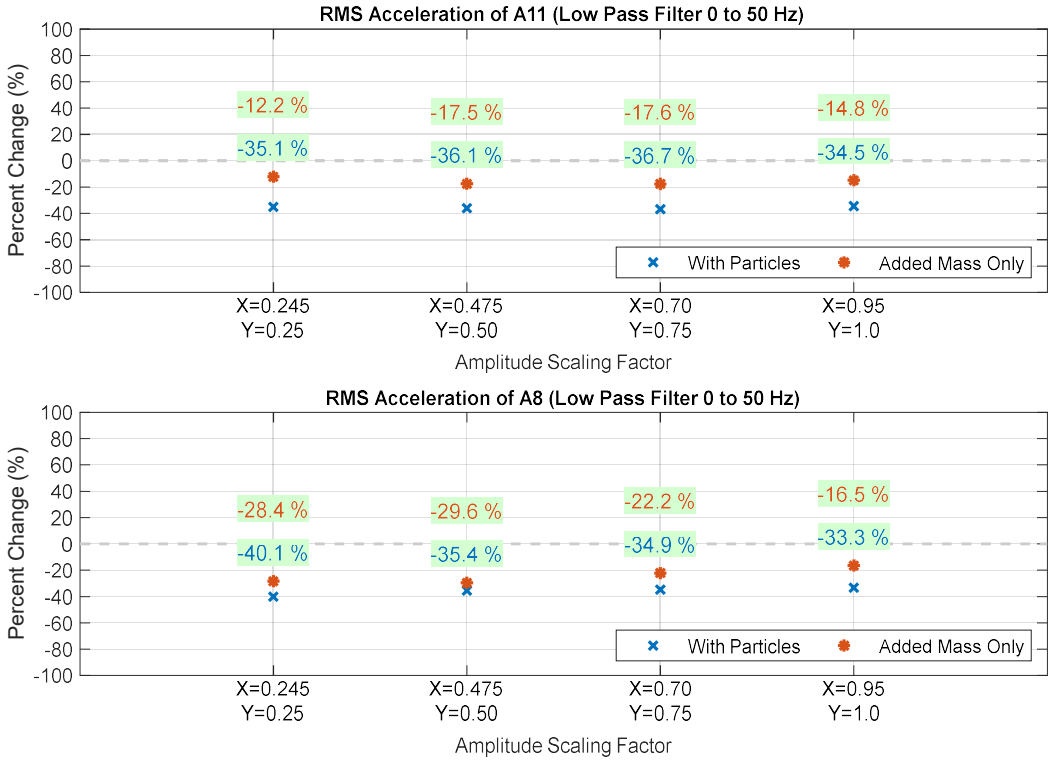


Figure 62. Percent change in RMS response of the +X and +Y sensors under varying excitation amplitudes applied simultaneously along the +X and +Y axes of the big shake table. Values are normalized to the corresponding no-particle configuration.

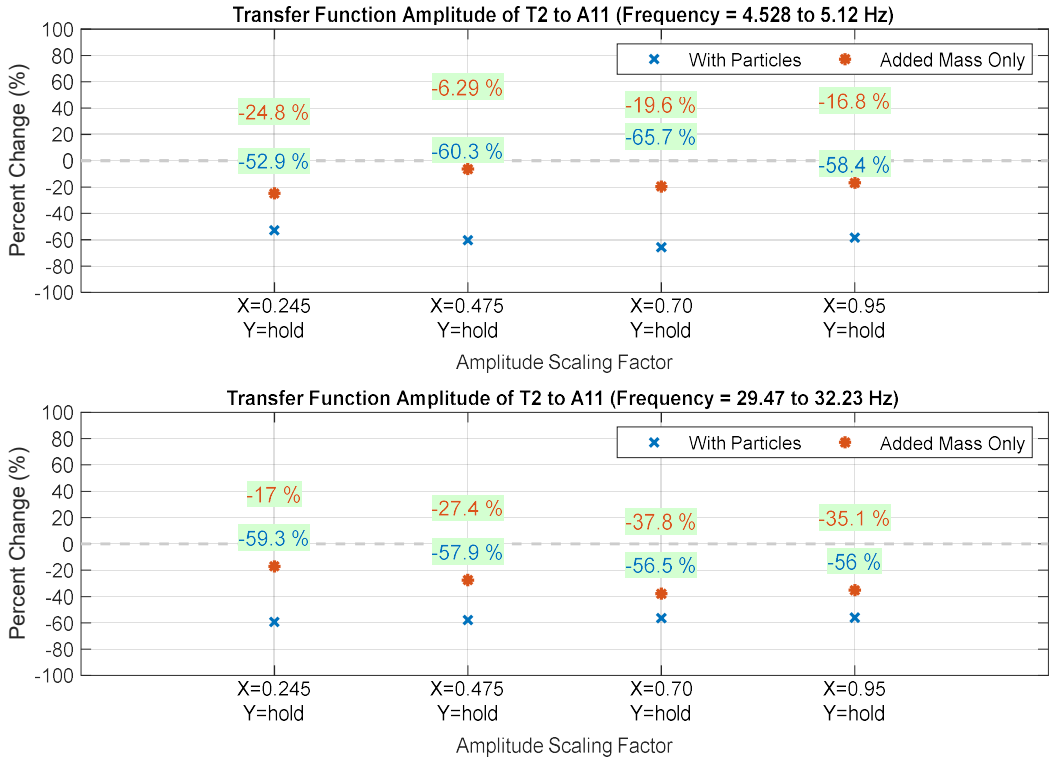


Figure 63. Percent change in transfer function amplitude response of the + X sensor at first bending mode and second bending/top breathing modes under varying excitation amplitudes applied in the +X axis of the big shake table. Values are normalized to the corresponding no-particle configuration.

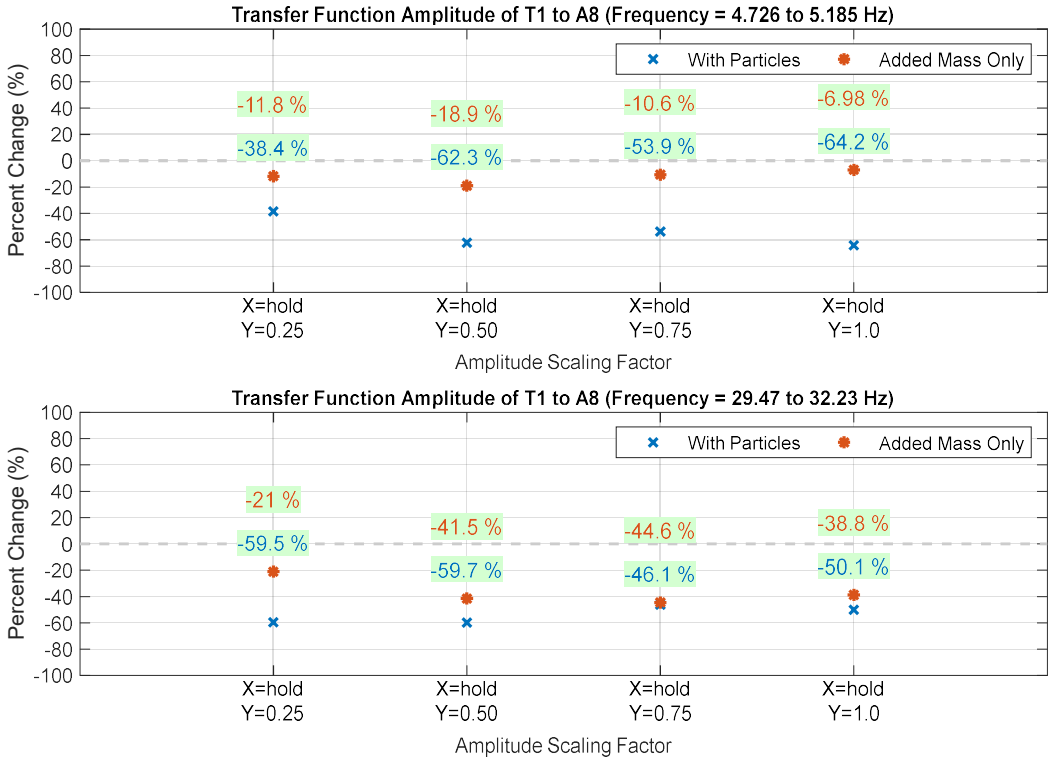


Figure 64. Percent change in transfer function amplitude response of the +Y sensor at first bending mode and second bending/top breathing modes under varying excitation amplitudes applied in the +Y axis of the big shake table. Values are normalized to the corresponding no-particle configuration.

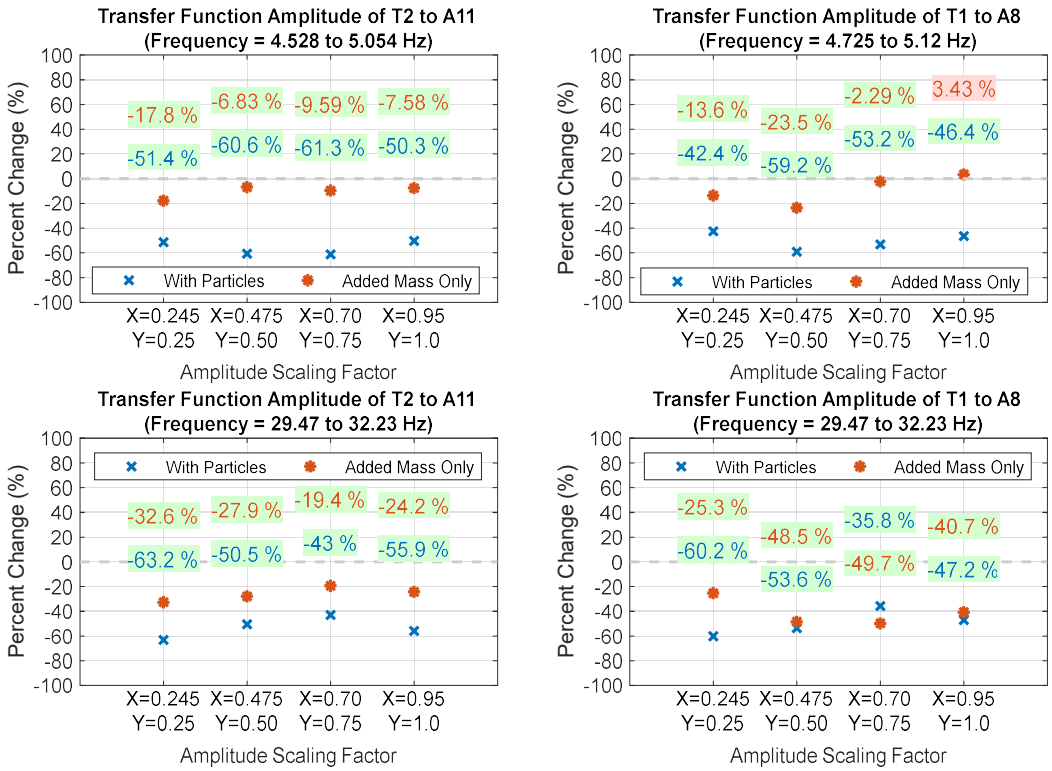


Figure 65. Percent change in transfer function amplitude response of the +X and +Y sensor at first bending mode and second bending/top breathing modes under varying excitation amplitudes applied simultaneously along the +X and +Y axes of the big shake table. Values are normalized to the corresponding no-particle configuration.

5.1.2 Particle Material Type

The purpose of the particle material study was to evaluate the ring particle damper performance with tungsten ball bearing compared to steel. Since tungsten particles are approximately 1.60 grams, 1.5 times more mass than steel at 1.06 grams, there could potentially be an increased performance due to the additional weight. At multiple excitation amplitudes, the study compared the steel packing ratio (44.28 g/cavity = 4.94% particle mass ratio) to the equivalent mass ratio of the tungsten (15 top /18 bottom = 44.50 g/cavity = 4.94% particle mass ratio) and an approximate tungsten packing ratio of free volume compared to the steel packing ratio (10 top/12 bottom = 62.10 g/cavity = 3.29% particle mass ratio).

Across all the response metrics, the three "with particles" cases indicated a negative percent change from the "no particles" case, and less than the "added mass" ratios. A consistent trend of the (10T/12B) tungsten packing ratio, which shows a decrease in damping performance compared to the two (15T/18B) cases (Figure 66). For the (15T/18B) steel and tungsten packing ratios, across all response metrics, displayed similar percent changes from the "no particles" case (Figure 67 and

Figure 68). No consistent trend was observed among the response metrics, indicating that neither material consistently outperformed the other.

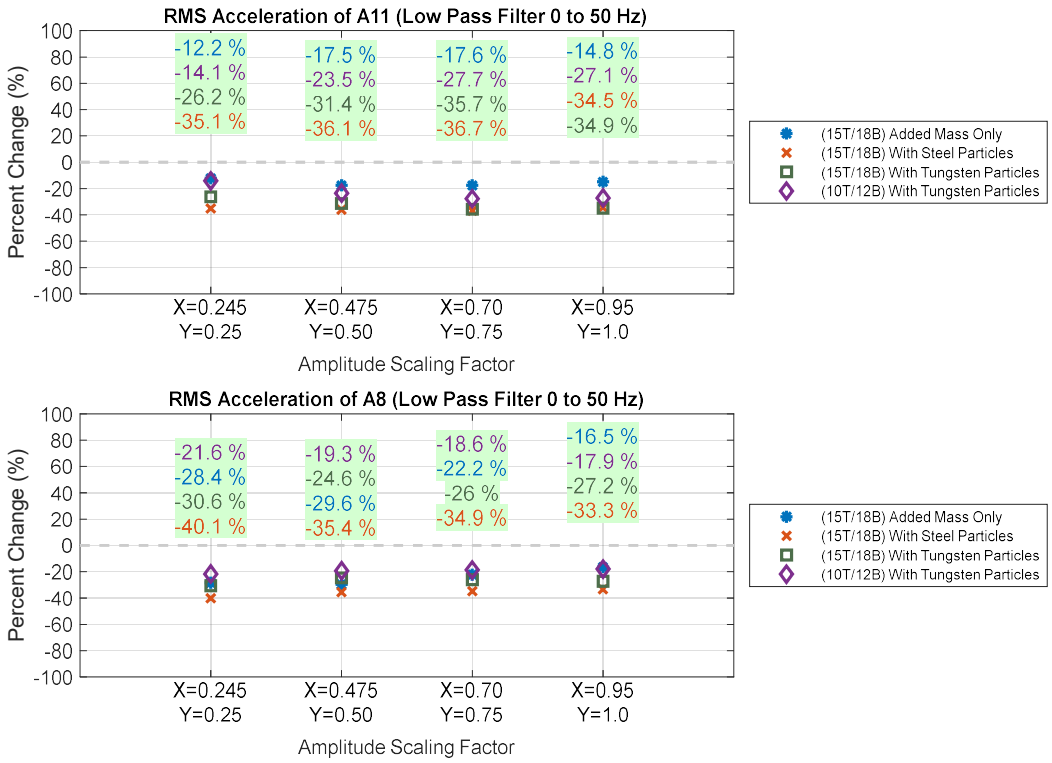


Figure 66. Percent change in RMS response of the +X and +Y sensors, comparing the particle material type under varying excitation amplitudes applied simultaneously in the +X and +Y axes of the big shake table. Particle packing ratios are defined as distinct top (T) and bottom (B) layers. Values are normalized to the corresponding no-particle configuration.

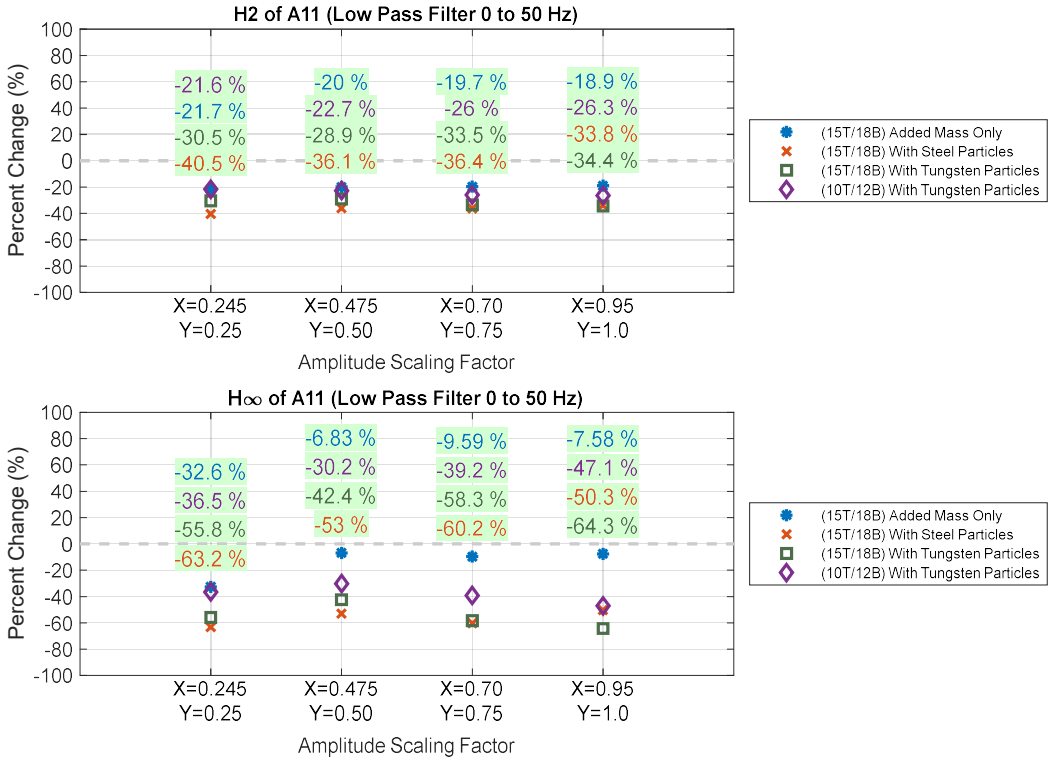


Figure 67. Percent change in frequency domain response metrics (H2 and H∞) of the +X sensor, comparing particle material type under varying excitation amplitudes applied simultaneously in the +X and +Y axes of the big shake table. Particle packing ratios are defined as distinct top (T) and bottom (B) layers. Values are normalized to the corresponding no-particle configuration.

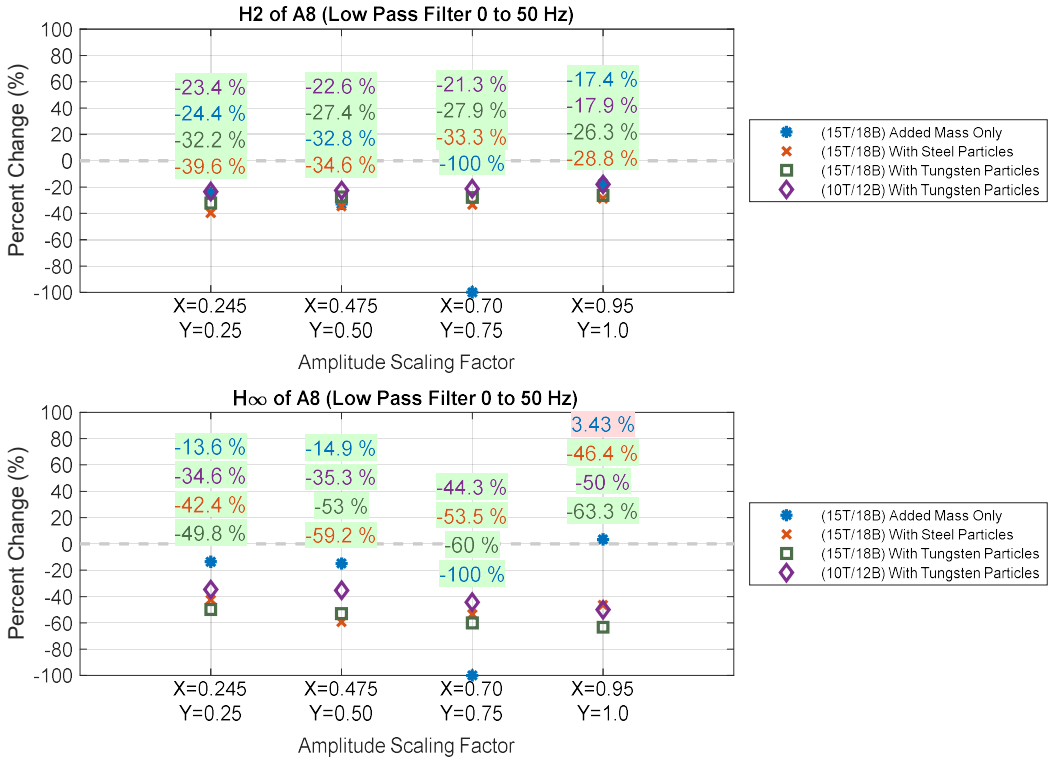


Figure 68. Percent change in frequency domain response metrics (H2 and H∞) of the +Y sensor, comparing particle material type under varying excitation amplitudes applied simultaneously in the +X and +Y axes of the big shake table. Particle packing ratios are defined as distinct top (T) and bottom (B) layers. Values are normalized to the corresponding no-particle configuration.

5.1.3 Multi-Directional Container Usage

An additional container usage study was performed to demonstrate the ring particle damper's effectiveness in mitigating multi-directional excitation with different container configurations. The study evaluated the damping performance of four containers filled in 0-degree orientation parallel to the direction of motion, four containers filled 45-degree offset relative to the ground motion (Figure 69). The experiments utilized 15 top and 18 bottom layer particle packing ratios with a corresponding "added mass" case. The mass particle ratio of the full container usage was 4.94%, and the two half-container usage configurations had a mass particle ratio of 2.47%. The mass particle ratios are relative to the total structural mass, 25.034 lbmass.

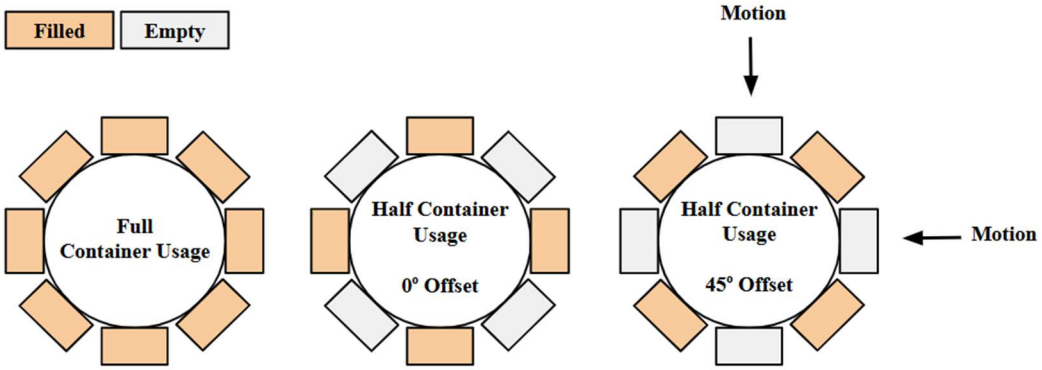


Figure 69. Multi-Direction Container Usage Study Configurations

Across all response metrics, each configuration demonstrated effective damping, with the "with particles" case producing negative percent differences relative to the "no particles" case. In most response metrics, the "with particles" percent difference was lower than the "added mass" cases, indicating the damping was primarily due to particle interactions rather than added mass effects (Appendix). As anticipated, the full container usage configuration exhibited higher percent differences from the "no particles" case. Similar to the initial container usage results on the small shake table, the 45- and 90-degree offsets exhibited similar dampening performance (Figure 70 and Figure 71), demonstrating that the ring particle damper is directionally independent from the applied excitation.

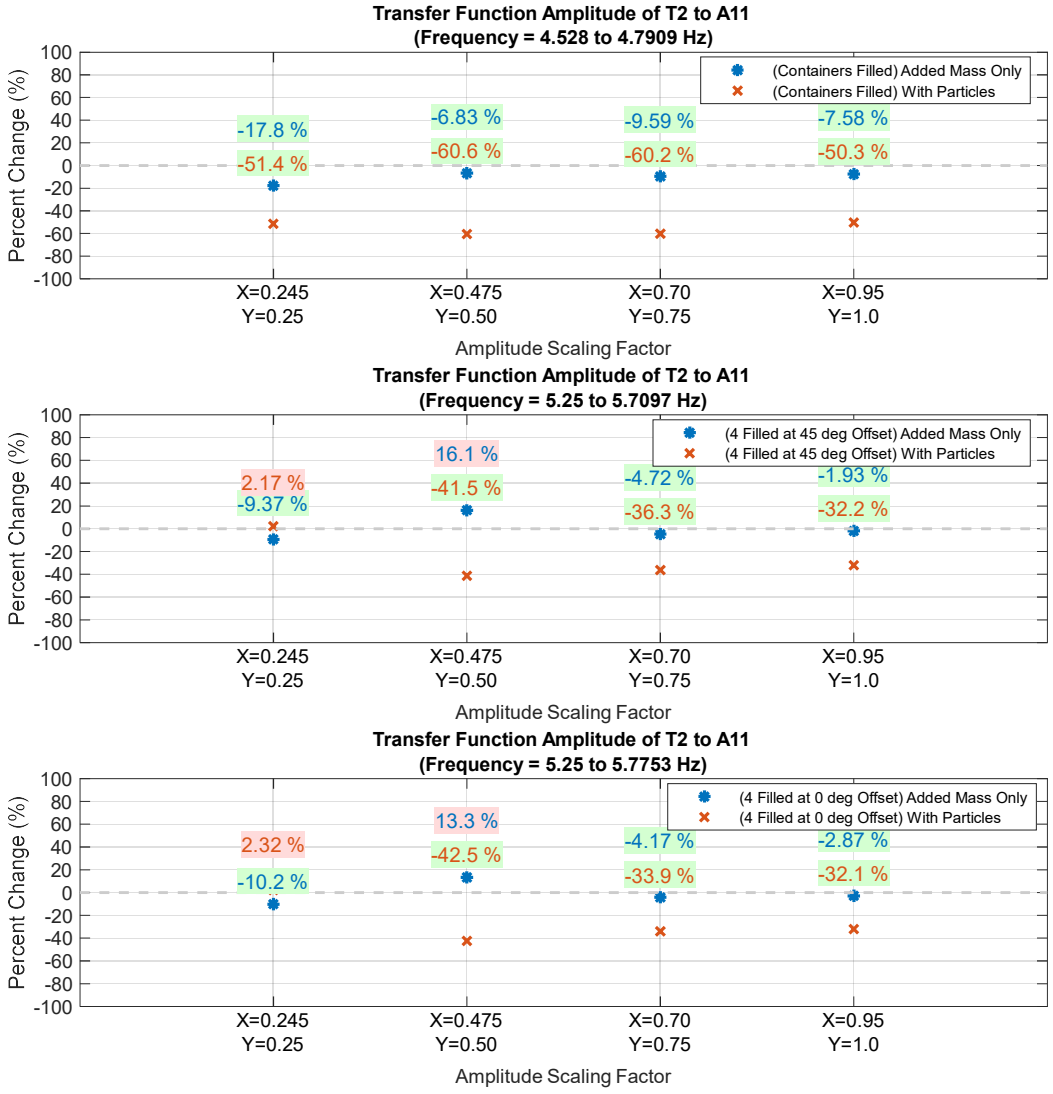


Figure 70. Percent change in transfer function amplitude response of the +X sensor at the first bending mode, comparing ring particle damper container usages under varying excitation amplitudes applied simultaneously in the +X and +Y axes of the big shake table. Values are normalized to the corresponding no-particle configuration.

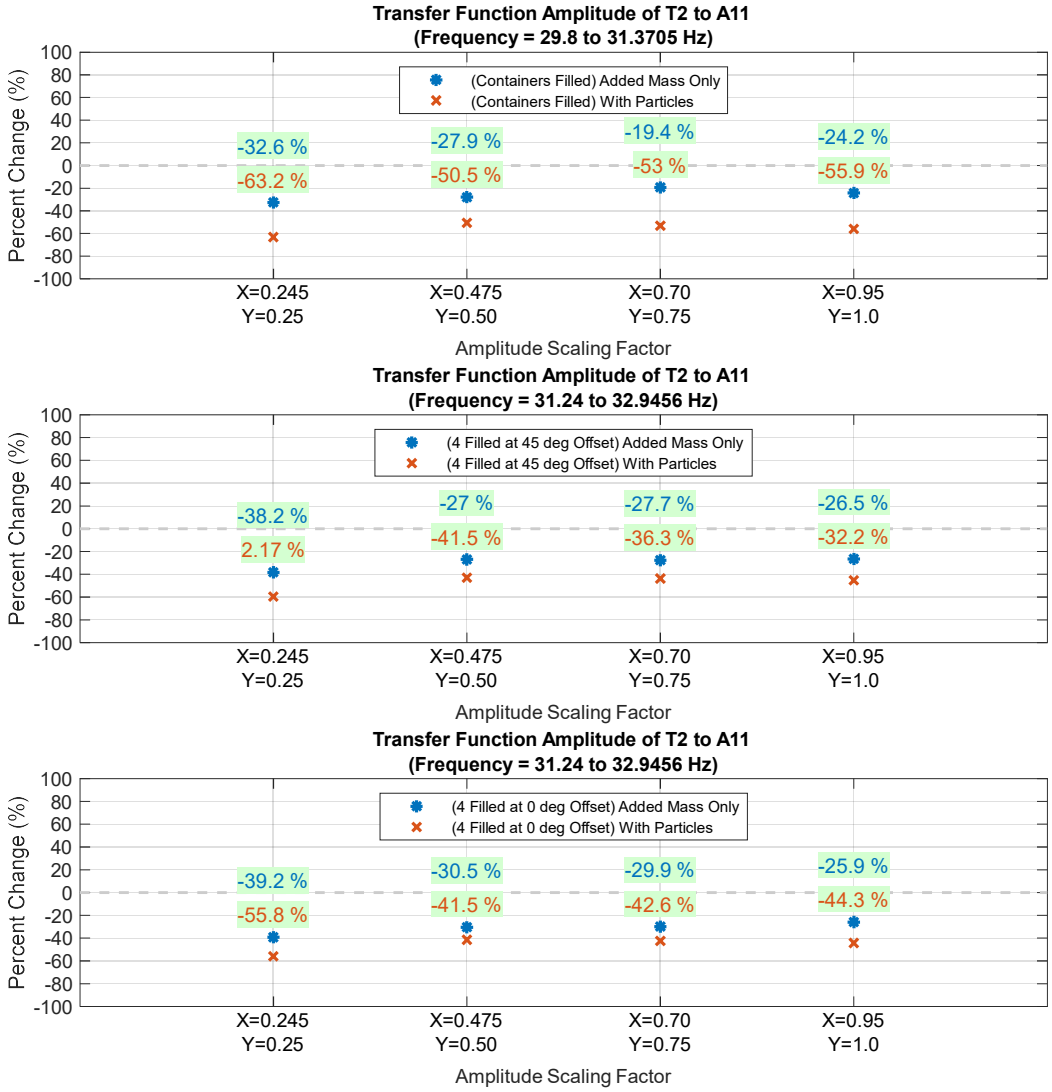


Figure 71. Percent change in transfer function amplitude response of the +X sensor at the second bending/ top breathing mode, comparing ring particle damper container usages under varying excitation amplitudes applied simultaneously in the +X and +Y axes of the big shake table. Values are normalized to the corresponding no-particle configuration.

5.1.4 Torsional Excitation

The torsional study was conducted to assess the device's effectiveness of mitigating vibrations. The host structure was subjected to four rotational ground motion amplitudes. The "with particles" cases containing the 15 top, 18 bottom steel and tungsten particle packing ratios (4.94% mass particle ratio) with corresponding "no particles" and "added mass" cases were tested. For most

response metrics, the ring particle damper exhibited effective damping at the top torsional sensors (A12-A8) (Figure 72). The steel and tungsten particles performed similarly across all response metrics. At the torsional modes, the ring particle damper exhibited effective damping at lower torsional amplitude ranges but was not consistent at higher input amplitudes (Figure 73). The "with particles" percent changes relative to the normalized "no particles" cases exhibited an overall lower damping performance compared to the previous translational excitation results.

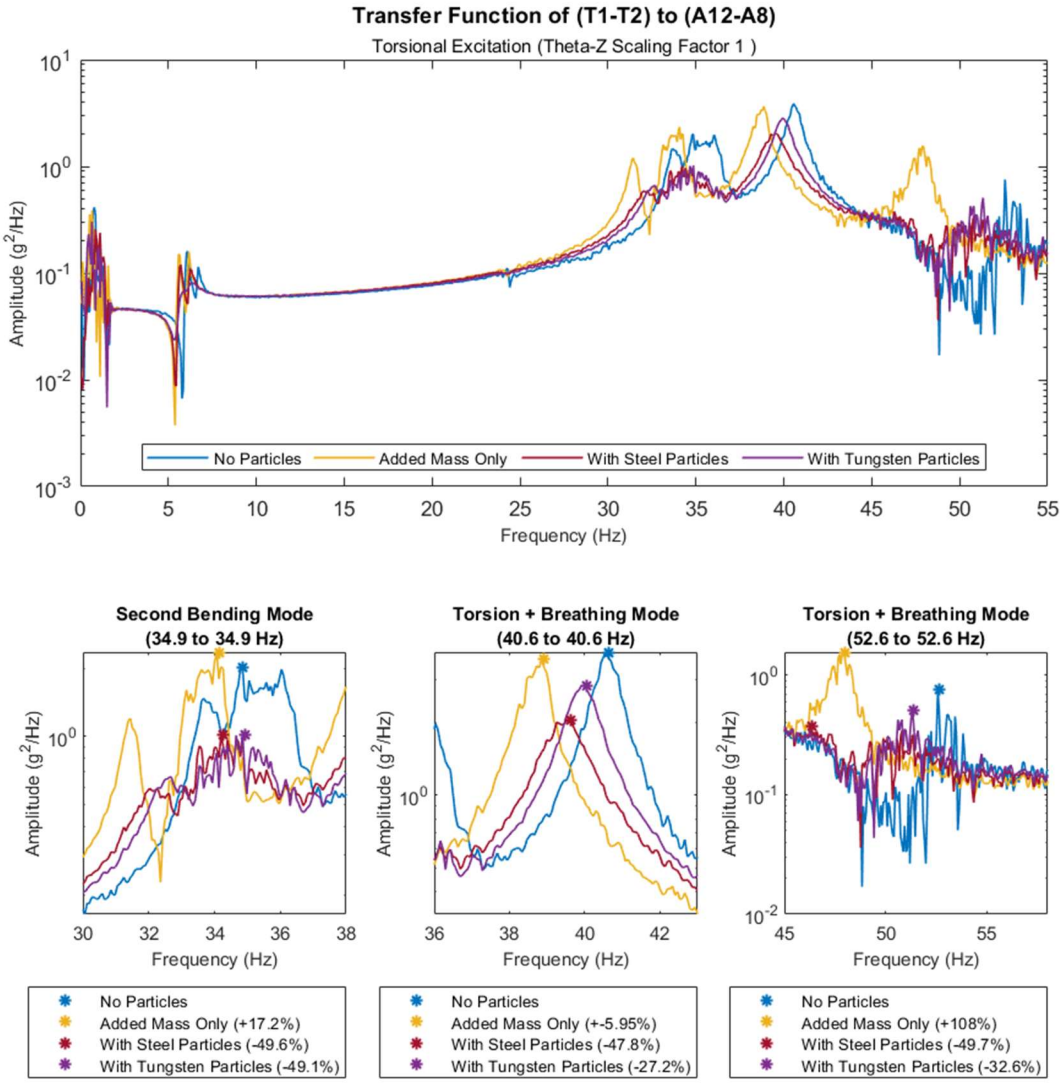


Figure 72. Frequency response function of the torsion sensor (A12-A8) considering input of base torsion as represented by sensor (T1-T2) at second bending modes and torsion/breathing modes, comparing particle material type under varying torsional excitation amplitudes applied in the theta-Z axis (scale factor = 1) of the big shake table. Values are normalized to the corresponding no-particle configuration.

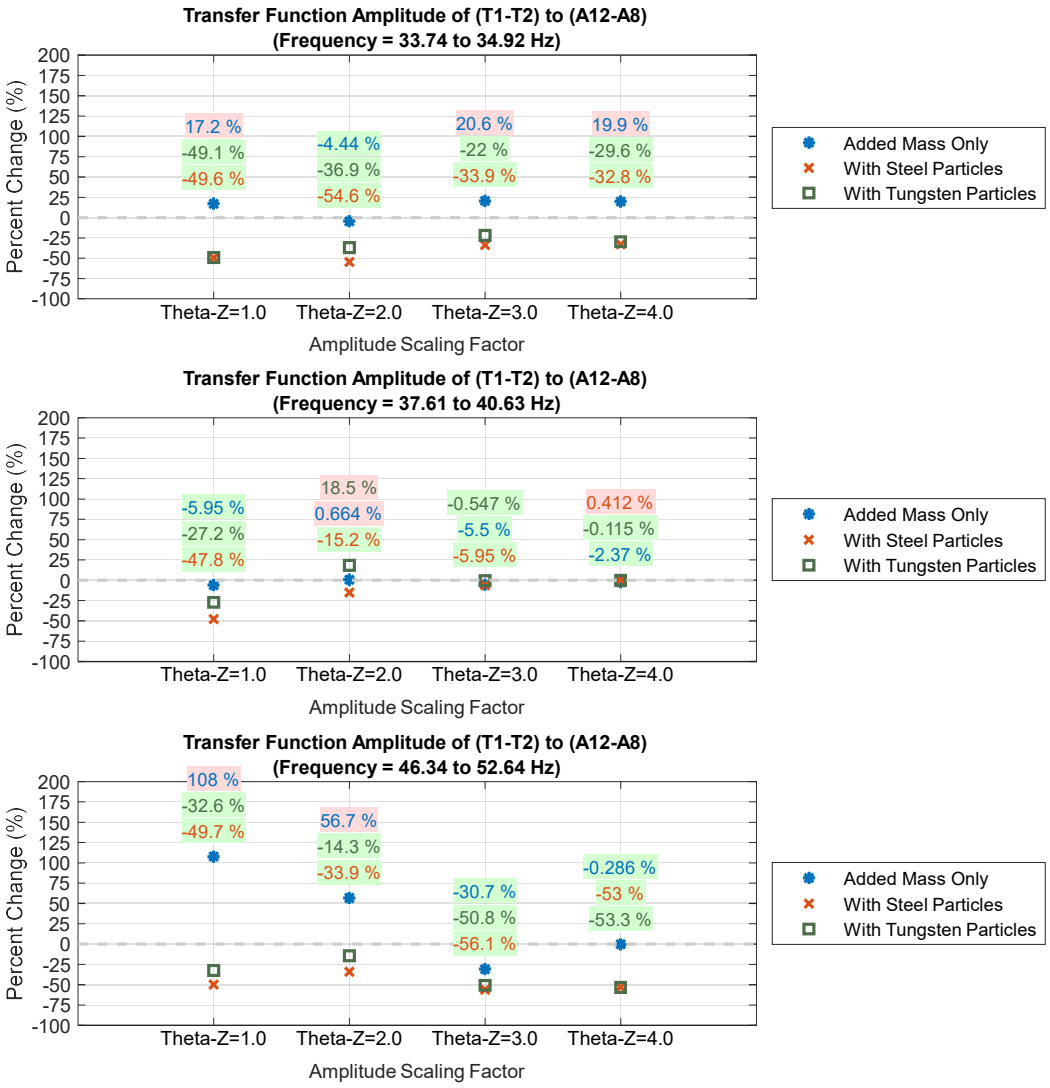


Figure 73. Percent change in transfer function response of the torsion sensor (A12-A8) considering input of base torsion as represented by sensor (T1-T2) at second bending modes and torsion/breathing modes, comparing particle material type under varying torsional excitation amplitudes applied in the theta-Z axis of the big shake table. Values are normalized to the corresponding no-particle configuration.

6. Lessons Learned

Throughout the project, valuable lessons were learned at each phase. Insights from the numerical experiments, 3D printing fabrication, and analyzing response metrics can inform future development of the ring particle damper. This section summarizes key lessons learned throughout the duration of the project.

6.1 Numerical Modal Analysis Using Autodesk Inventor

- Autodesk Inventor modal analysis helped identify natural frequencies and mode shapes. The first bending natural frequency was estimated to be close to the actual experimental values. However, the predicted frequencies for breathing and torsional modes differed by 10-20 Hz from the measured acceleration responses, and the mode shapes were less accurately characterized.
- While Autodesk Inventor's built-in modal analysis was useful, using the Nastran Inventor add-on is recommended for future numerical experiments. Convergence in the built-in analysis was difficult to determine, requiring a compromise between computation time and result variation. In contrast, the Nastran add-on provided a more comprehensive modal analysis, including mass participation data, and significantly reduced computation time.

6.2 3D Printing Fabrication and Construction

- 3D printing provided flexibility in fabricating the host structure, but a trial-and-error process was needed to achieve accurate tolerances. For example, the cylinder wall thicknesses were modeled at 0.05 in, but required 0.1 in to reliably produce a 0.05-inch hollow cylinder (~ 0.95-inch difference). Similarly, clearance holes for a No. 10 bolt (nominally 0.196 inch) required a 0.20 in. print to achieve a consistent fit (~0.004-inch difference).
- To mitigate overhang printing challenges, modeling a 45-deg sloped, connecting tab was incorporated where possible, creating a link between the overhang and outer circumference. The sloped tab eliminates the need for support material when printing. When supports were required, manually designed supports using a “snug” style proved more efficient and reliable than automatically generated supports in PrusaSlicer.
- A 100% infill was used to maintain consistency through the printed components. This was particularly effective for achieving the required mass of the mass-cap design to reflect the added mass effects. Additionally, the 100% infill in the leg components was beneficial in increasing the component stiffness, improving mounting stability on the shake table.
- The initial cylinder segment connection design was functional but tight and thin, leading to breakage during disassembly and high-amplitude loading. Increasing the male-tab thickness and connection slot size is recommended to improve ease of constructability and reduce failure during testing.
- Fabrication of the steel inserts in the lined cylinder segment was dimensionally constrained by the availability of rectangular steel tube products. A 1-inch by 1.5-inch rectangular steel

tube with a 0.0065” wall thickness was selected due to its comparable open cross-sectional area to the PLA cavity. Through an iterative printing approach, the original cylinder PLA design was modified to accommodate the inserts to have a snug-fit.

6.3 Instrumentation and Sensor Layout

- The twelve accelerometers provided sufficient data to characterize mode shapes, but more sensors are recommended to improve accuracy. With only twelve sensors, it was difficult to distinguish between breathing modes from second bending and torsional modes from breathing modes, particularly capturing radial expansion, contraction, and rotation.

7. Recommendations for Future Work

The ring particle damper shows promise as a solution for mitigating NASA hardware vibration. The project provides an experimental proof-of-concept, validating the device’s effectiveness in reducing multi-directional vibrations in a laboratory environment. The ring particle damper exhibited mitigation of multi-directional bending and breathing modes, as well as the potential damping capability for torsional modes.

To further advance the device, additional laboratory experimentation focused on torsional vibrations is recommended, as the tests conducted displayed varying performance indicators. This variability may be attributed to the limitations of the accelerometers selected for the experiments. Future studies will also need to consider larger-scale testing with more complex dynamic systems, with the device integrated into the configuration, such as a mounting enclosure or direct attachment to the host structure, and with materials used in typical space flight hardware. These host structures might include large cylindrical structures or smaller structures such as mounted equipment. Under more rigorous dynamic conditions, the ring particle damper must demonstrate effective energy dissipation under random vibration qualification testing using standard NASA specifications for flight environments. Further parametric studies under these qualification environments are needed to better understand the dynamic behavior and effectiveness of the ring particle damper.

8. Conclusions

The project investigated the effectiveness of the ring particle damper configuration to mitigate multi-directional, radial, and torsional vibrations similar to the environments of NASA hardware. The project focused on developing an understanding of how the device’s parameters influence its behavior and its effectiveness in mitigating multi-directional vibration, identifying key parameters of the device to help pursue future development. The main conclusions are summarized in the list below.

- The results demonstrate the device can effectively mitigate vibrations across a broad range of amplitudes and independent of input direction.

- Optimal performance coincides with the point of maximum displacement along the host structure, effectively reducing the first bending mode (40-60% reduction) without compromising the attenuation of the second bending mode.

- The ring particle damper's effectiveness depends on the available space for particle interaction. Both overly compacted and excessively free volume packing ratios reduce performance; an intermediate ratio provides the optimal damping.

- Through both the initial parametric studies and subsequent dynamic testing, the ring particle damper demonstrated effective mitigation of multi-directional, specifically in translational and radial mode shapes simultaneously.

- While the ring particle damper showed potential effectiveness in mitigating torsional responses, the variability in the response metrics indicates that consistent performance under rotational vibration is unclear.

Appendix A: Results from Initial Parametric Studies

Table of Contents

Appendix A: Results from Initial Parametric Studies 1
A.1 Optimal Particle Packing Ratio 3
A.2 Initial White Noise Excitation Amplitude 10
A.3 Initial Container Usage 13
A.4 Optimal Device Location 16
A.5 Cavity Layer Usage 22
A.6 Device Cavity Lining Material 25
A.7 Sinusoidal Excitation 28
A.8 Sine Sweep Excitation 33

A.1 Optimal Particle Packing Ratio

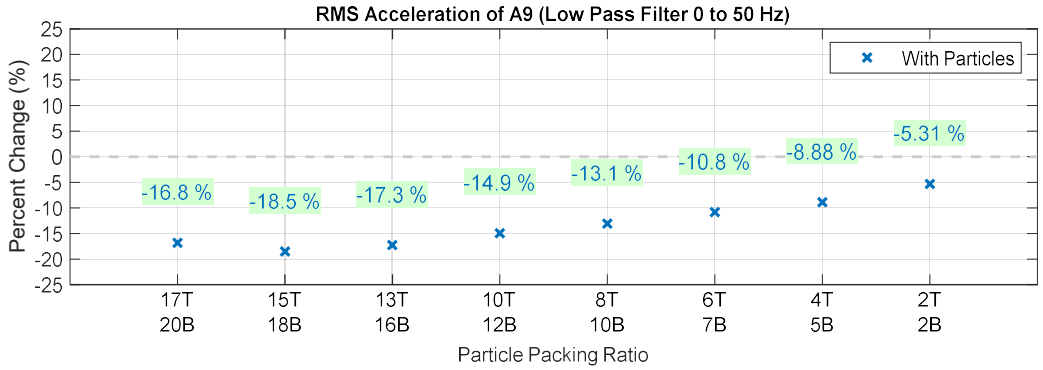


Figure A-1. Percent change in RMS response as a function of particle packing ratio (Study 1). Measurements from the top (T) and bottom (B) particle layers are shown. Values are normalized to the corresponding no-particle case.

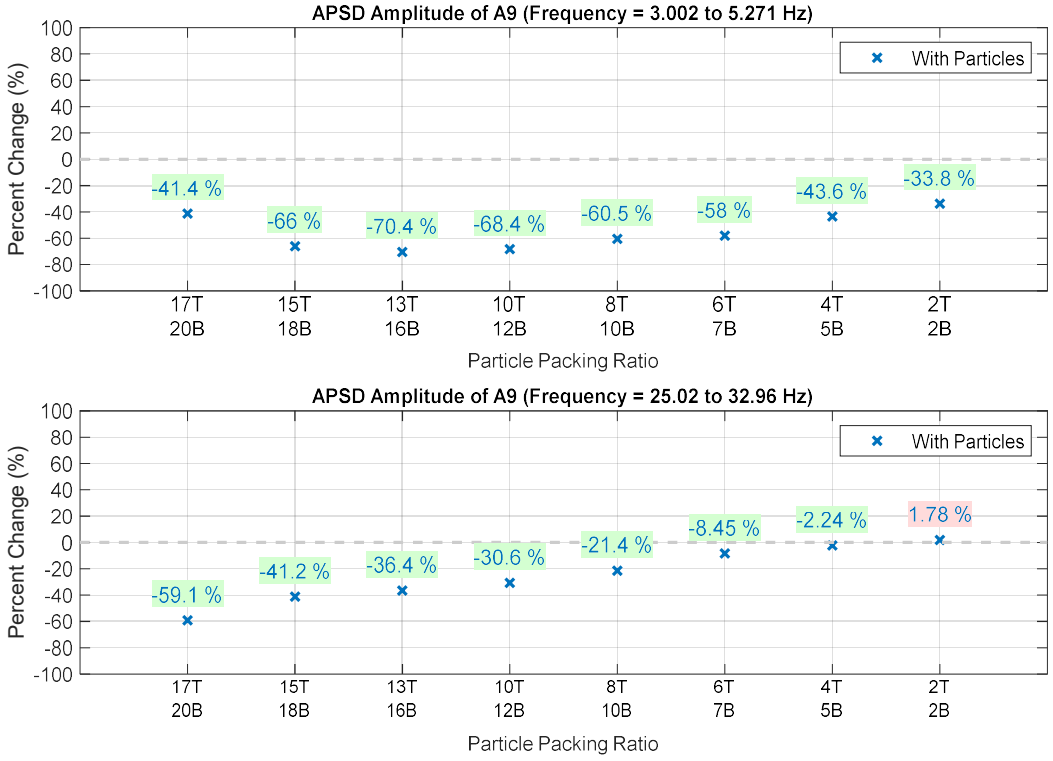


Figure A-2. Percent change in APSD amplitude responses at the first bending and second bending/top breathing modes as a function of particle packing ratio (Study 1). Measurements from the top (T) and bottom (B) particle layers are shown. Values are normalized to the corresponding no-particle case.

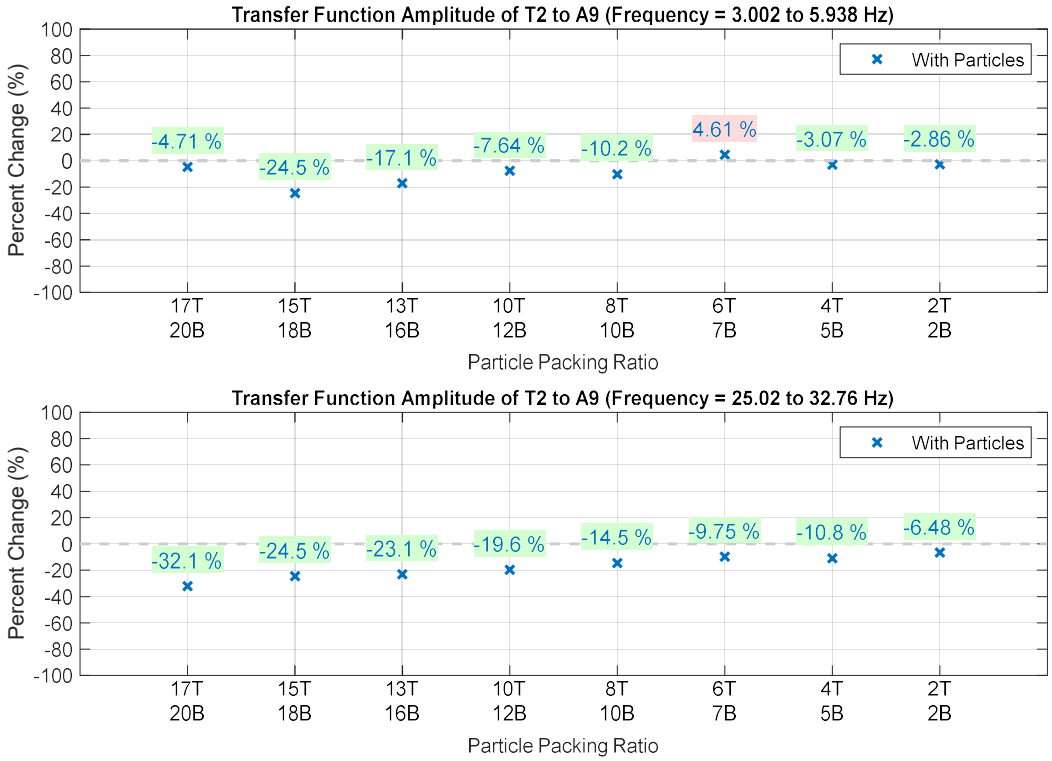


Figure A-3. Percent change in the transfer function amplitude responses at the first bending and second bending/top breathing modes as a function of particle packing ratio (Study 1). Measurements from the top (T) and bottom (B) particle layers are shown. Values are normalized to the corresponding no-particle case.

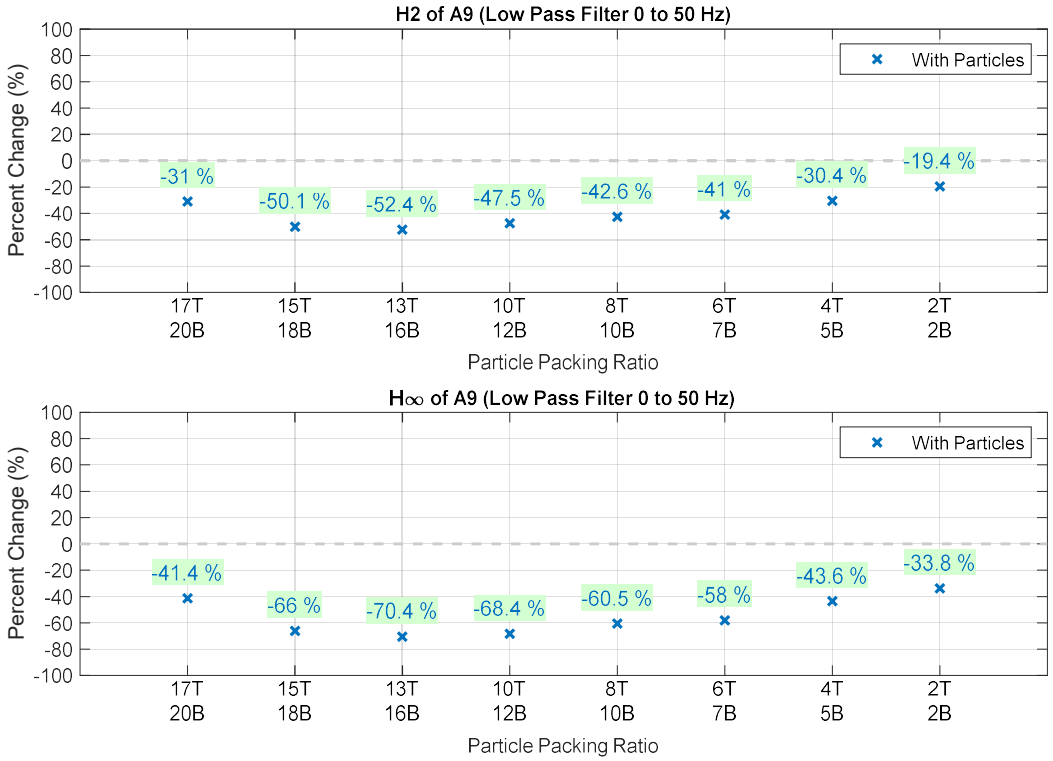


Figure A-4. Percent change in frequency domain response metrics (H2 and H∞) as a function of particle packing ratio (Study 1). Measurements from the top (T) and bottom (B) particle layers are shown. Values are normalized to the corresponding no-particle case.

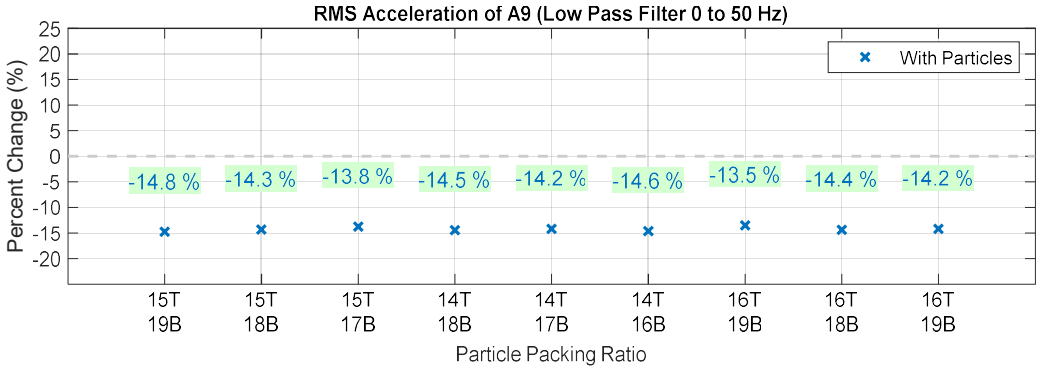


Figure A-5. Percent change in RMS response as a function of particle packing ratio (Study 2). Measurements from the top (T) and bottom (B) particle layers are shown. Values are normalized to the corresponding no-particle case.

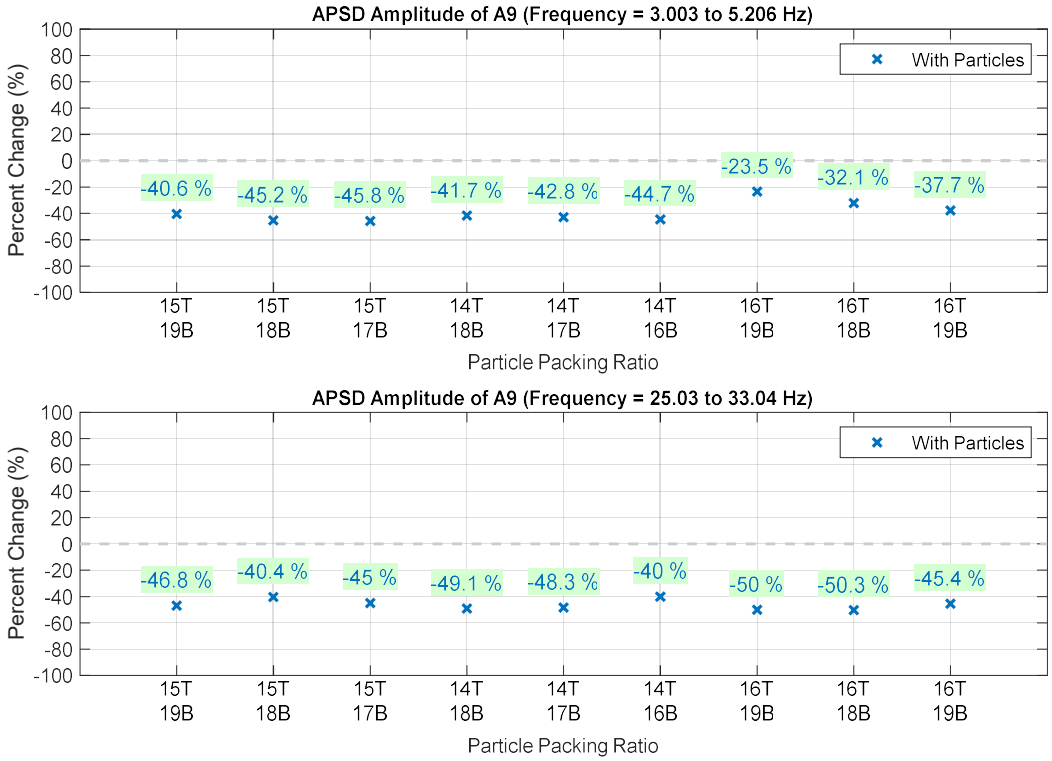


Figure A-6. Percent change in APSD amplitude responses at the first bending and second bending/top breathing modes as a function of particle packing ratio (Study 2). Measurements from the top (T) and bottom (B) particle layers are shown. Values are normalized to the corresponding no-particle case.

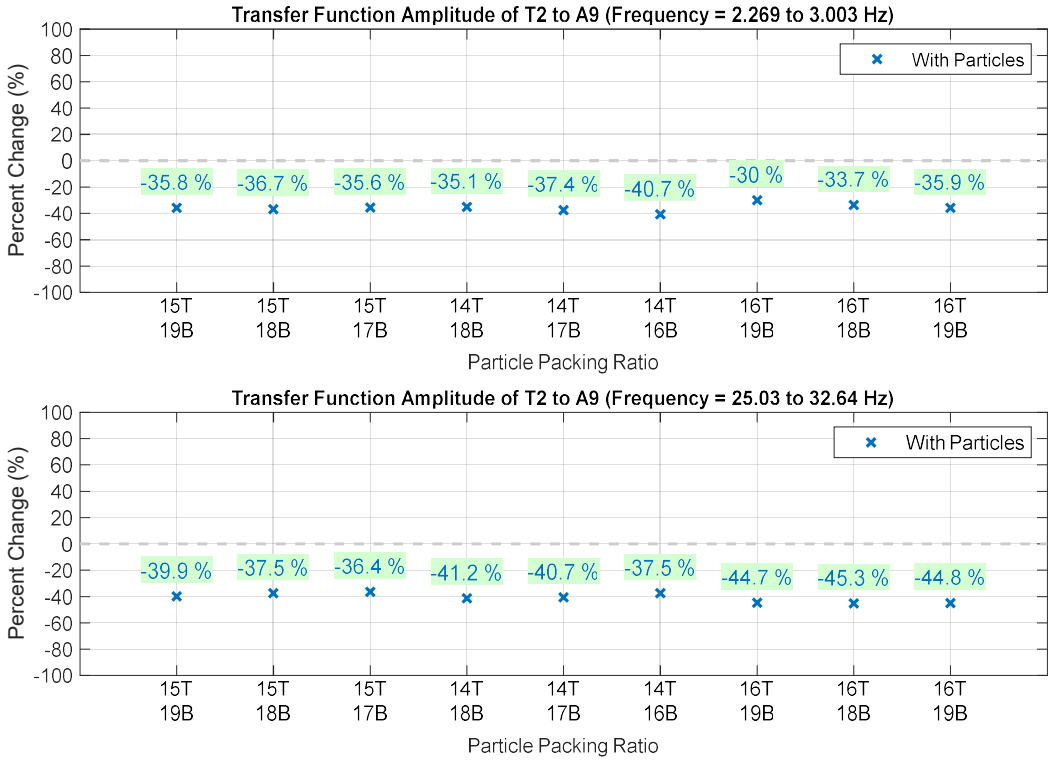


Figure A-7. Percent change in transfer function amplitude responses at the first bending and second bending/top breathing modes as a function of particle packing ratio (Study 2). Measurements from the top (T) and bottom (B) particle layers are shown. Values are normalized to the corresponding no-particle case.

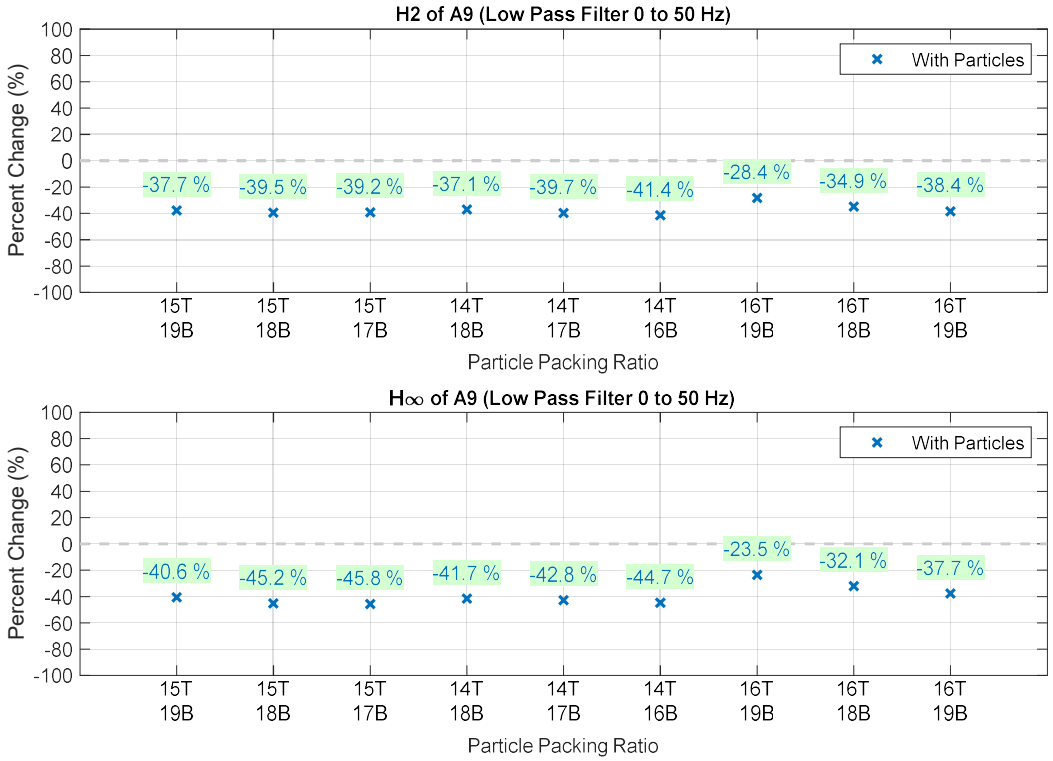


Figure A-8. Percent change in frequency domain response metrics (H2 and H∞) as a function of particle packing ratio (Study 2). Measurements from the top (T) and bottom (B) particle layers are shown. Values are normalized to the corresponding no-particle case.

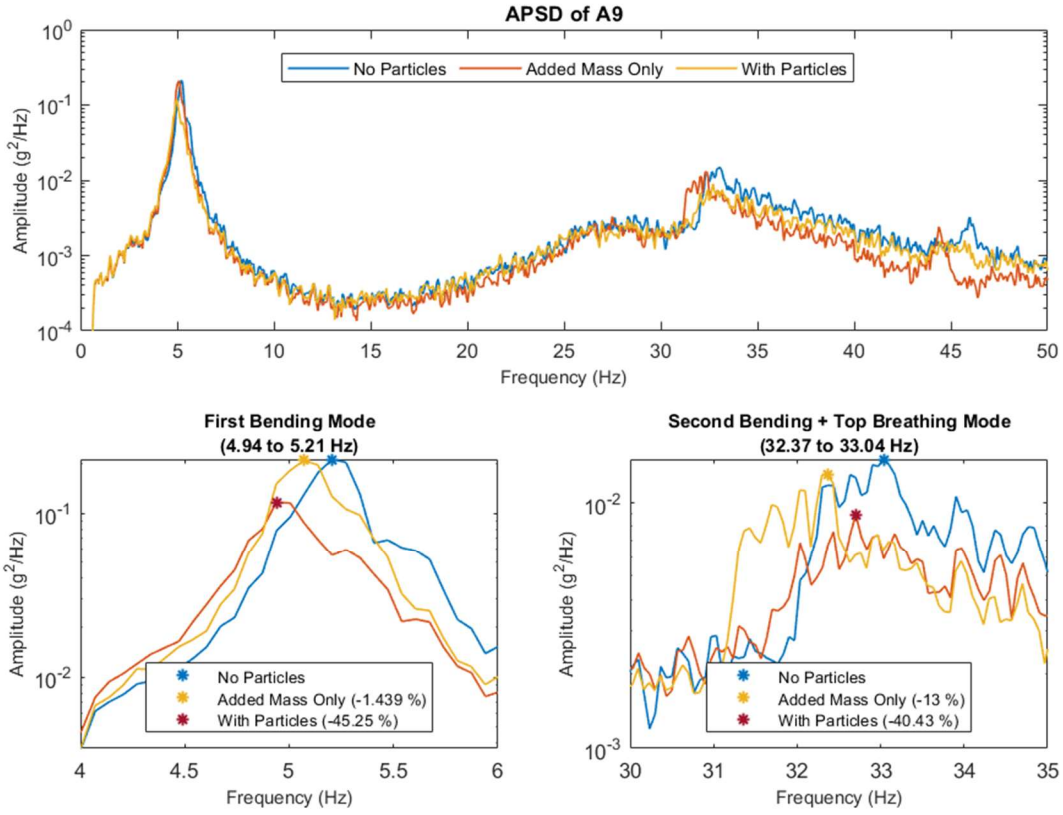


Figure A-9. Frequency response function for sensor, A9, comparing no-particle case, added mass case, and particle-filled 15 (T) and 18 (B) packing ratios. Percent changes are normalized with the corresponding no-particle case.

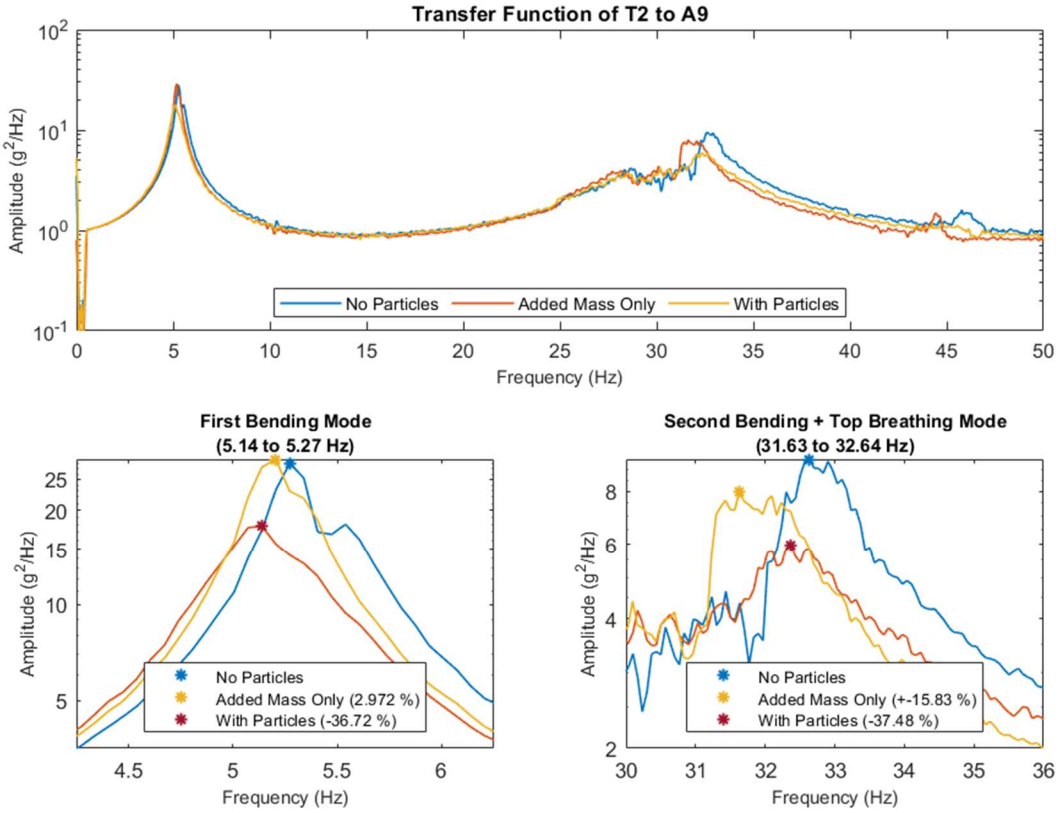


Figure A-10. Frequency response function for sensor, A9, comparing no-particle case, added mass case, and particle-filled 15 (T) and 18 (B) packing ratios. Percent changes are normalized with the corresponding no-particle case.

A.2 Initial White Noise Excitation Amplitude

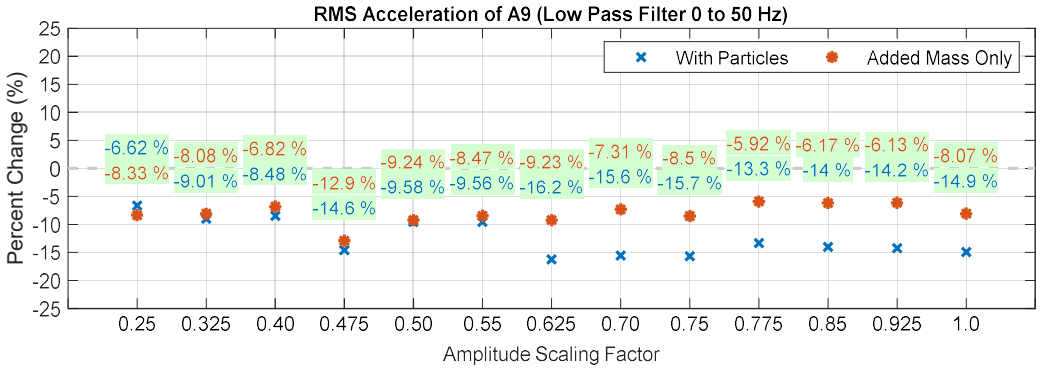


Figure A-11. Percent change in the RMS response with varying white-noise excitation amplitudes on the small shake table. Values are normalized to the corresponding no-particle case.

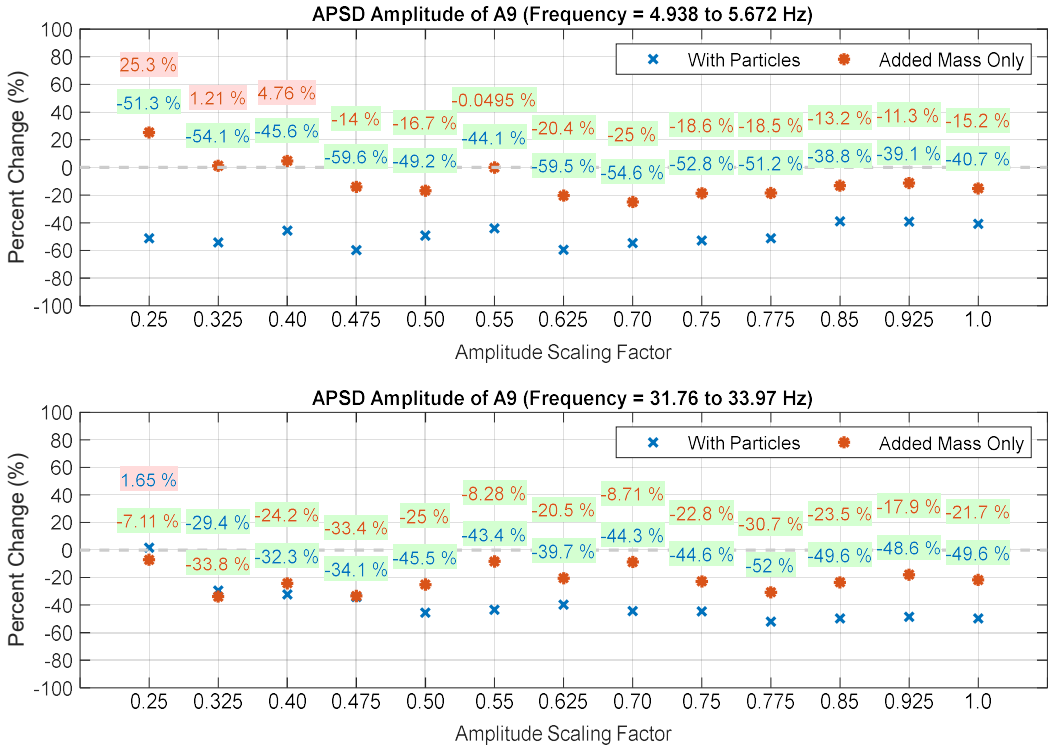


Figure A-12. Percent change in the APSD amplitude response at the first bending mode and second bending/top breathing modes with varying white-noise excitation amplitudes on the small shake table. Values are normalized to the corresponding no-particle case.

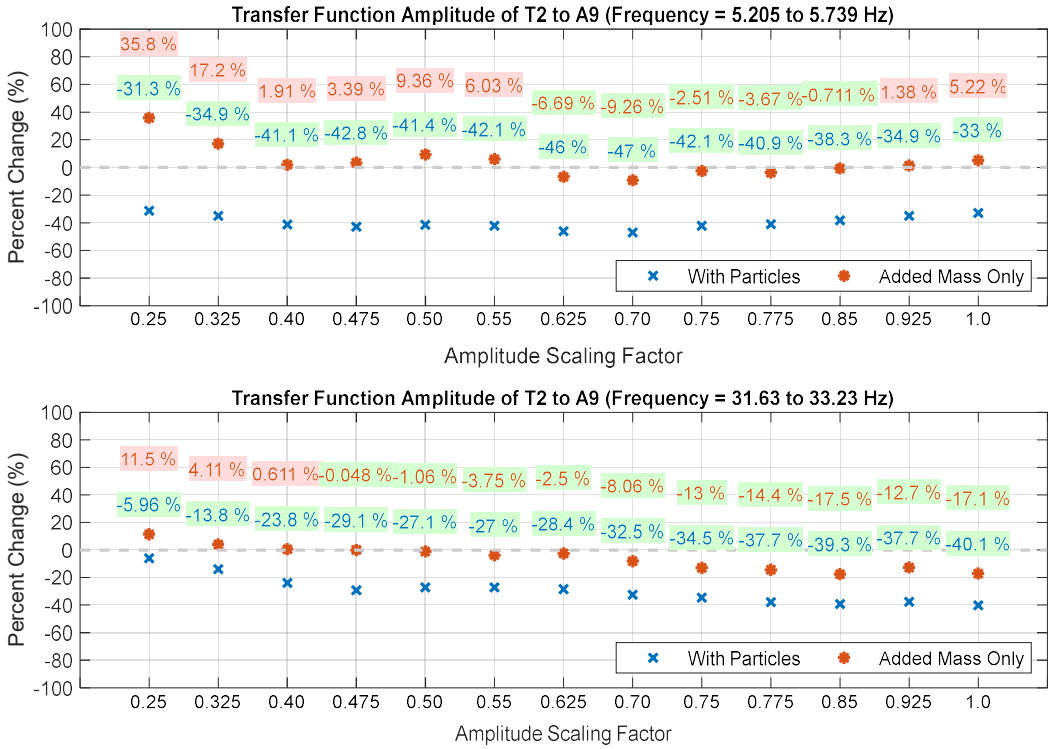


Figure A-13. Percent change in the transfer function amplitude response at the first bending mode and second bending/top breathing modes with varying white-noise excitation amplitudes on the small shake table. Values are normalized to the corresponding no-particle case.

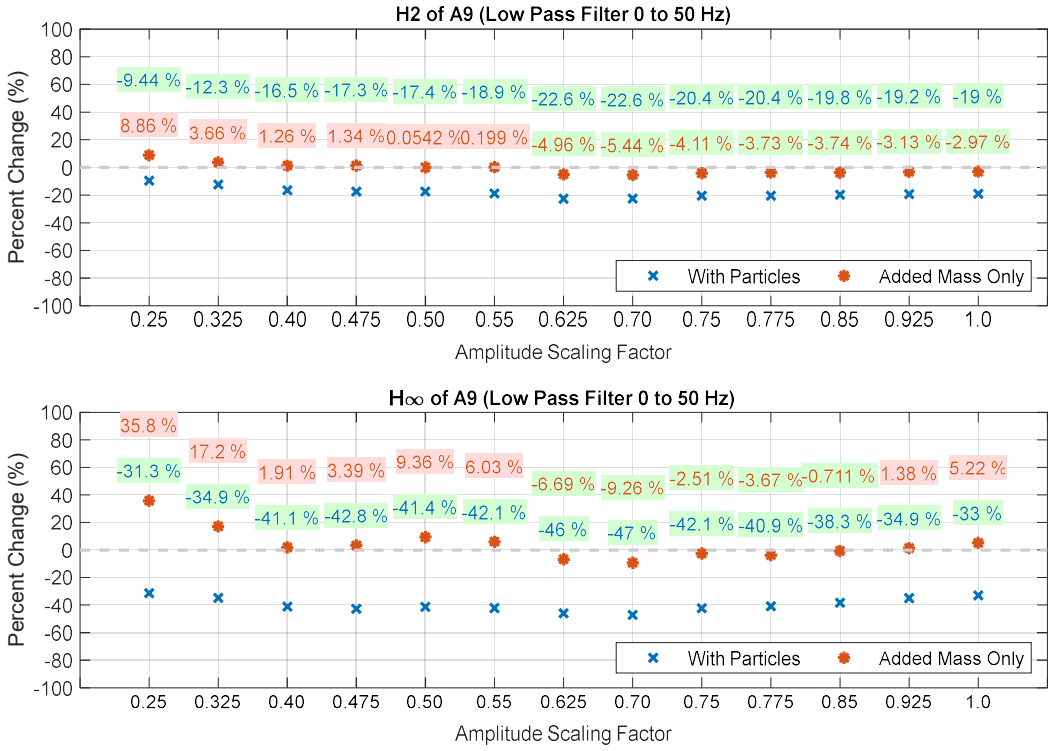


Figure A-14. Percent change in the frequency domain response metrics (H2 and H∞) with varying white-noise excitation amplitudes on the small shake table. Values are normalized to the corresponding no-particle case.

A.3 Initial Container Usage

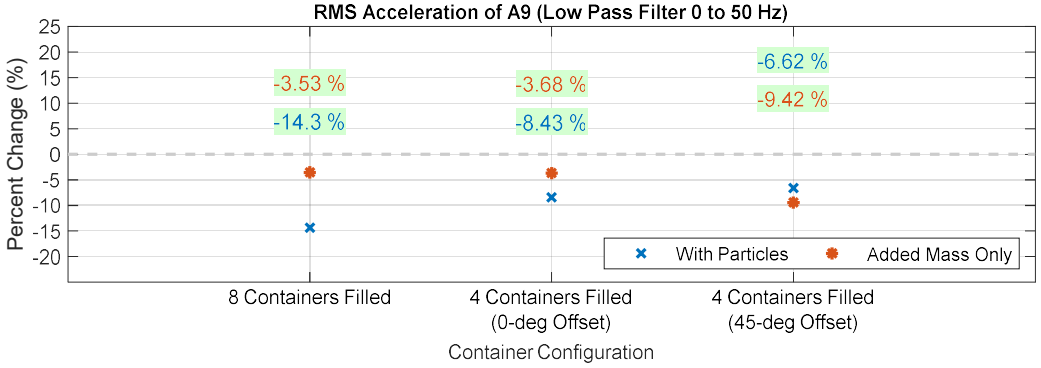


Figure A-15. Percent change in the RMS with respect to different particle damper container configurations on the small shake table. The values are normalized to the corresponding no-particle case.

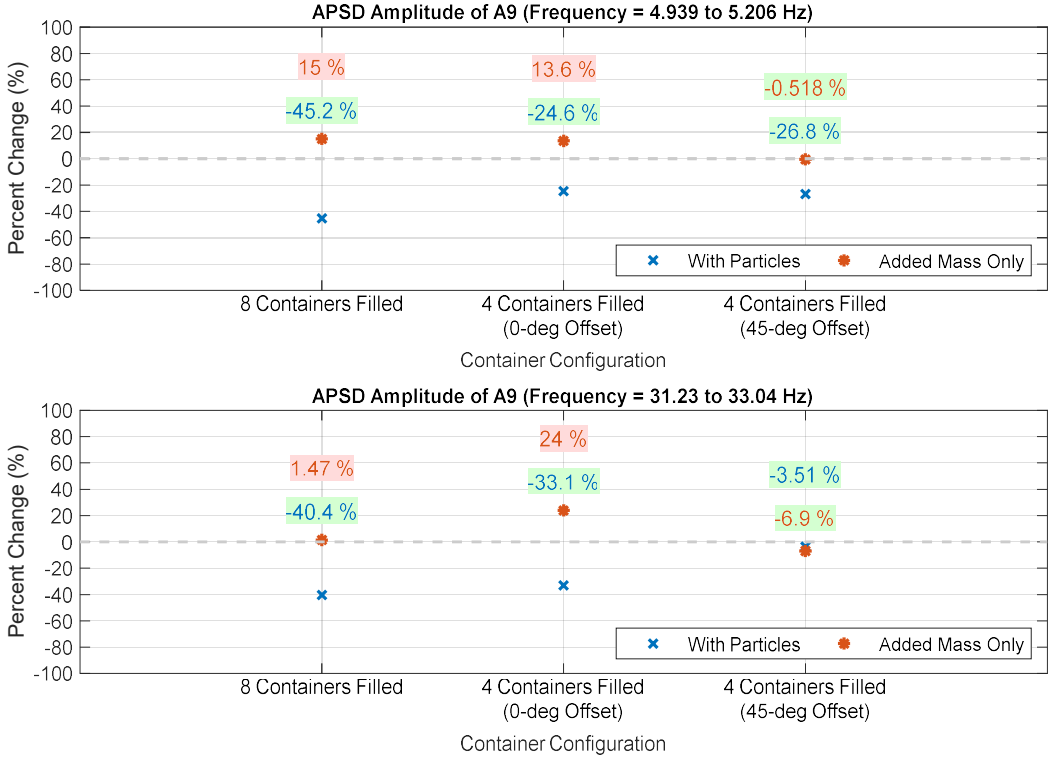


Figure A-16. Percent change in the APSD amplitude responses at the first bending mode and second bending/ top breathing modes with respect to different particle damper container configurations on the small shake table. The values are normalized to the corresponding no-particle case.

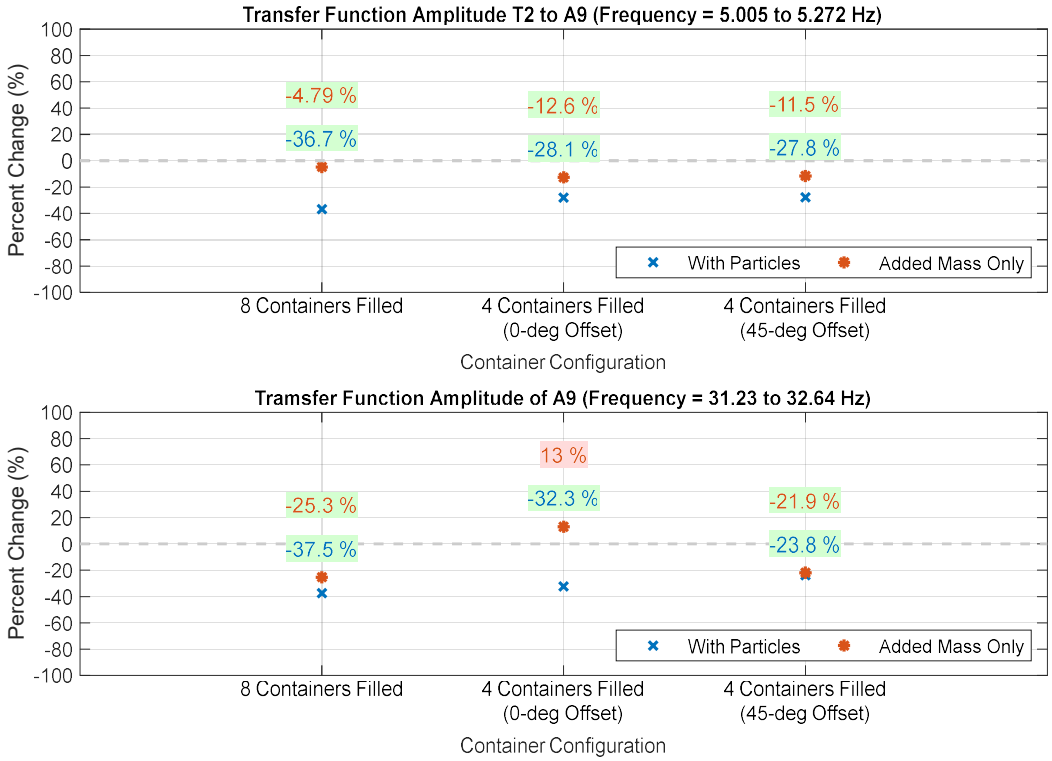


Figure A-17. Percent change in the transfer function amplitude responses at the first bending mode and second bending/ top breathing modes with respect to different particle damper container configurations on the small shake table. The values are normalized to the corresponding no-particle case.

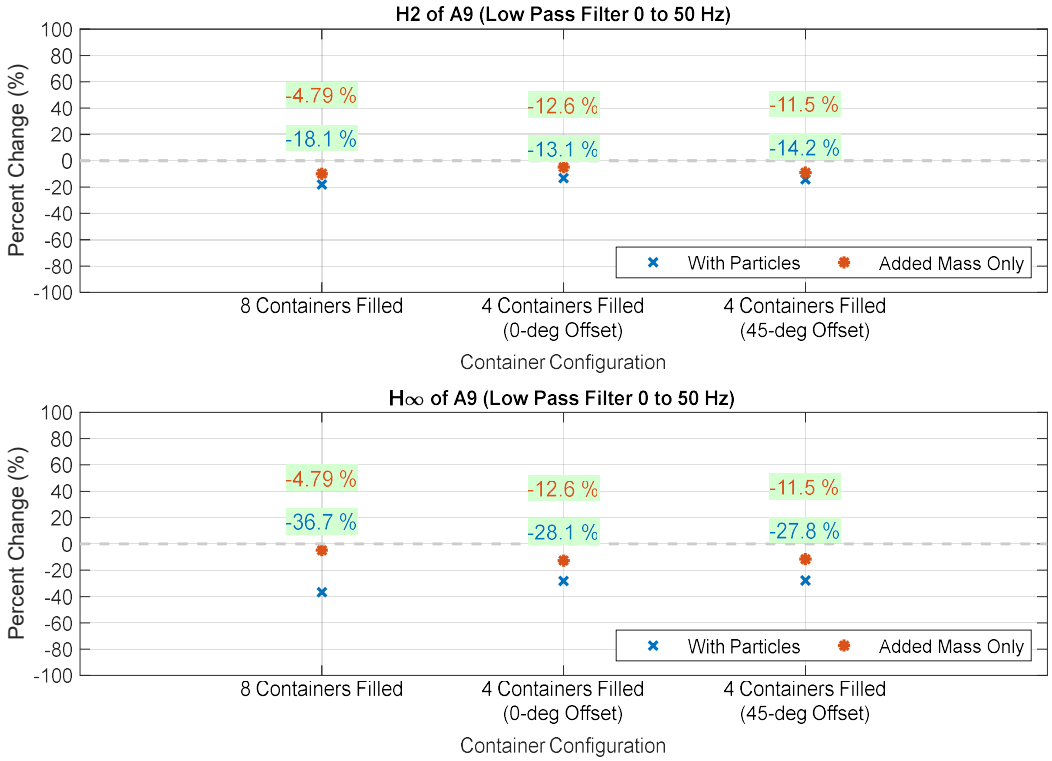


Figure A-18. Percent change in the frequency domain response metrics (H2 and H∞) with respect to different particle damper container configurations on the small shake table. The values are normalized to the corresponding no-particle case.

A.4 Optimal Device Location

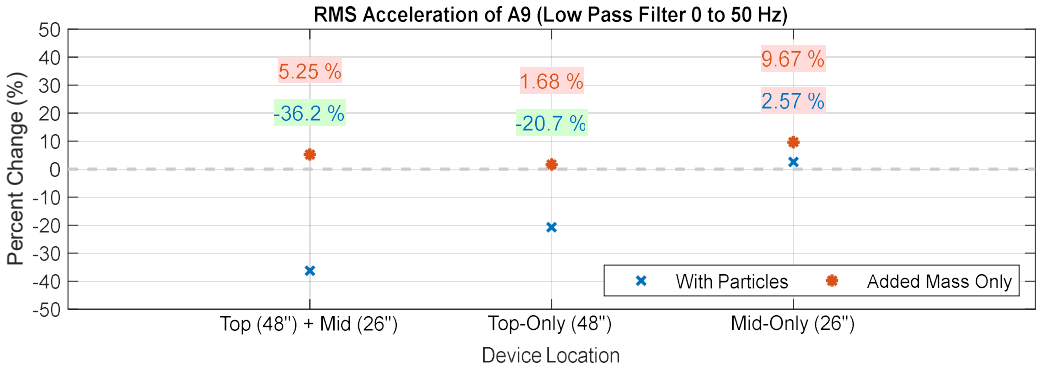


Figure A-19. Percent change in the RMS response for different ring particle damper locations along the height of the structure (Study 1). Elevations indicate the distance from the bottom of the structure. Values are normalized to the corresponding no-particle case.

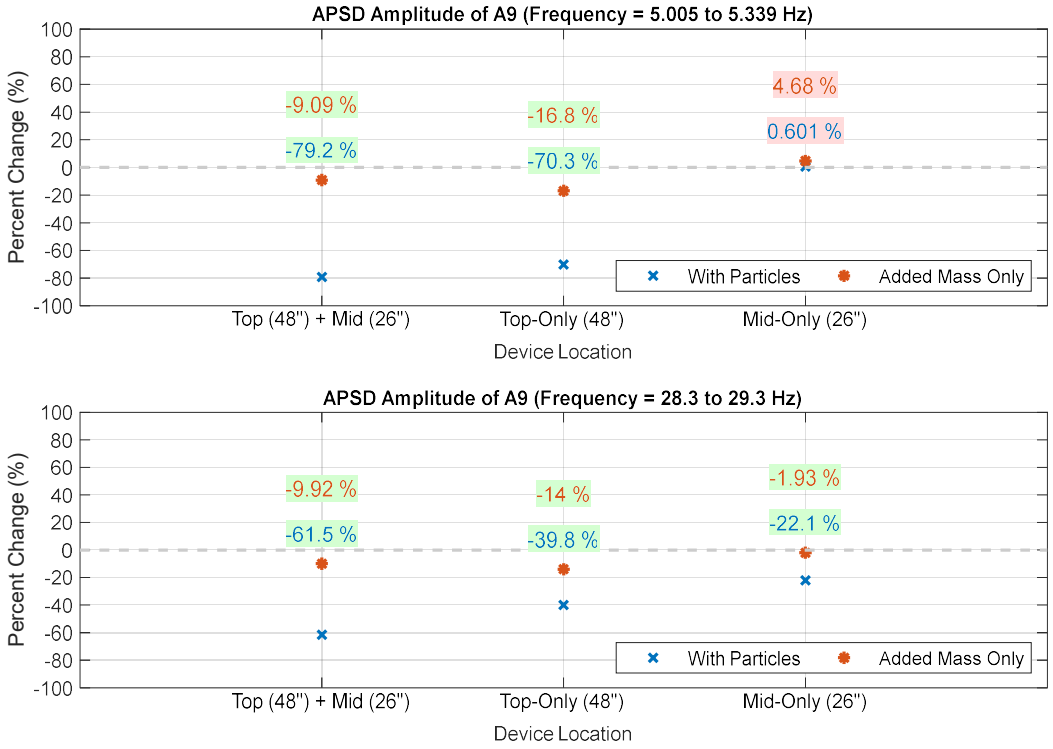


Figure A-20. Percent change in the APSD amplitudes at the first bending mode and second bending/top breathing modes for different ring particle damper locations along the height of the structure (Study 1). Elevations indicate the distance from the bottom of the structure. Values are normalized to the corresponding no-particle case.

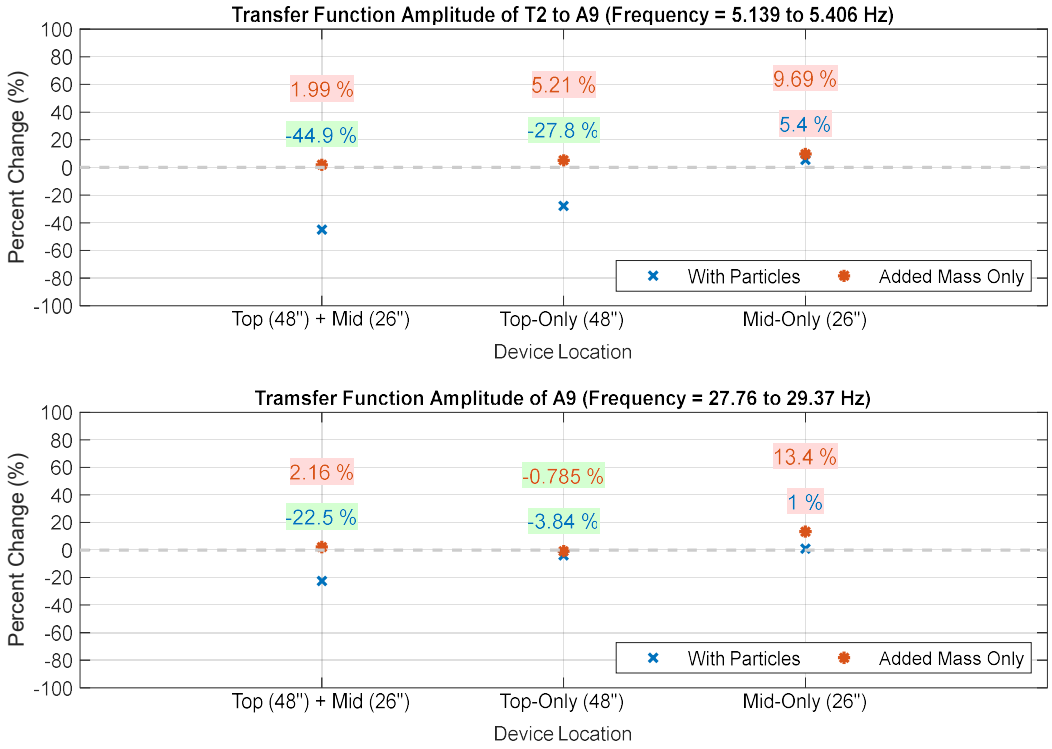


Figure A-21. Percent change in the transfer function amplitudes at the first bending mode and second bending/top breathing modes for different ring particle damper locations along the height of the structure (Study 1). Elevations indicate the distance from the bottom of the structure. Values are normalized to the corresponding no-particle case.

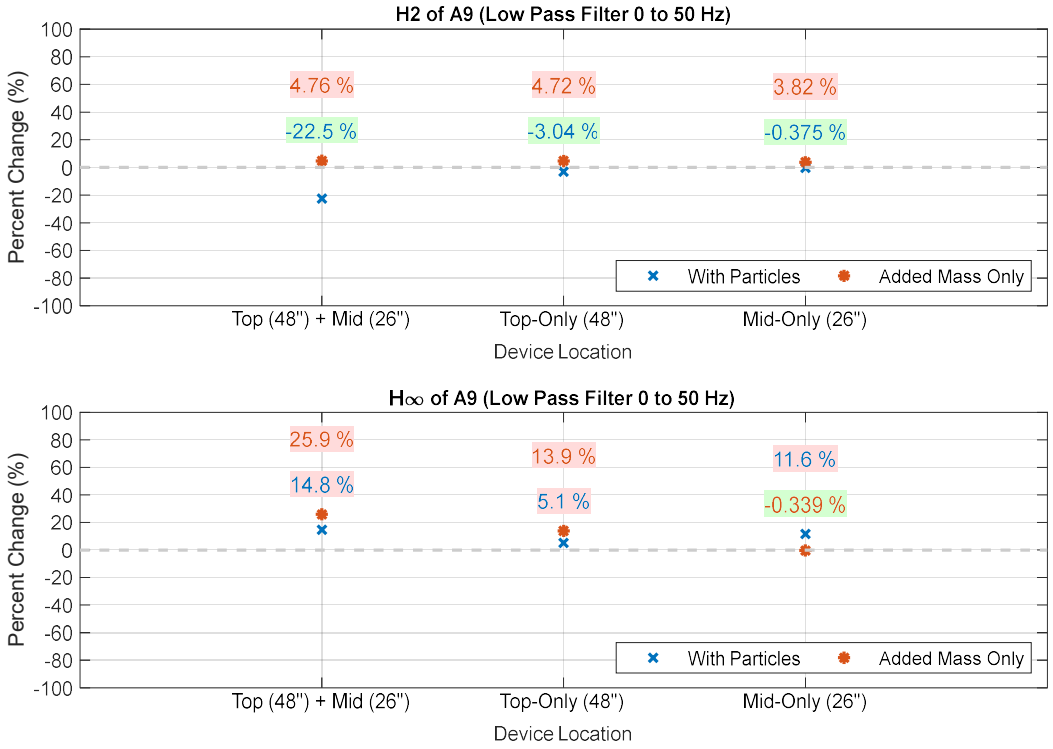


Figure A-22. Percent change in frequency domain response metrics (H2 and H∞) for different ring particle damper locations along the height of the structure (Study 1). Elevations indicate the distance from the bottom of the structure. Values are normalized to the corresponding no-particle case.

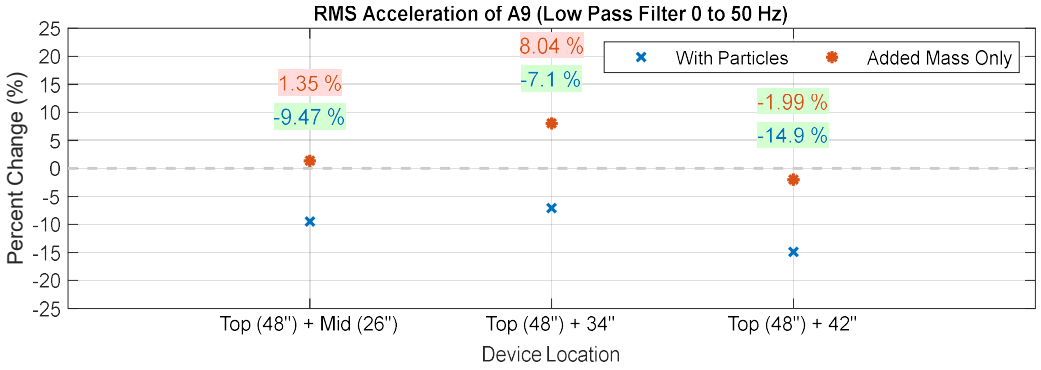


Figure A-23. Percent change in the RMS response for different ring particle damper locations along the height of the structure (Study 2). Elevations indicate the distance from the bottom of the structure. Values are normalized to the corresponding no-particle case.

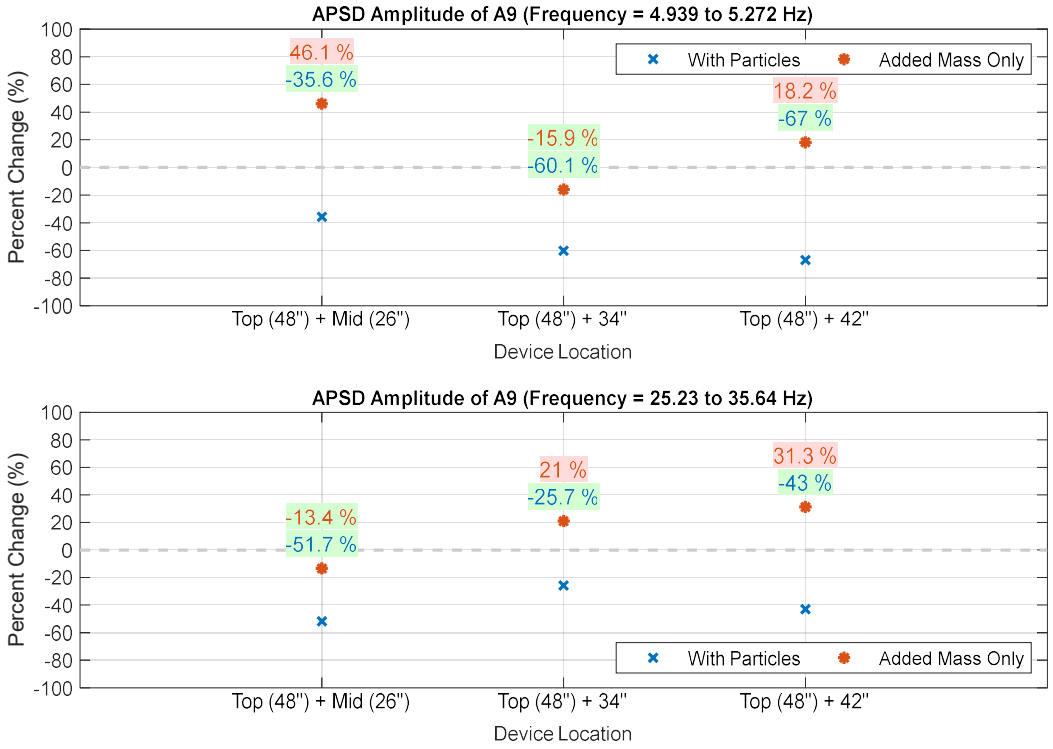


Figure A-24. Percent change in the APSD amplitudes at the first bending mode and second bending/top breathing modes for different ring particle damper locations along the height of the structure (Study 2). Elevations indicate the distance from the bottom of the structure. Values are normalized to the corresponding no-particle case.

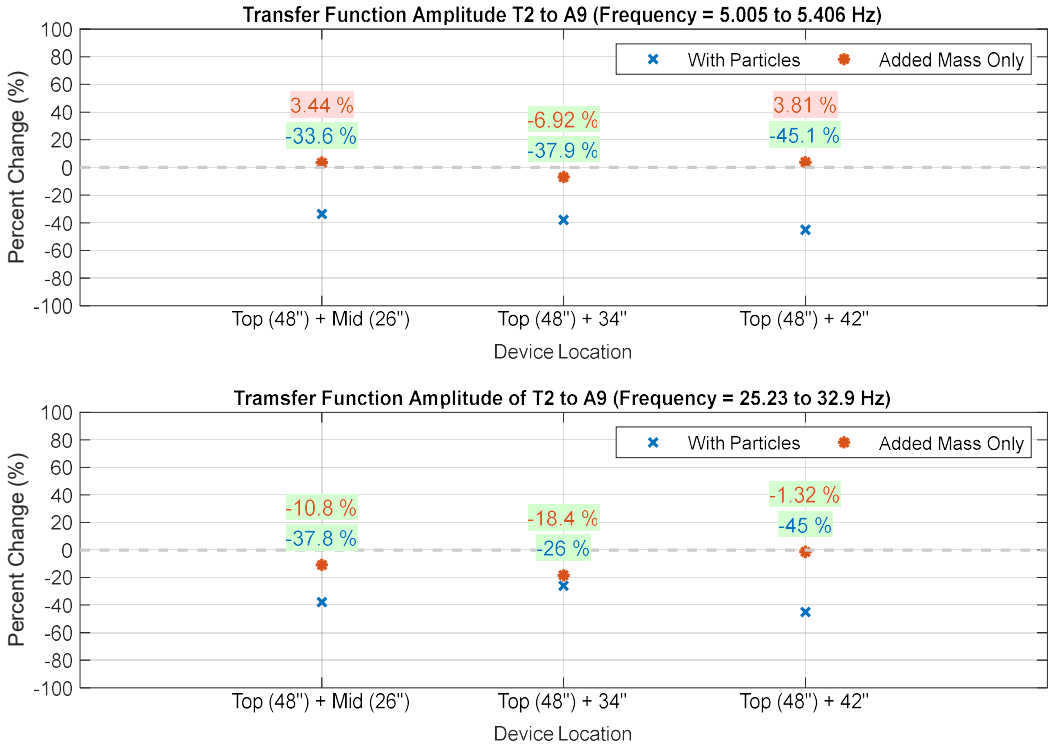


Figure A-25. Percent change in the transfer function amplitudes at the first bending mode and second bending/top breathing modes for different ring particle damper locations along the height of the structure (Study 2). Elevations indicate the distance from the bottom of the structure. Values are normalized to the corresponding no-particle case.

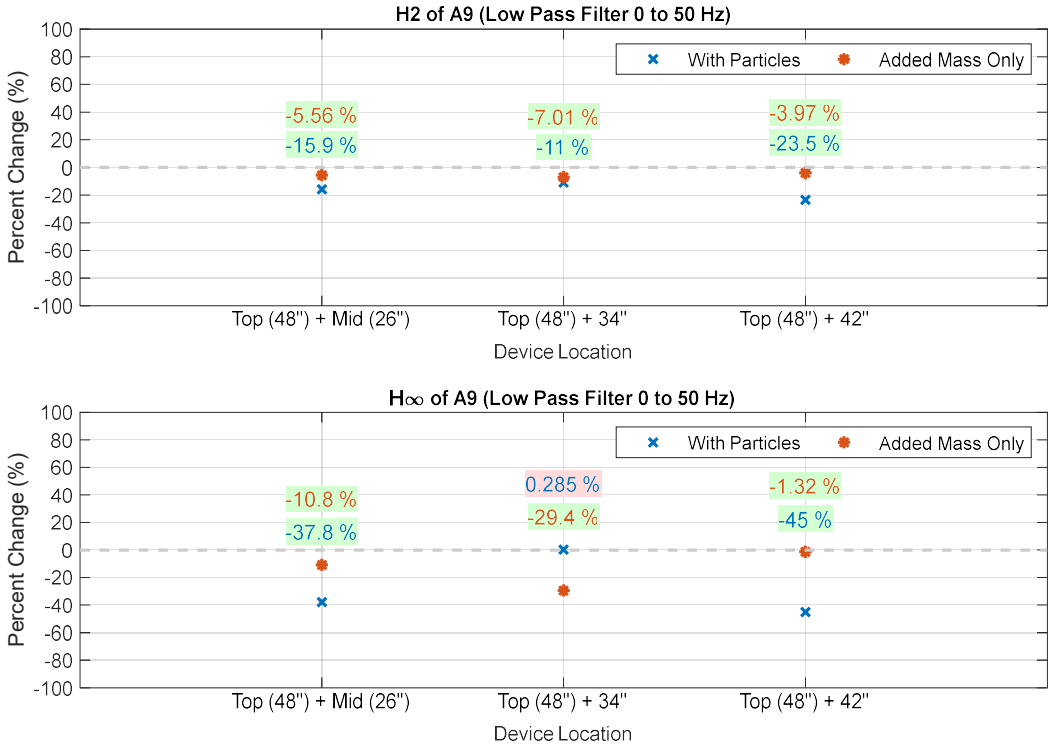


Figure A-26. Percent change in frequency domain response metrics (H2 and H∞) for different ring particle damper locations along the height of the structure (Study 2). Elevations indicate the distance from the bottom of the structure. Values are normalized to the corresponding no-particle case.

A.5 Cavity Layer Usage

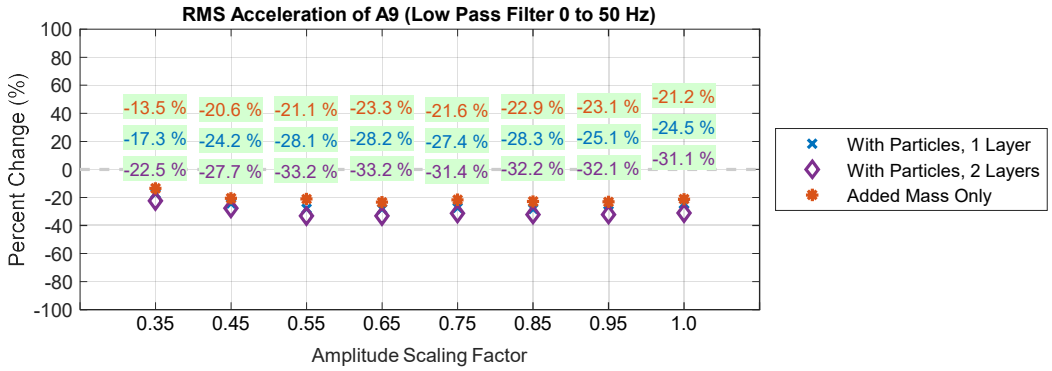


Figure A-27. Percent change in the RMS response for different cavity layer configurations. "1 Layer" represents the one cavity packed with 35 particles, and "2 Layers" refers to two cavities used with a (15 Top / 18 Bottom) packing ratio. Values are normalized to the corresponding no-particle case.

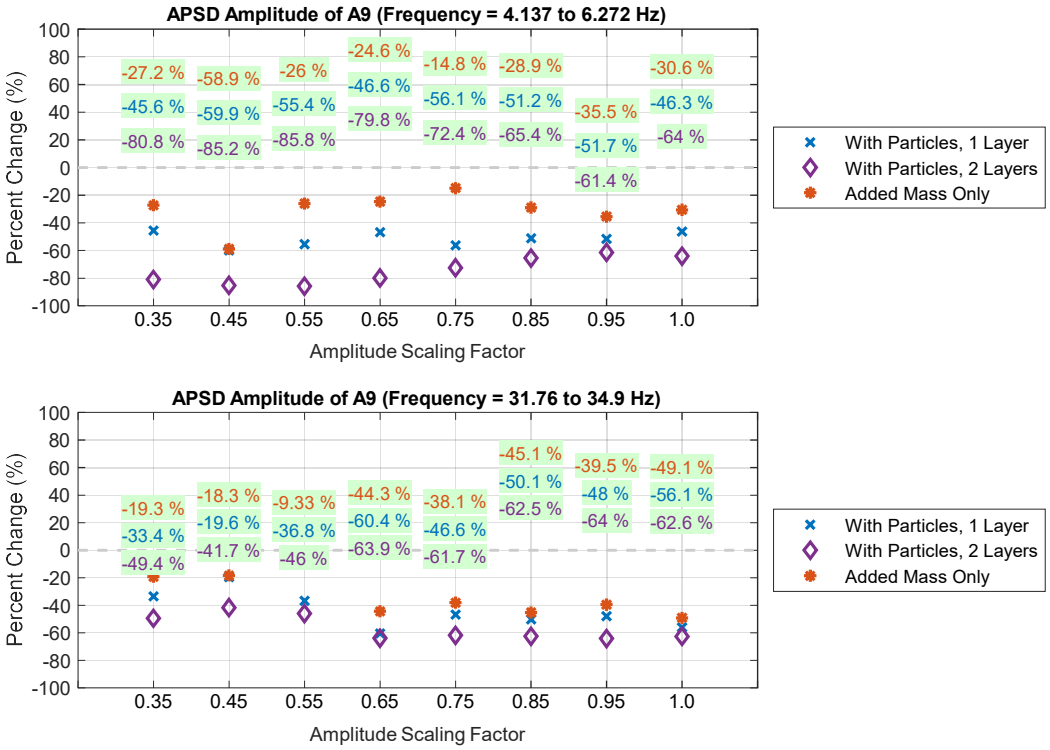


Figure A-28.Percent change in the APSD amplitude response for different cavity layer configurations at the first bending mode and the second bending/ top breathing mode. "1 Layer" represents the one cavity packed with 35 particles, and "2 Layers" refers to two cavities used with a (15 Top / 18 Bottom) packing ratio. Values are normalized to the corresponding no-particle case.

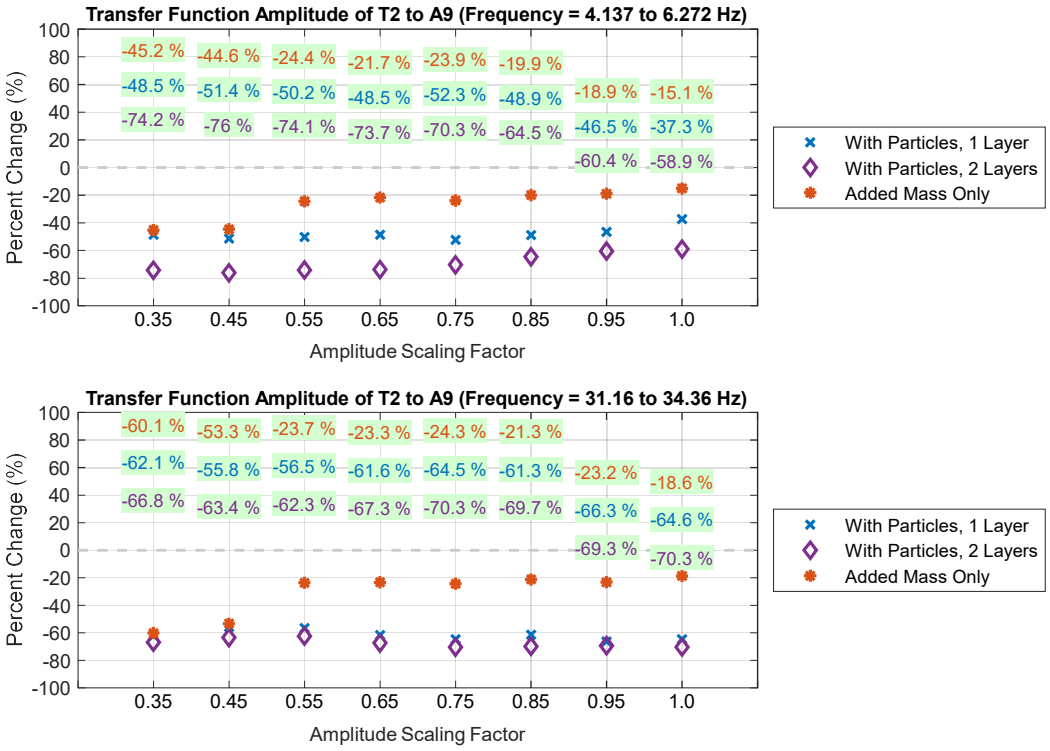


Figure A-29.Percent change in the transfer function amplitude response for different cavity layer configurations at the first bending mode and the second bending/ top breathing mode. "1 Layer" represents the one cavity packed with 35 particles, and "2 Layers" refers to two cavities used with a (15 Top / 18 Bottom) packing ratio. Values are normalized to the corresponding no-particle case.

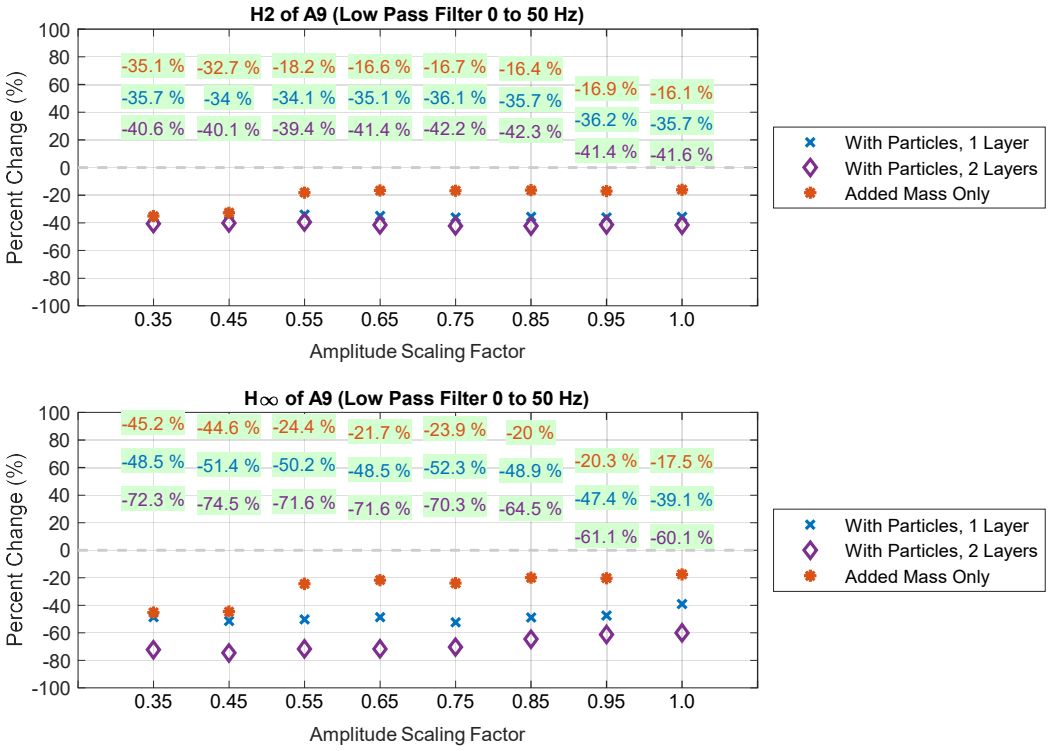


Figure A-30. Percent change in the frequency domain responses (H2 and H∞) for different cavity layer configurations. "1 Layer" represents the one cavity packed with 35 particles, and "2 Layers" refers to two cavities used with a (15 Top / 18 Bottom) packing ratio. Values are normalized to the corresponding no-particle case.

A.6 Device Cavity Lining Material

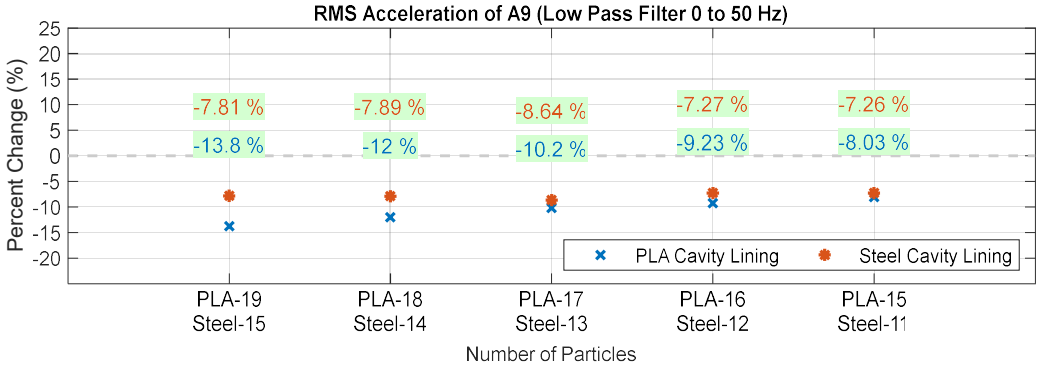


Figure A-31. Percent change in the RMS response as a function of different particle damper cavity materials. PLA and steel packing ratios are shown, and the percent changes are normalized with respect to the corresponding no-particle case.

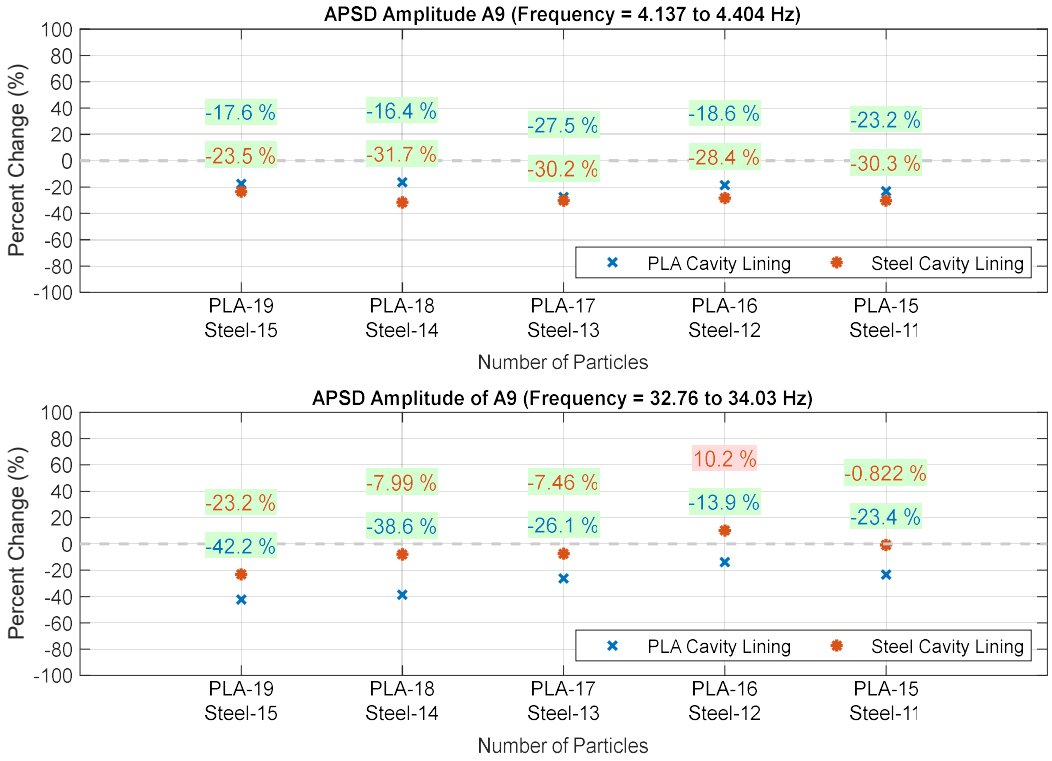


Figure A-32. Percent change in the APSD amplitude at the first bending mode and second bending/top breathing modes as a function of different particle damper cavity materials. PLA and steel packing ratios are shown, and the percent changes are normalized with respect to the corresponding no-particle case.

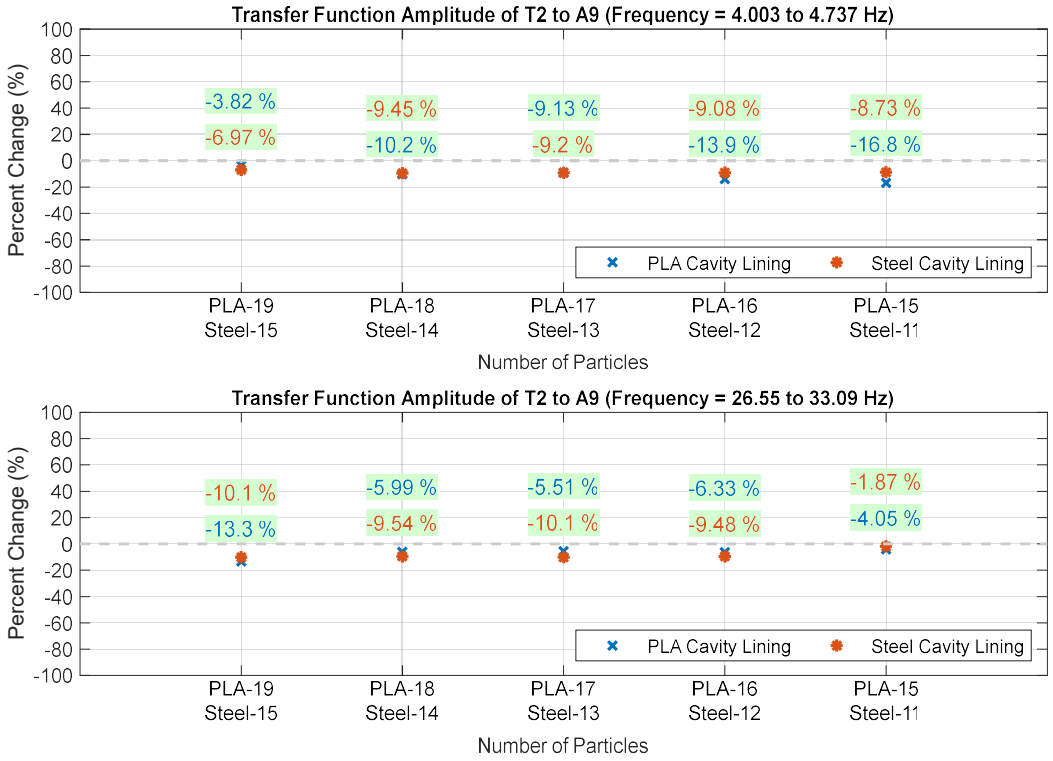


Figure A-33. Percent change in the transfer function amplitude at the first bending mode and second bending/top breathing modes as a function of different particle damper cavity materials. PLA and steel packing ratios are shown, and the percent changes are normalized with respect to the corresponding no-particle case.

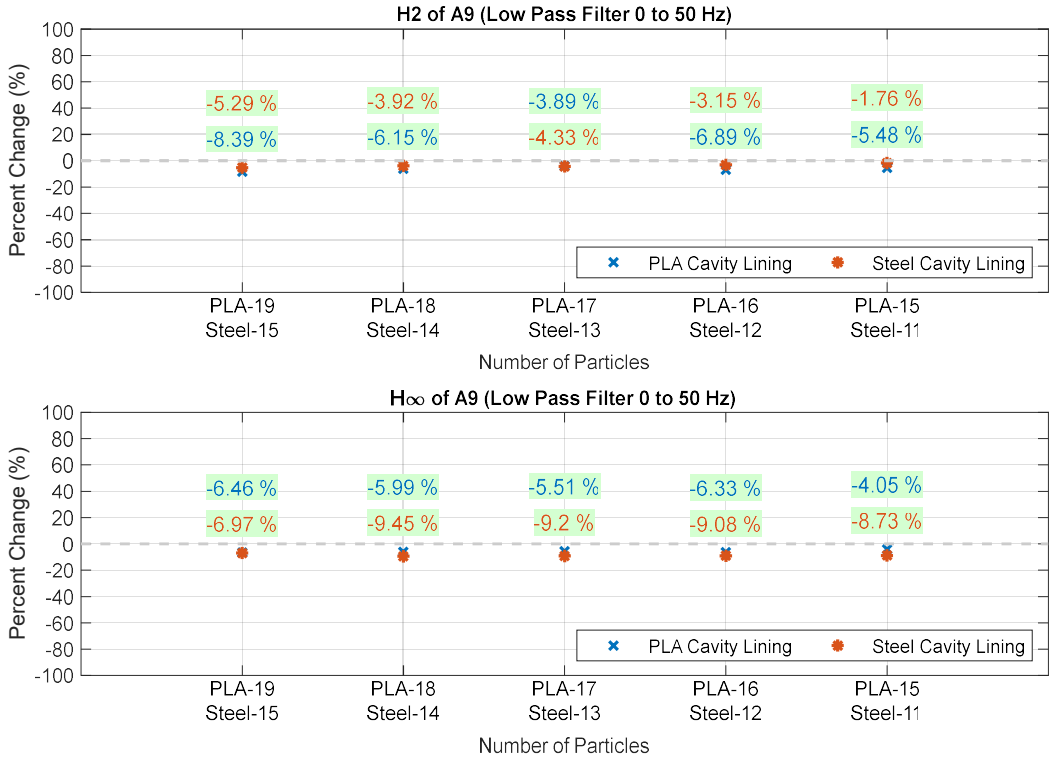


Figure A-34. Percent change in the frequency domain response metrics (H2 and H∞) as a function of different particle damper cavity materials. PLA and steel packing ratios are shown, and the percent changes are normalized with respect to the corresponding no-particle case.

A.7 Sinusoidal Excitation

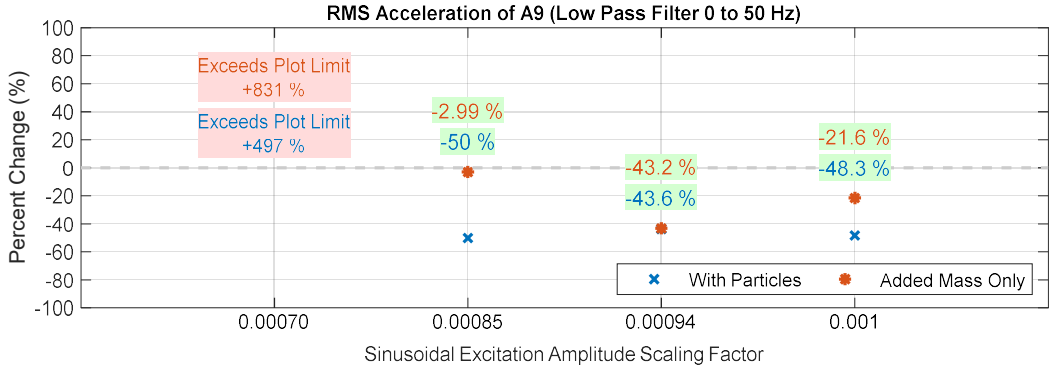


Figure A-35. Percent change in RMS response versus sinusoidal excitation amplitude. The excitation frequency was 5.21 Hz for the no-particle case, and 5.01 Hz for the with-particles and added mass cases. The percent changes are normalized to the corresponding no-particle cases.

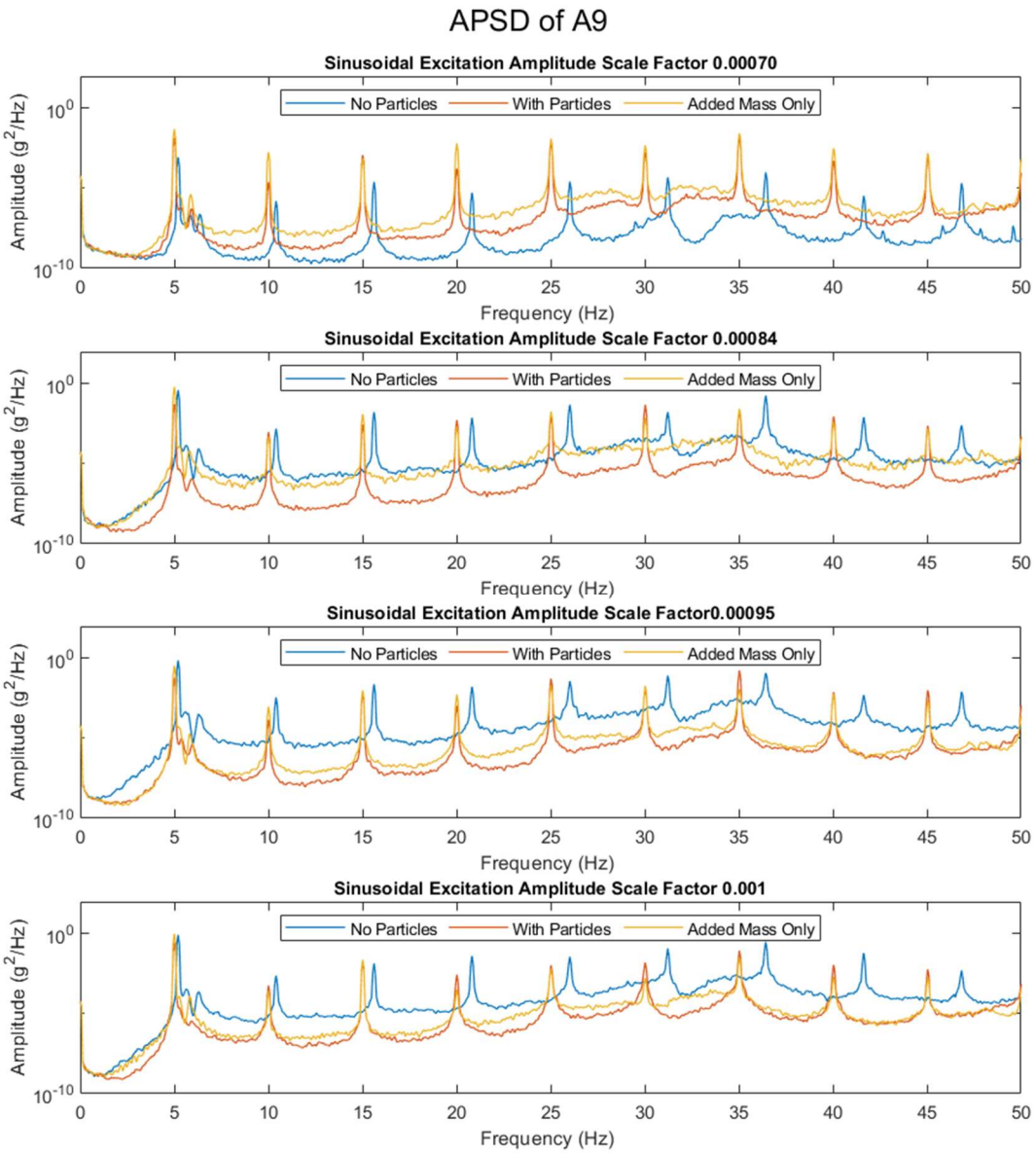


Figure A-36. Frequency response function of A9 under sinusoidal excitation, comparing the no-particle case, with-particle case, and added mass case at varying excitation amplitudes. The excitation frequency was 5.21 Hz for the no-particle configuration, and 5.01 Hz for the with-particles and added mass configurations.

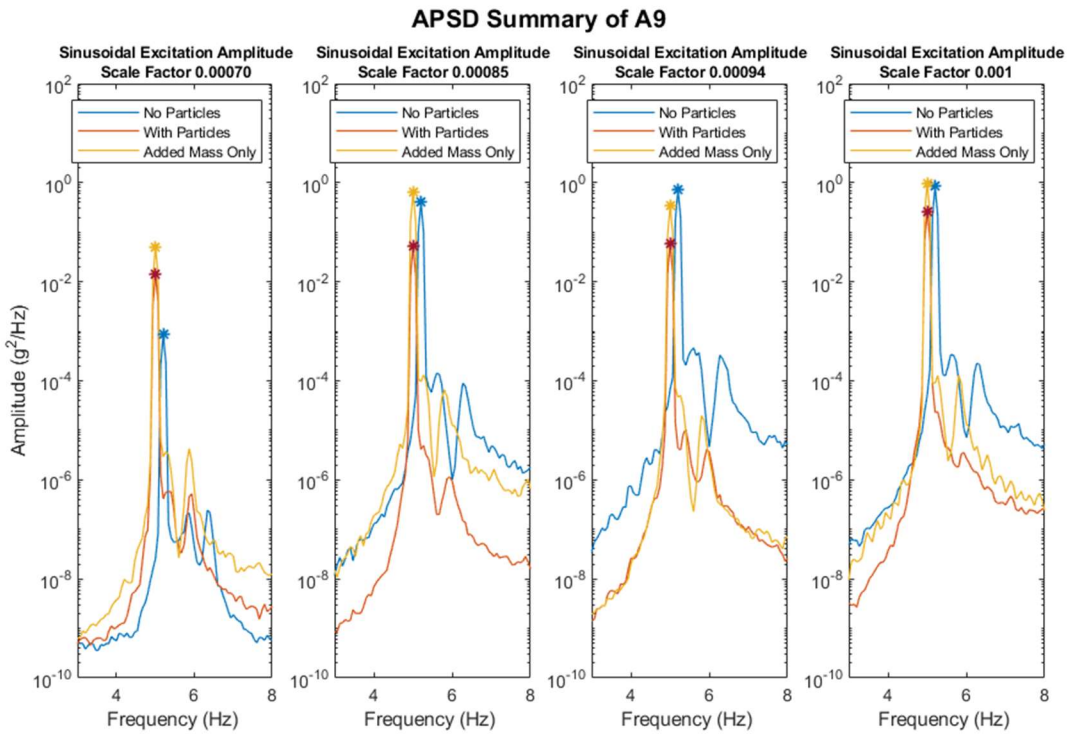


Figure A-37. Frequency response function at the first bending mode under sinusoidal excitation, comparing the no-particle case, the with-particle case, and the added mass case at varying excitation amplitudes. The excitation frequency was 5.21 Hz for the no-particle configuration, and 5.01 Hz for the with-particles and added mass configurations.

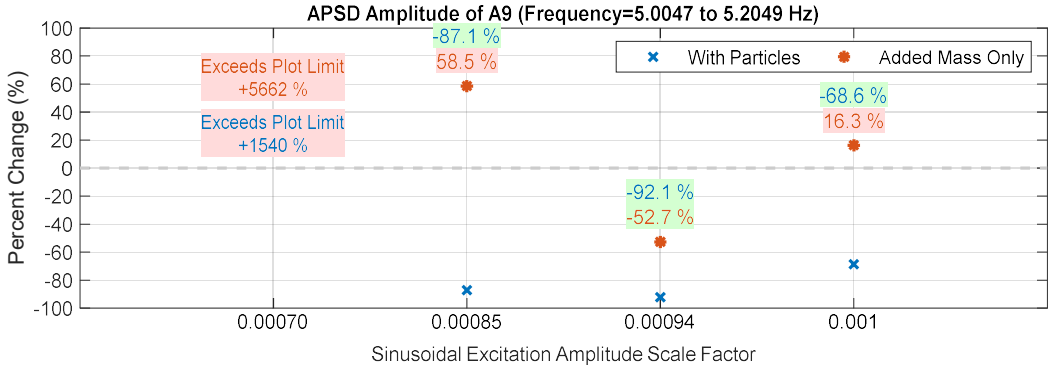


Figure A-38. Percent change in the APSD amplitude at the first bending mode under varying sinusoidal excitation amplitudes. The excitation frequency was 5.21 Hz for the no-particle configuration, and 5.01 Hz for the with-particles and added mass configurations. Values are normalized to the corresponding no-particle case.

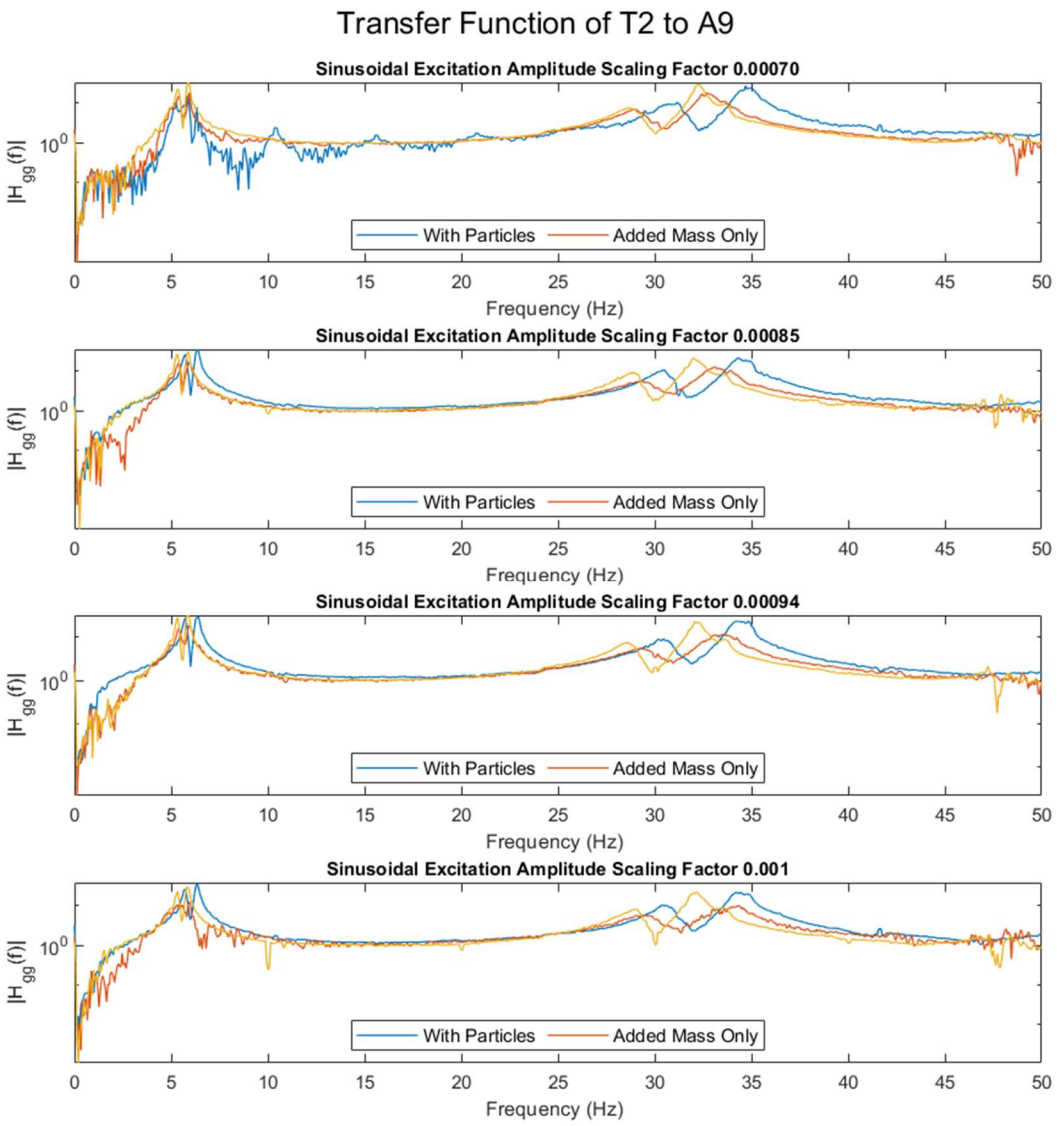


Figure A-39. Frequency response function of A9 under sinusoidal excitation, comparing the no-particle case, with-particle case, and added mass case at varying excitation amplitudes. The excitation frequency was 5.21 Hz for the no-particle configuration, and 5.01 Hz for the with-particles and added mass configurations.

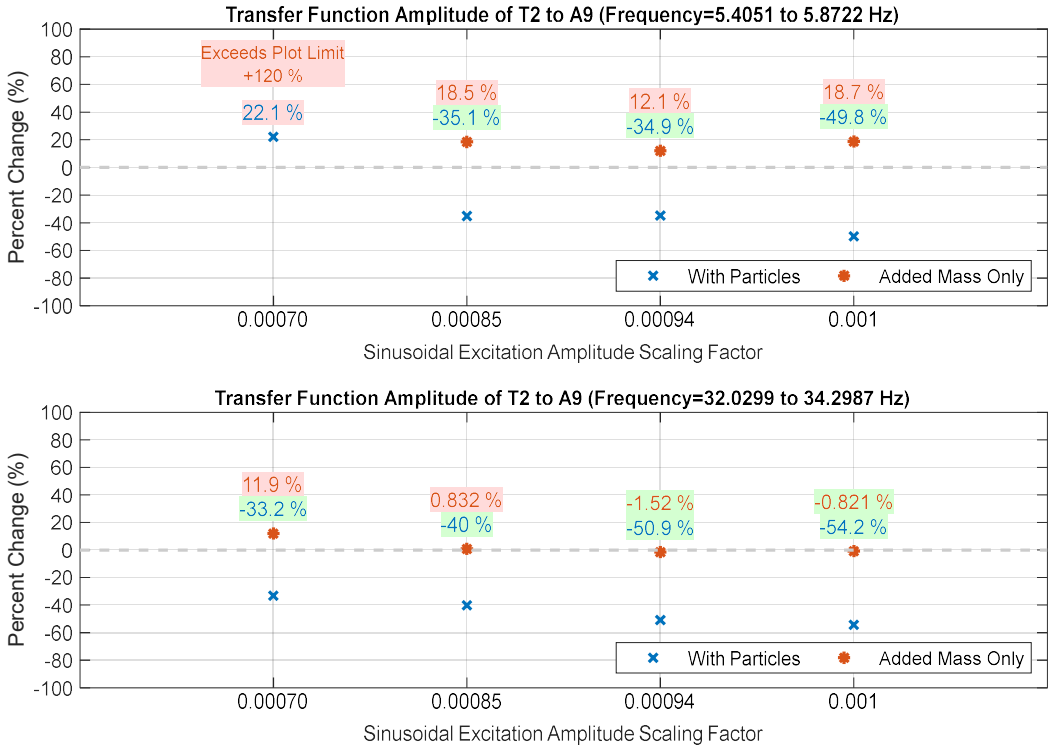


Figure A-40. Percent change in the transfer function amplitude at the first bending mode and second bending/top breathing modes under sinusoidal excitation amplitudes. The excitation frequency was 5.21 Hz for the no-particle configuration, and 5.01 Hz for the with-particles and added mass configurations. Values are normalized with respect to corresponding no-particle configurations.

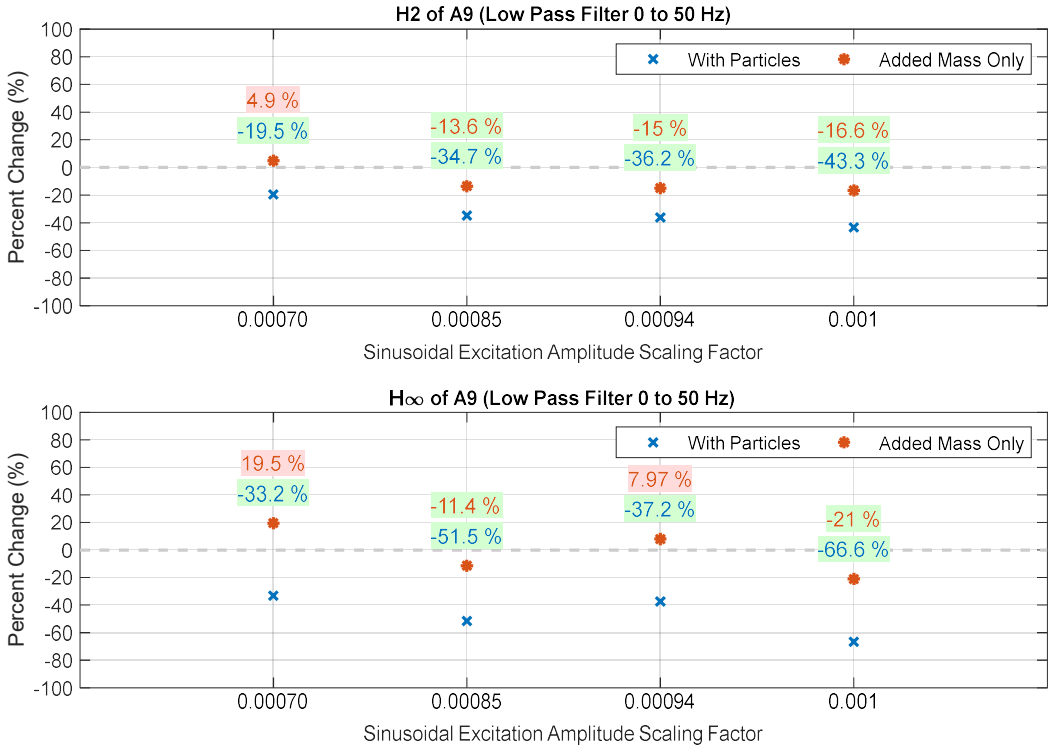


Figure A-41. Percent change in frequency domain response metrics (H2 and H∞) under sinusoidal excitation amplitudes. The excitation frequency was 5.21 Hz for the no-particle configuration, and 5.01 Hz for the with-particles and added mass configurations. Values are normalized with respect to corresponding no-particle configurations.

A.8 Sine Sweep Excitation

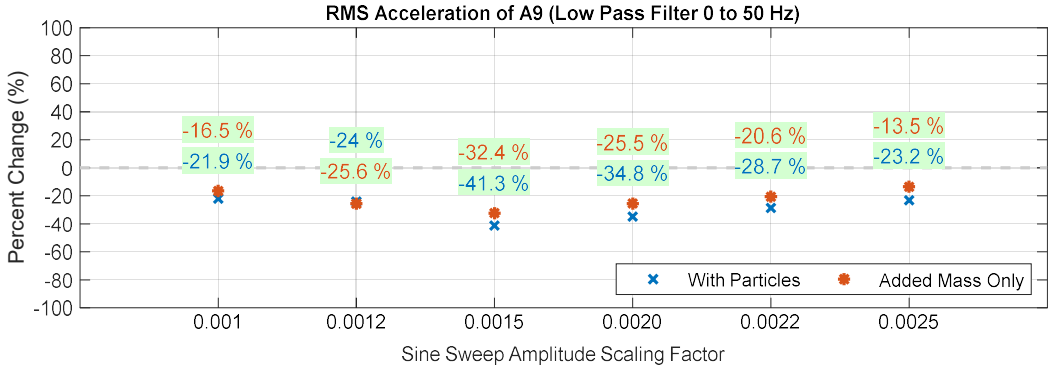


Figure A-42. Percent change in RMS response for a 30-second sine sweep test from 3.5 to 6.5 Hz at varying in excitation amplitude. Values are normalized to the corresponding no-particle case.

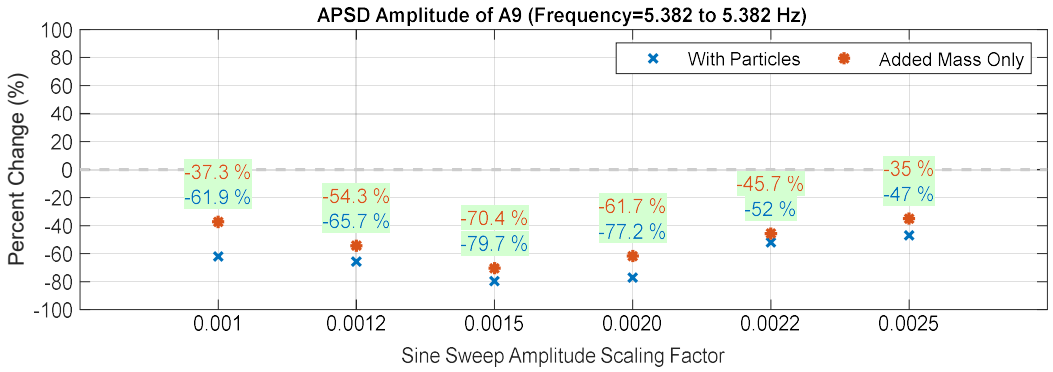


Figure A-43. Percent change in APSD amplitude response at first bending mode for a 30-second sine sweep test from 3.5 to 6.5 Hz at varying in excitation amplitude. Values are normalized to the corresponding no-particle case.

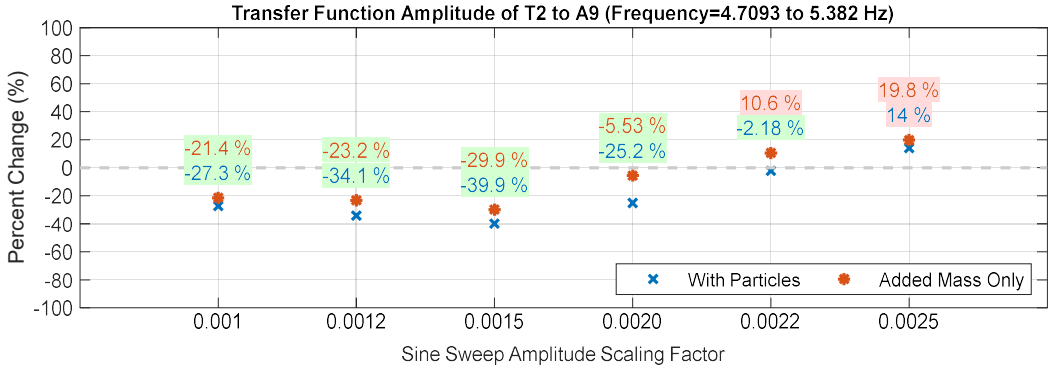


Figure A-44. Percent change in transfer function amplitude response at first bending mode for a 30-second sine sweep test from 3.5 to 6.5 Hz at varying in excitation amplitude. Values are normalized to the corresponding no-particle case.

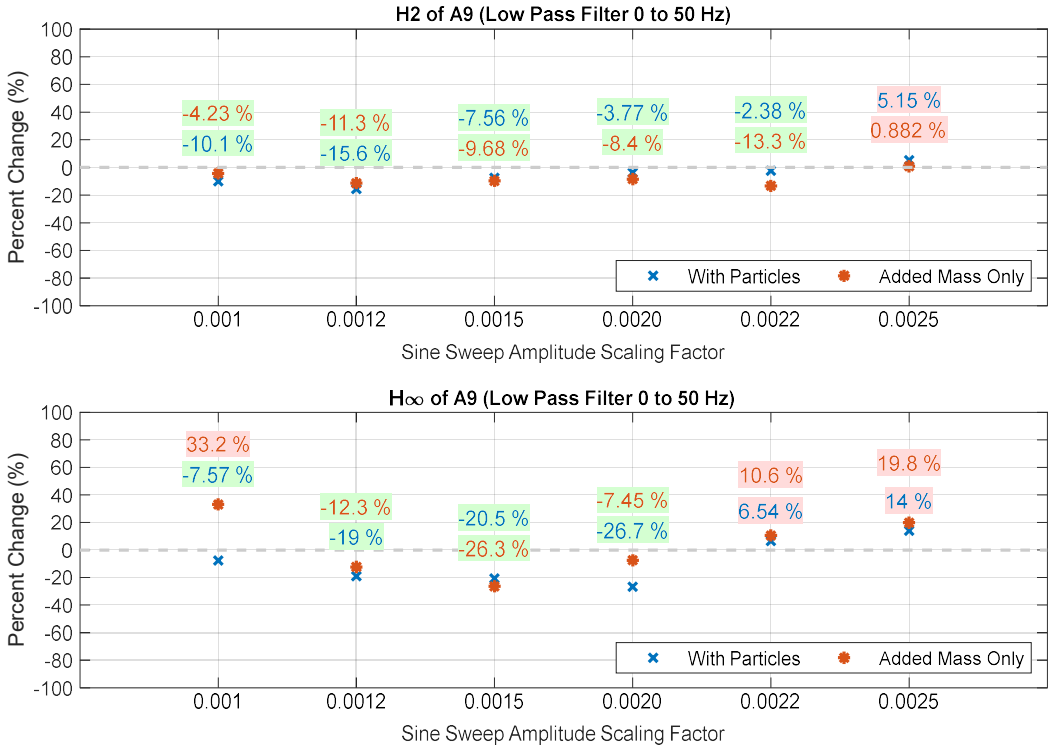


Figure A-45. Percent change in frequency domain response metrics (H2 and H∞) for a 30-second sine sweep test from 3.5 to 6.5 Hz at varying in excitation amplitudes. Values are normalized to the corresponding no-particle case.

Appendix B: Results from Effectiveness Demonstrations

Table of Contents

B.1 Multi-Directional White Noise Excitation Amplitude 3
B.2 Particle Material Type 13
B.3 Multi-Directional Container Usage 27
B.4 Torsional Excitation 55

B.1 Multi-Directional White Noise Excitation Amplitude

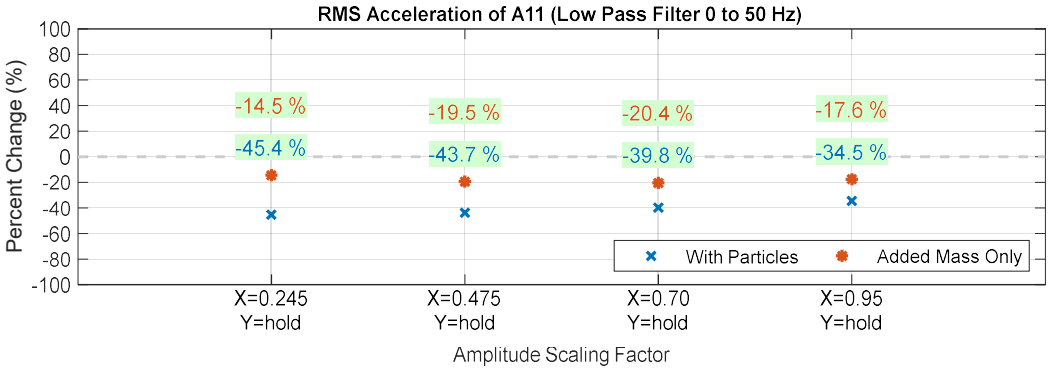


Figure B-1. Percent change in RMS response of the +X sensor under varying excitation amplitudes applied in the +X axis of the big shake table. Values are normalized to the corresponding no-particle configuration.

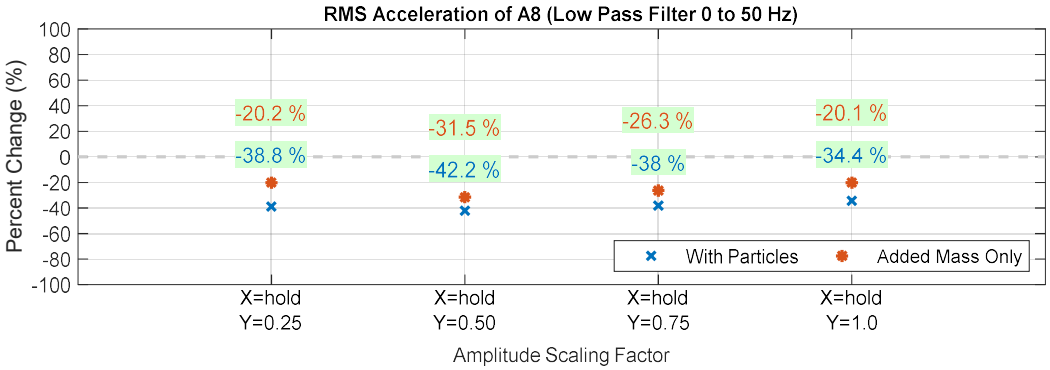


Figure B-2. Percent change in RMS response of the +Y sensor under varying excitation amplitudes applied in the +Y axis of the big shake table. Values are normalized to the corresponding no-particle configuration.

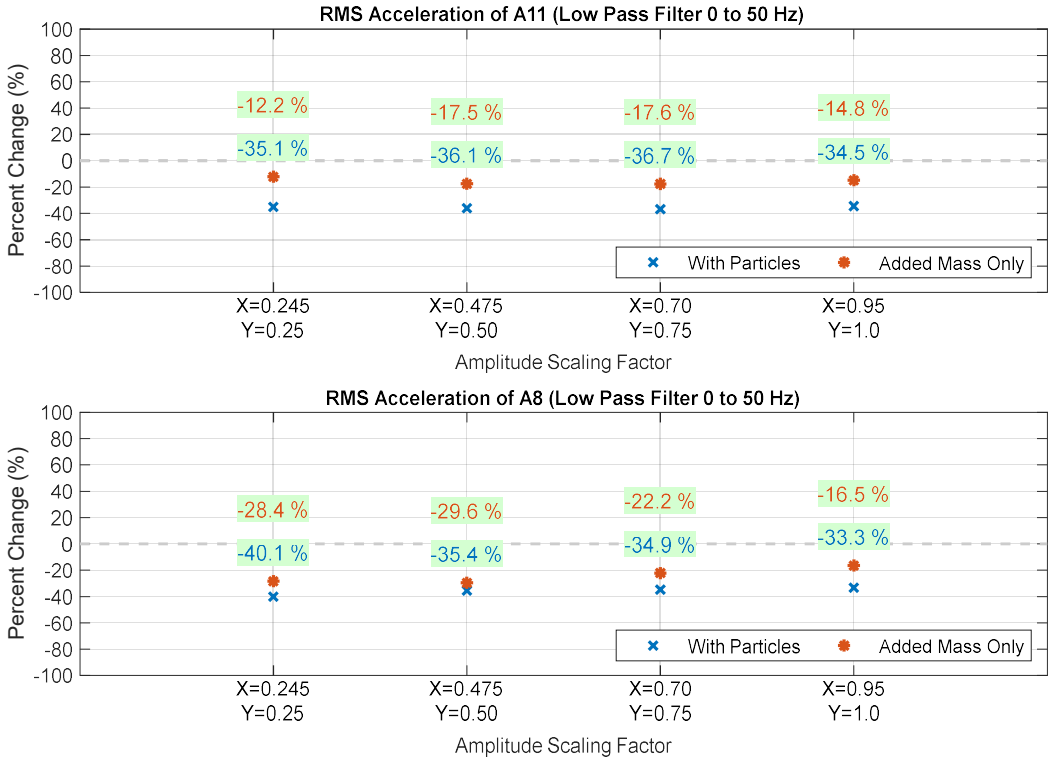


Figure B-3. Percent change in RMS response of the +X and +Y sensors under varying excitation amplitudes applied simultaneously along the +X and +Y axes of the big shake table. Values are normalized to the corresponding no-particle configuration.

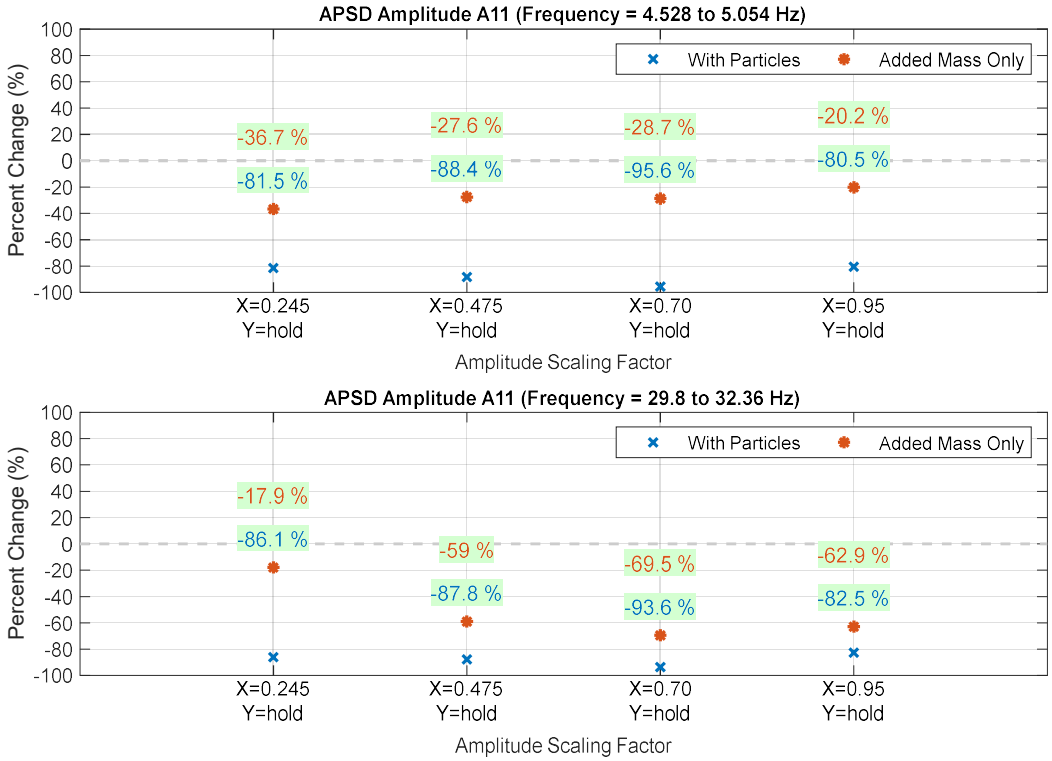


Figure B-4. Percent change in APSD amplitude response of the +X sensor at first bending mode and second bending/top breathing modes under varying excitation amplitudes applied in the +X axis of the big shake table. Values are normalized to the corresponding no-particle configuration.

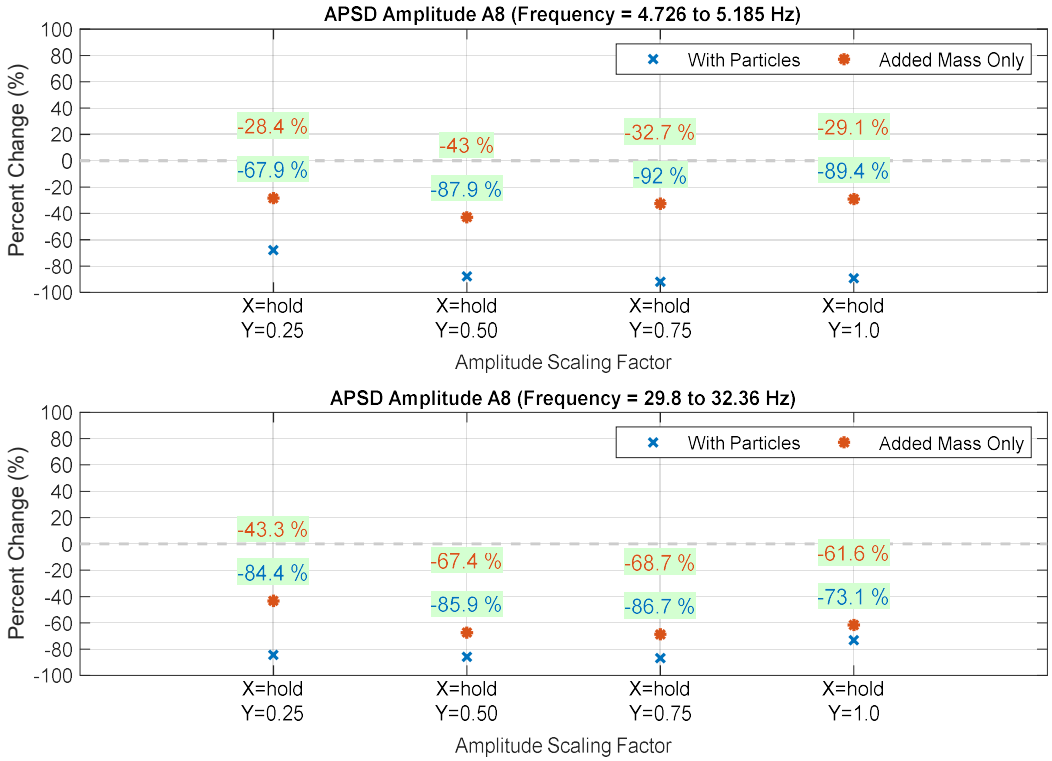


Figure B-5. Percent change in APSD amplitude response of the +Y sensor at first bending mode and second bending/top breathing modes under varying excitation amplitudes applied in the +Y axis of the big shake table. Values are normalized to the corresponding no-particle configuration.

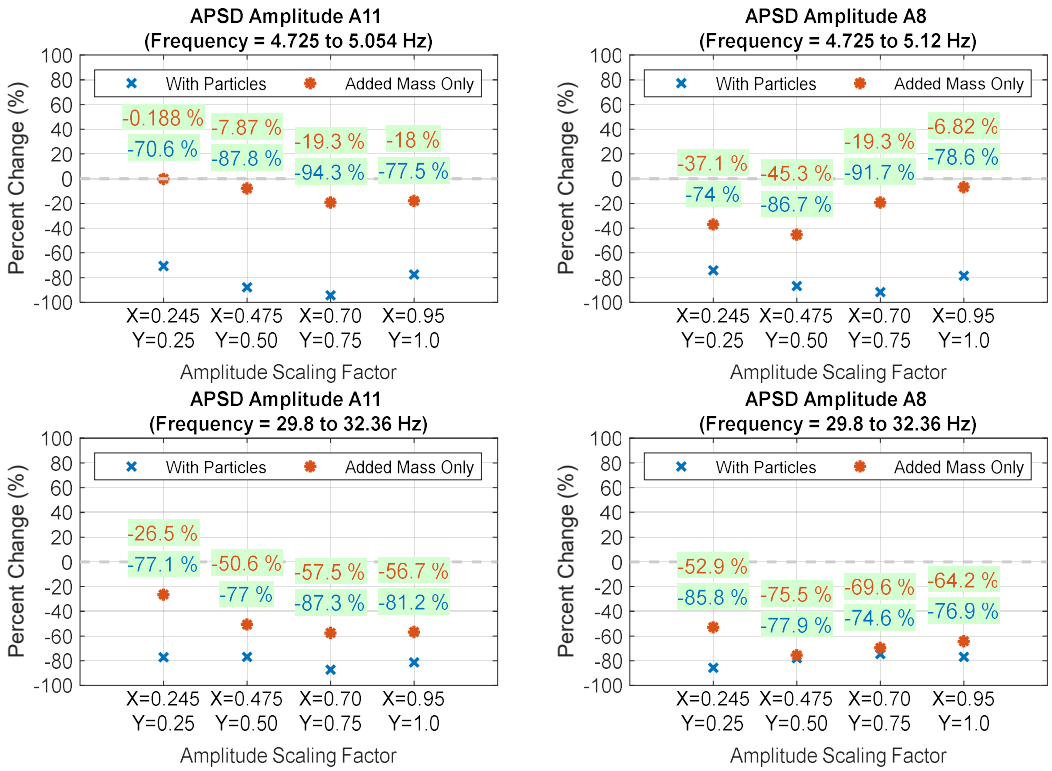


Figure B-6. Percent change in APSD amplitude response of the +X and +Y sensor at first bending mode and second bending/top breathing modes under varying excitation amplitudes applied simultaneously along the +X and +Y axes of the big shake table. Values are normalized to the corresponding no-particle configuration.

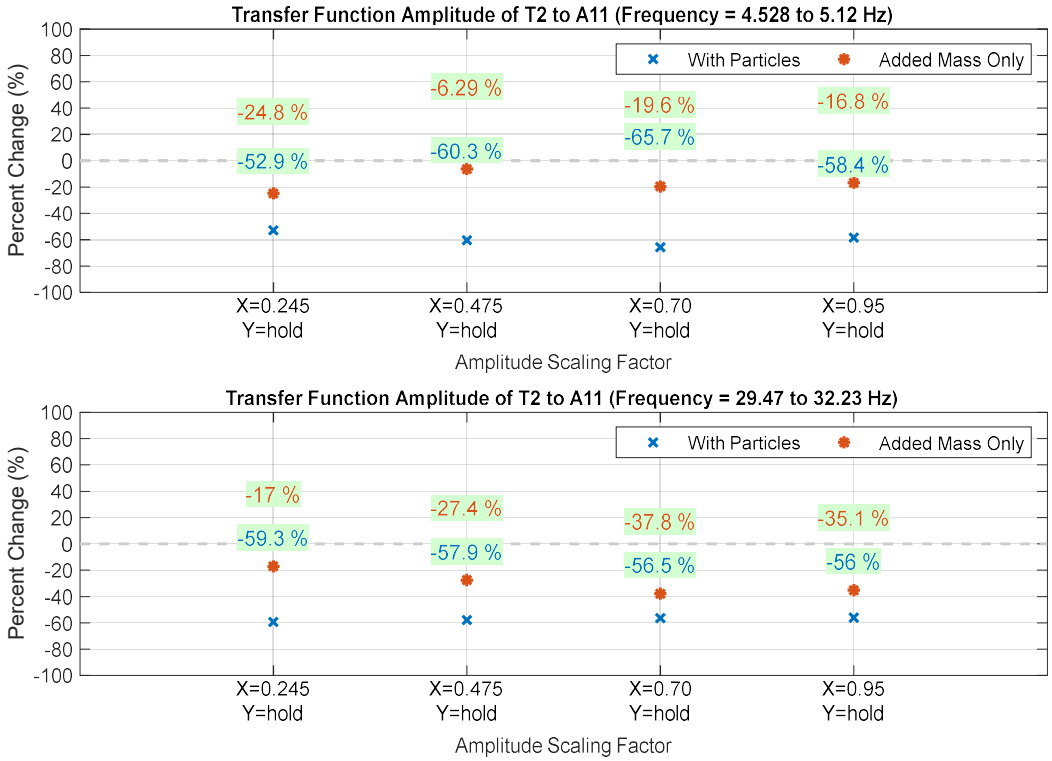


Figure B-7. Percent change in transfer function amplitude response of the + X sensor at first bending mode and second bending/top breathing modes under varying excitation amplitudes applied in the +X axis of the big shake table. Values are normalized to the corresponding no-particle configuration.

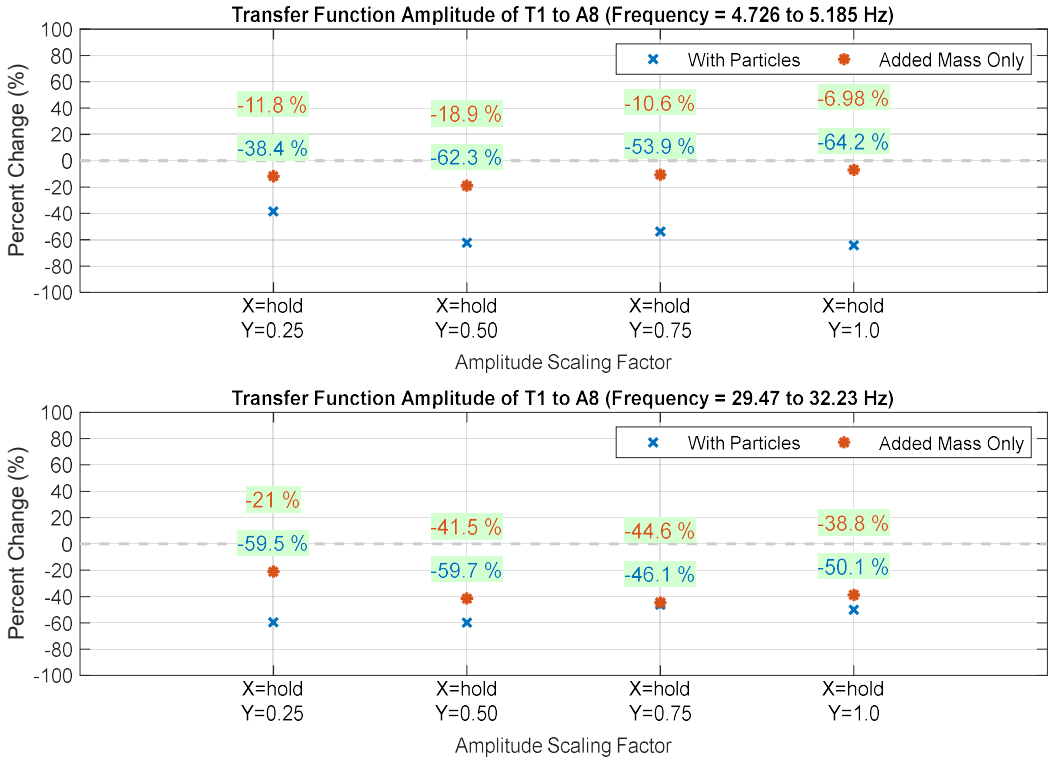


Figure B-8. Percent change in transfer function amplitude response of the +Y sensor at first bending mode and second bending/top breathing modes under varying excitation amplitudes applied in the +Y axis of the big shake table. Values are normalized to the corresponding no-particle configuration.

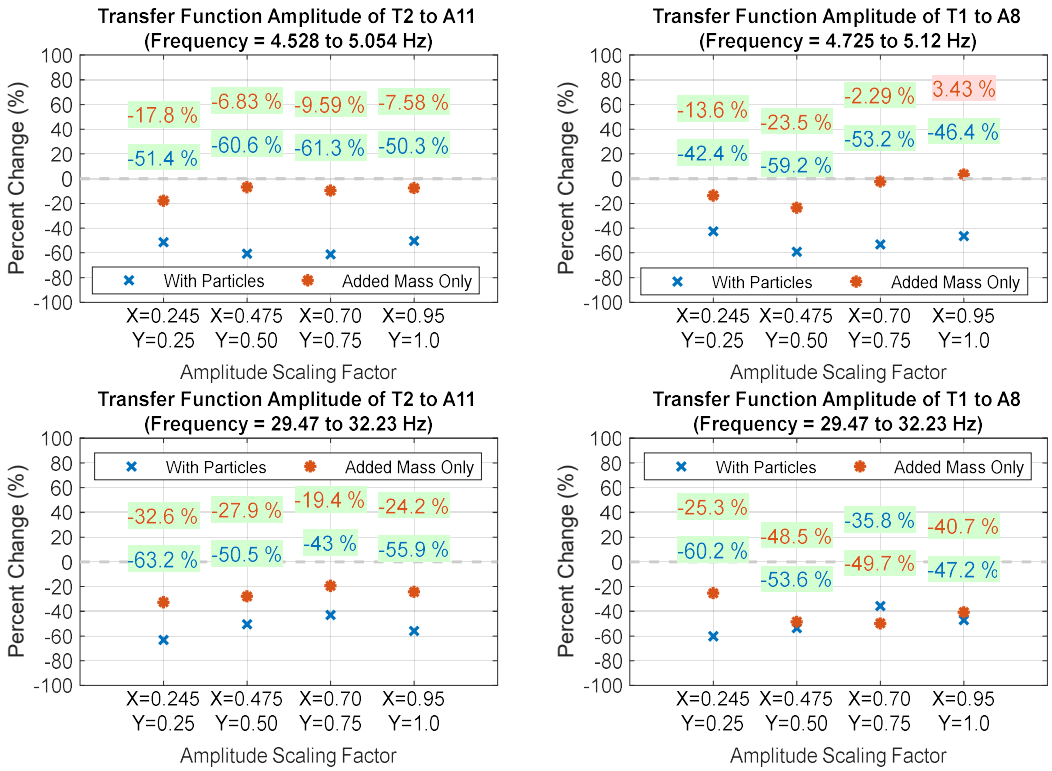


Figure B-9. Percent change in transfer function amplitude response of the +X and +Y sensor at first bending mode and second bending/top breathing modes under varying excitation amplitudes applied simultaneously along the +X and +Y axes of the big shake table. Values are normalized to the corresponding no-particle configuration.

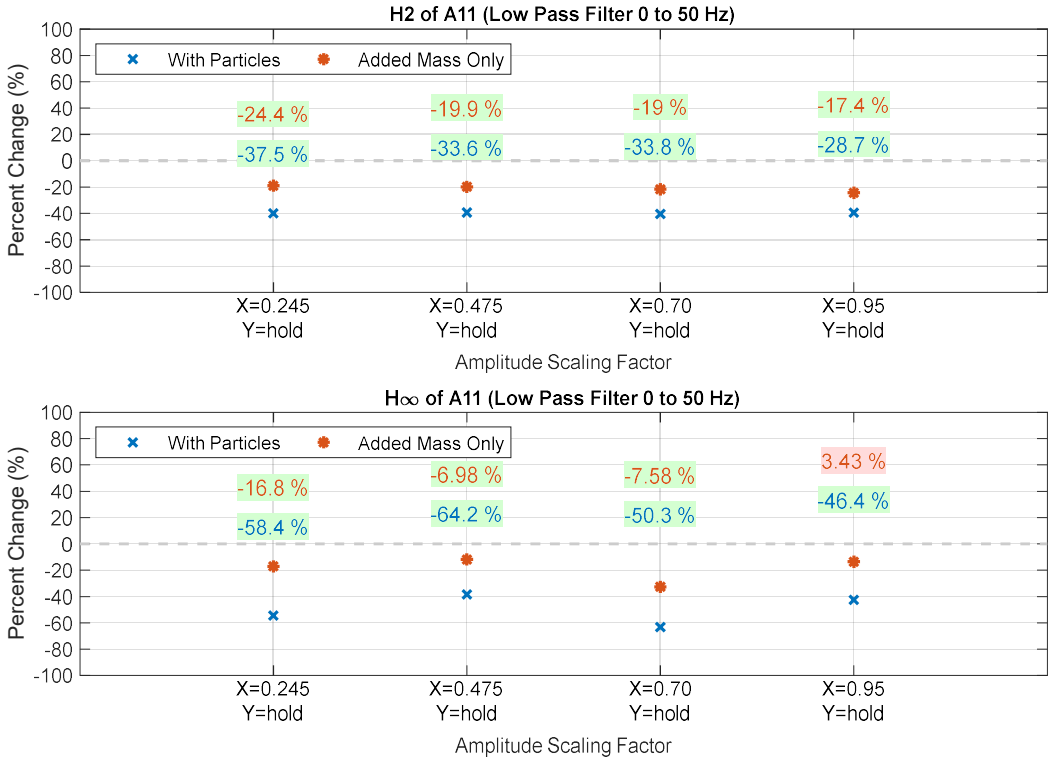


Figure B-10. Percent change in frequency domain response metrics (H2 and H∞) of the +X sensor under varying excitation amplitudes applied in the +X axis of the big shake table. Values are normalized to the corresponding no-particle configuration.

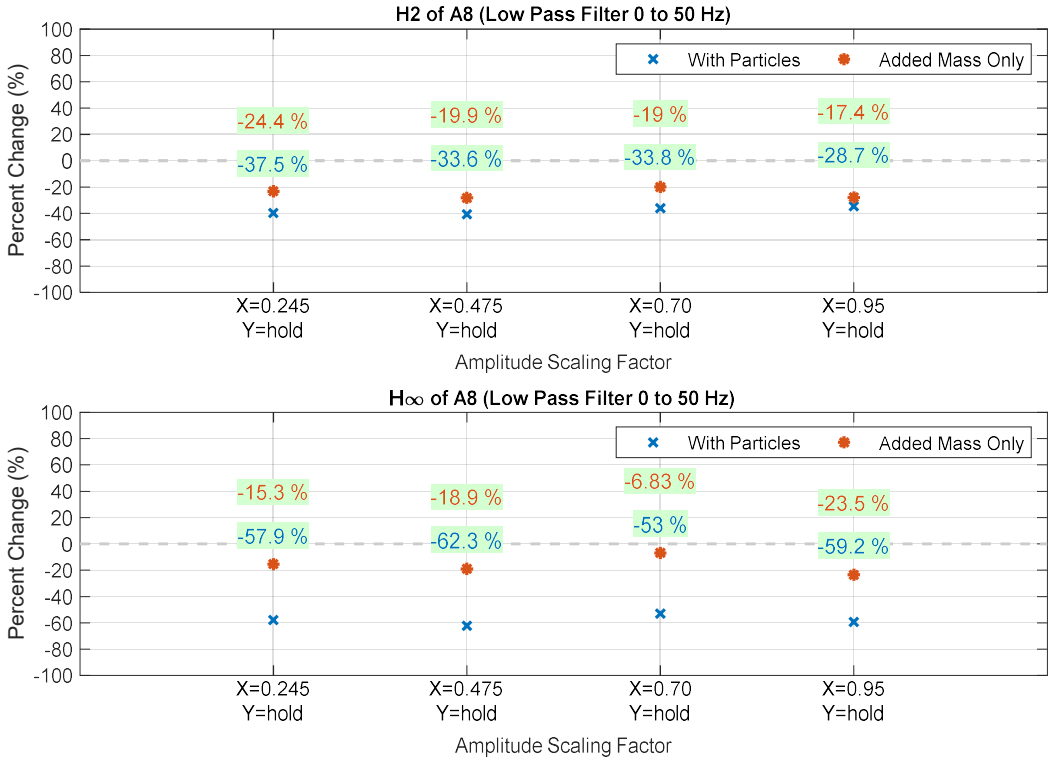


Figure B-11. Percent change in frequency domain response metrics (H2 and H∞) of the +Y sensor under varying excitation amplitudes applied in the +Y axis of the big shake table. Values are normalized to the corresponding no-particle configuration.

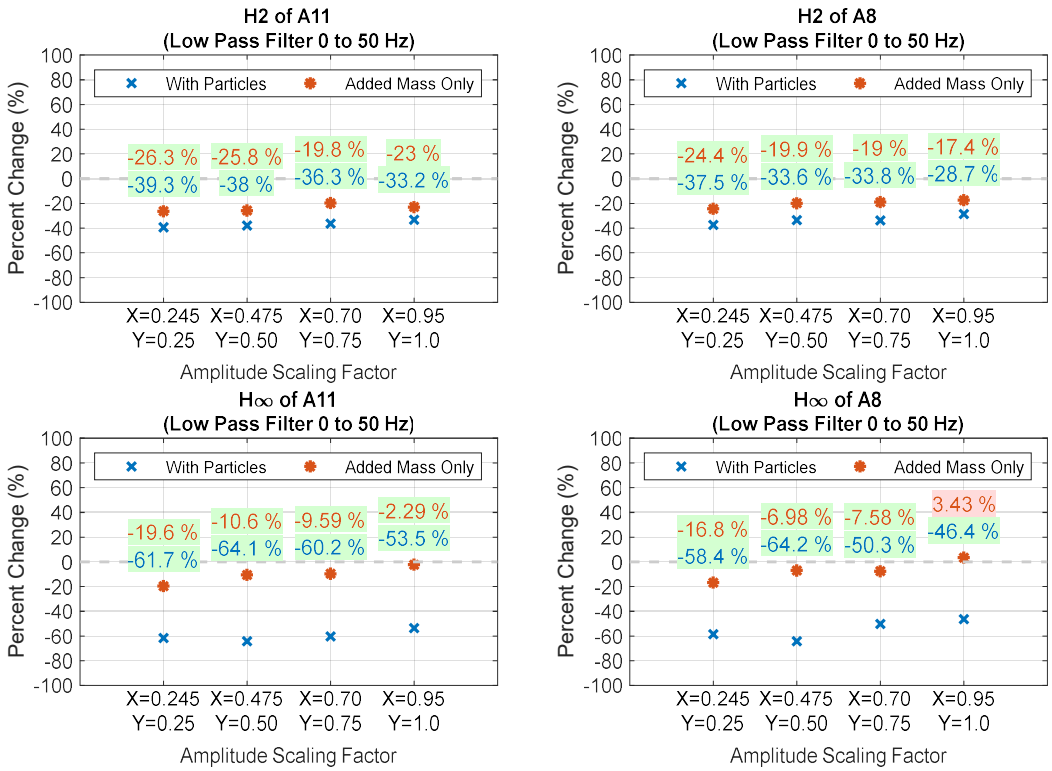


Figure B-12. Percent change in frequency domain response metrics (H2 and H∞) of the +X and +Y sensors under varying excitation amplitudes applied simultaneously in the +X and +Y axes of the big shake table. Values are normalized to the corresponding no-particle configuration.

B.2 Particle Material Type

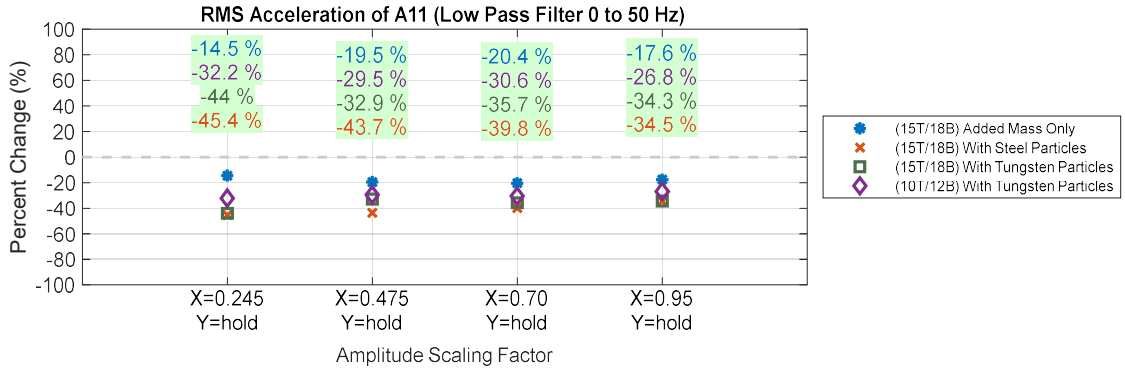


Figure B-13. Percent change in RMS response of the +X sensor, comparing the particle material type under varying excitation amplitudes applied in the +X axis of the big shake table. Particle packing ratios are defined as distinct top (T) and bottom (B) layers. Values are normalized to the corresponding no-particle configuration.

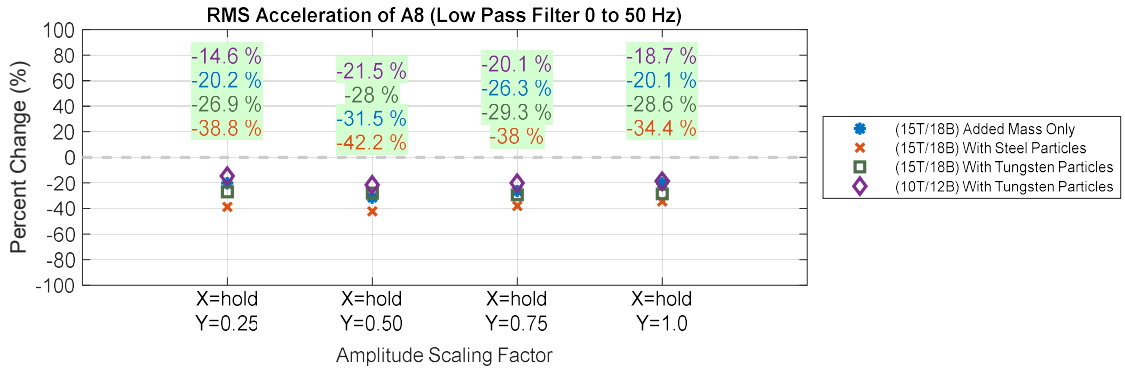


Figure B-14. Percent change in RMS response of the +Y sensor, comparing the particle material type under varying excitation amplitudes applied in the +Y axis of the big shake table. Particle packing ratios are defined as distinct top (T) and bottom (B) layers. Values are normalized to the corresponding no-particle configuration.

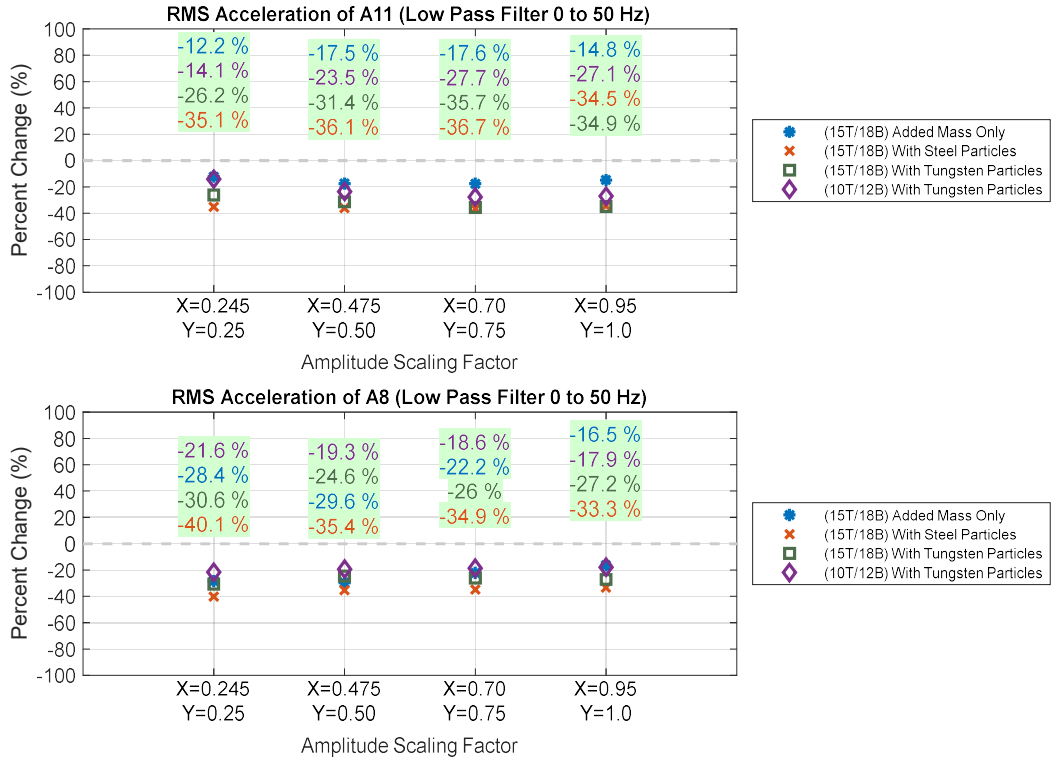


Figure B-15. Percent change in RMS response of the +X and +Y sensors, comparing the particle material type under varying excitation amplitudes applied simultaneously in the +X and +Y axes of the big shake table. Particle packing ratios are defined as distinct top (T) and bottom (B) layers. Values are normalized to the corresponding no-particle configuration.

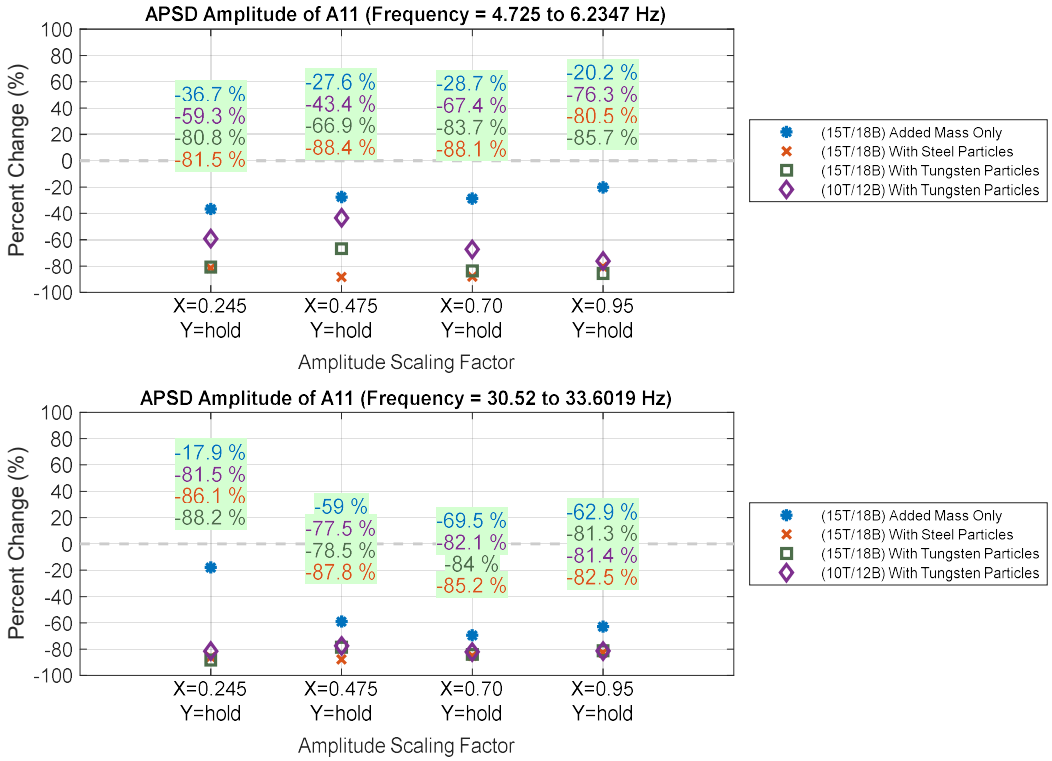


Figure B-16. Percent change in APSD amplitude response of the +X sensor at first bending mode and second bending/top breathing modes, comparing particle material type under varying excitation amplitudes applied in the +X axis of the big shake table. Particle packing ratios are defined as distinct top (T) and bottom (B) layers. Values are normalized to the corresponding no-particle configuration.

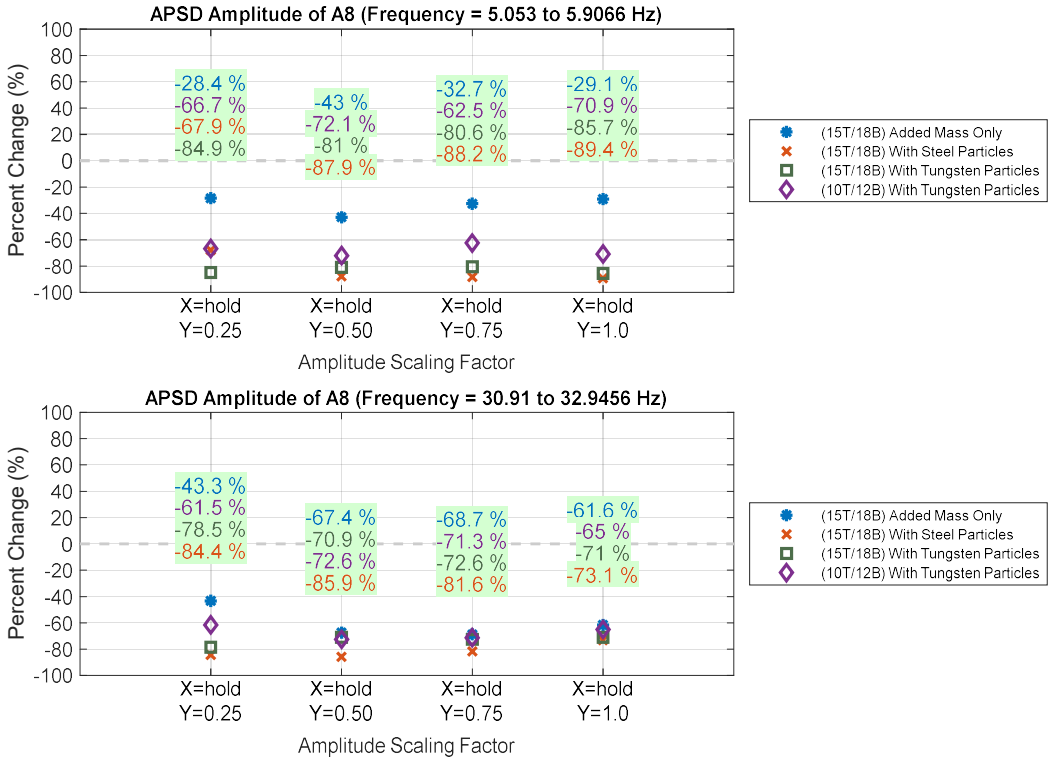


Figure B-17. Percent change in APSD amplitude response of the +Y sensor at first bending mode and second bending/top breathing modes, comparing particle material type under varying excitation amplitudes applied in the +Y axis of the big shake table. Particle packing ratios are defined as distinct top (T) and bottom (B) layers. Values are normalized to the corresponding no-particle configuration.

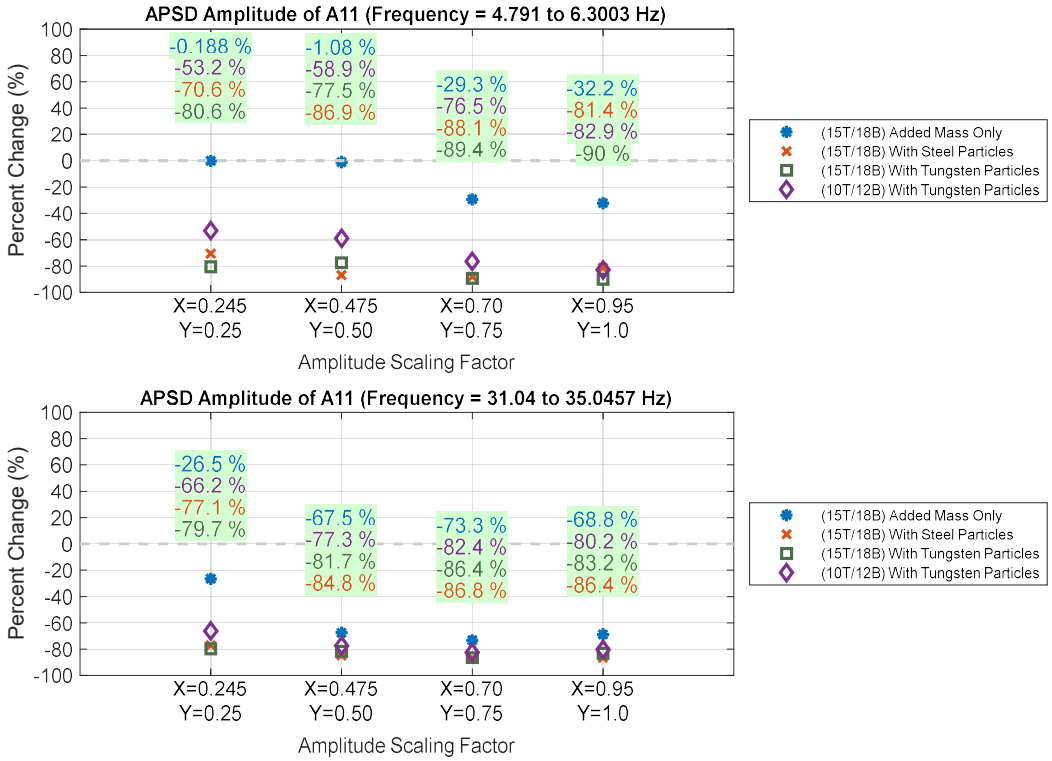


Figure B-18. Percent change in APSD amplitude response of the +X sensor at first bending mode and second bending/top breathing modes, comparing particle material type under varying excitation amplitudes applied simultaneously in the +X and +Y axes of the big shake table. Particle packing ratios are defined as distinct top (T) and bottom (B) layers. Values are normalized to the corresponding no-particle configuration.

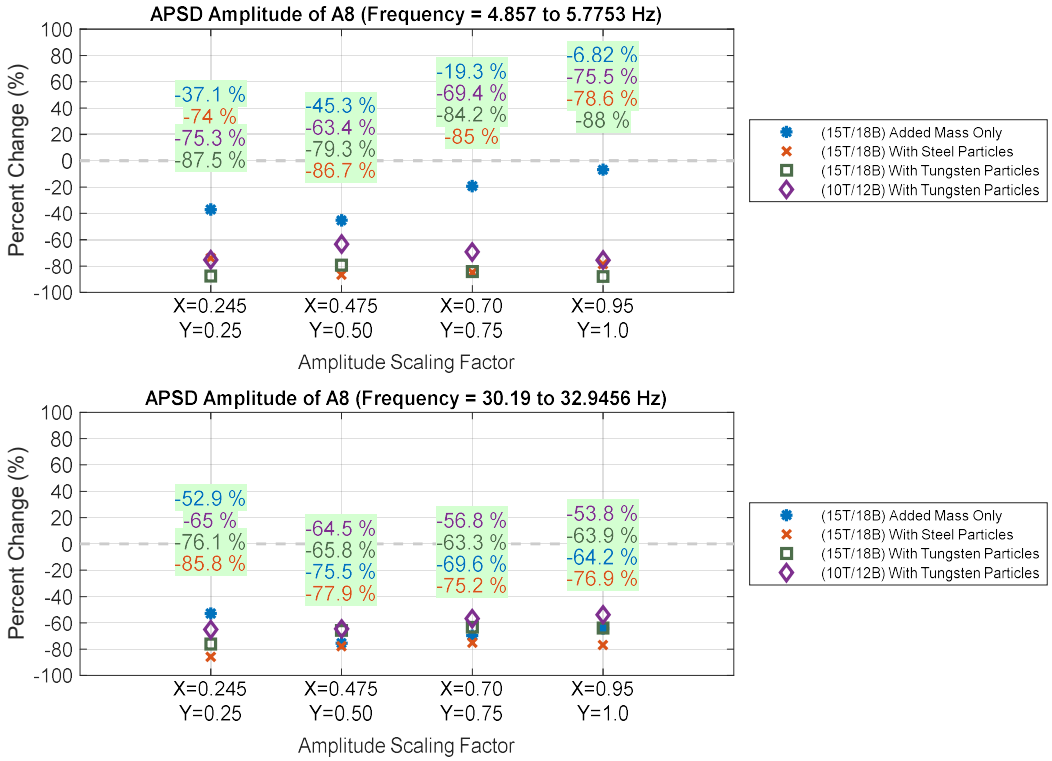


Figure B-19. Percent change in APSD amplitude response of the +Y sensor at first bending mode and second bending/top breathing modes, comparing particle material type under varying excitation amplitudes applied simultaneously in the +X and +Y axes of the big shake table. Particle packing ratios are defined as distinct top (T) and bottom (B) layers. Values are normalized to the corresponding no-particle configuration.

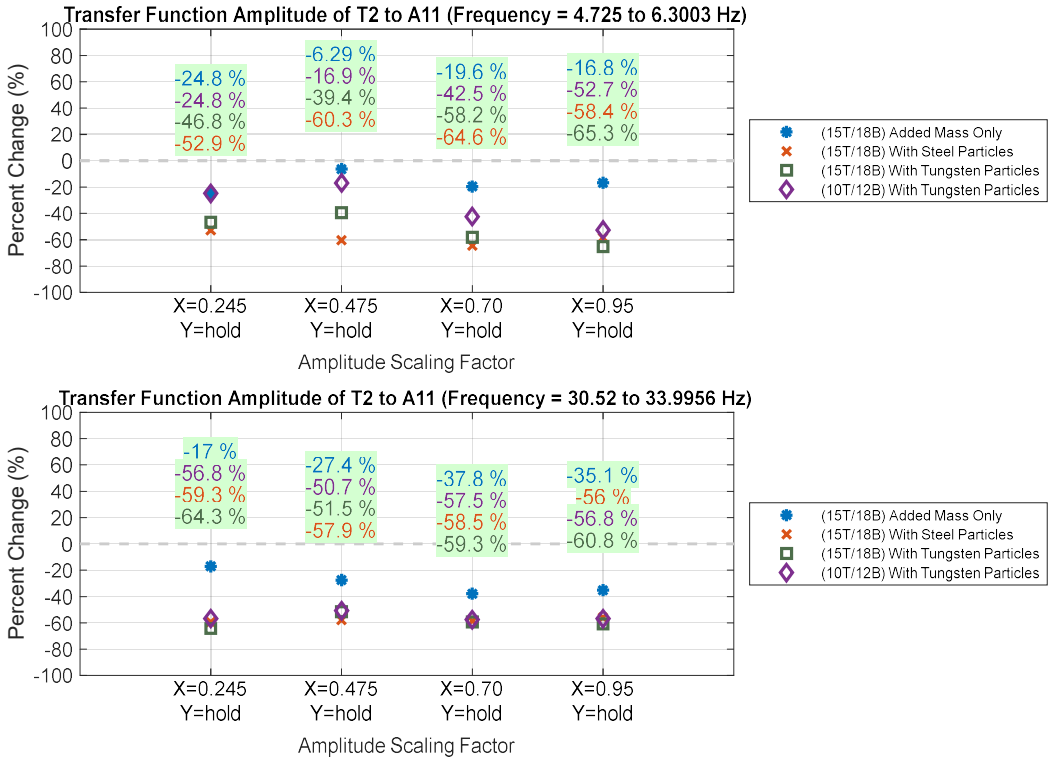


Figure B-20. Percent change in transfer function amplitude response of the +X sensor at first bending mode and second bending/top breathing modes, comparing particle material type under varying excitation amplitudes applied in the +X axis of the big shake table. Particle packing ratios are defined as distinct top (T) and bottom (B) layers. Values are normalized to the corresponding no-particle configuration.

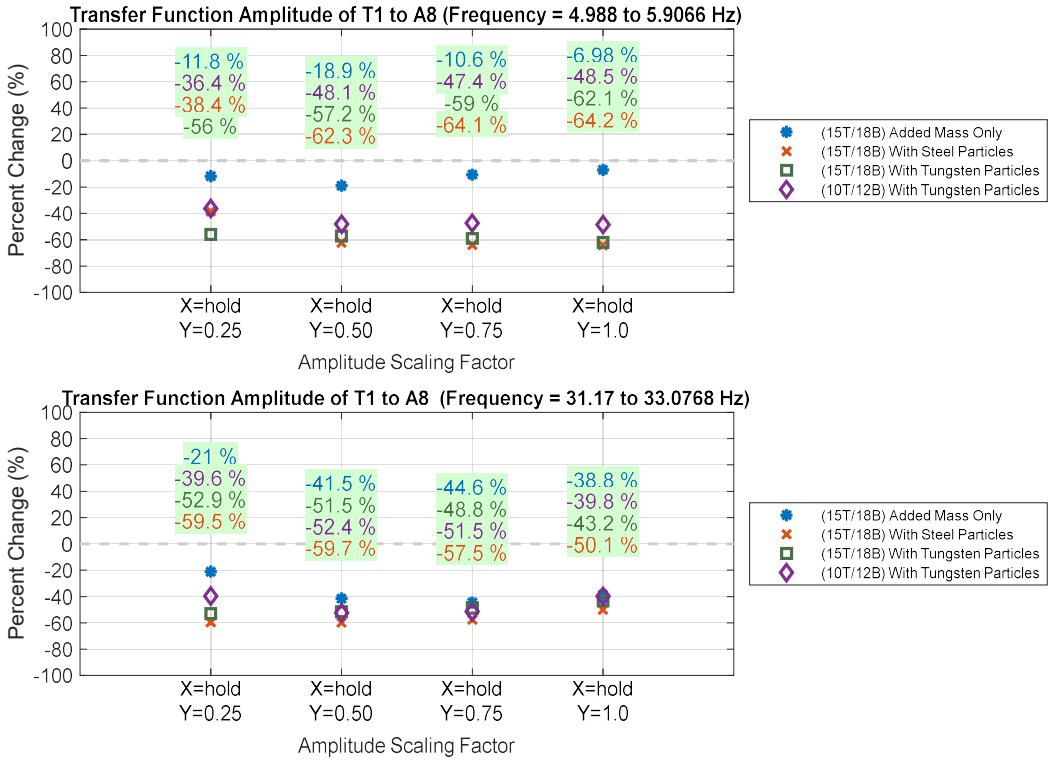


Figure B-21. Percent change in transfer function amplitude response of the +Y sensor at first bending mode and second bending/top breathing modes, comparing particle material type under varying excitation amplitudes applied in the +Y axis of the big shake table. Particle packing ratios are defined as distinct top (T) and bottom (B) layers. Values are normalized to the corresponding no-particle configuration.

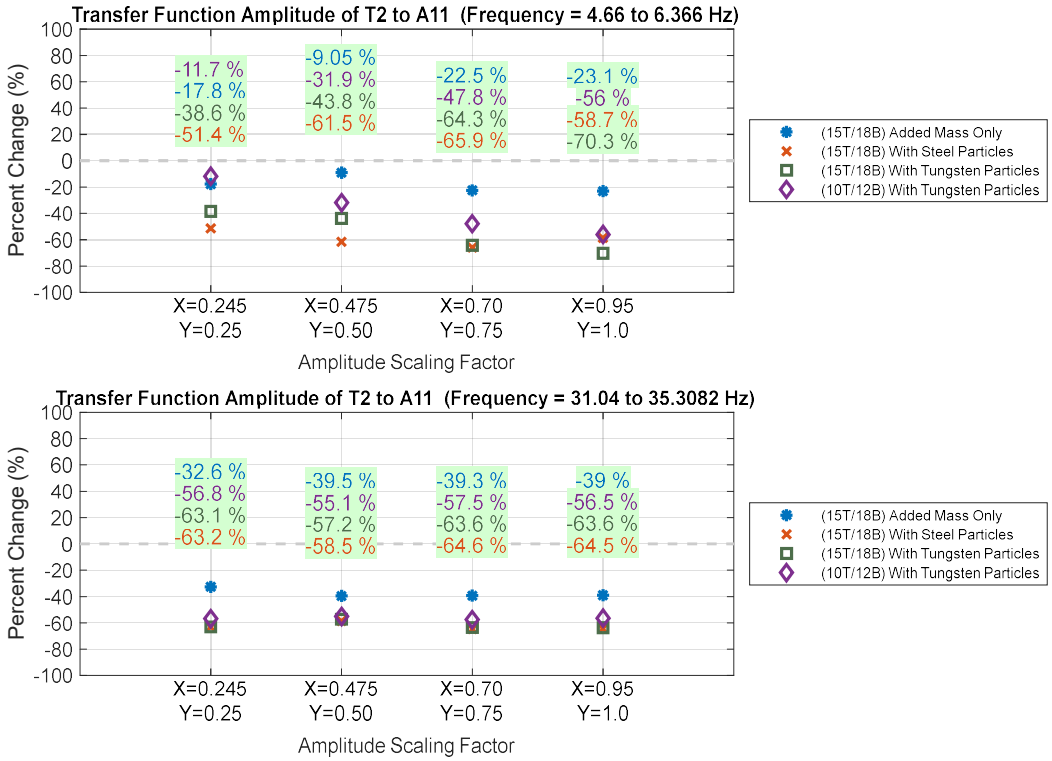


Figure B-22. Percent change in transfer function amplitude response of the +X sensor at first bending mode and second bending/top breathing modes, comparing particle material type under varying excitation amplitudes applied simultaneously in the +X and +Y axes of the big shake table. Particle packing ratios are defined as distinct top (T) and bottom (B) layers. Values are normalized to the corresponding no-particle configuration.

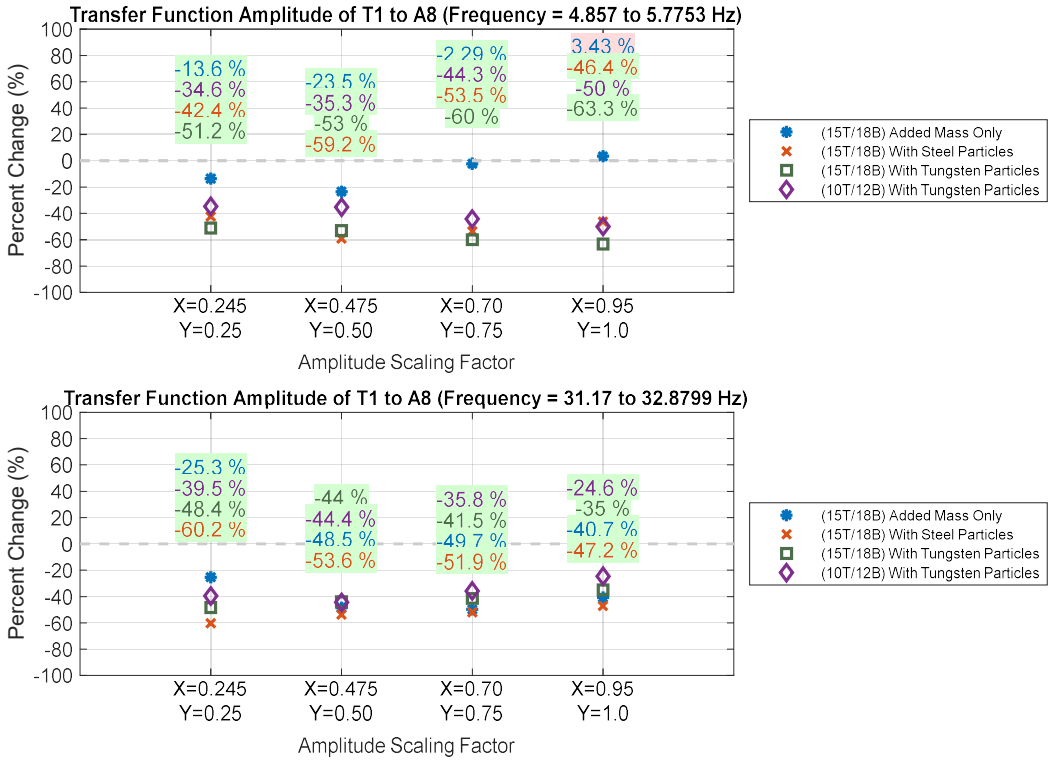


Figure B-23. Percent change in transfer function amplitude response of the +Y sensor at first bending mode and second bending/top breathing modes, comparing particle material type under varying excitation amplitudes applied simultaneously in the +X and +Y axes of the big shake table. Particle packing ratios are defined as distinct top (T) and bottom (B) layers. Values are normalized to the corresponding no-particle configuration.

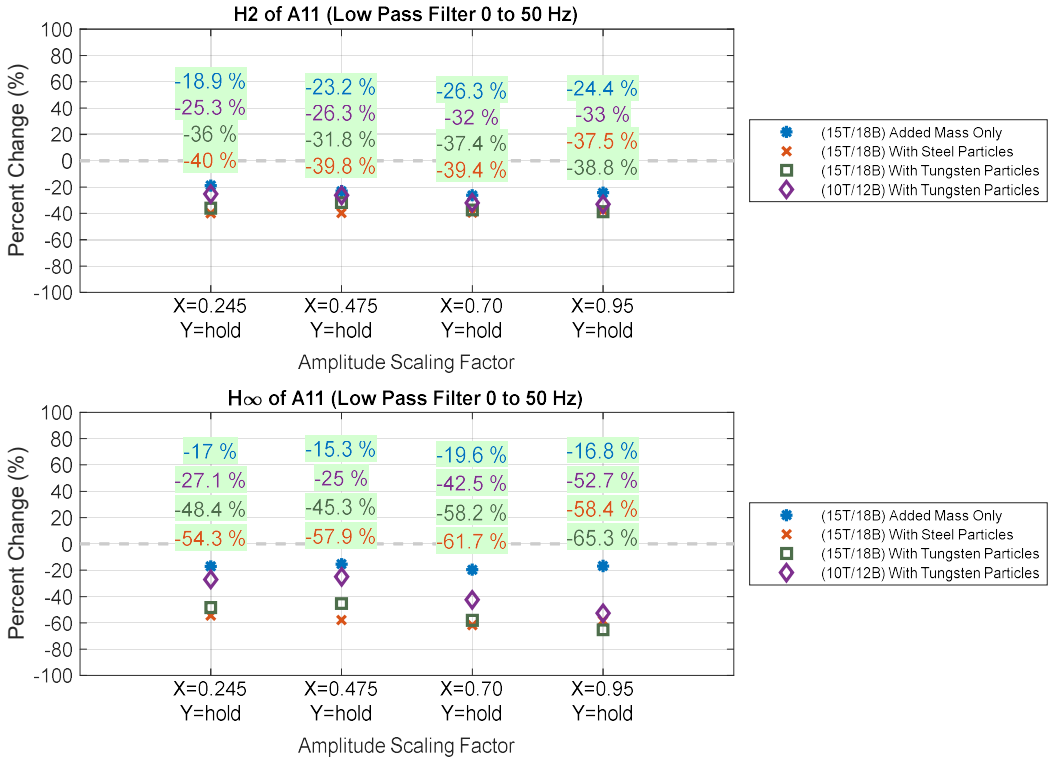


Figure B-24. Percent change in frequency domain response metrics (H2 and H∞) of the +X sensor, comparing particle material type under varying excitation amplitudes applied in the +X axis of the big shake table. Particle packing ratios are defined as distinct top (T) and bottom (B) layers. Values are normalized to the corresponding no-particle configuration.



Figure B-25. Percent change in frequency domain response metrics (H2 and H∞) of the +Y sensor, comparing particle material type under varying excitation amplitudes applied in the +Y axis of the big shake table. Particle packing ratios are defined as distinct top (T) and bottom (B) layers. Values are normalized to the corresponding no-particle configuration.

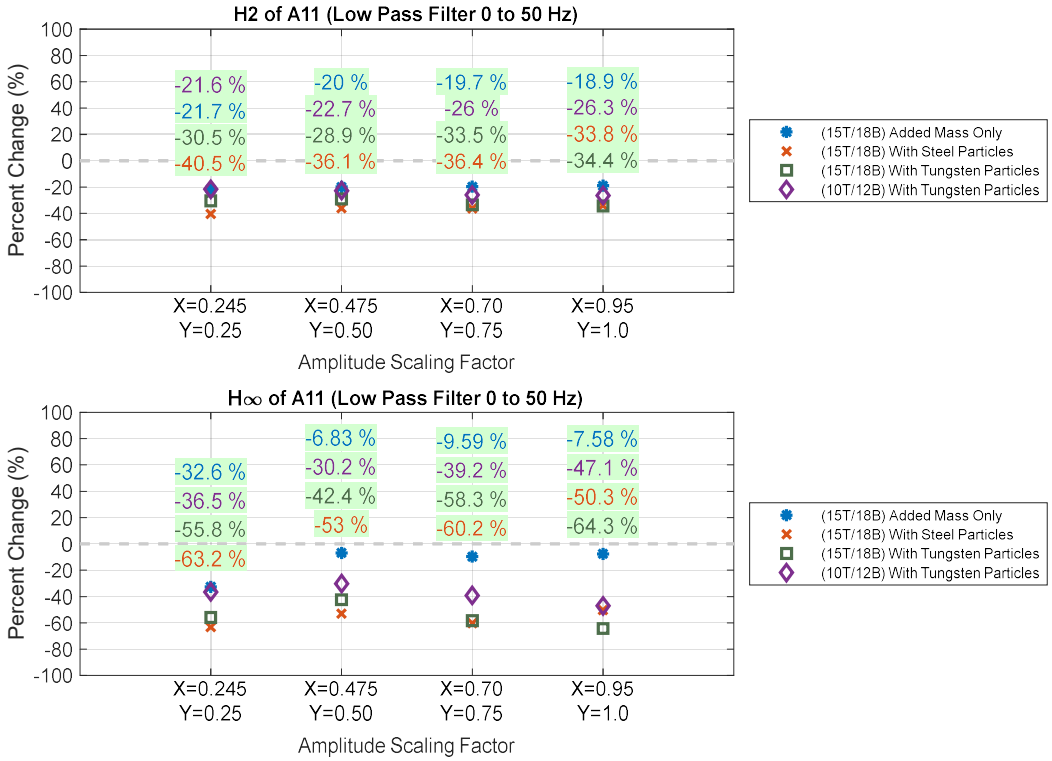


Figure B-26. Percent change in frequency domain response metrics (H2 and H∞) of the +X sensor, comparing particle material type under varying excitation amplitudes applied simultaneously in the +X and +Y axes of the big shake table. Particle packing ratios are defined as distinct top (T) and bottom (B) layers. Values are normalized to the corresponding no-particle configuration.

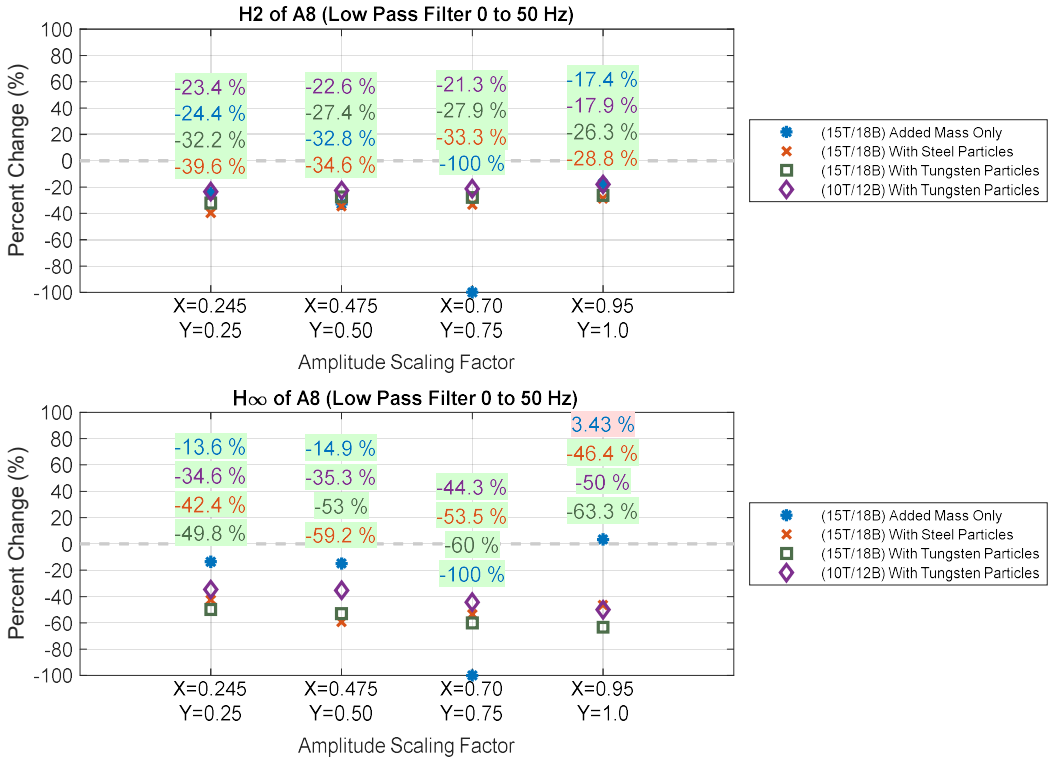


Figure B-27. Percent change in frequency domain response metrics (H2 and H∞) of the +Y sensor, comparing particle material type under varying excitation amplitudes applied simultaneously in the +X and +Y axes of the big shake table. Particle packing ratios are defined as distinct top (T) and bottom (B) layers. Values are normalized to the corresponding no-particle configuration.

B.3 Multi-Directional Container Usage



Figure B-28. Percent change in RMS response of the +X sensor, comparing ring particle damper container usages under varying excitation amplitudes applied in the +X axis of the big shake table. Values are normalized to the corresponding no-particle configuration.



Figure B-29. Percent change in RMS response of the +Y sensor, comparing ring particle damper container usages under varying excitation amplitudes applied in the +Y axis of the big shake table. Values are normalized to the corresponding no-particle configuration.



Figure B-30. Percent change in RMS response of the +X sensor, comparing ring particle damper container usages under varying excitation amplitudes simultaneously applied in the +X and +Y axes of the big shake table. Values are normalized to the corresponding no-particle configuration.



Figure B-31. Percent change in RMS response of the +Y sensor, comparing ring particle damper container usages under varying excitation amplitudes simultaneously applied in the +X and +Y axes of the big shake table. Values are normalized to the corresponding no-particle configuration.

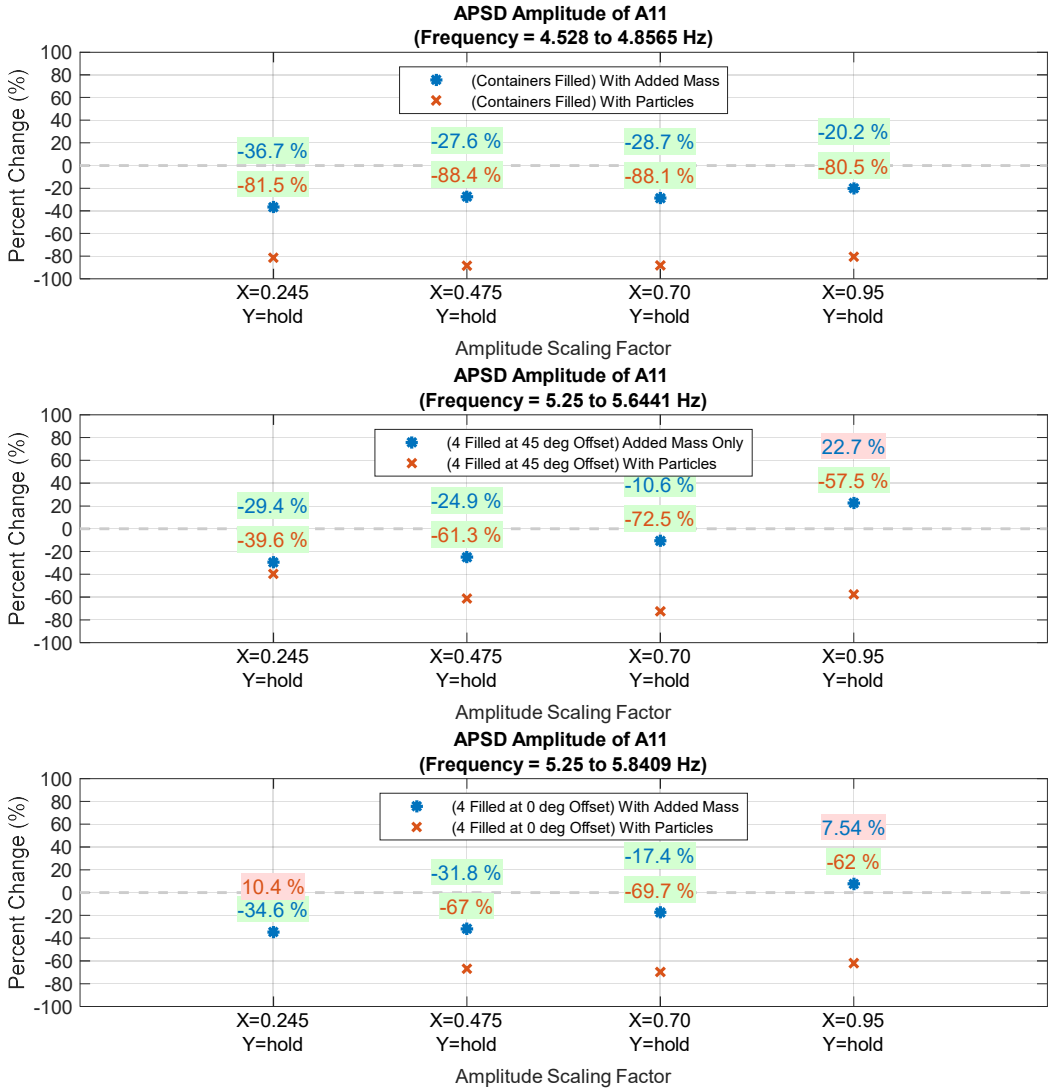


Figure B-32. Percent change in APSD amplitude response of the +X sensor at the first bending mode, comparing ring particle damper container usages under varying excitation amplitudes applied in the +X axis of the big shake table. Values are normalized to the corresponding no-particle configuration.

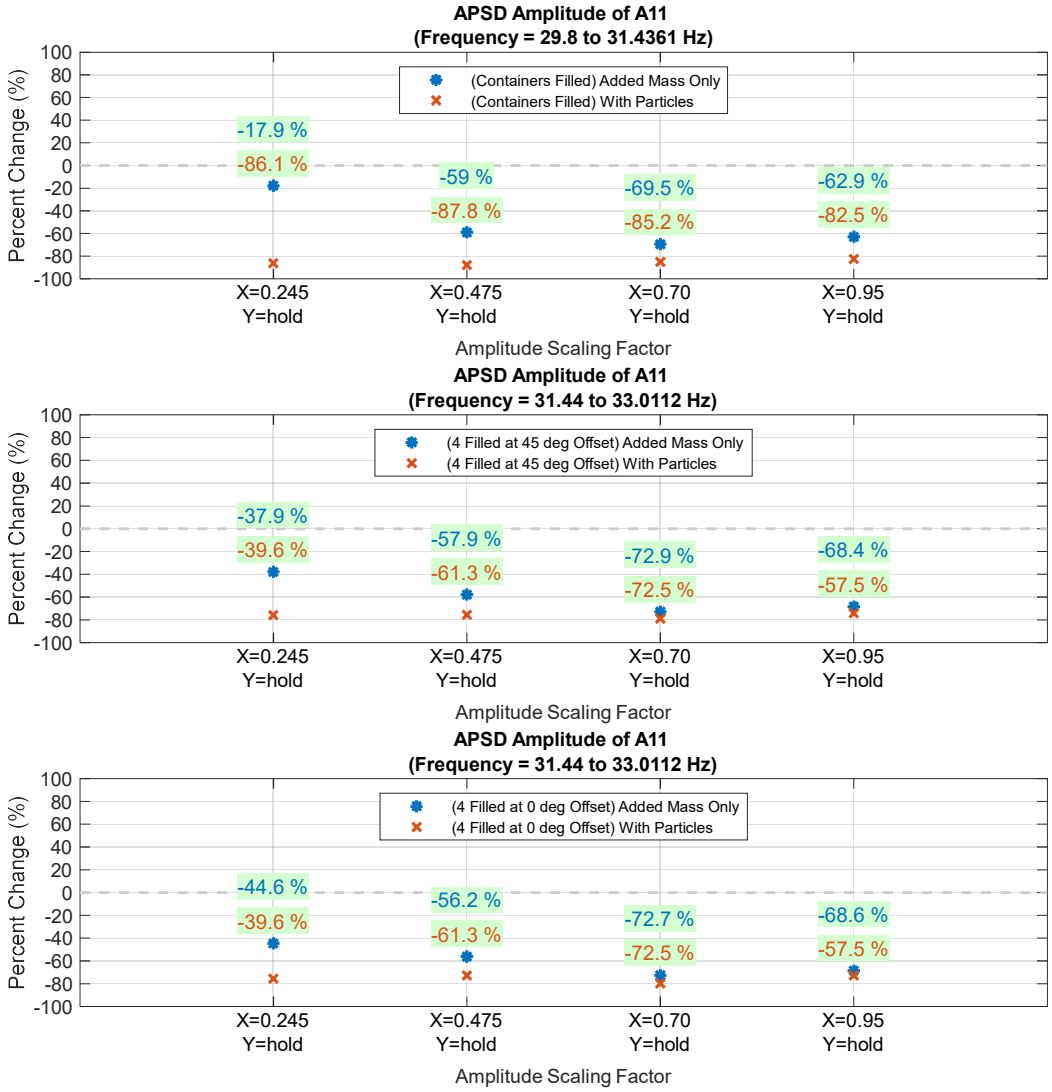


Figure B-33. Percent change in APSD amplitude response of the +X sensor at the second bending/top breathing mode, comparing ring particle damper container usages under varying excitation amplitudes applied in the +X axis of the big shake table. Values are normalized to the corresponding no-particle configuration.

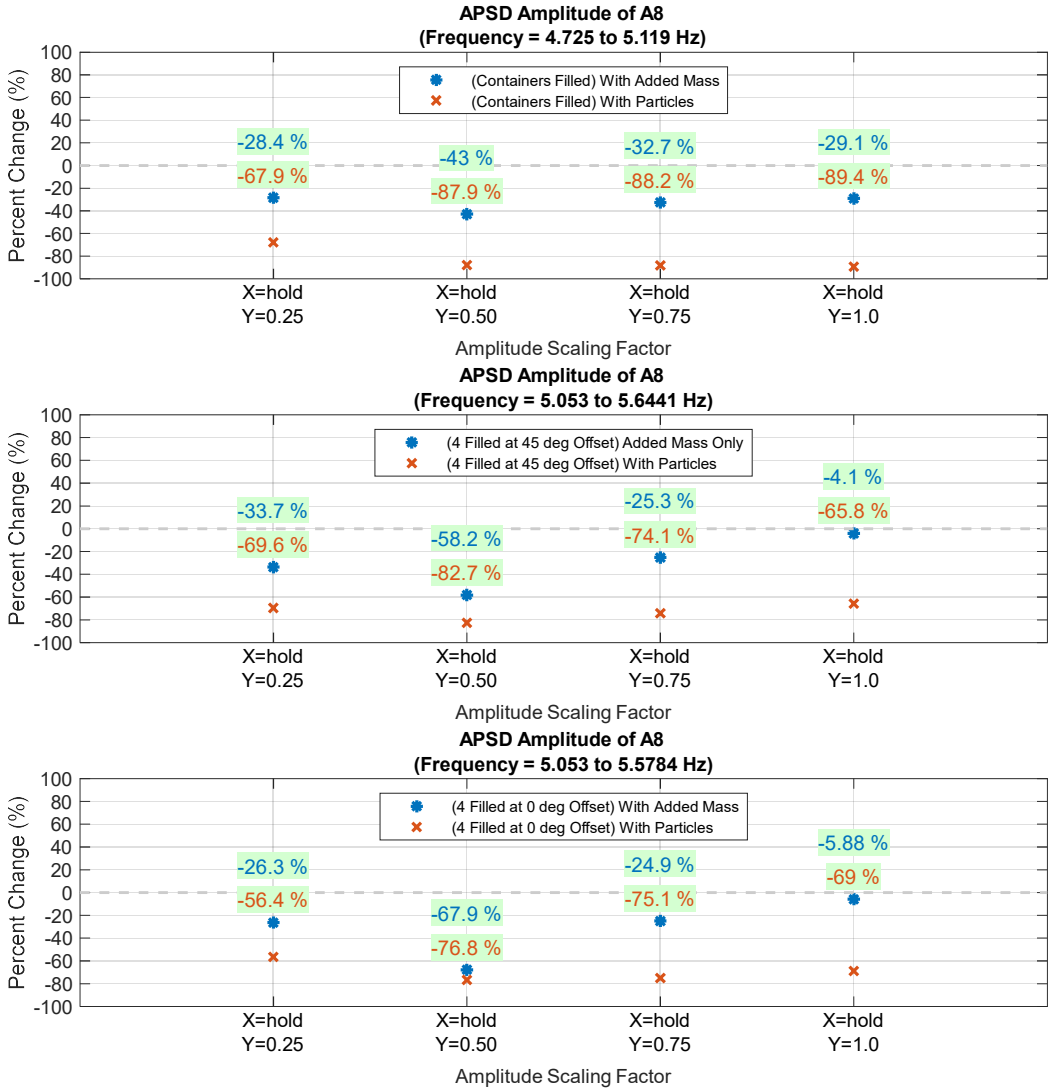


Figure B-34. Percent change in APSD amplitude response of the +Y sensor at the first bending mode, comparing ring particle damper container usages under varying excitation amplitudes applied in the +Y axis of the big shake table. Values are normalized to the corresponding no-particle configuration.

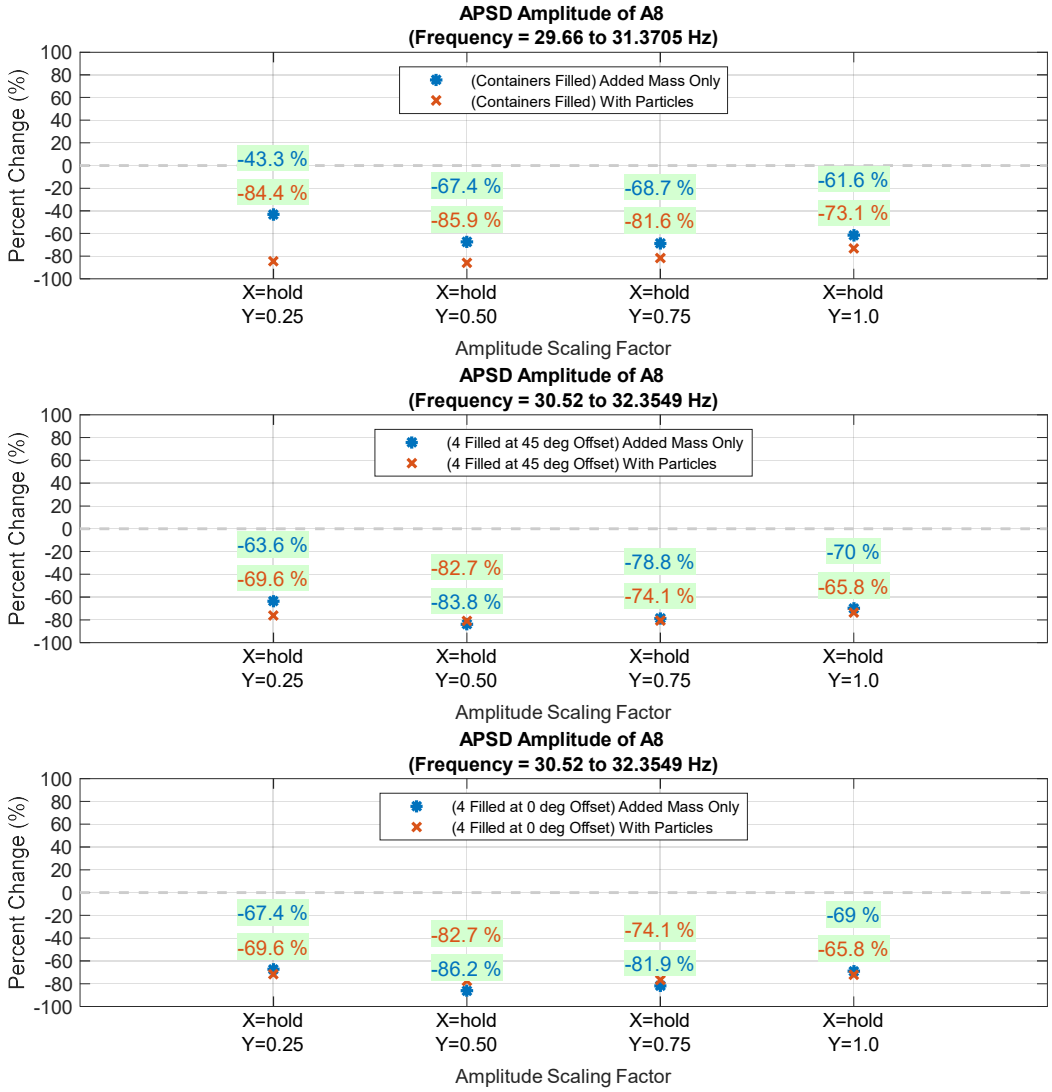


Figure B-35. Percent change in APSD amplitude response of the +Y sensor at the second bending/top breathing mode, comparing ring particle damper container usages under varying excitation amplitudes applied in the +Y axis of the big shake table. Values are normalized to the corresponding no-particle configuration.

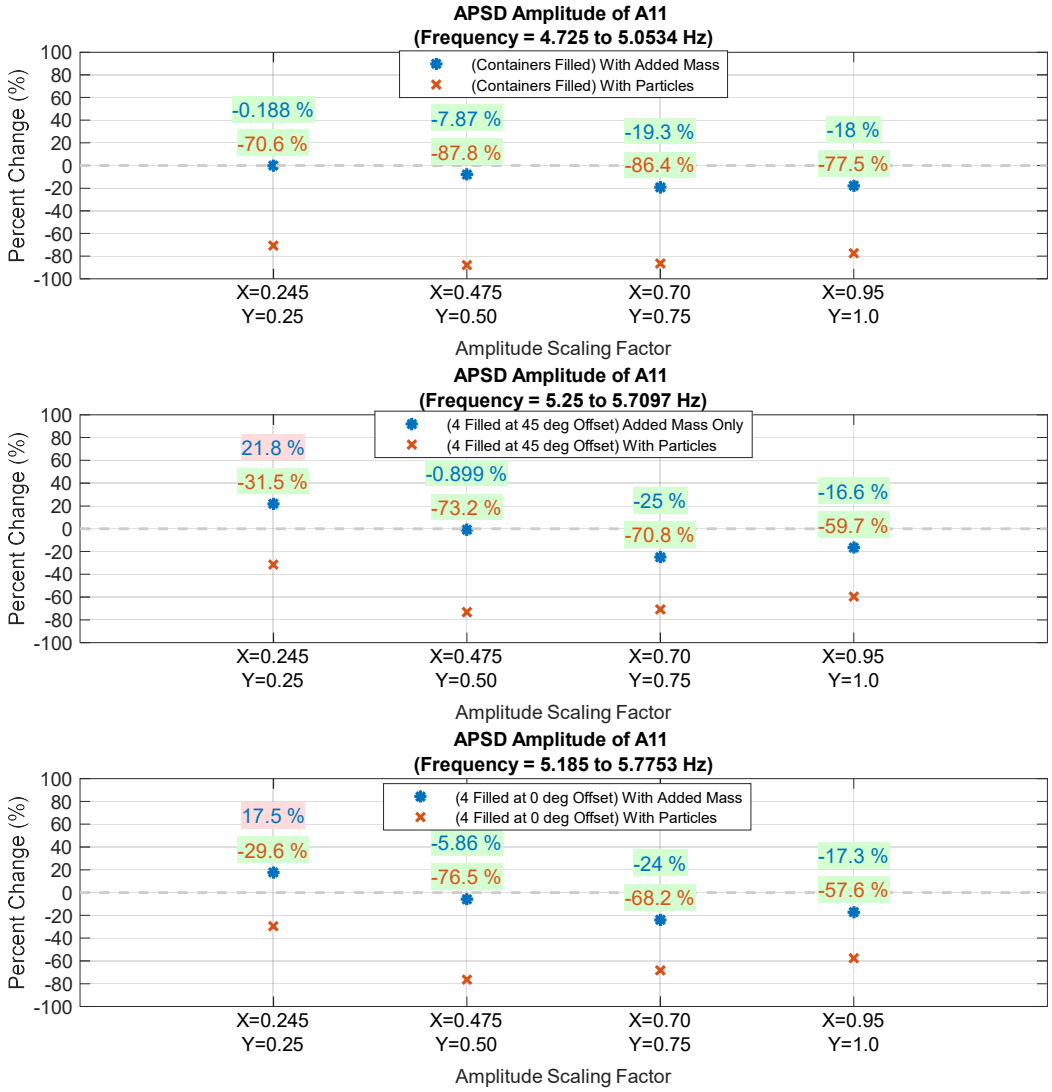


Figure B-36. Percent change in APSD amplitude response of the +X sensor at the first bending mode, comparing ring particle damper container usages under varying excitation amplitudes applied simultaneously in the +X and +Y axes of the big shake table. Values are normalized to the corresponding no-particle configuration.

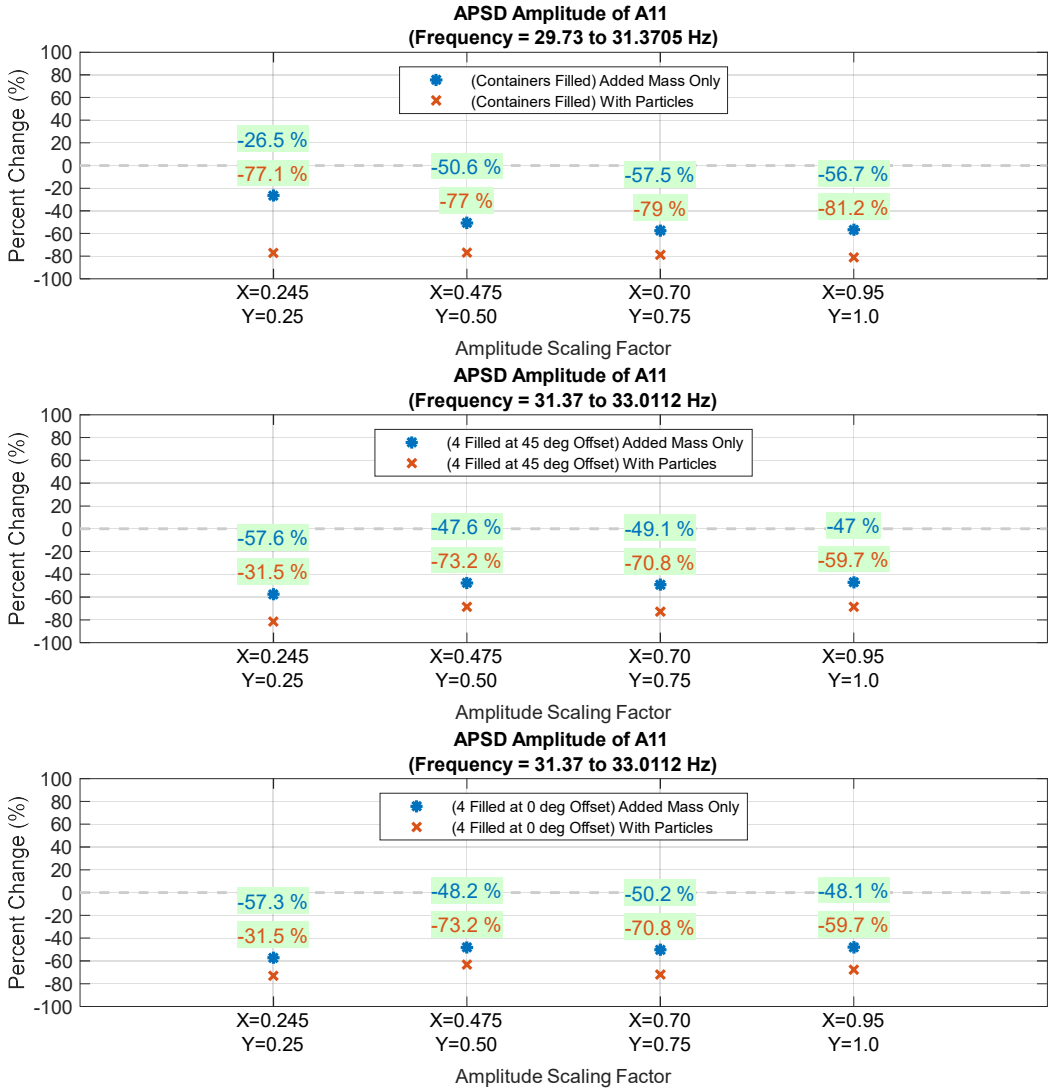


Figure B-37. Percent change in APSD amplitude response of the +X sensor at the second bending/top breathing mode, comparing ring particle damper container usages under varying excitation amplitudes applied simultaneously in the +X and +Y axes of the big shake table. Values are normalized to the corresponding no-particle configuration.

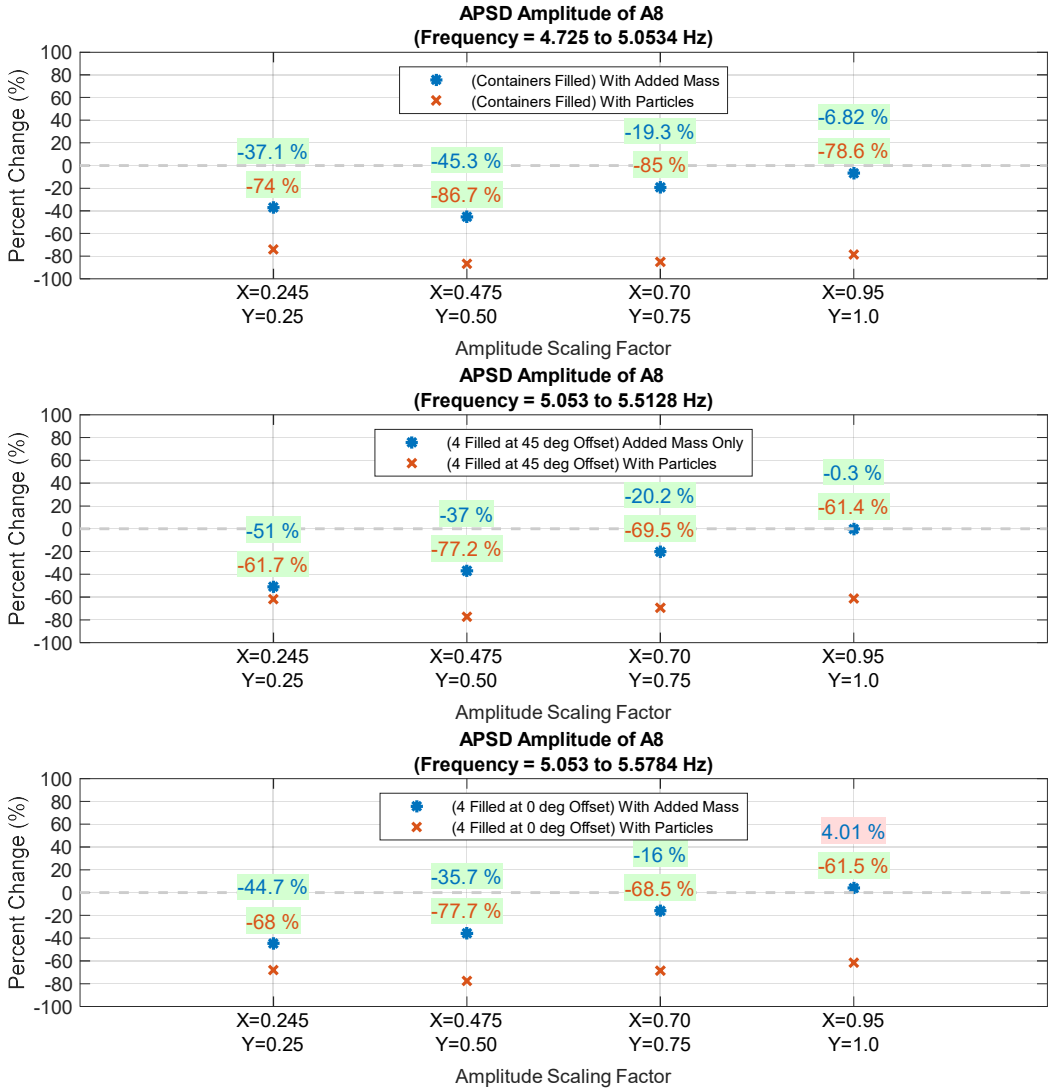


Figure B-38. Percent change in APSD amplitude response of the +Y sensor at the first bending mode, comparing ring particle damper container usages under varying excitation amplitudes applied simultaneously in the +X and +Y axes of the big shake table. Values are normalized to the corresponding no-particle configuration.



Figure B-39. Percent change in APSD amplitude response of the +Y sensor at the second bending/ top breathing mode, comparing ring particle damper container usages under varying excitation amplitudes applied simultaneously in the +X and +Y axes of the big shake table. Values are normalized to the corresponding no-particle configuration.

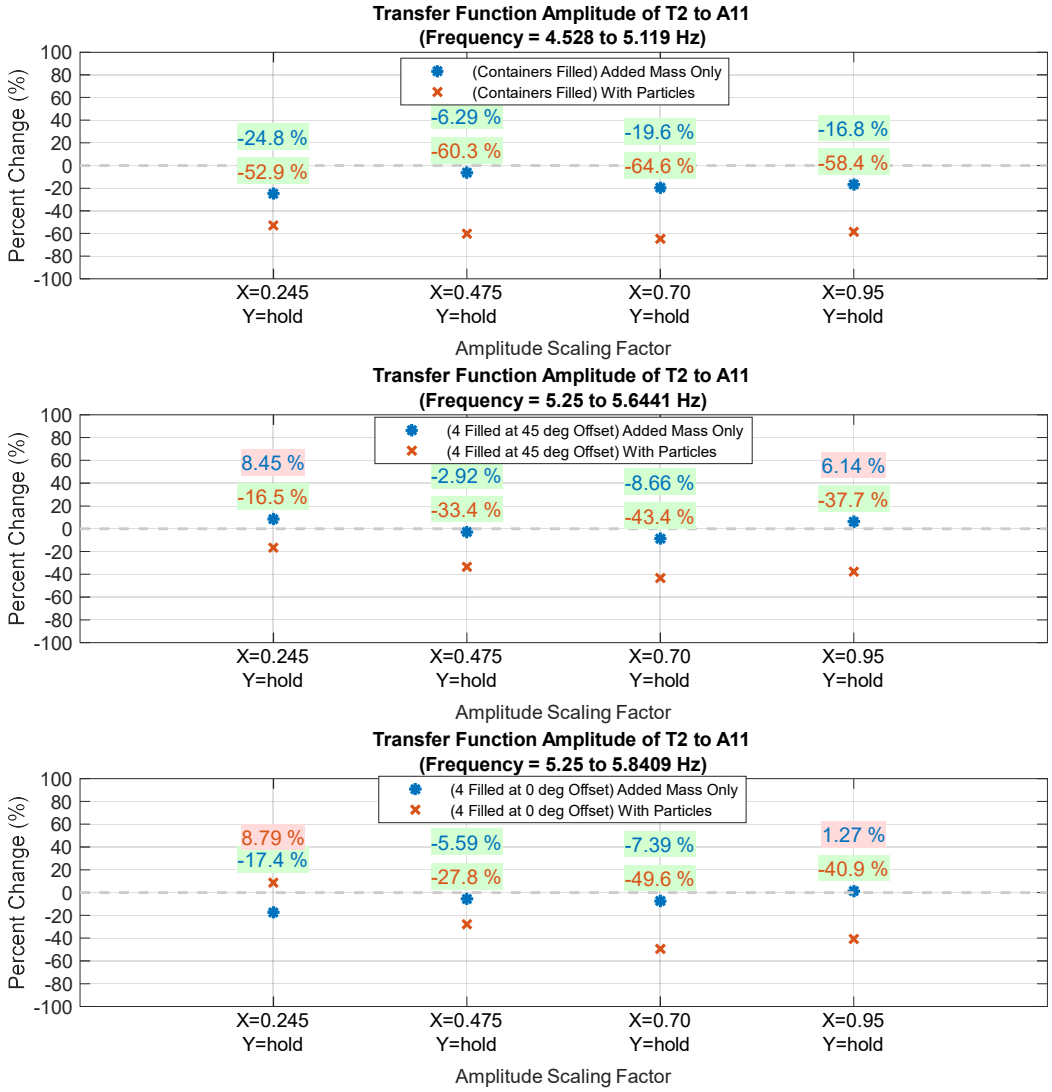


Figure B-40. Percent change in transfer function amplitude response of the +X sensor at the first bending mode, comparing ring particle damper container usages under varying excitation amplitudes applied in the +X axis of the big shake table. Values are normalized to the corresponding no-particle configuration.

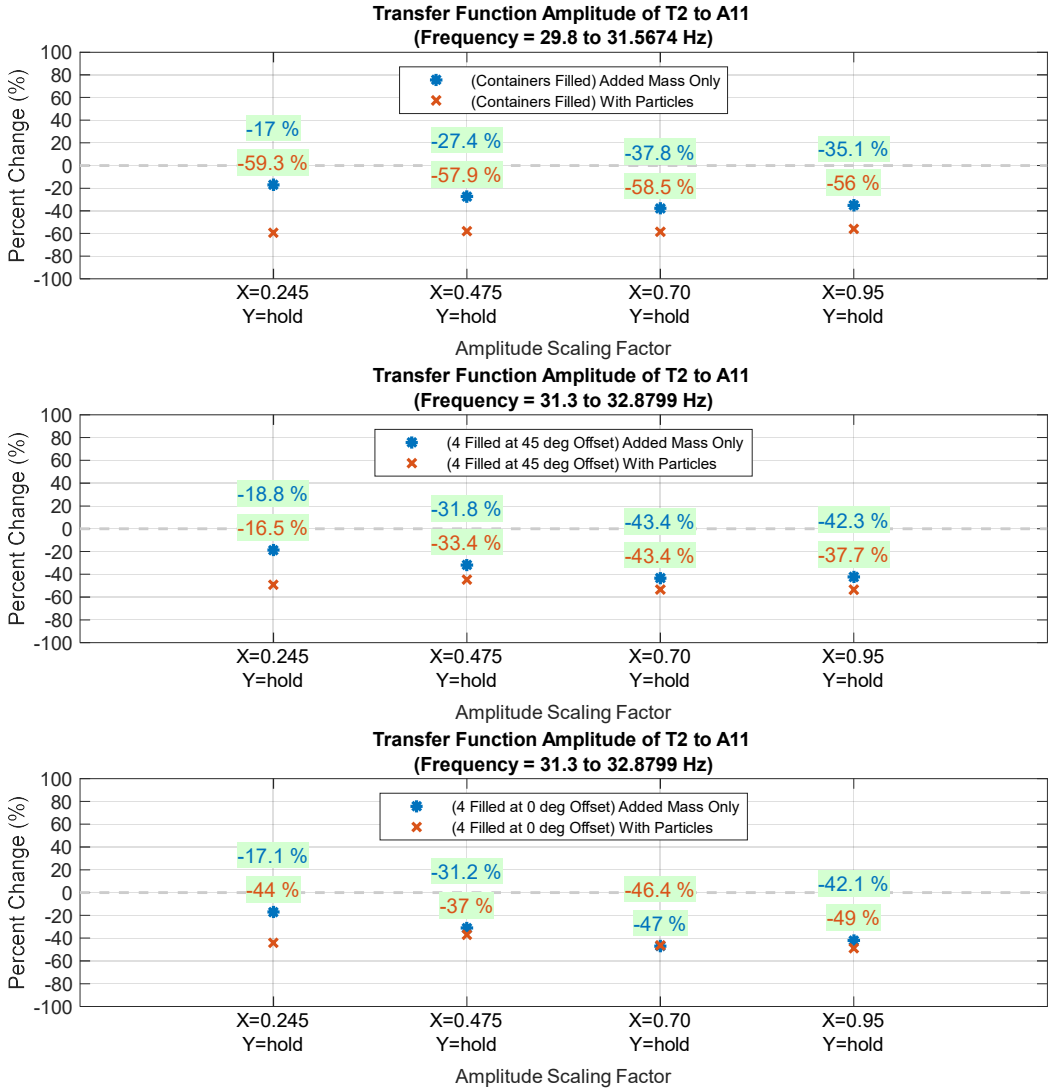


Figure B-41. Percent change in transfer function amplitude response of the +X sensor at the second bending/top breathing mode, comparing ring particle damper container usages under varying excitation amplitudes applied in the +X axis of the big shake table. Values are normalized to the corresponding no-particle configuration.

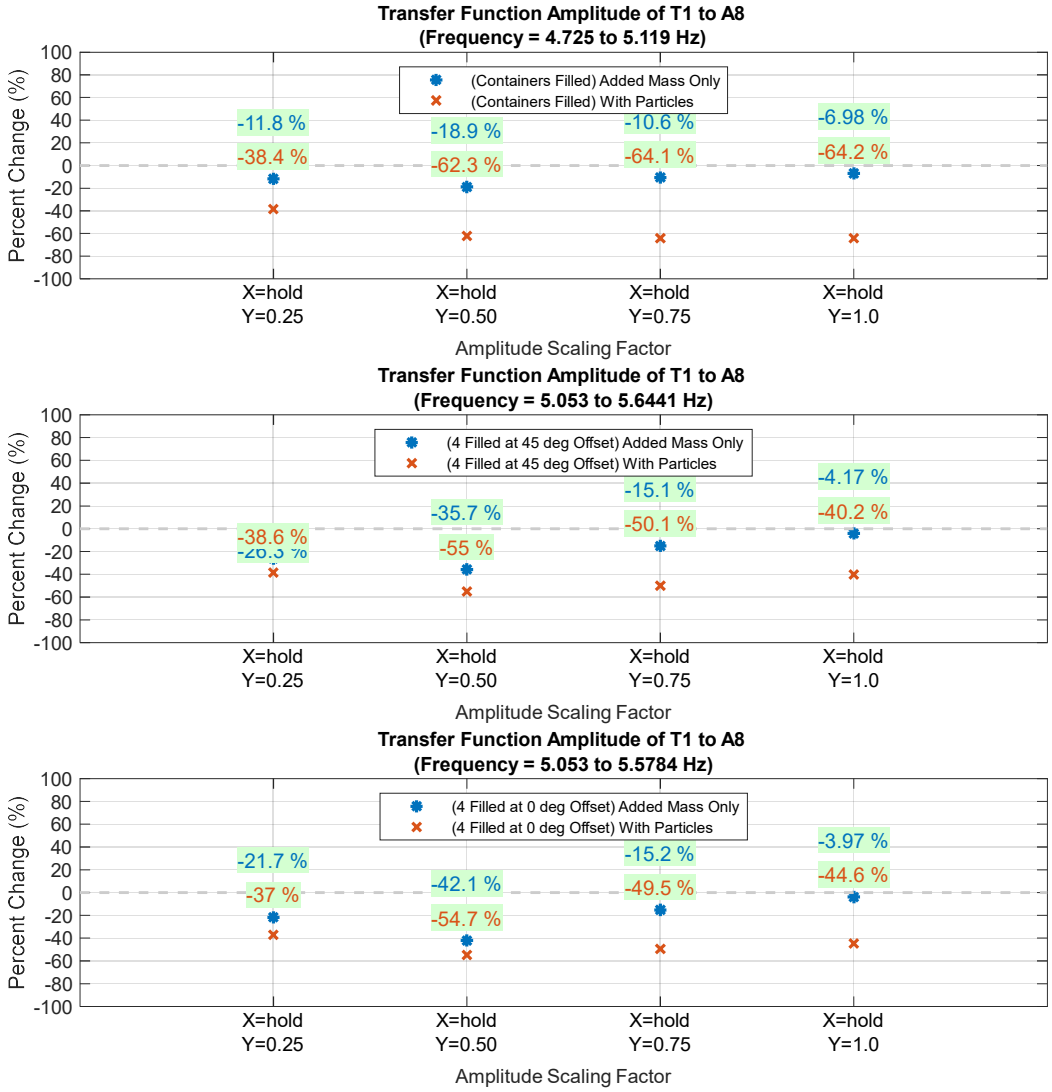


Figure B-42. Percent change in transfer function amplitude response of the +Y sensor at the first bending mode, comparing ring particle damper container usages under varying excitation amplitudes applied in the +Y axis of the big shake table. Values are normalized to the corresponding no-particle configuration.

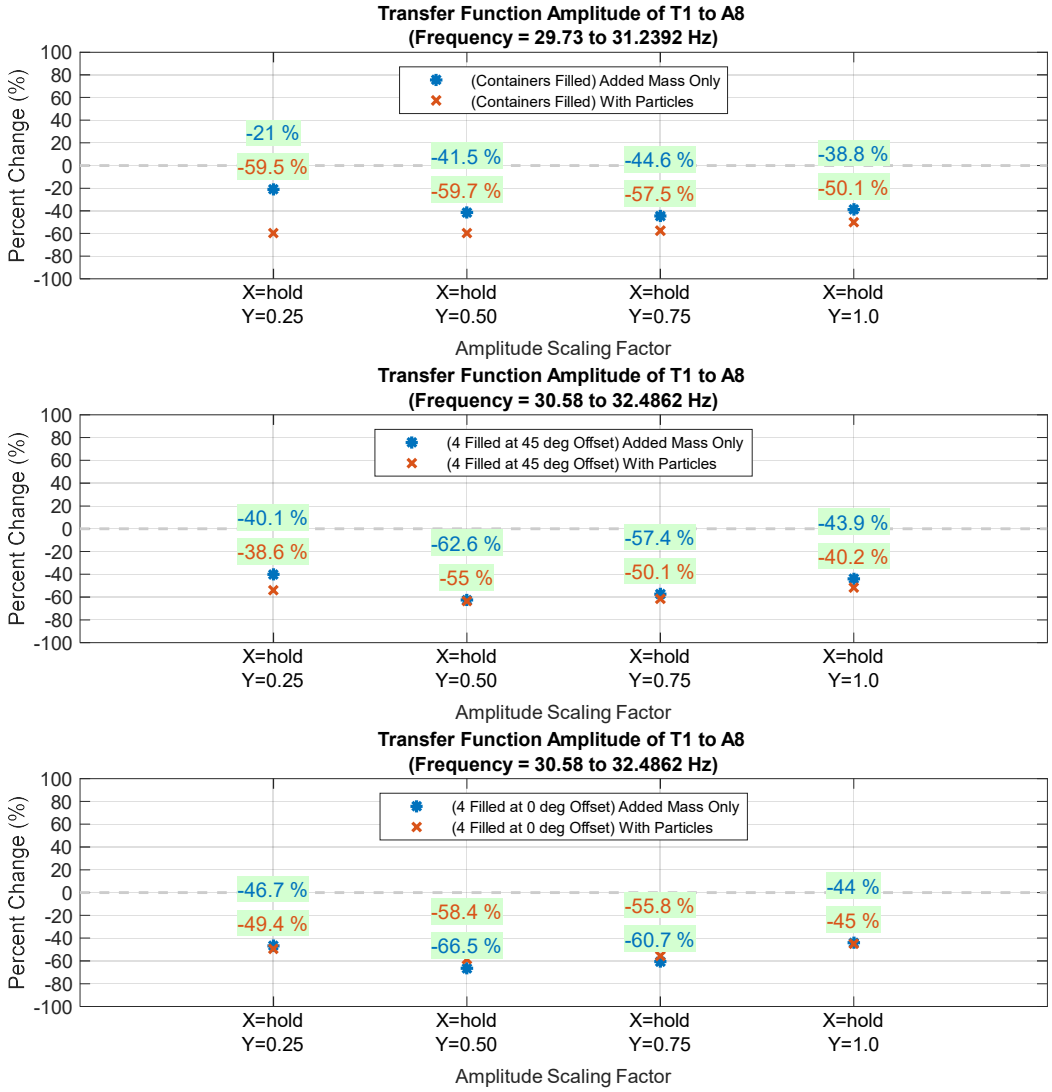


Figure B-43. Percent change in transfer function amplitude response of the +Y sensor at the second bending/top breathing mode, comparing ring particle damper container usages under varying excitation amplitudes applied in the +Y axis of the big shake table. Values are normalized to the corresponding no-particle configuration.

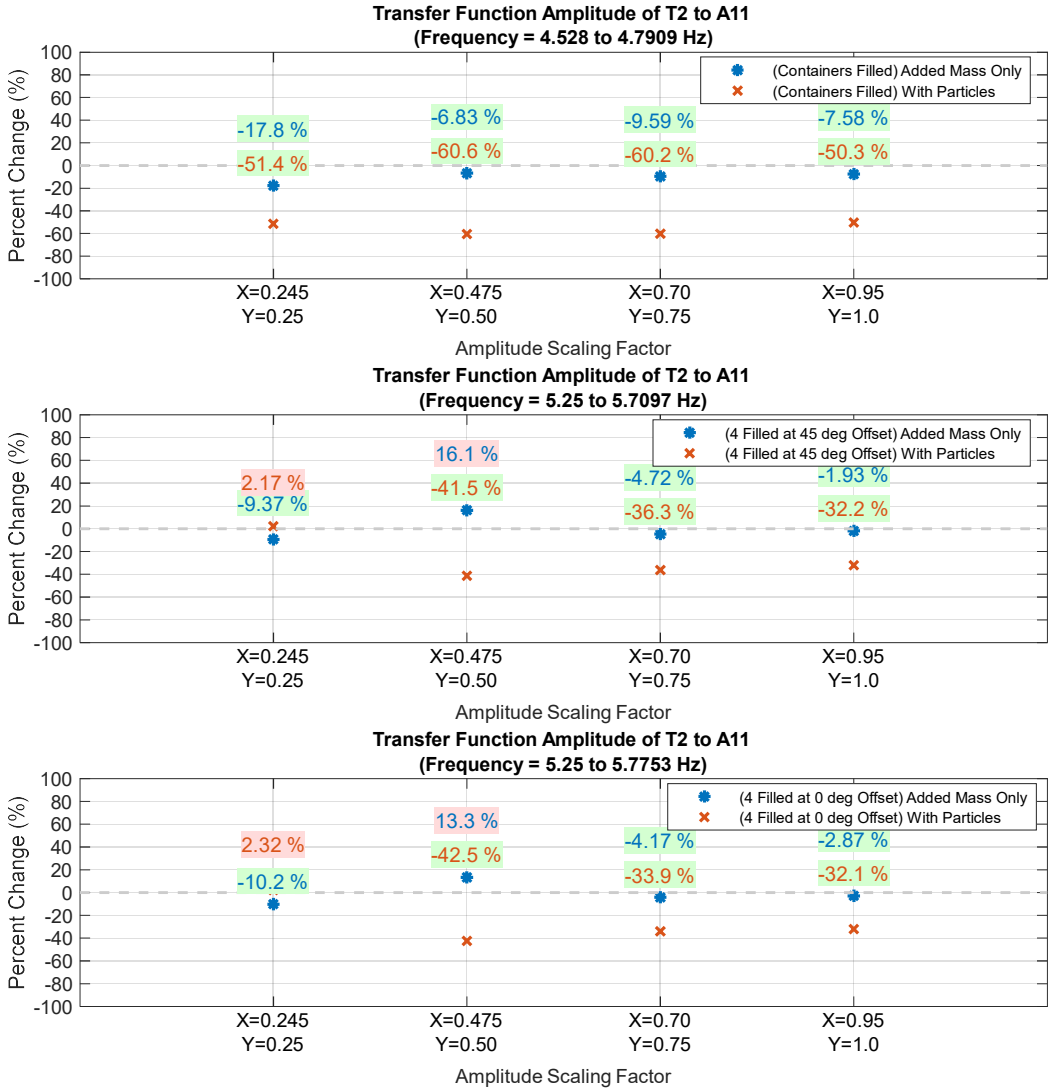


Figure B-44. Percent change in transfer function amplitude response of the +X sensor at the first bending mode, comparing ring particle damper container usages under varying excitation amplitudes applied simultaneously in the +X and +Y axes of the big shake table. Values are normalized to the corresponding no-particle configuration.

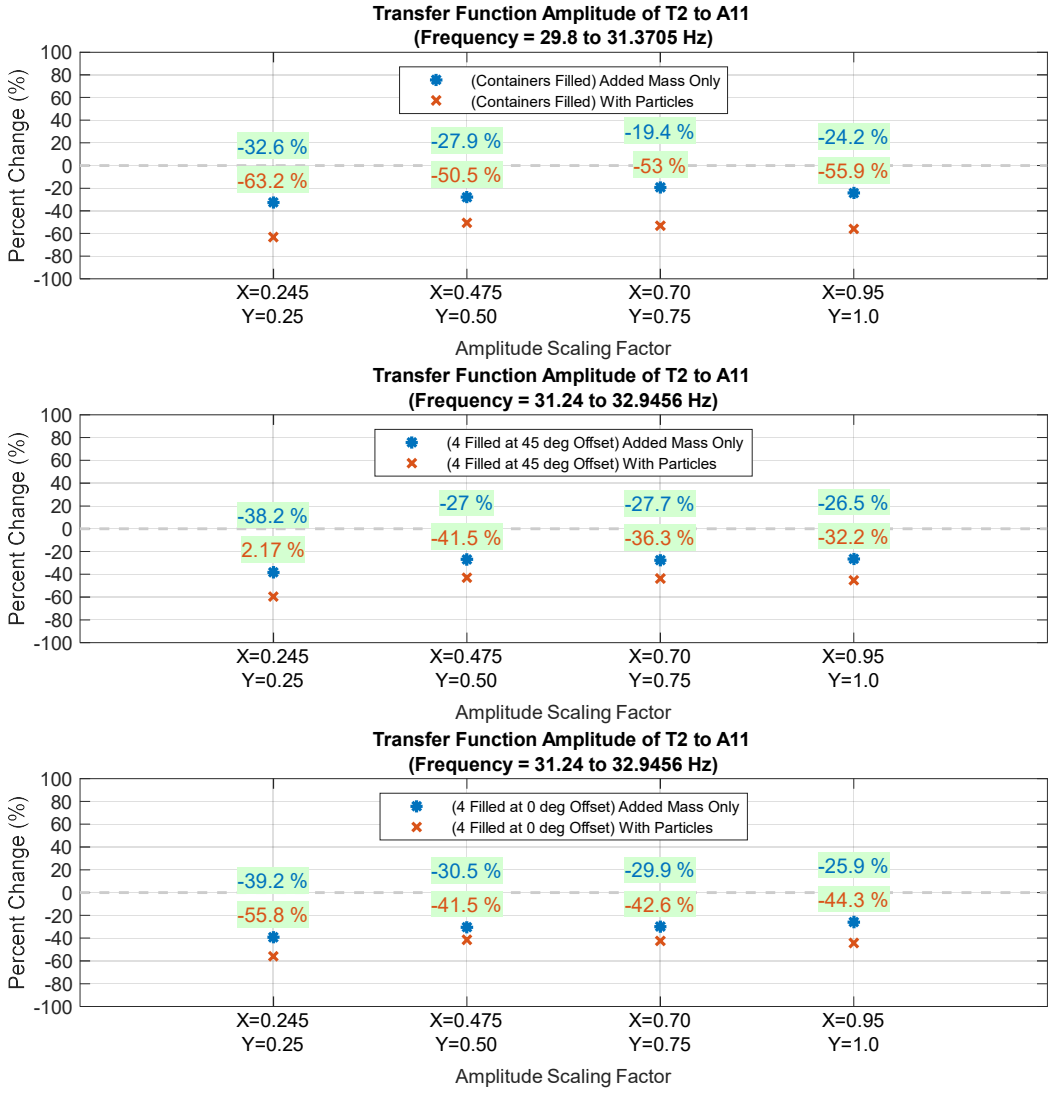


Figure B-45. Percent change in transfer function amplitude response of the +X sensor at the second bending/ top breathing mode, comparing ring particle damper container usages under varying excitation amplitudes applied simultaneously in the +X and +Y axes of the big shake table. Values are normalized to the corresponding no-particle configuration.

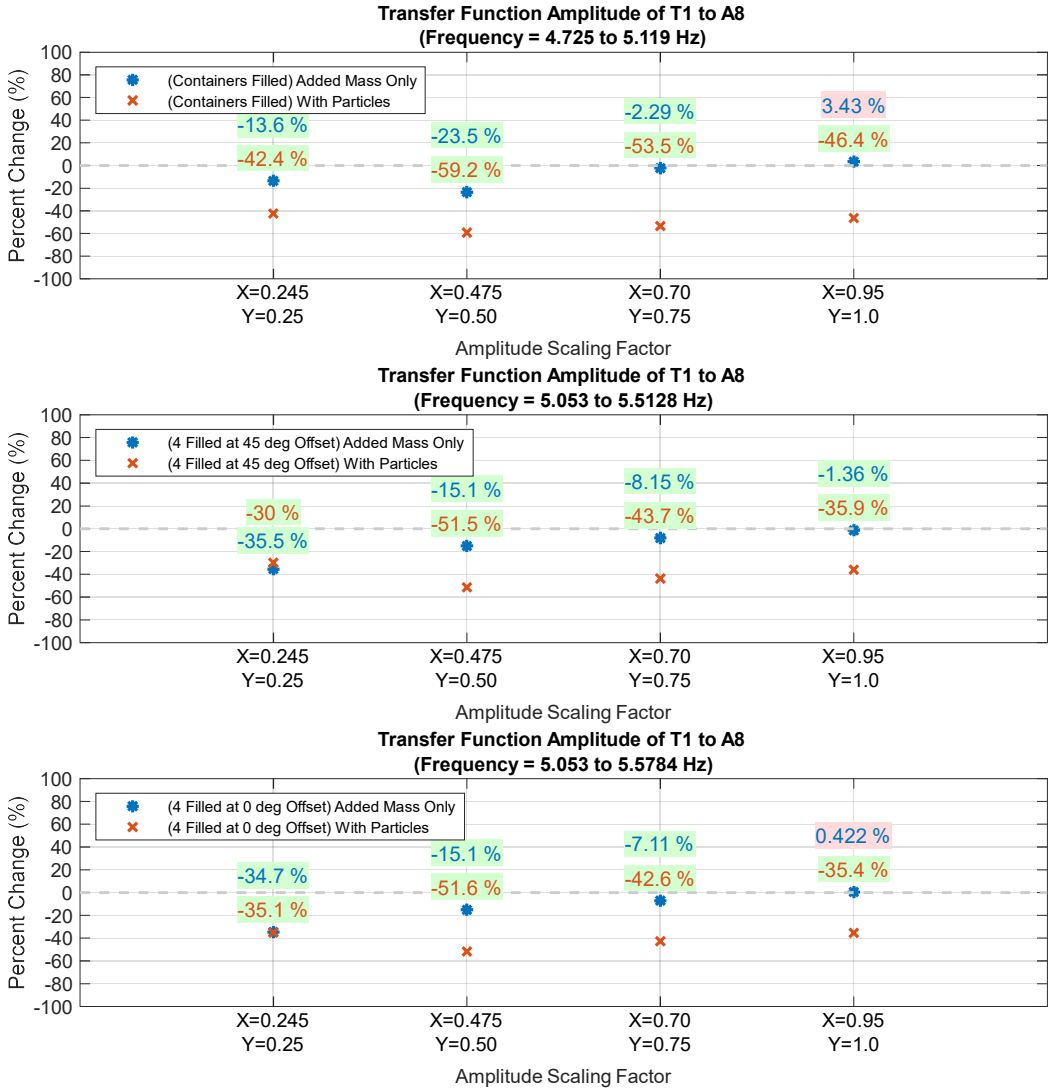


Figure B-46. Percent change in transfer function amplitude response of the +Y sensor at the first bending mode, comparing ring particle damper container usages under varying excitation amplitudes applied simultaneously in the +X and +Y axes of the big shake table. Values are normalized to the corresponding no-particle configuration.

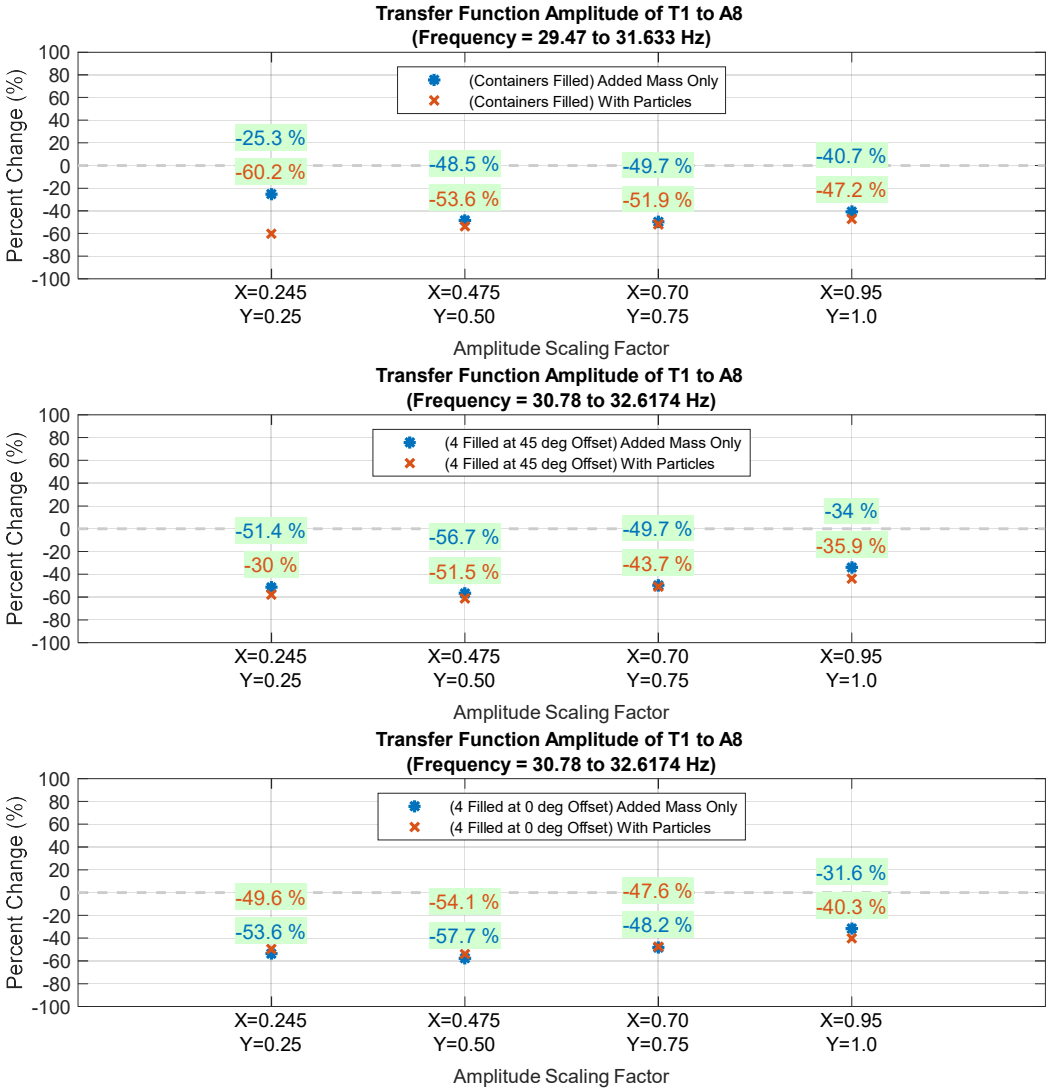


Figure B-47. Percent change in transfer function amplitude response of the +Y sensor at the second bending/ top breathing mode, comparing ring particle damper container usages under varying excitation amplitudes applied simultaneously in the +X and +Y axes of the big shake table. Values are normalized to the corresponding no-particle configuration.



Figure B-48. Percent change in H2 response of the +X sensor, comparing ring particle damper container usages under varying excitation amplitudes applied in the +X axis of the big shake table. Values are normalized to the corresponding no-particle configuration.



Figure B-49. Percent change in H∞ response of the +X sensor, comparing ring particle damper container usages under varying excitation amplitudes applied in the +X axis of the big shake table. Values are normalized to the corresponding no-particle configuration.



Figure B-50. Percent change in H2 response of the +Y sensor, comparing ring particle damper container usages under varying excitation amplitudes applied in the +Y axis of the big shake table. Values are normalized to the corresponding no-particle configuration.



Figure B-51. Percent change in H∞ response of the +Y sensor, comparing ring particle damper container usages under varying excitation amplitudes applied in the +Y axis of the big shake table. Values are normalized to the corresponding no-particle configuration.

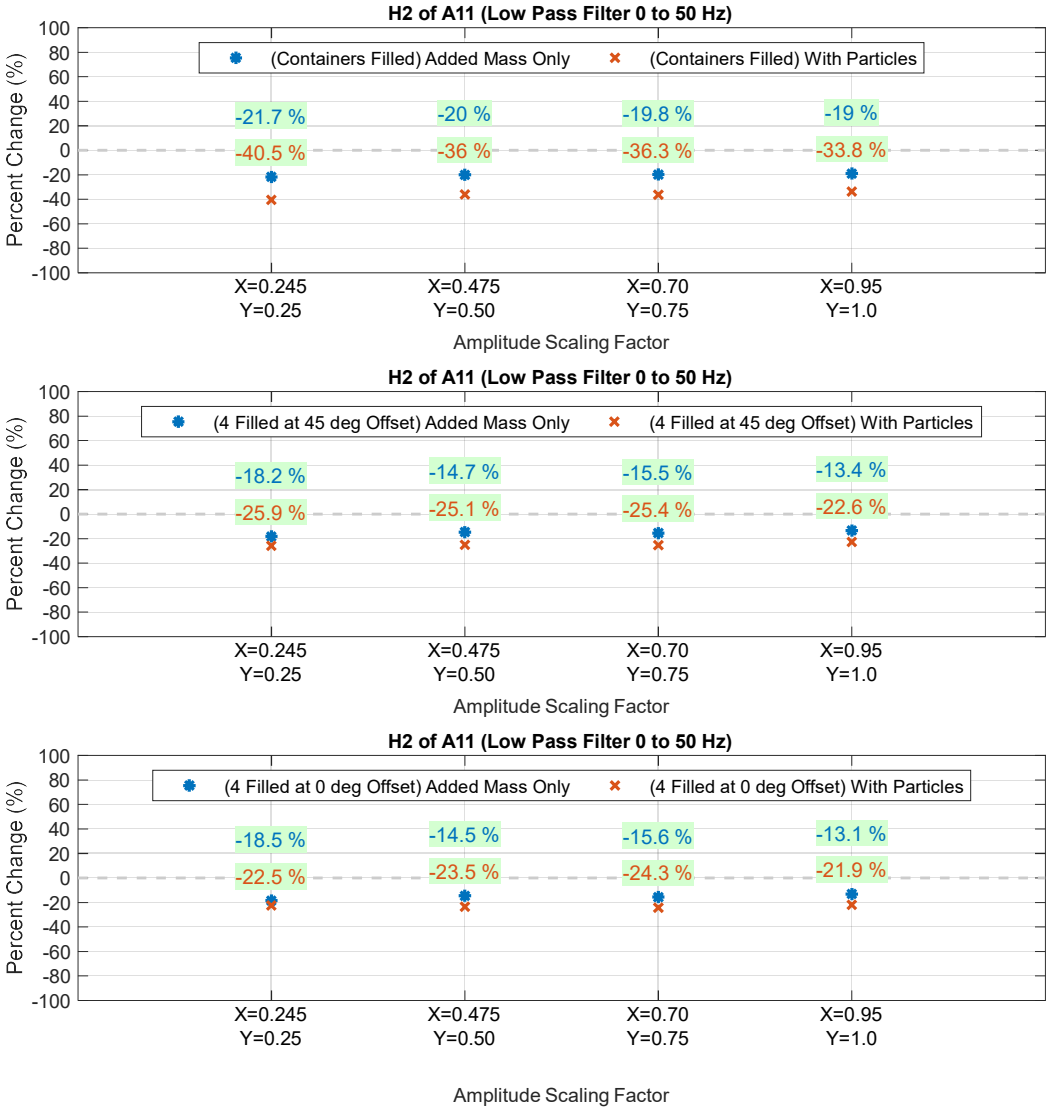


Figure B-52. Percent change in H2 response of the +X sensor, comparing ring particle damper container usages under varying excitation amplitudes applied simultaneously in the +X and +Y axes of the big shake table. Values are normalized to the corresponding no-particle configuration.

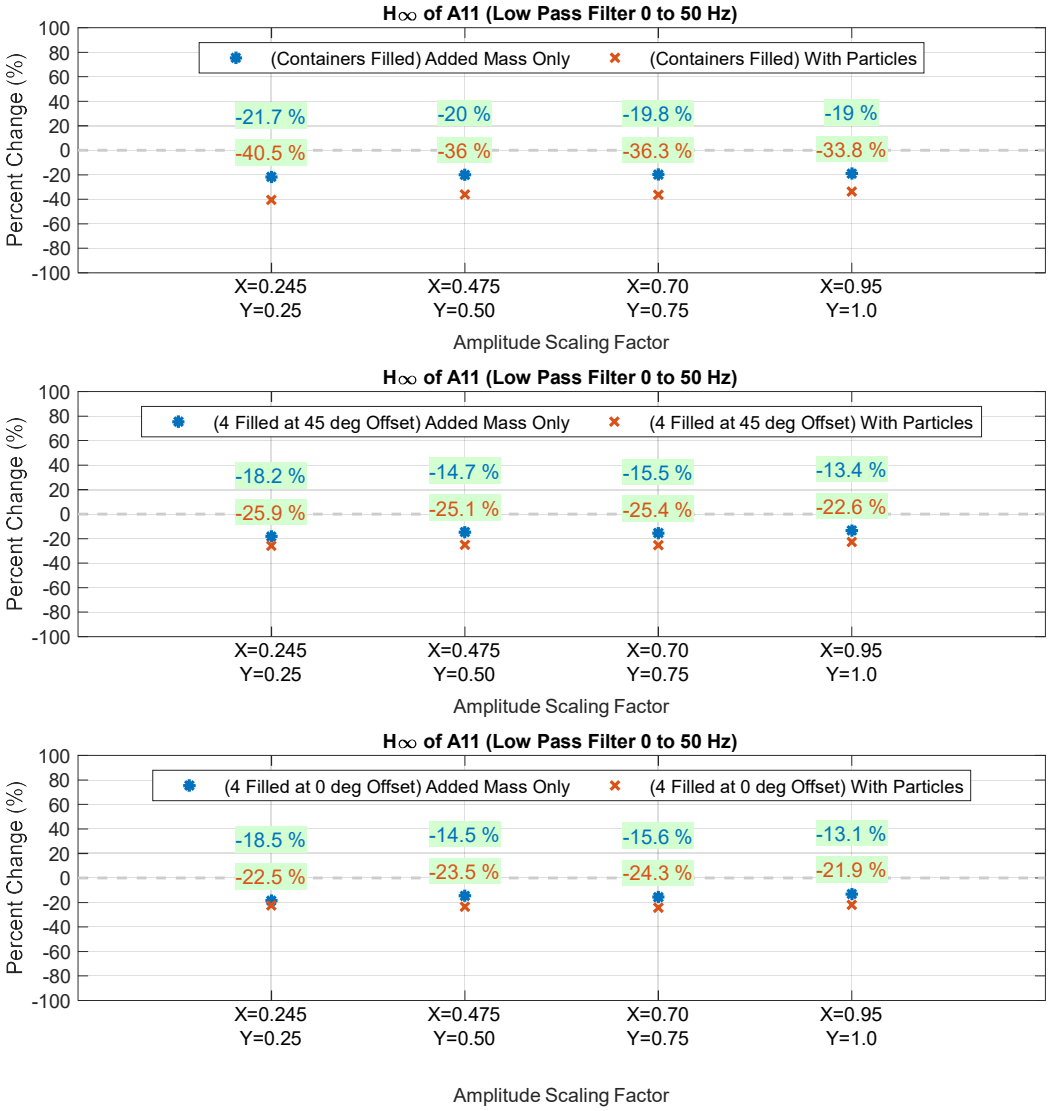


Figure B-53. Percent change in H∞ response of the +X sensor, comparing ring particle damper container usages under varying excitation amplitudes applied simultaneously in the +X and +Y axes of the big shake table. Values are normalized to the corresponding no-particle configuration.



Figure B-54. Percent change in H2 response of the +Y sensor, comparing ring particle damper container usages under varying excitation amplitudes applied simultaneously in the +X and +Y axes of the big shake table. Values are normalized to the corresponding no-particle configuration.



Figure B-55. Percent change in H∞ response of the +Y sensor, comparing ring particle damper container usages under varying excitation amplitudes applied simultaneously in the +X and +Y axes of the big shake table. Values are normalized to the corresponding no-particle configuration.

B.4 Torsional Excitation

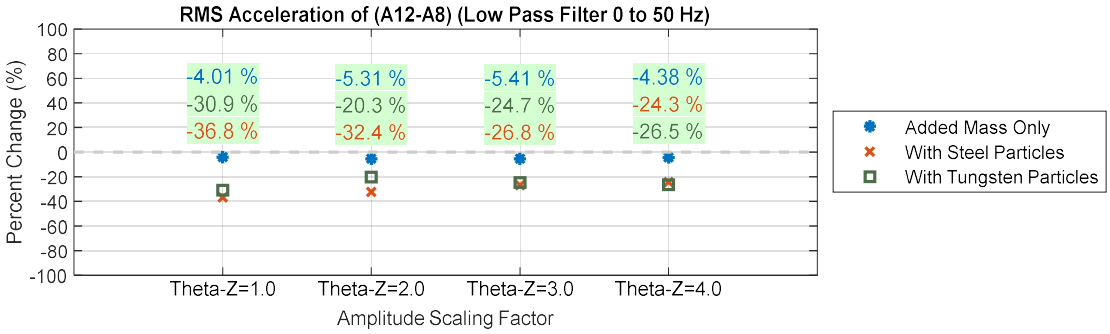


Figure B-56. Percent change in RMS response of the torsion sensor (A12-A8), comparing particle material type under varying torsional excitation amplitudes applied in the theta-Z axis of the big shake table. Values are normalized to the corresponding no-particle configuration.

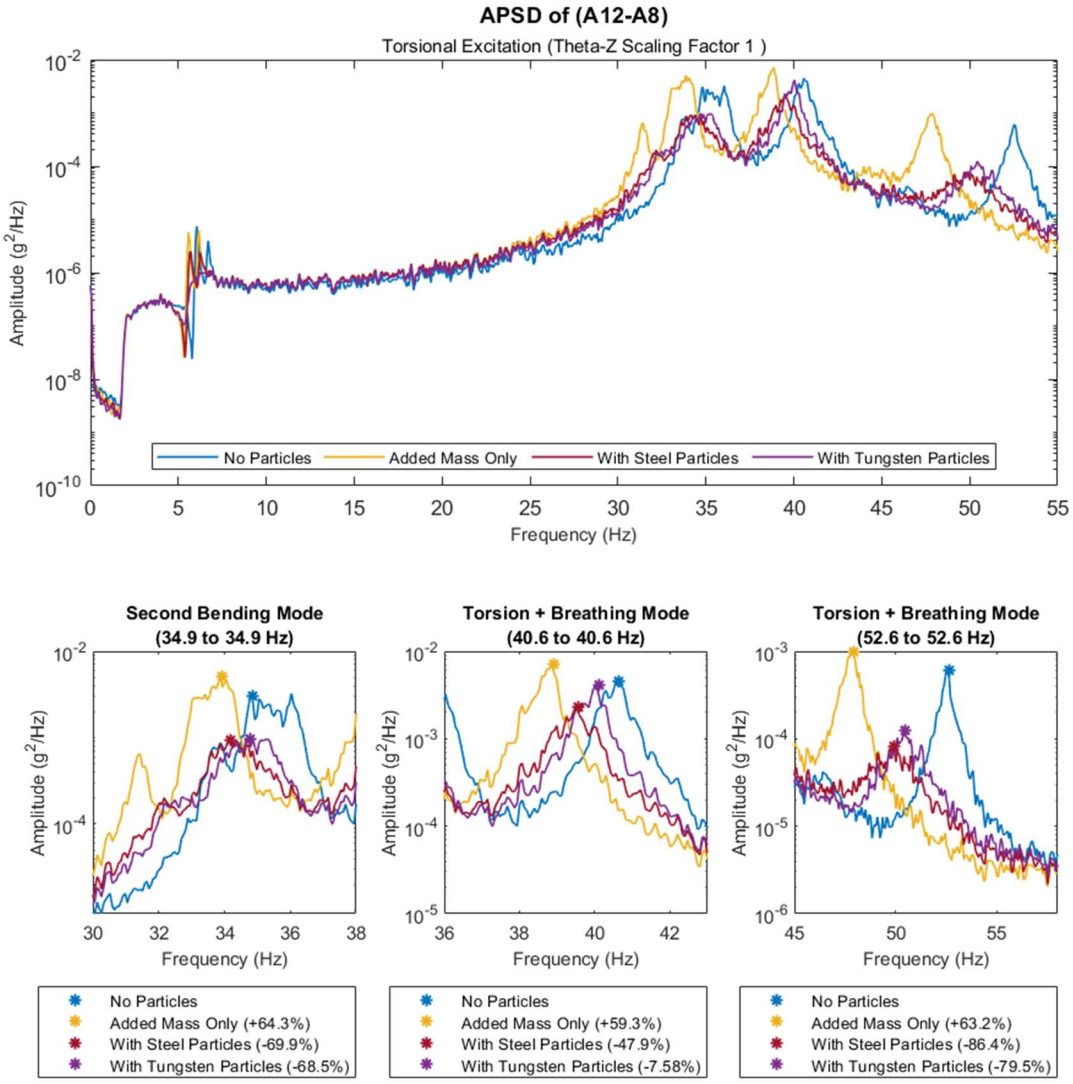


Figure B-57. Frequency response function of the torsion sensor (A12-A8) at second bending modes and torsion/breathing modes, comparing particle material type under varying torsional excitation amplitudes applied in the theta-Z axis (scale factor = 1) of the big shake table. Values are normalized to the corresponding no-particle configuration.

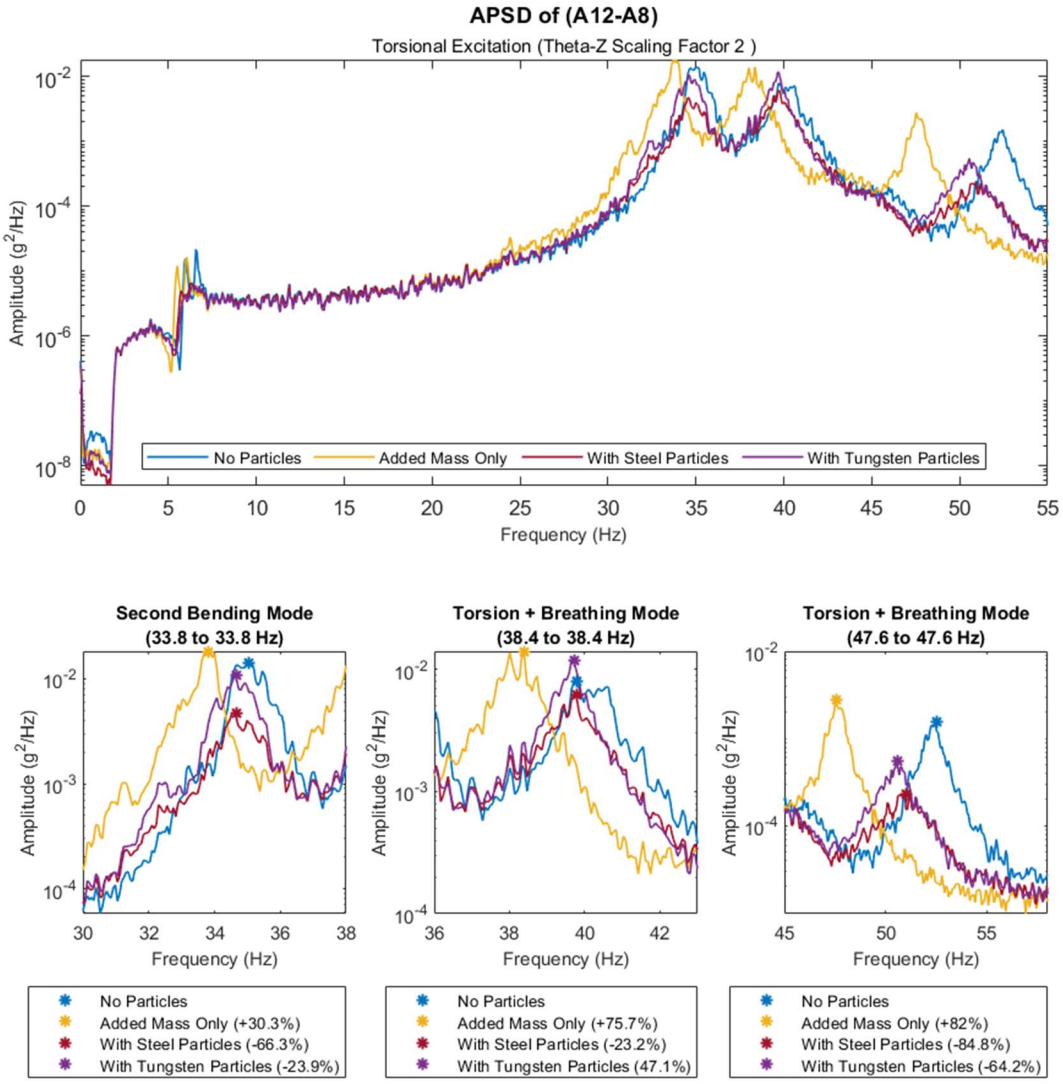


Figure B-58. Frequency response function of the torsion sensor (A12-A8) at second bending modes and torsion/breathing modes, comparing particle material type under varying torsional excitation amplitudes applied in the theta-Z axis (scale factor = 2) of the big shake table. Values are normalized to the corresponding no-particle configuration.

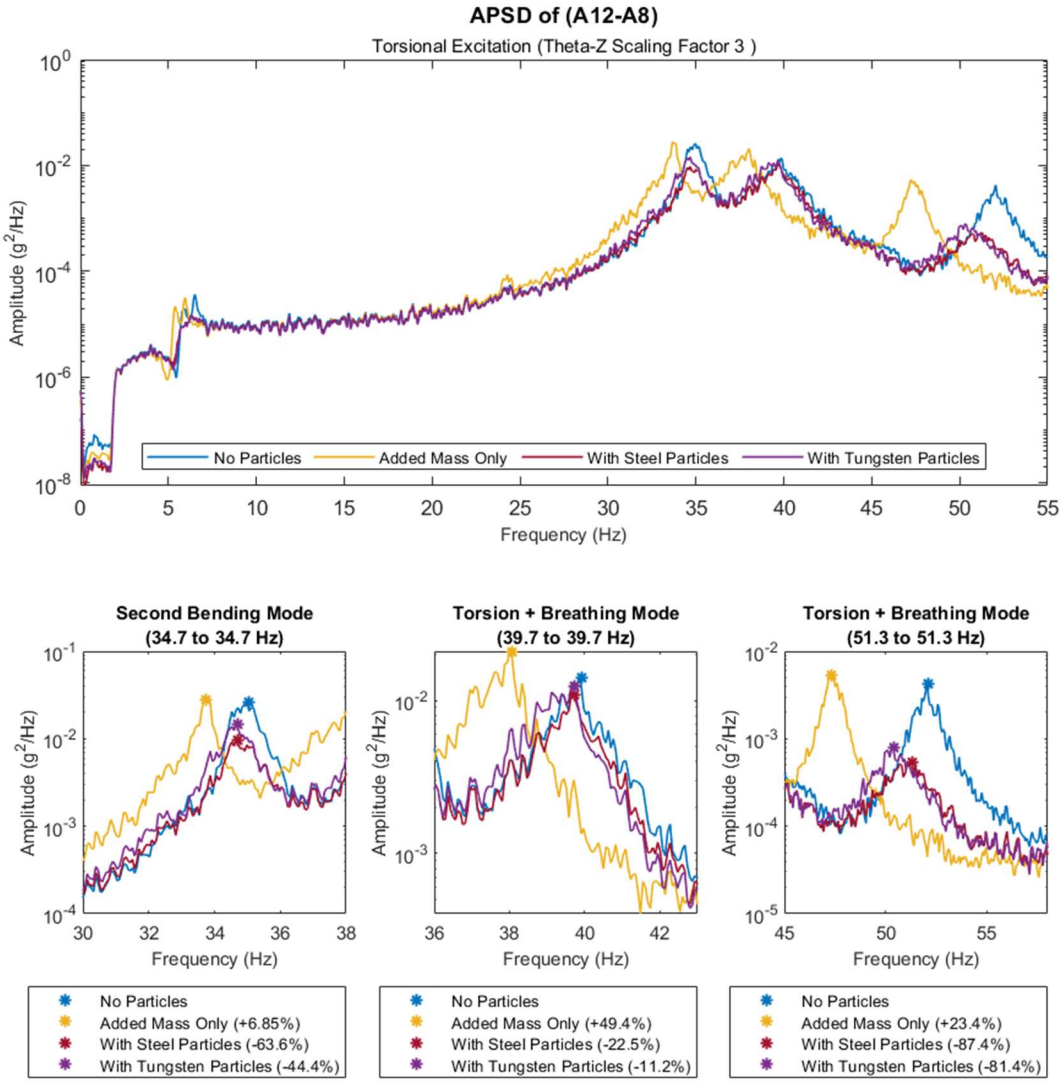


Figure B-59. Frequency response function of the torsion sensor (A12-A8) at second bending modes and torsion/breathing modes, comparing particle material type under varying torsional excitation amplitudes applied in the theta-Z axis (scale factor = 3) of the big shake table. Values are normalized to the corresponding no-particle configuration.

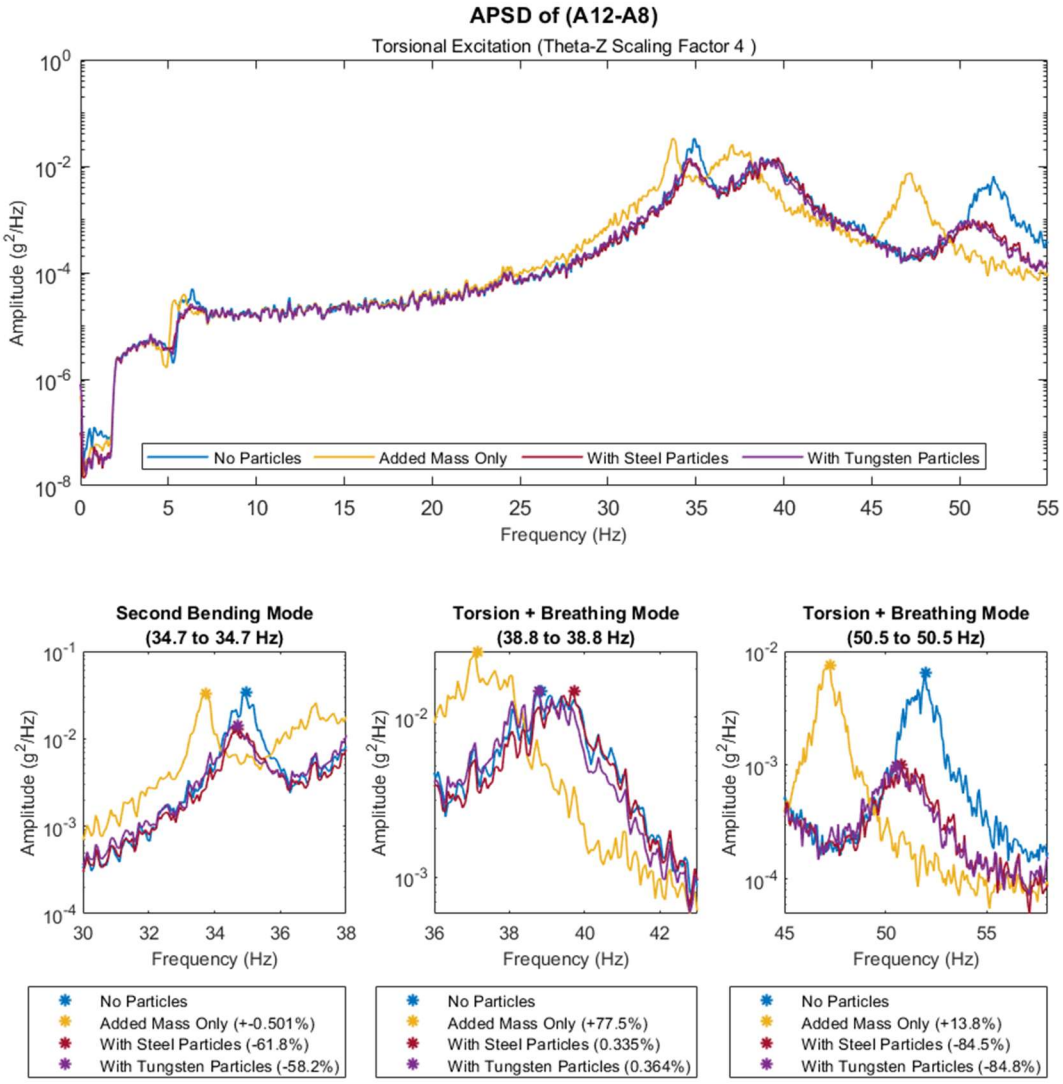


Figure B-60. Frequency response function of the torsion sensor (A12-A8) at second bending modes and torsion/breathing modes, comparing particle material type under varying torsional excitation amplitudes applied in the theta-Z axis (scale factor = 4) of the big shake table. Values are normalized to the corresponding no-particle configuration.

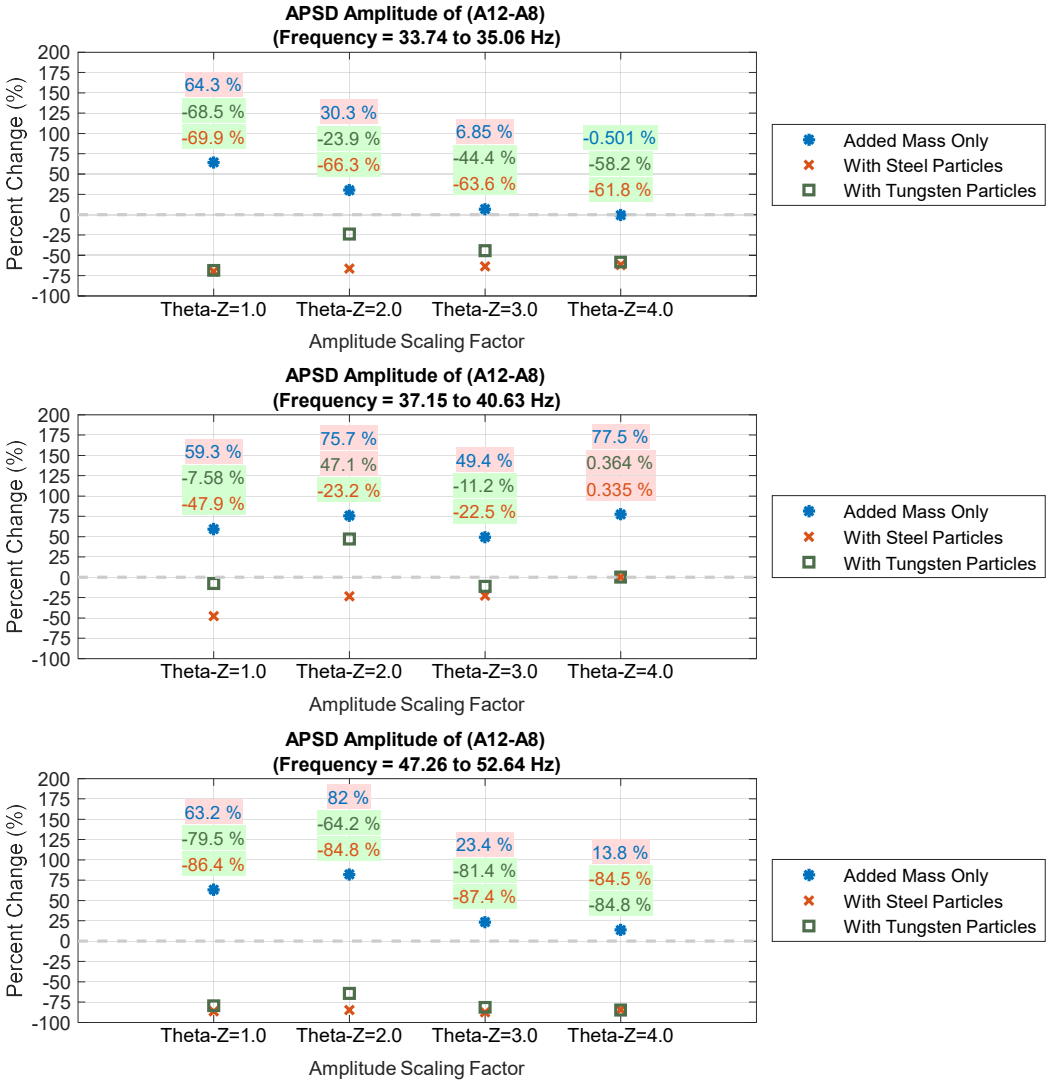


Figure B-61. Percent change in APSD amplitude response of the torsion sensor (A12-A8) at second bending modes and torsion/breathing modes, comparing particle material type under varying torsional excitation amplitudes applied in the theta-Z axis of the big shake table. Values are normalized to the corresponding no-particle configuration.

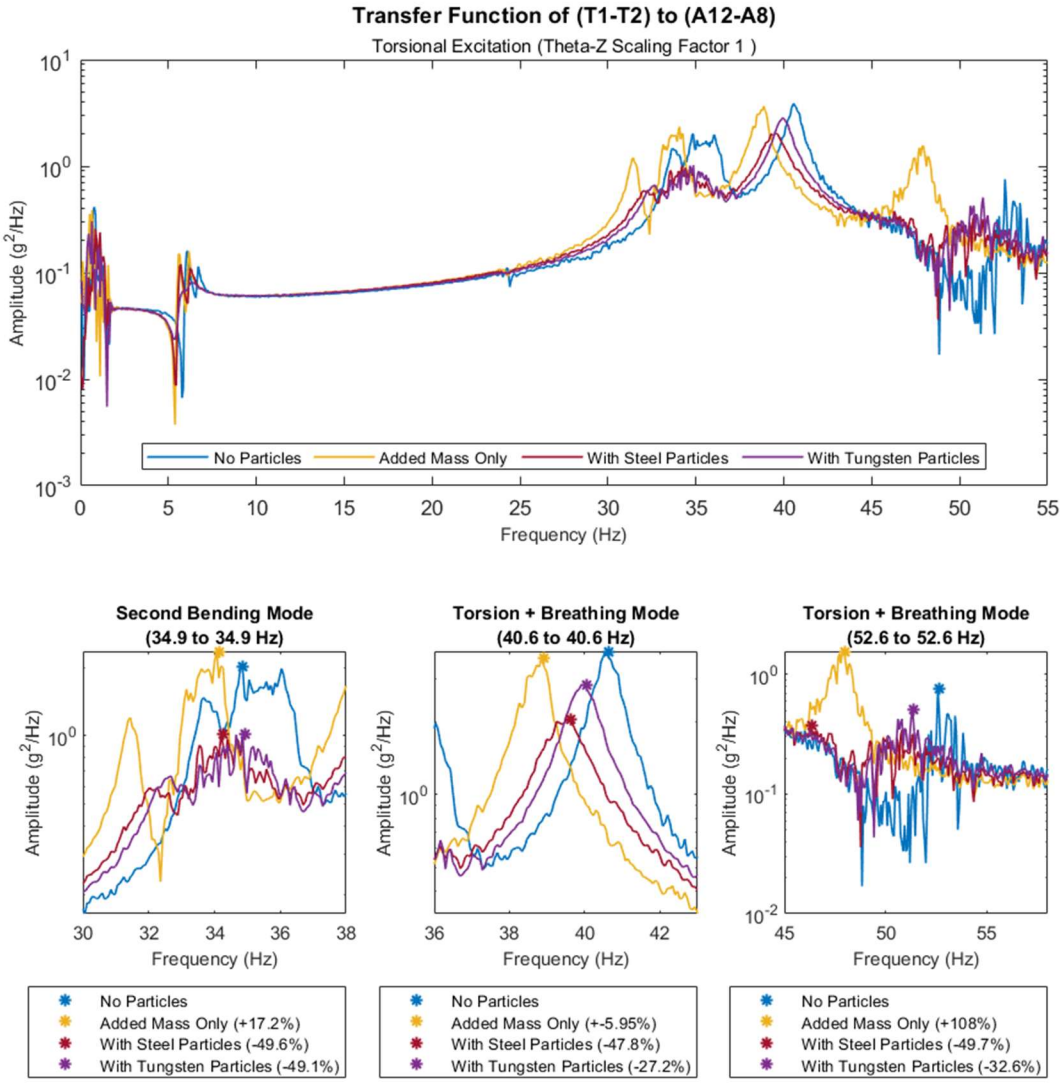


Figure B-62. Frequency response function of the torsion sensor (A12-A8) at second bending modes and torsion/breathing modes, comparing particle material type under varying torsional excitation amplitudes applied in the theta-Z axis (scale factor = 1) of the big shake table. Values are normalized to the corresponding no-particle configuration.

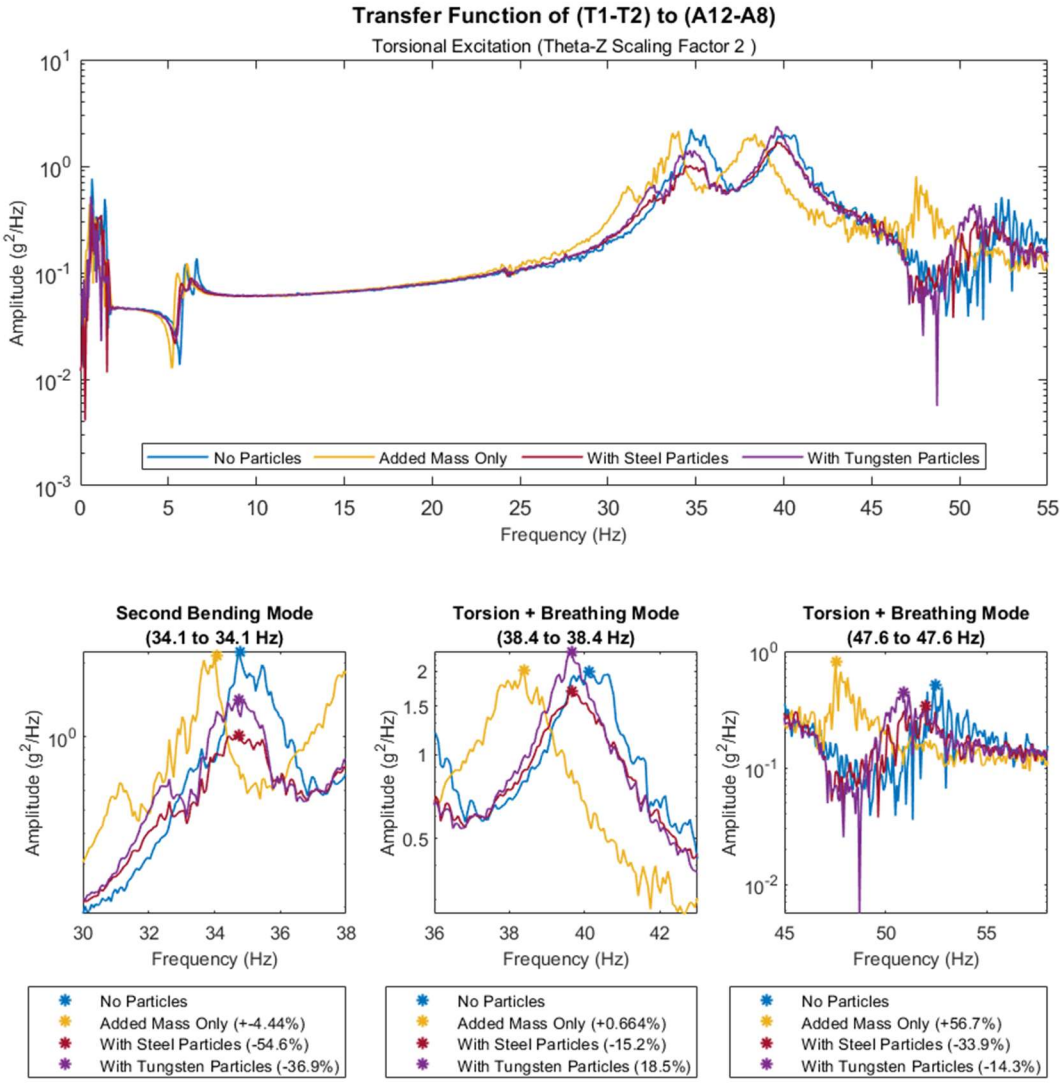


Figure B-63. Frequency response function of the torsion sensor (A12-A8) at second bending modes and torsion/breathing modes, comparing particle material type under varying torsional excitation amplitudes applied in the theta-Z axis (scale factor = 2) of the big shake table. Values are normalized to the corresponding no-particle configuration.

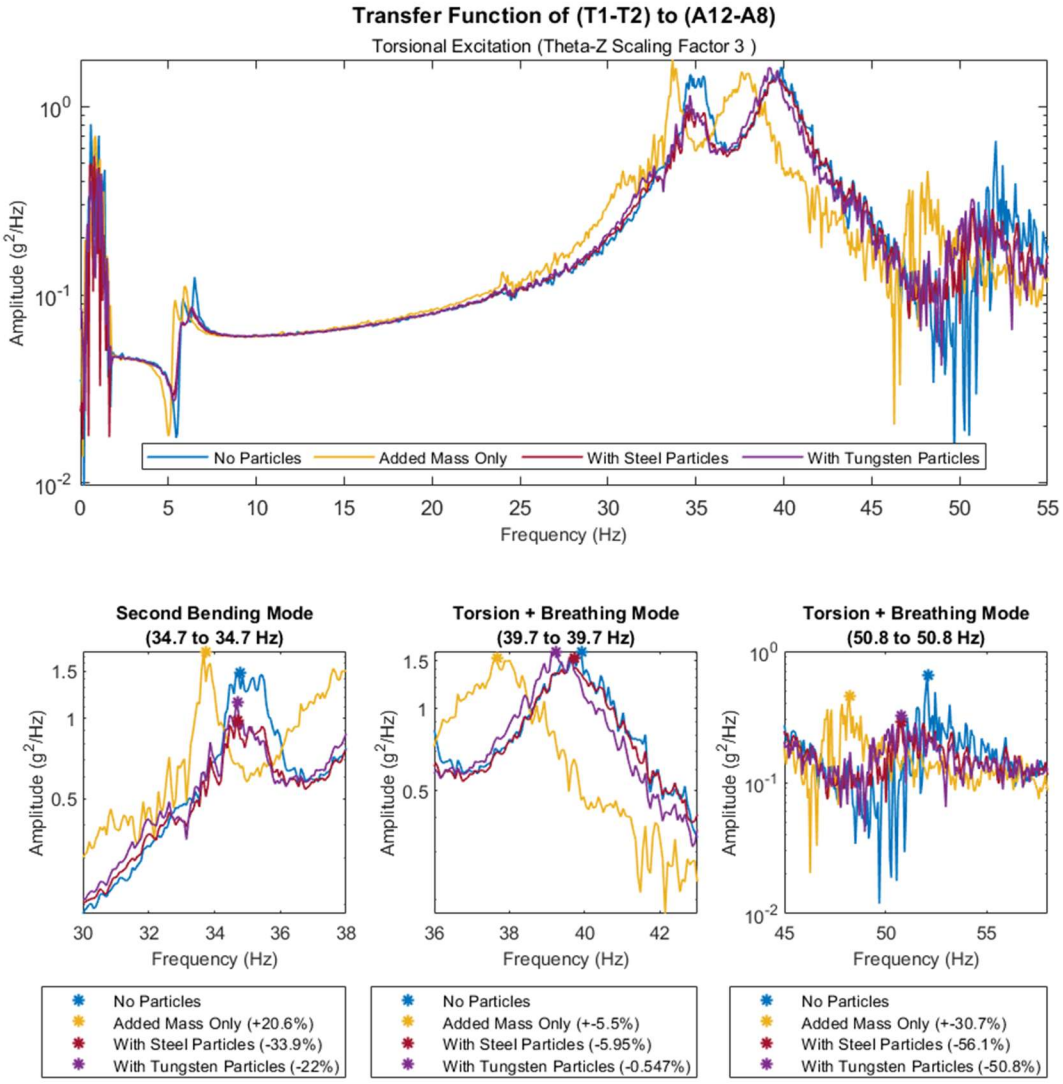


Figure B-64. Frequency response function of the torsion sensor (A12-A8) at second bending modes and torsion/breathing modes, comparing particle material type under varying torsional excitation amplitudes applied in the theta-Z axis (scale factor = 3) of the big shake table. Values are normalized to the corresponding no-particle configuration.

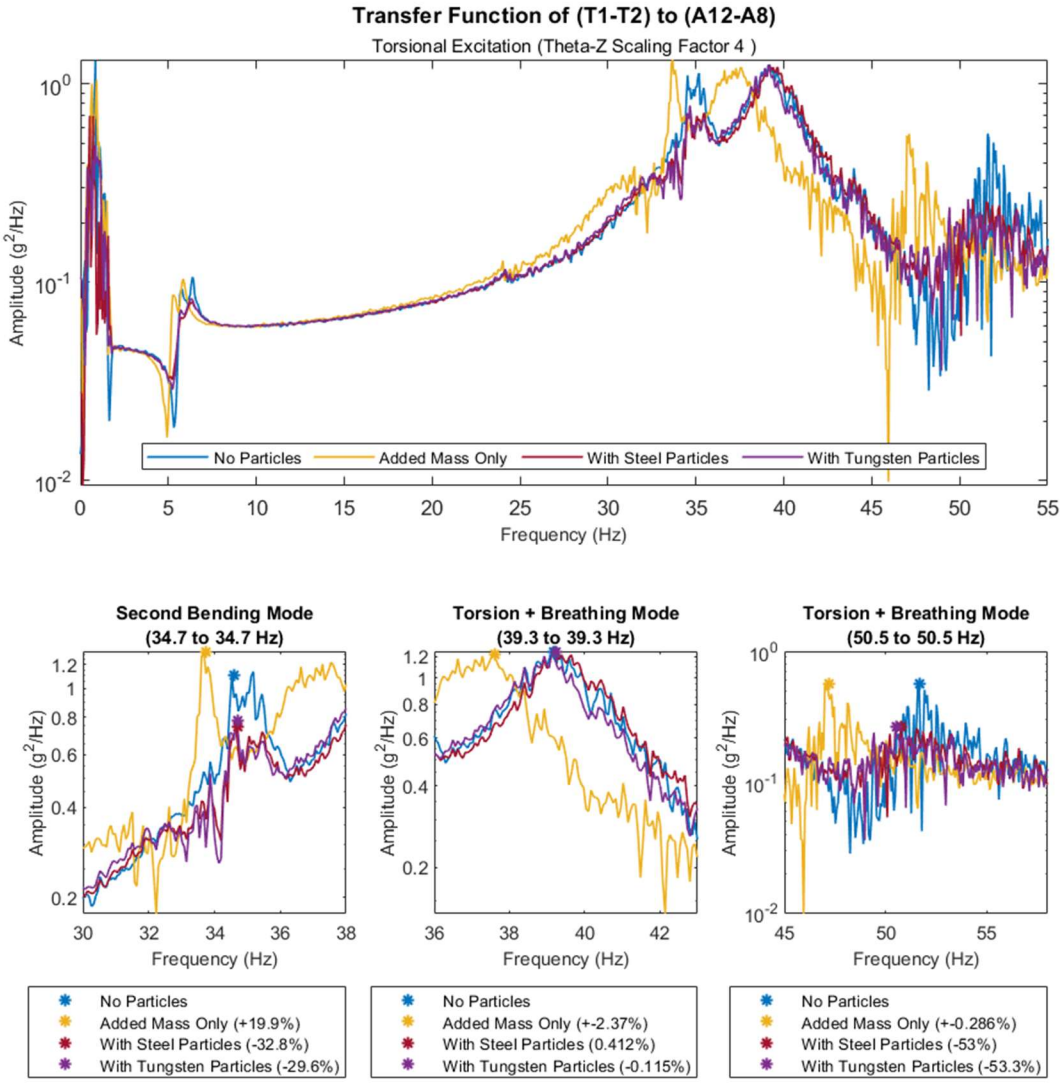


Figure B-65. Frequency response function of the torsion sensor (A12-A8) at second bending modes and torsion/breathing modes, comparing particle material type under varying torsional excitation amplitudes applied in the theta-Z axis (scale factor = 4) of the big shake table. Values are normalized to the corresponding no-particle configuration.

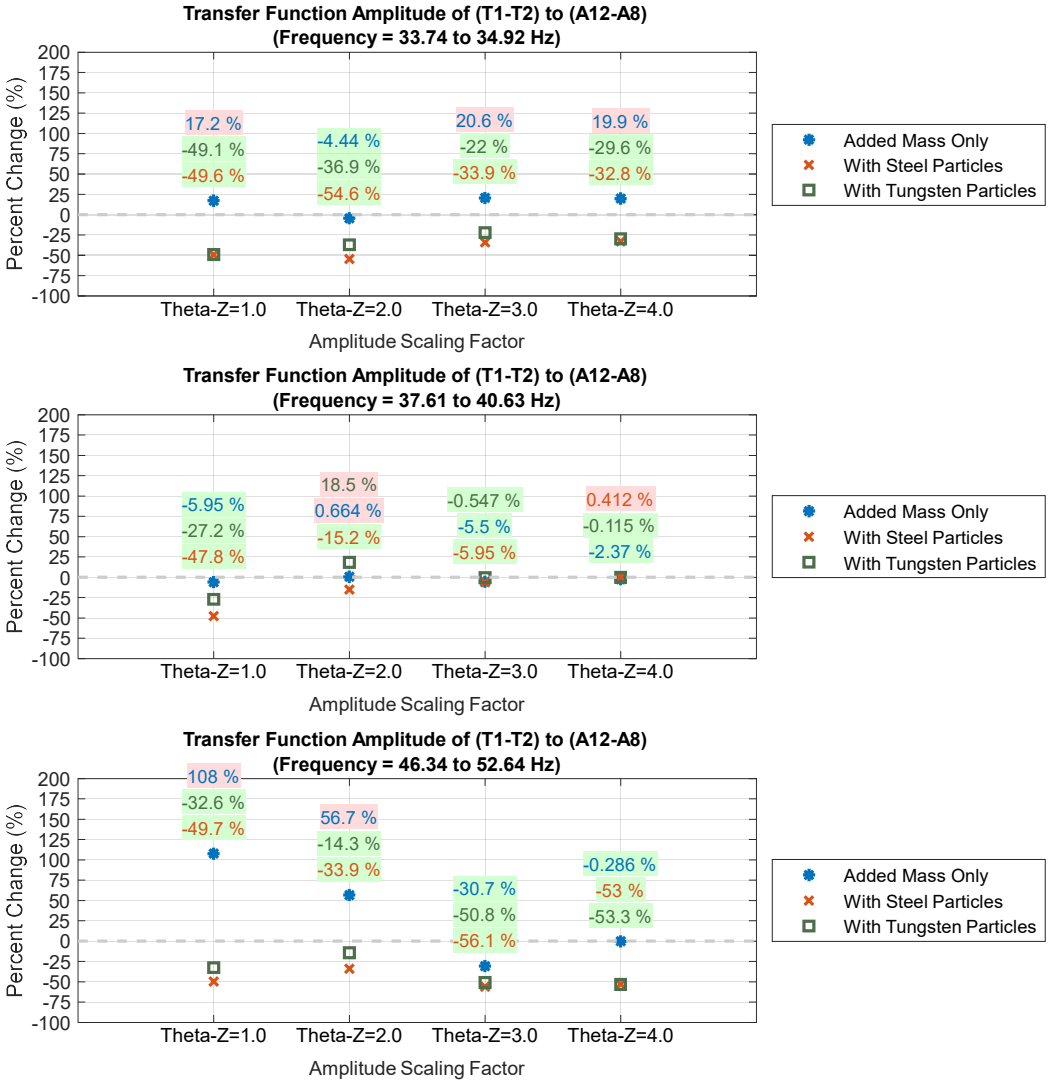


Figure B-66. Percent change in transfer function response of the torsion sensor (A12-A8) at second bending modes and torsion/breathing modes, comparing particle material type under varying torsional excitation amplitudes applied in the theta-Z axis of the big shake table. Values are normalized to the corresponding no-particle configuration.

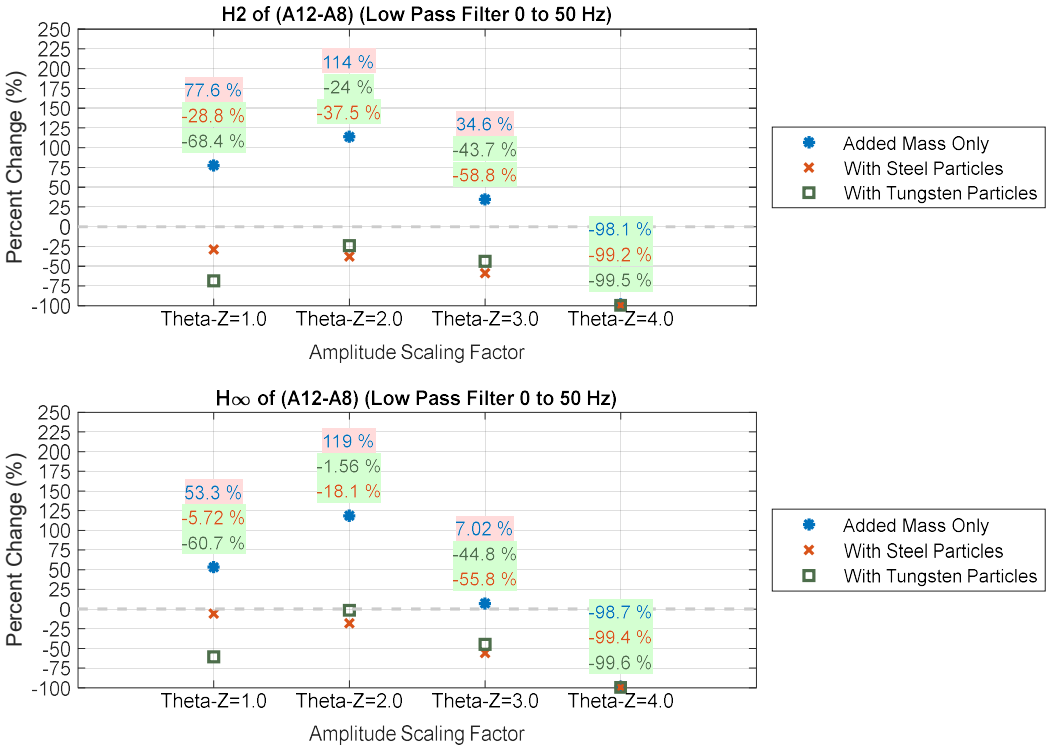


Figure B-67. Percent change in frequency domain response metrics (H2 and H∞) of the torsion sensor (A12-A8), comparing particle material type under varying torsional excitation amplitudes applied in the theta-Z axis of the big shake table. Values are normalized to the corresponding no-particle configuration.